Non-linear THz sources for time domain spectroscopy

Moses Eshovo Ojo

To cite this version:

Moses Eshovo Ojo. Non-linear THz sources for time domain spectroscopy. Physics [physics]. Université de Bordeaux, 2023. English. NNT : 2023BORD0126 . tel-04187137

HAL Id: tel-04187137
https://theses.hal.science/tel-04187137v1

Submitted on 24 Aug 2023

THÈSE PRÉSENTÉE
POUR OBTENIR LE GRADE DE

DOCTEUR DE
L'UNIVERSITÉ DE BORDEAUX

ÉCOLE DOCTORALE DES SCIENCES PHYSIQUES ET DE L'INGÉNIEUR
LASERS, MATIÉRE, NANOSCIENCES

Par Moses Eshovo OJO

Sources THz Non-lineaires pour la Spectroscopie Résolue en Temps

Soutenue le 24 Mai 2023

Membres du jury:

M. ZIMMER, Thomas	Professeur	Université de Bordeaux, Laboratoire IMS	Président
M. GARET, Frederic	Professeur	Université Savoie Mont-Blanc Laboratoire IMEP-LAHC	Rapporteur
M. GALLOT, Guilhem	Directeur de Recherche	Ecole Polytechnique Paris, Laboratoire LOB	Rapporteur
M. TORRES, Jeremie	Maître de conférences	Université de Montpellier, Laboratoire IES	Examinateur
M. BIGOURD, Damien	Chargé de Recherche	Université de Bordeaux, Laboratoire IMS	Directeur de thése
M. MOUNAIX, Patrick	Directeur de Recherche	Université de Bordeaux, Laboratoire IMS	co-Directeur de thése

Titre : Sources THz Non-lineaires pour la Spectroscopie Résolue en Temps

Résumé : L'objectif de cette thèse est d'étudier différents types de spectromètre dans le domaine THz grâce à une génération par rectification optique et une détection électrooptique. La génération THz a été réalisée à l'aide de deux cristaux non linéaires de ZnTe et BNA. En utilisant le ZnTe comme émetteur, un champ électrique THz bipolaire d'une durée de 1 ps a été généré par rectification optique associé à un spectre THz étroit centré à 0,5 THz. La détection a été réalisée par un échantillonnage électrooptique dans un cristal de ZnTe de 1 mm d'épaisseur. L'expérience a été réalisée à l'aide d'un laser ytterbium émettant un spectre centré à 1030 nm et une durée d'impulsion de 500 fs. De même, des impulsions THz à cycles multiples ont été générées en remplaçant l'émetteur de ZnTe par un cristal de BNA de 390 µm d'épaisseur. La durée de l'impulsion THz générée était inférieure à 1 ps, avec une bande passante spectrale de 0,5 THz et une fréquence centrale de 1,3 THz. En complément, la possibilité de générer et de détecter à la fois des impulsions THz de quelques picosecondes dans le même cristal a été démontrée. Les impulsions THz ont été caractérisées par une détection électrooptique monocoup. Du point de vue applicatif, des échantillons collectés au Nigeria sur un site industriel ont été notamment caractérisés par spectroscopie THz résolue en temps. En effet, les ondes térahertz (THz) sont apparues comme un nouvel outil scientifique et technologique, en particulier dans le domaine de l'industrie pétrolière et gazière. La spectroscopie THz peut détecter diverses vibrations intermoléculaires, du réseau en particulier les structures organiques comme le kérogène présent dans ces échantillons. Les données rapportées complètent d'autres analyses optiques (LIBS et SEM-EDX) et ont révélé plusieurs mélanges d'éléments en plus du carbone, constituant majeur des matières organiques de type kérogènes. Une nette inhomogénéité dans les échantillons a été révélée.

Mots clés : Impulsions THz, rectification optique, échantillonnage électrooptique, détection électrooptique monocoup, schistes bitumineux, imagerie et spectroscopie.

.

Title : Non-linear THz sources for Time Domain Spectroscopy

Abstract : The objective of this thesis is to investigate different types of spectrometers in the THz domain thanks to a generation by optical rectification and an electro-optical detection. THz generation was performed using two nonlinear crystals namely ZnTe and BNA. By using the ZnTe crystal as the emitter, a 1 ps long bipolar THz electric field was generated via optical rectification with a corresponding narrow THz spectrum whose frequency is centered at 0.5 THz. The detection was performed by electro-optic sampling in a 1 mm thick ZnTe crystal. The experiment was carried out using an Ytterbium-based laser whose center wavelength is at 1030 nm and a pulse duration of 500 fs. In the same vein, multicycle THz pulses were generated by replacing the ZnTe emitter with a 390 µm thick BNA crystal. The duration of the generated THz pulse was less than 1 ps, with a spectral bandwidth of 0.5 THz and a center frequency of 1.3 THz. In addition, the feasibility of both generating and detecting few picosecond THz pulse in the same crystal was also demonstrated. The THz pulse was characterized via the single shot electro-optic scheme. On the application point of view, petrological samples made of organic matter were characterized by THz time domain spectroscopy. The aim was to identify the elemental presence of Carbon which are a major constituent of organic matters. A clear inhomogeneity in the samples was revealed. As such, other optical analysis (LIBS and SEM-EDX) was carried out and it revealed several mixtures of elements in addition to Carbon.

Keywords : THz pulses, optical rectification, electro-optic sampling, single shot electro-optic detection, oil shales, spectroscopy and imaging.

Univ. Bordeaux - CNRS - UMR 5107, 33405 Talence, France

Conference presentations and proceedings

Ojo M .E.; Mounaix P.; Fauquet F.; Bigourd D. THz pulse generation and single shot detection in a single ZnTe Crystal. 47th International Conference on Infrared, Millimeter and Terahertz Waves (IRMMW-THz), Delft, Netherlands, 2022, 1-2. doi: 10.1109/IRMMW-THz50927.2022.9895739.

Ojo M. E.; Mounaix P.; Fauquet F.; Bigourd D. THz spectroscopic characterization of oil shales. 47th International Conference on Infrared, Millimeter and Terahertz Waves (IRMMW-THz), Delft, Netherlands, 2022, 1-2. doi: 10.1109/IRMMW-THz50927.2022.9895914.

Ojo M. E.; Mounaix P.; Fauquet F.; Bigourd D. THz generation and single shot detection in a single-crystal layout. French-German TeraHertz Conference 2022, Grande Motte, France. https://hal.archives-ouvertes.fr/hal-03777627/document

Ojo M. E.; Mounaix P.; Fauquet F.; Bigourd D. THz-based spectral images of oil shales. French-German TeraHertz Conference 2022, Grande Motte, France. https://hal.archives-ouvertes.fr/hal-03777626

Journal publications

Ojo M. E.; Fauquet F.; Mounaix P.; Bigourd D. THz Pulse Generation and Detection in a Single Crystal Layout. Photonics, 2023, 10, 1-11. https://doi.org/10.3390/photonics10030316

Ojo M. E.; Mounaix P.; Fauquet F.; Bigourd D. Investigation of Oil shale response using THz- TDS. Petroleum Technology Journal, 2021, 12, 81- 98. https://www.ptdjournal.com/?page_id=8

List of abbreviations

BPANN: Back Propagation Artificial Neural Network

CCD: Charge Coupled Device

CPA: Chirped Pulse Amplifier

DFG: Difference Frequency Generation

DTA: Differential Thermal Analysis

EM: ElectroMagnetic

EOS: Electro-Optical Sampling

FCA: Free Carrier Absorption

FROG: Frequency Resolved Optical Gating

FWHM: Full Wave at Half Maximum

LIBS: Laser Induced Breakdown Spectroscopy

LIA: Lock In Amplifier

OAPM: Off Axis Parabolic Mirror

OR: Optical Rectification

GC-MS: Gas Chromatography- Mass Spectrometer

PCA: Photoconductive Antennae

SEM-EDX: Scanning Electron Microscope-Electron Dispersive X-ray

THz-TDS: TeraHertz- Time Domain Spectroscopy

TGA: Thermo-Gravimetric Analysis

TPA: Two Photon Absorption

Résumé

Les sources THz ont été de plus en plus développées au cours des dernières décennies, en raison de la disponibilité et de la commercialisation croissantes de lasers Ti:Saphir ultrarapides générant des impulsions femtosecondes à la longueur d'onde centrale de 800 nm. Récemment, les lasers femtosecondes à ions ytterbium (Yb) sont devenus une alternative prometteuse aux sources Ti:Saphir en raison de leurs avantages évidents en termes de stabilité, de compacité et de puissance moyenne élevée grâce à un taux de répétition élevé rendant ces lasers très compétitifs. Ce travail de thèse exploite ces sources laser avec différents types de spectromètres dans le domaine THz grâce à une génération par redressement optique et une détection électro-optique. Les mécanismes d'émission et de détection ont d'abord été étudiés théoriquement et numériquement dans les chapitres 2 et 3 pour pouvoir concevoir des spectromètres résolus en temps. Les résultats expérimentaux de ce travail sont divisés en trois parties et décrits dans les chapitres 4 et 5. La première partie traite de la théorie de la génération et de la détection du THz. La deuxième partie traite des études expérimentales sur la génération et la détection d'impulsions THz, tandis que la troisième partie étudie l'application de la spectroscopie THz sur des échantillons de schiste bitumineux. Dans cette dernière partie, les mesures spectroscopiques ont été complétées par d'autres mesures optiques.

L'optimisation de la génération THz dans les cristaux non linéaires réside dans la compréhension théorique de la rectification optique. Ainsi, il a été réalisé que, pour un processus de génération efficace, la vitesse de groupe de l'impulsion optique doit être bien adaptée à la vitesse de phase de l'impulsion THz pour une source laser donnée. Même pour une longueur d'onde laser appropriée, l'épaisseur du cristal émetteur électro-optique (EO) peut limiter la bande passante THz du détecteur. Généralement, les cristaux plus minces favorisent la condition d'accord de phase au détriment de l’efficacité de détection du champ THz généré. Si les conditions d'accord de phase ne sont pas satisfaites, certaines techniques telles que le schéma de front d'impulsion incliné, le refroidissement cryogénique et le quasi-accord de phase sont généralement utilisées pour compenser le désaccord de phase. De plus, avec l'utilisation d'impulsions de pompe courtes et intenses, un spectre THz large et intense peut être généré en plus d'autres effets non linéaires tels que l'absorption de porteur libre (FCA) et l'absorption à deux photons (TPA) qui peuvent être préjudiciables à l'efficacité globale du processus de rectification optique. En effet, la largeur du spectre THz est limitée par la réponse spectrale du cristal émetteur. Dans le régime de mesure, la détection EO de l'impulsion THz est généralement effectuée dans un cristal non linéaire. L'effet Pockels constitue la base par laquelle la détection EO peut être obtenue en échantillonnant l'impulsion THz avec une sonde courte ou en superposant l'impulsion THz avec une impulsion sonde à dérive de fréquence. Ce dernier cas a typiquement un taux d'acquisition plus rapide que le premier. Outre la différence de temps d'acquisition entre l'échantillonnage EO et la détection monoccoup, les conditions EO pour une détection efficace sont essentiellement similaires. Des conditions telles qu'une grande réponse spectrale, un coefficient EO non linéaire élevé et un accord de phase dans le cristal du détecteur doivent être satisfaites pour une détection efficace d’un large

spectre. La réponse spectrale utilisable du cristal détecteur est limitée par l'épaisseur du cristal détecteur. Avec l'utilisation de cristaux plus fins, toute la largeur spectrale de la réponse peut être utilisée. Pour cette raison, un cristal avec un coefficient EO élevé est préférable.

Dans le chapitre présentant les résultats expérimetaux, une source laser ytterbium centrée à 1030 nm avec un taux de répétition de 42 kHz a été utilisée comme faisceau d'entrée du montage expérimental. En sortie de la source laser, la taille du faisceau est de 2024 µm de diamètre et la durée est de 500 fs (à pleine largeur à mi-hauteur) et il est polarisé linéairement. La configuration est principalement divisée en deux bras composés des bras de détection et de génération. Un séparateur de faisceau est placé sur le trajet de la source laser afin de réfléchir 35 % de la puissance laser d'entrée (c'est-à-dire le faisceau de sonde) pour la détection, tandis que 65 % de la puissance (c'est-à-dire l'impulsion de pompe) est transmise à l’autre bras pour la génération de l'impulsion THz. L'impulsion de pompe est ensuite focalisée sur le cristal émetteur en utilisant une lentille dont la distance focale est 500 mm. Au fur et à mesure que l'impulsion de pompe se propage à travers le cristal émetteur, les impulsions THz sont émises et diffractées. Afin de collecter efficacement le faisceau rayonné (c'est-à-dire l'impulsion optique et THz), un miroir parabolique hors axe de 50 mm de diamètre est placé en sortie du cristal de manière à collimater le faisceau rayonné. Il est ensuite focalisé par un second miroir parabolique sur un cristal détecteur EO. L'impulsion THz focalisée est superposée temporellement et spatialement sur le cristal détecteur avec l'impulsion sonde. Le décalage temporel relatif est balayée à l'aide d'une ligne à retard motorisée et contrôlée par ordinateur. En l'absence de champ THz, aucune phase ne sera induite dans l'impulsion de la sonde. Ainsi, l'impulsion de la sonde sera polarisée circulairement lors du passage par une lame quart d'onde positionnée devant polariseur. Cependant, en présence du champ THz, un changement d'indice de réfraction se produit dans le cristal de détection. Il en résulte un changement de phase des impulsions de la sonde lors de son passage à travers le cristal. Afin de mesurer le changement de phase induit, le polariseur est utilisé pour séparer les états de polarisation en transmettant et en réfléchissant les deux composantes. A l'aide d’une photodiode balancée, la différence de signal entre les deux composantes de polarisation est enregistrée. Afin de minimiser l'effet du bruit et d'améliorer le rapport signal sur bruit de la photodiode balancée, la sortie est connectée à une détection synchrone. L'intérêt particulier était d'étudier la forme du spectre THz généré avec les paramètres du laser. Avec l'utilisation du cristal ZnTe comme émetteur THz, une impulsion de 1 ps avec une bande passante étroite de 0,5 THz a été générée. On observe que l'effet non linéaire tel que le TPA peut être négligé car il existe une dépendance quadratique de la puissance THz sur l'intensité de pompe optique. Cela s’explique notamment par une énergie par impulsion du laser inférieure à 10 µJ. Dans ce cas, l'effet de saturation sur l'impulsion de la pompe peut ne pas avoir été significatif. L'intensité du signal THz peut être faible, bien qu'aucune caractérisation de l'intensité THz n'ait été effectuée.

La détection a été réalisée par échantillonnage EO dans un cristal de ZnTe de 1 mm d'épaisseur. Des différences marquées entre l'impulsion THz générée expérimentalement et simulée ont été observées. Ces différences ont été attribuées à la fonction de réponse du cristal, à la durée d'impulsion de la sonde et à l'effet de la diffraction. Afin d'optimiser la configuration expérimentale, nous suggérons d'utiliser un cristal plus fin pour l'EOS afin que la largeur spectrale complète de l'impulsion THz puisse être fidèlement mesurée. Bien que l'effet de diffraction puisse ne pas être complètement éliminé aux basses fréquences THz, l'utilisation d'un grand miroir parabolique (pour collimater le faisceau THz) est indiquée pour limiter l'effet de diffraction.

De même, des impulsions THz multi-cycles ont été générées en remplaçant l'émetteur ZnTe par un cristal organique BNA de 390 µm d'épaisseur. La détection a été réalisée par échantillonnage EO dans un cristal de ZnTe de 1 mm et 0,2 mm d'épaisseur. Le résultat du signal THz échantillonné dans les différents cristaux de ZnTe a indiqué des différences évidentes en termes de largeur spectrale du signal et de dynamique. Lorsque le cristal ZnTe de 1 mm est utilisé comme détecteur, l'impulsion THz échantillonnée avait une durée inférieure à 1 ps et un fréquence centrale d'environ 1,3 THz, tandis qu'une durée d'impulsion plus courte avec une fréquence centrale décalée a été réalisée avec l'utilisation du cristal plus fin. Pour comprendre l'écart entre ces résultats, la fonction de réponse de détection des deux cristaux a été comparée au spectre THz détecté. Il a été déduit de la comparaison qu'il est surprenant de détecter des fréquences supérieures à 0,8 THz lorsque le cristal de 1 mm est utilisé. Un cristal plus mince a donc été utilisé pour étendre la fréquence de coupure à 2,4 THz. Un spectre THz centré à 2 THz avec une durée d'impulsion de 0,5 ps a été mesuré par ce cristal plus fin. Ces résultats indiquent que la bande passante du signal THz généré est plus large que la fonction de réponse de détection du cristal ZnTe de 1 mm. En tant que telle, elle était insuffisante pour caractériser l'impulsion THz. Le remplacement du cristal plus épais par le cristal plus fin a élargi la limite de détection, mais le niveau de bruit a significativement affecté le signal. On a observé que la puissance du signal THz (mesurée en prenant l'intégrale au carré du champ électrique THz) variait quadratiquement avec l'intensité de la pompe, ce qui soutient en partie une exclusion des effets TPA et FCA qui entre en concurrence avec le processus de rectification optique. En comparant les signaux THz issus des cristaux de BNA et ZnTe, nous avons conclu que les impulsions THz sont multi-cycles dans le cas du BNA, tandis que les impulsions THz sont bipolaires dans le cas du ZnTe. En conclusion, je suggère qu'un cristal EO différent, par exemple un cristal GaP, puisse être utilisé comme cristal détecteur pour optimiser l'accord de phase et limiter l'absorption THz. Ainsi, un spectre THz plus large exempt d'artefacts devrait être mesuré.

Ensuite, un montage expérimental différent a été mis en place. Dans cette configuration, la génération et la détection de THz ont été effectuées dans un seul cristal de ZnTe. Le rayonnement THz généré a été caractérisé par une détection EO monocoup à l'aide d'un spectromètre optique standard et d'un diagnostic de caractérisation d’impulsion (de type FROG-Frequency Resolved Optical Gating). Un laser Ti:Sapphire centré à 800 nm délivre une impulsion à dérive de fréquence d'une durée de 3,6 ps. Dans cette configuration monocoup, l'impulsion THz est générée dans une première partie du cristal par le faisceau pompe incident puis elle induit un changement de phase sur un faisceau sonde présentant également une dérive de fréquence. L'impulsion THz générée au début du cristal rencontre alors l'impulsion de sonde dans la dernière partie du cristal. L'impulsion THz mesurée a une durée FWHM de 6,5 ps et a peu de cycles. Le spectre correspondant est centré à 0,1 THz avec une largeur de 0,1 THz. Les données expérimentales étaient bien conformes aux prédictions de la théorie de la rectification optique et de l'effet Fabry Pérot avec une contribution négligeable des effets non linéaires tels que les effets TPA et Kerr. Les composantes de polarisation du faisceau modulé par la sonde THz ont été récupérées indépendamment. Bien que l'objectif n'était pas d'étudier l'accordabilité du spectre THz à bande étroite, la fréquence peut être réglée en ajustant le taux de dérive de fréquence de la pompe via la distance entre les réseaux de diffraction dans la source laser. La bande spectrale optique de la sonde et sa dérive de fréquence utilisée dans la détection est un compromis entre la fenêtre temporelle et la résolution. Ce schéma peut être exploité pour plusieurs applications. Ces résultats soutiennent d'avantage la possibilité de réaliser des systèmes intégrés photoniques THz avec l'utilisation de cristaux de ZnTe. Habituellement, la configuration des sources et de la détection THz est relativement complexe et il est souvent nécessaire d'intégrer le système en combinant la génération et la détection. Notre étude peut également déboucher sur une application en physique de la matière condensée pour exciter les modes de phonons excités par un spectre THz à bande étroite accordable. Enfin, en tirant profit de schéma de détection monocoup, ce type de montage peut être implémenter pour étudier la dynamique moléculaire sur une échelle de temps ultra-rapide par spectroscopie résolue en temps pour les réactions chimiques et les transformations de phase.

Dans une partie de la thèse, la spectroscopie des schistes bitumineux a été étudiée dans le domaine THz. Les schistes bitumineux sont des sources de combustible non conventionnelles et sont particulièrement importants dans le contexte de la diminution des réserves de pétrole brut et de la hausse des prix du pétrole. Le schiste bitumineux dans de vastes gisements a été signalé dans de nombreux pays, dont le Nigéria. Le schiste bitumineux nigérian est appelé schiste bitumineux de Lopkanta. Des études de faisabilité économique sur l'exploration du schiste bitumineux de Lokpanta ont confirmé son potentiel pour l'approvisionnement en produits pétroliers même après la fin supposée de l'approvisionnement en pétrole brut (dans la région) d'ici 2057. Depuis la découverte du schiste bitumineux de Lokpanta, peu de travaux expérimentaux ont étudié leur potentiel en termes de rendement en huile. Bien que plusieurs techniques aient été utilisées pour caractériser ce schiste bitumineux, aucune investigation n'a été réalisée par spectroscopie THz. Les schistes bitumineux sont particulièrement sensibles au rayonnement THz en raison de la présence d'un constituant organique appelé kérogène. Le constituant kérogène du schiste bitumineux représente un petit pourcentage en masse du poids total car il détermine la qualité et la quantité du rendement en pétrole. Le kérogène est souvent dispersé dans la matrice de minéraux inorganiques présents dans les schistes bitumineux. L'objectif de ce travail est d'identifier qualitativement la présence élémentaire de Carbone qui se trouve être un constituant majeur du kérogène. Deux systèmes THz commerciaux (spectromètres TPS 3000 et TPS 4000 de TeraView) ont été utilisés respectivement en mode transmission et réflexion pour acquérir des images spectroscopiques des échantillons de schiste bitumineux. Une inhomogénéité claire dans les échantillons a été révélée par l'indice de réfraction et le coefficient d'absorption différents à certains points sélectionnés de l'échantillon. Le résultat des images spectroscopiques obtenues à la fois en mode réflexion et transmission a également révélé des différences marquées dans le modèle d'absorption à différentes fréquences THz. Sur la base de la spectroscopie THz actuelle et de la mesure d'imagerie, il semble impossible d'associer les modèles d'absorption à la présence de matières organiques en raison du grand modèle non homogène observé. Pour les travaux futurs, l'incorporation de la technique pyrolytique dans la spectroscopie THz et la mesure d'imagerie est suggérée. Dans cette technique, les schistes bitumineux seront chauffés au-dessus de la température ambiante de manière progressive. Par exemple, à chaque intervalle de 50°C dans le processus de chauffage, la spectroscopie et l'imagerie peuvent être effectuées après refroidissement de l'échantillon. Étant donné que les constituants des schistes bitumineux sont décomposés pendant la pyrolyse, une relation entre les signaux THz transmis / réfléchis peut-être tracée en fonction de la température pyrolytique pour révéler des modèles d'absorption variables sur l'amplitude du signal THz. Dans le résultat à obtenir, il est possible que les différentes étapes de la pyrolyse (c'est-à-dire la perte d'humidité, la décomposition des macromolécules (organiques) et la décomposition minérale) soient liées à l'amplitude du signal THz transmis. Ainsi, une conclusion raisonnable pourrait être tirée sur la présence relative d'humidité, de matières inorganiques ou organiques.

D'autre part, l'analyse THz dans ce travail a été complétée par des mesures SEM-EDX (Scanning Electron Microscopy-Energy Dispersive X-Rays Spectroscopy) et LIBS (Laser Induced Breakdown Spectroscopy) dans le but de vérifier le caractère non homogène des échantillons et de déterminer leur composition élémentaire. La carte SEM-EDX a révélé la composition élémentaire sur des échantillons sélectionnés du schistes bitumineux de Lopkanta. Bien qu'il existe une légère variation dans la composition entre les différents échantillons de schiste bitumineux, la composition en en général une combinaison de plus d'un des éléments suivants : Al, Si, Ca, O, K, C, Fe, Mg, Mn, Ti, S, C et Na. En fonction de la composition relative des éléments détectés, certains minéraux tels que le quartz, la calcite, le feldspath peuvent être présents. Les résultats concordent bien avec les travaux antérieurs sur les schistes bitumineux du Lokpanta. Dans toutes les analyses SEM-EDX, C a été détecté mais en petite quantité. La présence de matières organiques qui aurait pu être attribuée à la présence élémentaire de C, H et O n'a pas pu être affirmée (en raison de l'absence de H). Cependant, la composition minérale élémentaire typique du schiste bitumineux de Lopkanta a été fidèlement déterminée. Afin de vérifier les résultats SEM-EDX, une mesure LIBS a été effectuée sur les échantillons. Les résultats LIBS ont confirmé la présence d'une large liste d'éléments comprenant Ca, Al, Na, K, Ti, Si, Mg et Fe en plus d'oligo-éléments tels que Sr, Rb et Ba. Les résultats expérimentaux, qui sont en accord étroit avec les travaux antérieurs sur les schistes bitumineux de Lopkanta, n'ont pas confirmér la présence de carbone. Ainsi, il se peut que le pourcentage de C dans l'échantillon soit relativement faible, ce qui est en accord avec les résultats issus du SEM-EDX. Il est important de noter que, dans tous les résultats LIBS, l'azote n'a pas été détecté. Cela concorde également avec le résultat SEM-EDX.

Introduction en Français

Les ondes térahertz (THz) sont des rayonnements électromagnétiques couvrant la région du spectre entre l'infrarouge et les micro-ondes. Ils représentent le lien entre la photonique et l'électronique. Le spectre THz varie généralement de 0,1 à 100 THz. Typiquement, 1 THz correspond à 300 µm de longueur d'onde, 4,1 meV d'énergie de photon et 1 picoseconde de période.

Les scientifiques se sont efforcés d'atteindre des fréquences THz en convertissant les sources laser à haute fréquence vers les basses fréquences. Les sources THz en laboratoire sont très diverses. Les sources THz courantes sont principalement classées en 3 groupes à savoir les antennes photoconductrices, les cristaux non linéaires et les sources à base de plasma. Pour la détection du rayonnement THz, il existe de vastes systèmes et mécanismes disponibles pour la détection. Selon la possibilité de détecter le champ électrique ou la puissance de l'impulsion THz, les détecteurs peuvent être regroupés en détecteurs cohérents ou incohérents. Les détecteurs cohérents (tels que les détecteurs PCA, électro-optiques et basés sur un plasma dans l'air) peuvent récupérer à la fois le champ et la phase THz, tandis que les détecteurs incohérents (tels que les bolomètres, les cellules de Golay et les détecteurs pyroélectriques) ne peuvent récupérer que la puissance ou l'intensité.

Des efforts considérables pour développer des sources THz utiles pour des applications ont été réalisés. Les applications impliquent l'identification de tissus cancéreux dans des échantillons biologiques, la caractérisation de revêtements de médicaments dans l'industrie pharmaceutique, l'étude de l'art/de la peinture, la détection de pesticides/substances nocives dans les produits agricoles, la détection d'explosifs et d'autres armes de destruction massive ainsi que l’analyse de pétrole. Les schistes bitumineux, qui sont des sources non conventionnelles de combustible, sont particulièrement importants dans le contexte d'une baisse des réserves de pétrole brut et d'une hausse des prix du pétrole. Afin de se préparer à la fin des sources de pétrole conventionnelles, les efforts sont depuis orientés vers l'évaluation du potentiel de rendement en pétrole des schistes bitumineux de différents pays. Le schiste bitumineux est une roche mère combustible, composée de minéraux et de matière organique, c'est-à-dire de kérogène. Ils sont capables de générer de l'huile de schiste et du gaz de schiste ainsi que d'autres produits pétroliers lorsqu'ils sont soumis à des réactions pyrolytiques. Le schiste bitumineux dans des gisements étendus a été signalé dans des pays tels que les États-Unis d'Amérique (États-Unis), l'Estonie, la Chine et le Brésil. Les États-Unis possèdent la plus grande réserve de schiste bitumineux au monde, avec un total de 3340 milliards de tonnes. D'autres pays possèdent une quantité considérable de réserves de schiste bitumineux comme la Chine, Israël, Roumanie, Égypte, Allemagne, Jordanie, Maroc, Turquie et Nigeria. Le premier schiste bitumineux au Nigeria, a été trouvé dans la région de Lopkanta de l'État d'Imo, et il est donc appelé schiste bitumineux de Lopkanta. Jusqu'à présent, aucune investigation n'a été menée sur les schistes bitumineux de Lopkanta en utilisant la spectroscopie ou l’imagerie THz. Cependant, plusieurs travaux ont été menés pour étudier la réponse THz des schistes bitumineux provenant d'autres pays. Dans la littérature, les propriétés optiques de ces schistes bitumineux telles que l'indice de réfraction, le coefficient d'absorption et l'anisotropie de l'indice de réfraction ont été corrélées avec leurs rendements en pétrole, leur maturité et leurs compositions chimiques. Dans ce travail, nous tentons d'explorer l'utilisation de la spectroscopie/imagerie THz afin de caractériser les schistes bitumineux de Lopkanta.

Ce manuscrit est organisé en cinq chapitres. Le chapitre 1 est général et introduit les sources de génération, les détecteurs et les applications dans le domaine THz. Dans le chapitre 2, la théorie de la génération d'impulsions THz par redressement optique est discutée. En effet, les travaux expérimentaux ont été réalisés avec des cristaux de ZnTe et de BNA qui ont été identifiés comme sources de rectification optique d'impulsion THz. Le chapitre 3 traite la théorie de la détection THz par échantillonnage électrooptique et de la détection monocoup. Dans le chapitre 4, les résultats expérimentaux des impulsions THz générées sont présentés. Le chapitre est globalement divisé en deux parties. Dans la première partie, les impulsions THz générées par les cristaux de ZnTe et BNA sont caractérisées par échantillonnage électrooptique. Puis dans la seconde partie, une détection monocoup est effectuée dans un cristal de ZnTe. Les résultats expérimentaux impliquant l'analyse optique du schiste bitumineux de Lokpanta sont présentés au chapitre 5. La spectroscopie THz a été réalisée en plus de deux autres méthodes optiques à savoir ; Spectroscopie d’émission atomique de plasma induit par laser (LIBS) et mesure au microscopie électronique à balayage combiné à la spectroscopie de rayon X à dispersion d’énergie (SEM-EDX). Des sources THz commerciales ont été utilisées pour effectuer le THz-TDS en mode transmission et en mode réflexion.

Introduction in English

Terahertz (THz) waves are electromagnetic radiation covering the region of the spectrum between infrared and microwaves. They represent the link between photonics and electronics. The THz spectrum generally ranges from 0.1 to 100 THz. Typically, 1 THz corresponds to 300 μm of wavelength, 4.1 meV of photon energy and 1 picosecond of period.

Scientists have tried to reach THz frequencies by converting high frequency laser sources to low frequencies. THz sources in the laboratory are very diverse. Common THz sources are mainly classified into 3 groups' namely photoconductive antennas (PCA), nonlinear crystals and plasma based sources. For the detection of THz radiation, there are extensive systems and mechanisms available for detection. Depending on the possibility of detecting the electric field or the power of the THz pulse, the detectors can be grouped into coherent or incoherent detectors. Coherent detectors (such as PCA, electro-optical, and air plasma-based detectors) can recover both the THz field and phase, while incoherent detectors (such as bolometers, Golay cells and pyroelectric detectors) can only retrieve the power or intensity of the THz radiation.

Considerable efforts to develop THz sources for useful applications have been made. The applications involve the identification of cancerous tissues in biological samples, characterization of drug coatings in the pharmaceutical industries, study of art/paints, detection of pesticides/harmful substances in agricultural products, detection of explosives and other weapons of mass destruction as well as oil analysis (in oil and gas industry). Oil shales, which are unconventional sources of fuel, are particularly important in the context of declining crude oil reserves and rising oil prices. In order to prepare for the end of conventional oil sources, efforts are sine directed towards assessing the oil yield potential of oil shale from different countries. Oil shale as a combustible source rock is composed of minerals and organic matter (i.e. kerogen). They are capable of producing shale oil and shale gas as well as other petroleum products when subjected to pyrolytic reactions. Oil shale in extensive deposits has been reported in countries such as the United States of America (USA), Estonia, China and Brazil. The United States has the largest reserves of oil shale in the world, with a total of 3340 billion tons. Other countries such as China, Israel, Romania, Egypt, Germany, Jordan, Morocco, Turkey and Nigeria have considerable amount of oil shale. The first oil shale in Nigeria, was found in the Lopkanta region of Imo State, and hence it is called Lopkanta oil shale. So far, no investigation has been carried out on the Lopkanta oil shales using THz spectroscopy/imaging. However, several works have been carried out to study the THz response of oil shales from other countries. In the literature, the optical properties of these oil shales such as refractive index, absorption coefficient and refractive index anisotropy have been correlated with their oil yields, maturity and chemical compositions. In a part of this work, an attempt to explore the use of THz spectroscopy/imaging to characterize the Lopkanta oil shales is carried out.

This manuscript is organized into five chapters. Chapter 1 is a general introduction and highlights the common table-top THz sources, detectors and applications of THz technology. In chapter 2, the theory of THz pulse generation by optical rectification is discussed since in this work the experimentation has been carried out with ZnTe and BNA crystals (which have been identified as optical rectification of THz sources). Chapter 3 deals with the theory of THz detection by electro-optical sampling and single-shot detection. In chapter 4, the experimental results of the generated THz pulses are presented. The chapter is broadly divided into two parts. In the first part, the THz pulses generated by ZnTe and BNA crystals are characterized by electro-optical sampling. Then in the second part, a combined generation and single-shot detection is performed in a ZnTe crystal. In chapter 5, experimental results involving the optical analysis of Lokpanta oil shale are presented. Commercial THz sources were used to perform THz-TDS/imaging in both transmission and reflection mode. The THz spectroscopy/imaging were performed in addition to two other optical methods namely Laser Induced Breakdown Spectroscopy (LIBS) and Scanning Electron Microscopy-Energy Dispersive X-Ray Spectroscopy (SEM-EDX).

Table of Contents

Chapter 1

General Introduction

Terahertz (THz) waves are electromagnetic radiation covering the region of the spectrum between infrared and microwave. They represent the link between photonics and electronics as shown in Fig. 1. 1. THz spectrum usually ranges from 0.1 -100 THz. Typically, 1 THz corresponds to 300 µm in wavelength, 4.1 meV in photon energy, and 1 picosecond in period **[1]**. Traditionally, THz frequencies are too high to be generated by solid-state electronic devices. As a result of the lack of adequate THz sources, this region has been referred to as a spectral gap. What makes the THz range interesting is the fact that, for most matter their vibrational and rotational levels lie in this range **[1]**. Practically, there are two approaches for THz generation namely up-conversion and down-conversion. In electronics, efforts have been made to up-convert multi-GHz to THz frequency level with multiplier chain. On the other hand, photonics scientists have made effort to achieve THz frequencies by down-conversion of high frequency laser sources. In what follows, the common table-top sources of THz pulse that are photonics-based shall be highlighted.

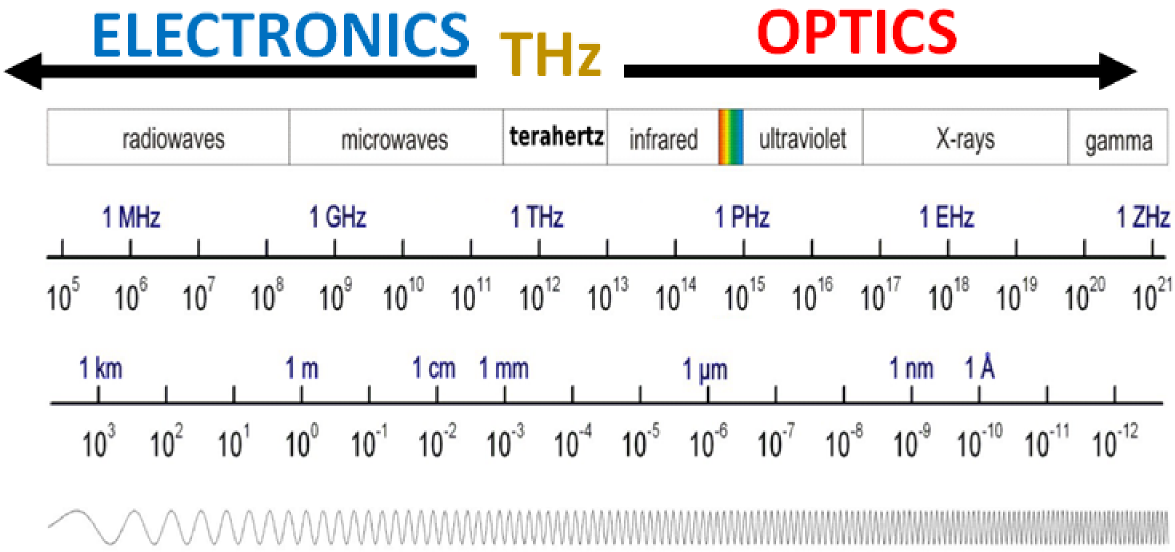

Fig. 1.1 THz frequency region in the electromagnetic spectrum. THz frequencies represent the missing spectral between electronics and optics.

1.1 THz sources

THz sources are widely diversified. Depending on the material medium, the common THz sources can be classified into 3 groups namely photoconductive antennas, nonlinear crystals and plasma sources.

Photoconductive Antenna

The use of photoconductive antenna (PCA) is among the earliest method for the generation of THz pulses. This technique was first introduced by Auston in the early 1980's **[2]**. PCA consists of a semiconductor material (usually GaAs or InGaAs **[3]**) with a short carrier lifetime and an electrode structure composed of either gold or aluminum. The electrodes are typically biased with a voltage of about 10 to 50 V. When a laser pulse hits the biased gap of the semiconductor, free carriers are created, and are accelerated by the bias field. The rapid change in polarization induced by the ultrafast acceleration of the carriers generates a sub-picosecond, single-cycle coherent electromagnetic pulse in the THz range. The magnitude and efficiency of the generated THz pulse depends on the applied electric bias, the pulse duration of the femtosecond laser and the carrier rise time (a material dependent property). Nowadays, large aperture PCA are commonly used as the semiconductors substrate in order to improve the efficiency of the process **[4]**.

Non-linear crystals sources

Another widely used method for ultrashort THz pulse generation is optical rectification of femtosecond laser pulses in nonlinear crystals. Optical rectification (OR) was first demonstrated in KDP crystals in 1962 by using 100 ns pulses from a ruby laser **[5]**. Compared with PCA's, THz generation using OR of femtosecond laser pulses is usually much simpler, with no need for an external high-voltage power supply. In general, the laser pulses induce a time-dependent non-linear polarization within the crystal. This polarization may contain many frequency components, which can result in the emission of electromagnetic waves in the THz spectral range. Ideally, the spectral bandwidth of the generated THz pulse depends on the frequency components of the incident laser pulse. However, in reality, in order to generate high energy THz pulses with high efficiency, several conditions need to be fulfilled. First of all, in addition to the non-centrosymmetric crystal structure, the medium needs to be transparent at all the frequencies involved, and possess a relatively high damage threshold to tolerate the high intensities of the incident laser **[6-7]**. Secondly, many other material properties should be carefully considered, such as absorption, diffraction, saturation and phase matching conditions. Among these, the matching between the optical group velocity and the THz phase velocity is one of the most crucial factors for an efficient OR process, which ultimately determines the crystal thickness and orientation **[8-9]**.

Plasma-based sources

THz pulse can also be emitted from gaseous plasma. This method was first proposed and demonstrated in 1993 **[10]**. When an intense femtosecond laser pulse is focused in air, plasma is generated due to the ionization of the air molecules. Plasma emits a broad continuum of coherent radiation from which the THz pulses are also emitted through four wave mixing (FWM). In recent times, the efficiency of this process has been improved by mixing the fundamental (at ω) and second harmonics (at 2ω) of the laser fields **[11-12]**. By using this two-color method, improved efficiency has been recorded. The generation of ultra-broad band THz pulses containing frequencies up to 100 THz has been demonstrated by using ultra-short pulses **[13]**. By replacing the air medium with noble gases, the THz generation efficiency has also been significantly improved. The pressure of the target gas also strongly influences the THz generation efficiency **[14]**. THz generation in plasma is advantageous in that there is no damage threshold for the emitter since the gaseous target is continuously replenished and that the available bandwidth of the THz pulses is essentially limited only by the duration of the pump laser pulse **[11]**.

1.2 THz detectors

Vast detector systems and mechanism are available to detect THz pulse. Depending on the possibility to either detect the electric field or power of the THz pulse, the detectors can be grouped as coherent or incoherent detectors. Coherent detectors (such as PCA, electro-optic and air-based detectors) can retrieve both the THz field and phase, while incoherent detectors (such as bolometers, Golay cells and pyroelectric detectors) can only retrieve the power or intensity of the THz pulse. A brief summary of the underlying detection mechanism will be highlighted in this section.

PCA detectors

THz pulses can be detected by using PCA. The mechanism of THz detection by PCA is an inverse process of the generation in PCA but without the need of an external bias voltage. In PCA detectors, a femtosecond probe laser illuminates the gap of the PCA and excites carriers into the conduction band. The THz field to be measured accelerates the carriers, leading to a transient photocurrent inside the PCA detector. The measured photocurrent depends both on the incident THz electric field and the surface conductivity of the PCA **[15]**. Importantly, the bandwidth of the detectable THz pulse is determined by the characteristics of the laser pulse and the PCA substrate. As a result, materials with short carrier lifetime (such as low-temperature grown GaAs (LT-GaAs) and doped GaAs) are usually selected **[16-18]**.

Electro-Optic detectors

Electro-optic (EO) detectors utilizes the Pockels effect in an EO crystal. When the THz pulses are incident on the crystals, the Pockels effect causes a linear change in the refractive index of the crystal. This results to the change in the phase of an incoming beam (commonly referred to as probe beam) that passes through the crystal. By measuring the change in the phase of the probe beam, the THz electric field can then be determined **[19-20]**. EO technique can be broadly divided into two methods namely EO Sampling (EOS) and single shot detection. In EOS, a short probe beam is used to temporally scan the THz field, while in a typical single shot detection, a long and usually chirped probe is overlapped with the THz pulse without a necessary need for sampling. Though the acquisition time required by the single shot detection are generally less than the EOS, they are often limited by their spectral resolution. To this end several variations of this techniques have been proposed and implemented. The differences between these variations lies majorly in the encoding algorithm. They are namely space-time encoding and angle-time encoding **[21-22]**.

Air-based detectors

Air-based detectors uses a technique similar to the THz generation process from plasma. In this technique, air is used as the nonlinear medium for detection. In essence, it involves interacting a weak fundamental laser field (ω), with the THz pulse **[23-24]**. This process which can be described by FWM model results to the generation of the second harmonic (2ω) of the fundamental field. In practice it is the intensity of the second harmonic that is retrieved, but not its electric field. Thus, the intensity of the second harmonic is measured in order to retrieve the THz characteristic and therefore the phase information is lost. In order to realize a coherent measurement, a DC or an AC field is usually applied at the focus point between the laser and THz pulse. An important feature of the Air-based technique is that the detectable THz bandwidth is only limited by the optical pulse duration **[11]**.

THz Power detectors

THz power detectors are incoherent detectors. They are capable of detecting only the THz intensity. As such, the phase information of the THz pulse is completely lost. The commonly used power detectors are namely; bolometers, pyro-electric detectors and Golay cells. Golay cells consist of a filled gas chamber with an absorbing substance and a flexible membrane. As the THz pulses are absorbed by the Golay cells, the gases heat up and expand. By quantifying the volumetric expansion of the gases, the THz power can be inferred. While in the case of bolometers and pyroelectric detectors, the incident THz pulses causes a temperature change in the detectors from which the THz power can be measured **[25-27]**.

1.3 General application of THz technology

Considerate effort to develop THz sources for useful applications have been realized. Here, a brief review on some examples of the general application shall be mentioned.

Biological application

THz radiation has very low photon energy and does not cause any ionization hazard for biological tissues. This feature makes THz radiation attractive for biomedical applications **[28]**. Defective body tissues such as cancer often induces increased blood supply to the affected tissue and a local increase in tissue water content which can be utilized as contrast for THz imaging of cancerous tissues. As a result, brain tumors have been identified via THz imaging as well as cancerous breast tissues **[29-32].**

Pharmaceutical application

Sugar coating, film coating and press coating are common methods used to deposit coatings on tablets. These coatings are used to modify the properties of drugs. The thickness, uniformity and density of these coatings influences the tablet performance. As such advanced quality control are required to characterize coating quality. Due to the advantageous penetration depth that THz radiation offers, they have been widely used to evaluate and characterize drug coatings **[33-35].**

Art and painting
THz is valuable for the investigation of art and cultural paintings since no radiation risk is associated with deep penetration. Several studies have shown that THz imaging is capable of revealing features which cannot be seen by other optical inspection. Obscured mural painting, oil canvas painting, panel painting, apsidal wall painting among others have been investigated with THz imaging **[36-39].**

Agricultural application
The application of THz spectroscopy in the agriculture industry is premised on the detection of pesticides and harmful substances in agricultural products. In conjunction with the partial least square method, THz-Time Domain Spectroscopy (THz-TDS) have been used to quantify the relative amounts of pesticides in food powders. In addition, the relative difference in absorption peaks and refractive index of selected food samples have been used to identify food samples containing no pesticides **[40-42]**.

Security application
The detection of explosives and other weapons of mass destruction have been carried out with THz spectroscopy. The absorption spectral of explosives such as 2, 3-dinitro toluene, 4-nitro toluene and 2, 6-dinitro toluene have been carried out with both THz reflection and transmission spectroscopy **[43-44]**. Moreover, THz spectroscopy have also been proven to be able to detect hidden explosives **[45].**

Condensed matter application
The meV energy scale of THz pulses have enabled the possibility to probe low-energy carrier dynamics in various electronic materials, such as superconductors **[46]**. On one hand, certain materials can emit THz pulse through the ultrafast modulation of photo-excited carriers from which THz emission spectroscopy can be performed. For example, high-critical temperature superconductors, manganites, ferromagnetics and multiferroics have been examined using THz emission spectroscopy **[47-49]**.

1.4 THz application in oil and gas-based industry

THz spectroscopy is also gaining a huge attention in the oil and gas-based industry. Since a part of this work, involves THz spectroscopy measurement with rock samples reported to be oil shales, we will commence this section by first discussing the relevance of oil shales, and this will be followed by a general application of THz technology in the petroleum community.

Oil shales which are unconventional sources of fuel are particularly important in the context of a decline in the crude oil reserves and rise in oil prices. In order to prepare for the futuristic tail off in the conventional oil sources, efforts are since geared towards evaluating the oil yield potential of oil shale of different countries. Oil shale is a combustible source rock, composed of minerals and organic matter (i.e. kerogen). The kerogen content of the oil shale are insoluble substances dispersed within the matrix of the inorganic minerals **[50-52]**. Oil shale are capable of generating shale oil and oil shale-gas as well as other petroleum products when subjected to pyrolytic reactions **[53-56].** Shale oil and oil shale-gas are chemically identical to the products of fossil fuel, and thus serve as a substitute for conventional crude oil and natural gas respectively. By adopting an efficient mining technique, they could be particularly useful when the price of crude oil rises or when the hydrocarbon reserves of the fossil fuel is no longer economical for exploration **[57-60]**. Oil shale in widespread deposits has been reported in countries such as United States of America (USA), Estonia, China, and Brazil. USA has the largest oil shale reserve in the world, with the total of 3340 billion tons. Other countries with considerable amount of oil shale reserves includes among others China, Israel, Romania, Egypt, Germany, Jordan, Morocco, Turkey, and Nigeria **[61-63]**. The first oil shale in Nigeria, was found in Lopkanta area of Imo state, and therefore called Lopkanta oil shale. Lokpanta is geologically situated in the Lower Benue Trough of Nigeria. The oil shale reserve of the region has been estimated at 5.76 billion tones, of which 1.70 billion barrels are recoverable **[64-65]**. Moreover, economic feasibility studies on the exploration of the Lokpanta oil shale has endorsed its potential to supply petroleum products even after the supposed end of crude oil supply (in the region) by the year 2057 **[66-67]**. Since the discovery of the Lokpanta oil shale, there have been only a few numbers of experimental works to identify their oil yield potential. Several techniques have been employed to characterize the Nigerian oil shale namely: the Fischer Assay method (combined with geochemical analysis), Infra-Red Spectroscopy Analysis, Gas Chromatography-Mass Spectrometer (GC-MS) and Thermal Analysis (Thermo Gravimetric, TGA & Differential Thermal Analysis, DTA). As no single method is ideal **[68-69]**, a combination of two or more of these techniques were employed by the researchers. Until now, no investigation has been carried out on the Lopkanta oil shale using THz spectroscopy/imaging. However, several works have been carried out to study the THz response of oil shales obtained from other countries. In the literature, the optical properties of such oil shales such as refractive index, absorption coefficient and refractive index anisotropy were correlated with their oil yields, maturity and chemical compositions **[70]**. In a part of this work, an attempt to explore the use of THz spectroscopy/imaging in order to characterize the Lopkanta oil shales shall be examined.

Other than the unconventional sources of fuel, fossil fuels which are conventional fuel sources have also been investigated with THz spectroscopy in addition to other geological methods. Due to the mechanical action during oil-well drilling, the fossil fuels are released as crude oil and natural gas **[71]**. In what follows, we shall highlight some general applications of THz spectroscopy in oil well reservoir and the analysis of crude oil/natural gas properties.

Analysis of petroleum products

Petroleum products obtained by processing crude oil uses chemical and physical methods to change their viscosity, fluidity and wax content. In recent times magnetic fields have also been applied because of their low investment and easy maintenance. In addition, the applied magnetic fields affect the rheological properties of the crude oil. However, the resulting effect due to the applied magnetic field is still unclear. A proper understanding of this process is useful in order to manipulate the properties of the petroleum products. To this end, a THz-TDS was performed to provide an insight into this process. The absorption and extinction coefficient obtained by performing the THz-TDS shows that, the induced magnetic field results to a disaggregation of the suspended colloidal particles in wax bearing crude oil **[72].**

Sorting out identical crude oil

Following exploration, it is important to appropriately identify the sources and components of the crude oil/natural gas for subsequent and proper processing. With the use of THz spectroscopy in combination with multivariate statistical method (Principal Component Analysis **[73]**), obvious difference has been observed in the oil produced by seven (7) oil fields. The refractive index and absorption coefficients were retrieved. Then the distribution of the refractive index was calculated with Principal Component Analysis. Identical oil shale samples were found to possess similar principal components and vice versa. Similarly, the distribution of the absorption coefficient was also computed and similar observance was found **[74].**

Compositional evaluation of natural gas

The composition of the main constitients of natural gas (which are methane ethane and propane) have been qualitatively and quantitatively analyzed using THz-TDS. These components were artificially mixed in different proportions to obtain several mixtures. The THz amplitude and the time delay within each sample mixtures were extracted and found to correlate with the concentration of the different components. Moreover, back-propagation artificial neural networks (BPANN) method was used to build a quantitative model between the THz spectra and natural gas concentrations. These results indicate that THz is a promising tool for the qualitative and quantitative detection of natural gas **[75-76].**

Assessment of oil yield of bedrocks

The research regarding oil–gas adsorption in tight reservoirs has important practical significance. In a particular study, the adsorption dynamics in oil– gas reservoirs were simulated using active carbon to absorb water molecules **[77]**. Since the hydrogen bond collective network formed by water molecules changes on a picosecond timescale, the THz spectrum was found to be sensitive to fluctuations in the dipole moment of the water content. Their results showed that, THz technology can identify the different stages of the adsorption process of water molecules into the pores of active carbon. Thus, providing an alternate means to characterize the oil-bearing capacity of parent rocks **[77]**. The term “reservoir’s seepage law” is used to describe the flow of oil within cracks in underground rocks. A better understanding of the reservoir’s seepage law during mining process is essential to improve oil recovery and predict future performance of the oil field, especially for the low permeability reservoirs. A sample of a sandstone reservoir was measured with a reflective THz-TDS **[78]**. Before each measurement, the cores were firstly deoiled and saturated with water, then flooded with kerosene in order to simulate the real situation underground. Slices of the samples were scanned by THz- TDS to obtain the distribution of oil and water in the entire core. The presence of kerosene, water and remaining oil was clearly displayed by THz tomography **[78].**

Correlating bedrock maturity with THz absorption

According to modern hydrocarbon generation theory, the hydrocarbon evolution paths of sedimentary organics such as kerogens can be divided into three stages namely diagenesis, catagenesis, and metagenesis. The reflectance of vitrinite ($R_0\%$) which is defined as the proportion of normal incident light reflected by a plane polished surface of vitrinite, is used to describe the maturity stage of kerogens and their oil yielding potential. Lower $R_0\%$ corresponds to immature kerogen and vice versa. In a THz spectroscopy experiment, different kerogen samples with known $R_0\%$ were analyzed **[79]**. By comparing the $R_0\%$ with the corresponding absorption coefficient of the samples, it indicates that less matured kerogen which has the potential to yield oils are lower in absorption coefficient than matured kerogen which are potentially able to yield gases. This shows that there exists a relation between the THz absorption and the maturity level of kerogens **[79].** Also, by irradiating bulk samples (halite rocks), THz-TDS has been used in addition to other methods to evaluate the evolutionary stage in the halite rocks **[80].**

Analysis of crude oil by-products

THz spectroscopy also finds useful application in the analysis of pyrolytic products. Semi-coke which is a by-product of pyrolysis are generally lower in oil concentrations and finds useful application in chemical industry. The characterization of this by-product can serve as an indicator to optimize their utilization. A correlation between absorption coefficient and oil contents have been established in semi-coke. Peak values of THz absorption coefficient have been associated to semi-cokes with low oil concentration **[81].**

The rest of this manuscript is organized into four other chapters. In **chapter 2**, the theory of THz pulse generation by optical rectification is discussed. This is because the experiment work were performed with ZnTe and BNA crystals which have been identified as optical rectification sources of THz pulse. The conditions for an efficient generation of the THz pulses were investigated. These conditions include; the orientation of the pump pulse polarization with respect to the crystal, the effect of phase mismatch between the pump and the generated THz pulse as well as other effects that competes with the efficiency of the process such as Two Photon absorption, Free carrier Absorption and diffraction effects. Also, the utilization of BNA crystals are studied with respect to the characteristics of the incident laser. **Chapter 3** discusses the theory of the THz detection by EOS and single shot detection. The relative orientation of the crystal with respect to the probe and THz pulse for maximum detection are examined. Certain parts of the discussion compare the performance of ZnTe and GaP crystals since they are the commonly used EO crystals in literatures. The last part of the chapter describes the principle of single shot detection and highlights the variations in the method. In **chapter 4**, the experimental results of the generated THz pulses are presented. The experimental set-ups are explained with a brief review of relevant literatures having a similar design. The chapter is broadly divided into three parts. The first part discusses the THz generated in the ZnTe crystal by using a 500 fs laser centered at 1030 nm with a repetition rate of 42 kHz, while the second part discusses the THz generated in the BNA crystal using the same experimental set-up as in ZnTe crystal. EOS was performed to characterize the generated THz pulses. In the third part, a single ZnTe crystal was used to both generate and detect THz pulse from an 800 nm laser which was initially chirped to 2 ps. Experimental results involving the optical analysis of Lokpanta oil shale are presented in **chapter 5**. THz spectroscopy were carried out in addition to two other optical methods namely; Laser Induced Breakdown Spectroscopy (LIBS) and Scanning Electron Microscope-Energy Dispersive X-rays (SEM-EDX) technique. Commercial THz sources were used to perform the THz-TDS in both transmission and reflection mode. The LIBS and SEM-EDX techniques were employed to assist in the interpretation of the THz spectral images.

1.5 Bibliography of chapter 1

[1] Roskos H. G.; Thomson M.D.; Kreb M.; Loffler T. Broadband THz emission from gas plasmas induced by femtosecond optical pulses: From fundamentals to applications. Laser & Photon, 2007, 1, 349–368. doi:10.1002/lpor.200710025.

[2] Auston D. H.; Smith P. R. Generation and detection of millimeter waves by picosecond photoconductivity. Applied Physics Letter, 1983, 43, 1. doi:10.1063/1.94468.

[3] Nathan M. B.; Magda O. E. Review of terahertz photoconductive antenna technology. Optical Engineering, 2017, 56. https://doi.org/10.1117/1.OE.56.1.010901

[4] Benicewicz P. K.; Roberts J. P.; Taylor A. J. Scaling of terahertz radiation from large-aperture biased InP photoconductors. Optics Letters, 1993, 18, 1332. doi:10.1364/ol.18.001332.

[5] Bass M.; Franken P. A.; Ward J. F.; Weinreich G. Optical Rectification. Physical Review Letters, 1962, 9, 446–448. doi:10.1103/PhysRevLett.9.446.

[6] Huang S.W.; Granados E.; Huang W. R.; Hong K.H.; Zapata L. E.; Kärtner F. X. High conversion efficiency, high energy terahertz pulses by optical rectification in cryogenically cooled lithium niobate. Optics Letters, 2013, 38, 796. doi:10.1364/OL.38.000796.

[7] Fülöp J.A.; Tzortzakis S.; Kampfrath T. Laser Driven Strong Field Terahertz Sources. Advanced Optical Materials, 2019, 1900681. doi:10.1002/adom.201900681.

[8] Brunner F. D. J.; Schneider A.; Günter P. Velocity-matched terahertz generation by optical rectification in an organic nonlinear optical crystal using a Ti:sapphire laser. Applied Physics Letters, 2009, 94, 061119. doi:10.1063/1.3080214.

[9] Ravi K.; Huang W. R.; Carbajo S.; Nanni E. A.; Schimpf D. N.; Ippen E. P.; Kärtner F. X. Theory of terahertz generation by optical rectification using tilted-pulse-fronts. Optics Express, 2015, 23. doi:10.1364/oe.23.005253.

[10] Hamster H.; Sullivan A.; Gordon S.; White W.; Falcone R. Subpicosecond, electromagnetic pulses from intense laser-plasma interaction. Physical review letters, 1993, 71, 2725–2728. doi:10.1103/physrevlett.71.2725.

[11] Minami Y.; Kurihara T.; Yamaguchi K.; Nakajima M.; Suemoto T. High-power THz wave generation in plasma induced by polarization adjusted two-color laser pulses. Applied Physics Letters, 2013, 102, 041105. doi:10.1063/1.4789773.

[12] Oh T. I.; You Y. S.; Jhajj N.; Rosenthal E. W.; Milchberg H. M.; Kim K. Y. Scaling and saturation of high-power terahertz radiation generation in two-color laser filamentation. Applied Physics Letters, 2013, 102, 201113. doi:10.1063/1.4807790.

[13] Hafez H. A.; Chai X.; Ibrahim A.; Mondal S.; Férachou D.; Ropagnol X; Ozaki T. Intense terahertz radiation and their applications. Journal of Optics, 2016, 18, 093004. doi:10.1088/2040-8978/18/9/093004.

[14] Nazarov D. D.; Mitrofanov A. V.; Sidorov B. D. A.; Chan M.V.; Shcheglov P.A.; Zheltikov A.M.; Panchenko V.Y. Enhancement of THz Generation by Two-Color TW Laser Pulses in a Low-Pressure Gas. Journal of Infrared, Millimeter, and Terahertz Waves, 2020. doi:10.1007/s10762-020-00689-z.

[15] Lee Y.S. Principles of terahertz science and technology Principles of Terahertz Science and Technology. Berlin: Springer 2009.

[16] Kono S.; Tani M.; Sakai K. Ultra-broad band photoconductive detection: Comparison with free-space electro-optic sampling. Applied physics letters, 2001, 79, 898–900. doi:10.1063/1.1394719.

[17] Zhang J.; Hong Y.; Braunstein S.L.; Shore K.A. Terahertz pulse generation and detection with LT-GaAs photoconductive antenna. IEE Proc. Opto electron, 2004, 151. doi:10.1049/ip-opt:20040113.

[18] Singh A.; Pal S.; Surdi H.; Prabhu S. S.; Mathimalar S.; Nanal V.; Pillay R. G.; Döhler G. H. Carbon irradiated semi insulating GaAs for photoconductive terahertz pulse detection. Optics Express, 2015, 23, 6656. doi:10.1364/OE.23.006656.

[19] Wu Q.; Zhang X.-C. Free-space electro-optic sampling of terahertz beams. Applied Physics Letter 1995, 67, 3523–0. doi:10.1063/1.114909.

[20] Gallot G.; Grischkowsky D. Electro-optic detection of terahertz radiation. J. Opt. Soc. Am. B, 1999, 16, 1204–0. doi:10.1364/JOSAB.16.001204.

[21] Teo S. M.; Ofori O.; Benjamin K.; Werley C. A.; Nelson K. A. Invited Article: Single-shot THz detection techniques optimized for multidimensional THz spectroscopy. Review of Scientific Instruments, 2015, 86, 051301. doi:10.1063/1.4921389.

[22] Schmidhammer U.; Waele V. D.; Marquès J.R.; Bourgeois N.; Mostafavi M. Single shot linear detection of 0.01–10 THz electromagnetic fields. Appl Phys B, 2009, 94, 95–101. doi:10.1007/s00340-008-3262-5.

[23] Wang T.; Iwaszczuk K.; Wrisberg E. A.; Denning E. V.; Jepsen P. U. Linearity of Air-Biased Coherent Detection for Terahertz Time-Domain Spectroscopy. Journal of Infrared, Millimeter, and Terahertz Waves, 2016, 37, 592–604. doi:10.1007/s10762-015-0242-9

[24] Dai J.; Xie X.; Zhang X.C. Detection of Broadband Terahertz Waves with a Laser-Induced Plasma in Gases. Physical Review Letters, 2006, 97, 103903. doi:10.1103/PhysRevLett.97.103903.

[25] Vicarelli L.; Tredicucci A.; Pitanti A. Micromechanical Bolometers for Subterahertz Detection at Room Temperature. ACS Photonics, 2022, 9, 2, 360–367. https://doi.org/10.1021/acsphotonics.1c01273.

[26] Yingxin W.; Ziran Z.; Zhiqiang C.; Linghui W. 37th International Conference on Infrared, Millimeter, and Terahertz Waves (IRMMW-THz) - Characterization of Golay detector for the absolute power measurement of terahertz radiation. IEEE, 2012, 1–2. doi:10.1109/IRMMW-THz.2012.6380076.

[27] Oleg V. M.; Jaime C.G.; Yahya M. M.; Igor V. M. Improvement of an InfraRed Pyroelectric Detector Performances in THz Range Using the Terajet Effect. Applied Sciences, 2021. doi:10.3390/app11157011.

[28] Smolyanskaya O.A.; Chernomyrdin N.V.; Konovko A.A.; Zaytsev K.I.; Ozheredov I.A.; Cherkasova O.P.; Nazarov M.M.; Guillet J.P.; Kozlov S.A.; Kistenev Y.V.; Coutaz J.L.; Mounaix P.; Vaks V.L.; Son J.H.; Cheon H.; Wallace V.P.; Feldman Y.; Popov I.; Yaroslavsky A.N.; Shkurinov A.P.; Tuchin V.V. Terahertz biophotonics as a tool for studies of dielectric and spectral properties of biological tissues and liquids. Progress in Quantum Electronics, 2018, 62. https://doi.org/10.1016/j.pquantelec.2018.10.001.

[29] Lulu W. Terahertz Imaging for Breast Cancer Detection. Sensors, 2021, 21, 6465. https://doi.org/10.3390/s21196465.

[30] Gezimati M.; Singh G. Advances in terahertz technology for cancer detection applications. Opt. Quant. Electron 2023, 55, 151. https://doi.org/10.1007/s11082-022-04340-0.

[31] Cassar Q.; Al-Ibadi A.; Mavarani L.; Hillger P.; Grzyb J.; MacGrogan G.; Zimmer T.; Pfeiffer U. R.; Guillet J-P.; Mounaix P. Pilot study of freshly excised breast tissue response in the 300 – 600 GHz range. Biomed. Opt. Express, 2018, 9, 2930-2942.

[32] Cassar Q.; Caravera S.; MacGrogan G.; Bücher T.; Hillger P.; Zimmer T.; Guillet J-P.; Mounaix P. Terahertz refractive index-based morphological dilation for breast carcinoma delineation. Sci Rep **11**, 6457 (2021). https://doi.org/10.1038/s41598-021-85853-8

[33] Seo K.S.; Bajracharya R.; Lee S. H.; Han H.K. Pharmaceutical Application of Tablet Film Coating. Pharmaceutics, 2020, 12, 853. doi:10.3390/pharmaceutics12090853.

[34] Lin H.; Dong Y.; Shen Y.; Axel Z. J. Quantifying Pharmaceutical Film Coating with Optical Coherence Tomography and Terahertz Pulsed Imaging: An Evaluation. Journal of Pharmaceutical Sciences, 2015, 104, 3377–3385. doi:10.1002/jps.24535.

[35] Brock D.; Zeitler J. A.; Funke A.; Knop K.; Kleinebudde P. Evaluation of critical process parameters for intra-tablet coating uniformity using terahertz pulsed imaging. European Journal of Pharmaceutics and Biopharmaceutics, 2013, 85, 1122–1129. doi:10.1016/j.ejpb.2013.07.004.

[36] Abraham E.; Younus A.; Delagnes J.C.; Mounaix P. Non-invasive investigation of art paintings by terahertz imaging. Appl. Phys. A 100, 585–590 (2010). https://doi.org/10.1007/s00339-010-5642-z.

[37] Dandolo C. L. K.; Jepsen P. U. Wall Painting Investigation by Means of Non-invasive Terahertz Time-Domain Imaging (THz-TDI): Inspection of Subsurface Structures Buried in Historical Plasters. Journal of Infrared Millimeter and Terahertz Waves, 2015, 37, 198–208. doi:10.1007/s10762-015-0218-9.

[38] Walker G.; Bowen J.; Jackson J.; Matthews W.; Labaune J.; Mourou G.; Menu M.; Hodder I. Sub-surface Terahertz Imaging through Uneven Surfaces: Visualizing Neolithic Wall Paintings in Çatalhöyük, in Conference on Lasers and Electro-Optics. OSA Technical Digest (online) Optica Publishing Group paper, 2012. https://doi.org/10.1364/CLEO_SI.2012.CTu3B.4.

[39] Fukunaga K.; Ikari T.; Iwai K. THz pulsed time-domain imaging of an oil canvas painting: a case study of a painting by Pablo Picasso. Applied Physics A, 2016, 122. doi:10.1007/s00339-015-9558-5

[40] Yuefan H.; Hongjian Z. Qualitative and Quantitative Detection of Pesticides with Terahertz Time-Domain Spectroscopy. IEEE Transactions on Microwave Theory and Techniques, 2010, 58, 2064–2070. doi:10.1109/tmtt.2010.2050184.

[41] Qin B.; Li Z.; Luo Z.; Li Y.; Zhang H. Terahertz time-domain spectroscopy combined with PCA-CFSFDP applied for pesticide detection. Optical and Quantum Electronics, 2017, 49. doi:10.1007/s11082-017-1080-x.

[42] Qingxiao M.; Yan T.; Chun L.; Ling J. Simultaneous quantitative determination of low-concentration ternary pesticide mixtures in wheat flour based on terahertz spectroscopy and BPNN. Food Chemistry, 2022, 377, 132030. 1016/j.foodchem.2021.132030.

[43] Campbell M. B.; Heilweil E. J. Noninvasive detection of weapons of mass destruction using terahertz radiation. Terahertz for Military and Security Applications, 2003. doi:10.1117/12.504297.

[44] Chen Y.; Liu H.; Deng Y.; Veksler D. B.; Shur M. S.; Zhang X.C.; Spicer J. B. Spectroscopic characterization of explosives in the far-infrared region. Terahertz for Military and Security Applications, 2004. doi:10.1117/12.540945.

[45] Chen J.; Chen Y.; Zhao H.; Bastiaans G. J.; Zhang X..C. Absorption coefficients of selected explosives and related compounds in the range of 0.1-2.8 THz. Optics Express, 2007, 15, 12060. doi:10.1364/oe.15.012060.

[46] Orenstein J.; Corson J.; Oh S.; Eckstein, J.N. Superconducting fluctuations in $Bi_2Sr_2Ca_{1-x}Dy_xCu_2O_{8+\delta}$ as seen by terahertz spectroscopy. Ann. Phys, 2006, 518: 596-605. https://doi.org/10.1002/andp.200651807-814.

[47] Kida N.; Murakami H.; Tonouchi M. Terahertz Optics in Strongly Correlated Electron Systems. Terahertz Optoelectronics, 2005, 271–330. doi:10.1007/10828028_8.

[48] Takahashi K.; Kida N.; Tonouchi M. Terahertz Radiation by an Ultrafast Spontaneous Polarization Modulation of Multiferroic BiFeO3 Thin Films. Physical Review Letters, 2006, 96. doi:10.1103/physrevlett.96.117402.

[49] Beaurepaire E.; Turner G. M.; Harrel S. M.; Beard M. C.; Bigot J.Y.; Schmuttenmaer C. A. Coherent terahertz emission from ferromagnetic films excited by fem to second laser pulses. Applied Physics Letters, 2004, 84, 3465–3467. doi:10.1063/1.1737467.

[50] Bouamoud R.; Moine E.; Mulongo M. R.; Hamidi A.; Halim M.; Arsalane S. Type Ikerogen-richoilshale from the Democratic Republic of the Congo: mineralogical description and pyrolysis kinetics. Petroleum science, 2020, 17,255–267.

[51] Miao X.; Chen M.; Li Y.; Zhan H.; Zhao K.; Yue W. Simultaneous determination of organic distribution and content in oil shale by terahertz imaging. Energy and Fuels 2020, 34, 1664-1668.

[52] Alstadt K.; Katti D.; Katti K. An insituFTIRstep-scan photo acoustic investigation of kerogen and minerals in oilshale. Spectro chemical ActaPart A, 2012, 89, 105–113.

[53] Ma Y.; Zhou S.; Li J.; Li Y.; Chen K.; Zhang Y.; Fu D. Pyrolysis characteristics analysis of Chang-7 oil shale using thermal analysis and pyrolysis-gas. Energy Exploration and Exploitation, 2020, 36, 1006–1021.

[54] Al-Harahsheh M.;Al-Ayed O.; Robinson J.; Kingman S.; Al-Harahsheh A.; Tarawneh K.; Saeid A.; Barranco. Effect of demineralization and heating rate on the pyrolysis kinetics of Jordanian oil shales. Fuel Processing Technology, 2011, 92, 1805–1811.

[55] Qing W.; Baizhong S.; Aijun H.; Jingru B.; Shaohua L. Pyrolysis characteristics of Huadian oil shales. Oil Shale, 2007, 24, 147–157.

[56] Williams P.; Chishti H. Two stage pyrolysis of oil shale using a zeolite catalyst. Journal of Analytical and Applied Pyrolysis, 2000, 55, 217–234.

[57] Akash A.; Jaber J.O. Characterization of shale oil as compared to crude oil and some refined petroleumproducts. Energy Sources, 2003, 25, 1171–1182.

[58] Fenton D.; Henning H.; Richardson R. The chemistry of shale oil and its refined products. Oil Shale, TarSands, and Related Materials, 2009, 21, 315-325.

[59] Zhang L.; Zhang X.S. L.; Wang Q. Comprehensive utilization of oil shale and prospect analysis. Energy Procedia, 2012, 17, 39 –43.

[60] Yanga Q.; Yang Q.; Man Y.; Zhang D.; Zhou H. Techno economic and environmental evaluation of oil shale to liquid fuels process in comparison with conventional oil refining process. Journal of cleaner production, 2020, 255, 120198.

[61] Altun N.E.; Hicyilmaz C.; Hwang Y.; Bagci A.S.; Kok M.V. Oilshales in the world and Turkey; reserves, current situation, and future prospects: Areview.Oilshale, 2016, 23, 211-227.

[62] Bartis J. ; Tourrette T. ; Dixon L. ; Peterson D. ; Cecchine G. Oil shale developments in the United States; prospects and policy issues. Published by RAND cooperation, 2005, ISBN0-8330-3848-6.

[63] Dyn J. Geology and resources of some world oil-shale deposits.Scientific Investigations Report, 2006, 2005-5294.

[64] Ehinola O.; Sonibare O.; Akanbi O. Economic evaluation, recovery techniques and environmental implications of the oilshale deposits in the Abakiliki Anticlinorium, South eastern Nigeria. OilShale, 2005, 22, 5-19.

[65] Sonibare O.; Ehinola O.; Egashira R. Thermal and geochemical characterization of Lokpanta oil shales, Nigeria. Energy Conversion and Management, 2005, 46, 2335–2344.

[66] Osuji L. The future of petroleum in Nigeria and prospects of shale oil as an alternative energy supplier. J. chem. soc. Nigeria, 2015, 40, 14.

[67] Okon A.; Olagunju D. Economic estimation of oil shale development methods in Nigeria. J. of Scientific and Eng. Research, 2017, 4, 397-408.

[68] Mohammed A.; Peter C.; Alan C. Evaluation of several methods of extraction of oil from a Jordanian oil shale. Fuel, 2012, 92, 281-287.

[69] Rub Z.E.; Kujawa J.; Albarahmieh E.; Rifai N.A.; Qaimari F.; Gharabli S.A. High through put screening and characterization methods of Jordanian oil shale as a case study. Energies, 2019, 12, 3148.

[70] Ojo M. E.; Mounaix P.; Fauquet F.; Bigourd D. Investigation of Oil shale response using THz-TDS. Petroleum Technology Journal, 2021, 12, 81-98. https://www.ptdjournal.com/?page_id=8

[71] Cordes E. E.; Jones D. O. B.; Schlacher T. A.; Amon D. J.; Bernardino A. F.; Brooke S.; Witte U. Environmental Impacts of the Deep-Water Oil and Gas Industry: A Review to Guide Management Strategies. Frontiers in Environmental Science, 2016, 4. doi:10.3389/fenvs.2016.00058.

[72] Jiang C.; Zhao K.; Zhao L. J.; Jin W. J.; Yang Y. P.; Chen S. H. Probing Disaggregation of Crude Oil in a Magnetic Field with Terahertz Time-Domain Spectroscopy. Energy & Fuels, 2014, 28, 483–487. doi:10.1021/ef401984u.

[73] Klaus Backhaus, Bernd Erichson, Sonja Gensler, Rolf Weiber, Thomas Weiber. Multivariate Analysis (An Application-Oriented Introduction) chapter 8, pages 451-530. ISBN: 978-3-658-32588-6.

[74] Zhan H.; Wu S.; Bao R.; Ge L.; Zhao K. Qualitative identification of crude oils from different oil fields using terahertz time-domain spectroscopy. Fuel, 2015,143, 189–193. doi: 10.1016/j.fuel.2014.11.047.

[75] Ge L. N.; Zhan H. L.; Leng W. X.; Zhao K.; Xiao L. Z. Optical Characterization of the Principal Hydrocarbon Components in Natural Gas Using Terahertz Spectroscopy. Energy & Fuels, 2015, 29, 1622–1627. doi:10.1021/ef5028235.

[76] Leng W.; Zhan H.; Ge L.; Wang W.; Ma Y.; Zhao K.; Xiao L. Rapidly determinating the principal components of natural gas distilled from shale with terahertz spectroscopy. Fuel, 2015, 159, 84–88. doi:10.1016/j.fuel.2015.06.072.

[77] Zhan H.; Wu S.; Bao R.; Zhao K.; Xiao L.; Ge L.; Shi H. Water adsorption dynamics in active carbon probed by terahertz spectroscopy. RSC Advances, 2015, 5, 14389–14392. doi:10.1039/c4ra14730h.

[78] Bao R.; Miao X.; Feng C.; Zhang Y.; Zhan H.; Zhao K.; Wang M.; Yao J. Characterizing the oil and water distribution in low permeability core by reconstruction of terahertz images. Science China Physics, Mechanics & Astronomy, 2016, 59, 664201. doi:10.1007/s11433-016-5792-x.

[79] Bao R.; Wu S.; Zhao K.; Zheng L.; Xu C. Applying terahertz time-domain spectroscopy to probe the evolution of kerogen in close pyrolysis systems. Science China Physics, Mechanics and Astronomy, 2013, 56, 1603–1605. doi:10.1007/s11433-013-5085-6.

[80] Rima B.; Qian M.; ChunLian W.; TianYu C.; Chen D.; HongLei Z.; XinYang M.; ChengJing F.; LiYing Z.; LiZhi X. Terahertz spectroscopic characteristics of the geological diagenetic and metallogenic evolution. Scienta Sinca Physica, Mechanica & Astronomica, 2015, 45, 084203-084203. https://doi.org/10.1360/SSPMA2015-00139.

[81] Bao R.; Li Y.; Zhan H.; Zhao K.; Wang W.; Ma Y.; Xiao L. Probing the oil content in oil shale with terahertz spectroscopy. Science China Physics, Mechanics & Astronomy, 2015, 58, doi:10.1007/s11433-015-5731-2

Chapter 2

Theory of THz Pulse Generation in Non-linear Crystals

Inorganic and organic nonlinear crystals are important emitters of THz pulses. An understanding of the underlining mechanism of the emission process is pertinent in order to optimize the efficiency of the process. In view of this, this chapter is dedicated to treat the theory of THz generation by optical rectification and examine the factors that limits the scalable THz amplitude and spectral bandwidth. Specific attention will be given to ZnTe and BNA crystals since the experimental results of this work were based on these crystals.

2.1 Nonlinear polarization

Optical rectification is a second order nonlinear effect corresponding to the generation of low-frequency radiation by frequency difference. Physically, optical rectification is the low-frequency response of a nonlinear material to the envelope of an intense laser pulse. This response will give rise to a nonlinearly induced second order polarization described as **[1],**

$$P_i^{NL}(\omega_{THz}) = \int_{-\infty}^{\infty} \epsilon_o \; \chi_{ijk}^{(2)} \; (\omega_{THz}, \omega, -\omega) \; E_j(\omega) \; E_k^*(\omega) \; d\omega \tag{2-1}$$

where, E_j and E_k^* describes the electric field of the incident laser field. The permitivity of free space is denoted as ϵ_0. The index *i,* indicates the cartesian coordinates (*x*,*y*,*z*) of the induced non-linear polarization. $\chi_{ijk}^{(2)}$ describes the second-order nonlinear susceptibility tensor element of the crystal system which usually consist of 27 tensor elements **[2].** Since the product of E is symmetric in j and k (i.e. $\chi_{ijk}^{(2)} = \chi_{ikj}^{(2)}$), it implies that the 27 tensor elements can be reduce to 18 tensor elements i.e. $\chi_{ijk}^{(2)} \rightarrow \chi_{im}^{(2)}$. Generally, for a ZnTe crystal, the only elements of the nonlinear susceptibility tensor that are non-zero are $\chi_{14} = \chi_{25} = \chi_{36}$ **[3],** thus,

$$\chi^{(2)}_{ijk} = \chi^{(2)}_{im} = \begin{pmatrix} 0 & 0 & 0 & \chi_{14} & 0 & 0 \\ 0 & 0 & 0 & 0 & \chi_{25} & 0 \\ 0 & 0 & 0 & 0 & 0 & \chi_{36} \end{pmatrix} \qquad (2\text{-}2)$$

Where

i	*m*	*jk*
1	1	11
2	2	22
3	3	33
	4	23 32
	5	13 31
	6	12

Assuming that the input electric field is linearly polarized and impinges with normal incidence on two zinc-blende crystals as shown in Fig. 2.1 and Fig. 2.2 (cut at (110) plane (111) plane respectively).

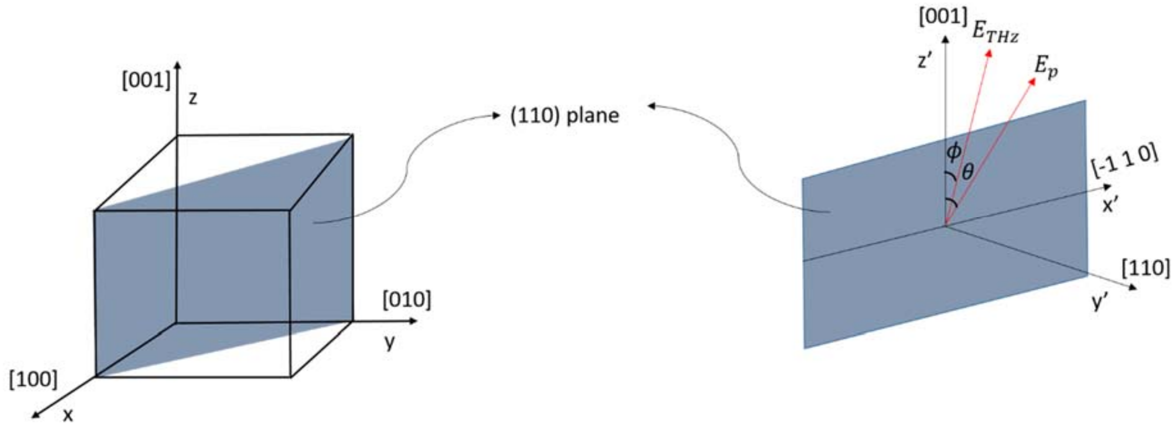

Fig. 2.1 Crystallographic coordinate system for the (110) zinc-blende crystal.

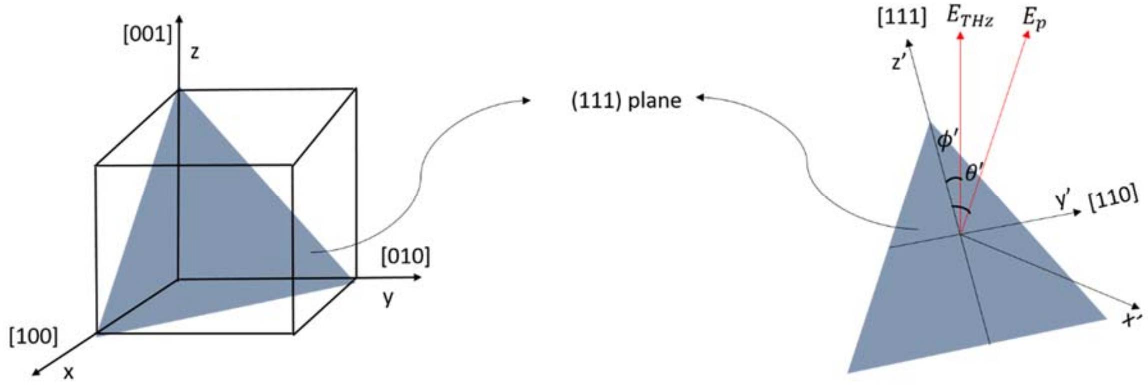

Fig. 2.2 Crystallographic coordinate system for the (111) zinc-blende crystals.

The electric field components of the pump pulse in the laboratory frame are defined as follows **[3],**

$$E_{110} = E_0\left(\frac{\sqrt{2}}{2}sin\theta, -\frac{\sqrt{2}}{2}sin\theta, cos\theta\right) \tag{2-2}$$

And,

$$E_{111} = E_0\left(\frac{\sqrt{2}}{2}sin\theta' - \frac{\sqrt{6}}{6}cos\theta', -\frac{\sqrt{2}}{2}sin\theta' - \frac{\sqrt{6}}{6}cos\theta', \frac{\sqrt{6}}{3}cos\theta'\right) \tag{2-3}$$

where x', y', z' refers to the laboratory frame. E_0 refers to the amplitude of the pump pulse, θ refers to the angle between the (110) crystal's z'-axis and the pump beam polarization E_p, while θ' refers to the angle between the (111) crystal's z'-axis and the pump beam polarization, while ϕ refers to the angle between the THz pulse E_{THz}, and the (110) crystal's z'-axis. In what follows, a description of the nonlinear polarization in the form of matrix equation will be performed. Thus, by using equations (2-1) and (2-2), the induced nonlinear polarization is now,

$$\begin{pmatrix} P_x \\ P_y \\ P_z \end{pmatrix} = \epsilon_0 \begin{pmatrix} 0 & 0 & 0 & \chi_{14} & 0 & 0 \\ 0 & 0 & 0 & 0 & \chi_{25} & 0 \\ 0 & 0 & 0 & 0 & 0 & \chi_{36} \end{pmatrix} \begin{pmatrix} E_x^2 \\ E_y^2 \\ E_z^2 \\ 2E_yE_z \\ 2E_xE_z \\ 2E_xE_y \end{pmatrix} \tag{2-4}$$

$$\begin{pmatrix} P_x \\ P_y \\ P_z \end{pmatrix} = \epsilon_0\, \chi_{14}^{(2)} \begin{pmatrix} 2E_xE_z \\ 2E_xE_z \\ 2E_xE_y \end{pmatrix} \tag{2-5}$$

Since measurement can only be performed in the laboratory frame, it makes sense to define a rotation matrix R, that performs the transformation into the laboratory frame,

$$\begin{pmatrix} x' \\ y' \\ z' \end{pmatrix} = R \begin{pmatrix} x \\ y \\ z \end{pmatrix} = \frac{1}{\sqrt{2}} \begin{pmatrix} 1 & 1 & 0 \\ -1 & 1 & 0 \\ 0 & 0 & \sqrt{2} \end{pmatrix} \begin{pmatrix} x \\ y \\ z \end{pmatrix} \tag{2-6}$$

So, the induced nonlinear polarization in the laboratory frame can be expressed as follows,

$$\begin{pmatrix} P_{x\prime} \\ P_{y\prime} \\ P_{z\prime} \end{pmatrix} = R \begin{pmatrix} P_x \\ P_y \\ P_z \end{pmatrix} = \chi_{14}^{(2)} E_0^2 \begin{pmatrix} 0 \\ sin2\theta \\ -sin^2\theta \end{pmatrix} \tag{2-7}$$

Given that the modulus of the nonlinear polarization is proportional to that of the generated THz electric field **[3]**, then for the case of the (110) cut crystal one obtains **[3],**

$$\left|\boldsymbol{E}_{THz,110}\right| \propto |\boldsymbol{P}| = \epsilon_0 \ \chi_{14}^{(2)} \ E_0^2 \left[-3\left(sin^2\theta - \frac{2}{3}\right)^2 + \frac{4}{3}\right]^{\frac{1}{2}} \tag{2-8}$$

Where $|\boldsymbol{P}| = \sqrt{P_{x\prime}^2 + P_{y\prime}^2 + P_{z\prime}^2}$

It is straightforward to observe, that the amplitude of the generated THz field depends on θ. A plot of the THz amplitude versus angular dependency is as shown in Fig. 2.3. The maximum THz amplitude is obtained when $\theta \approx 55°$, and it is equivalent to,

$$\left|\boldsymbol{E}_{THz,110}\right| \propto \epsilon_0 \sqrt{\frac{4}{3}} \ \chi_{14}^{(2)} \ E_0^2 \tag{2-9}$$

Furthermore, the polarization direction of the generated THz field can be predicted as,

$$tan\phi = \frac{P_{y\prime}}{P_{z\prime}} = -2 \ cot\theta \tag{2-10}$$

This implies that, the direction of the THz field depends on θ, as such when $\theta \approx 55°$, $\phi = 55°$ implying that the THz field vector will be aligned along the same polarization direction as the pump pulse.

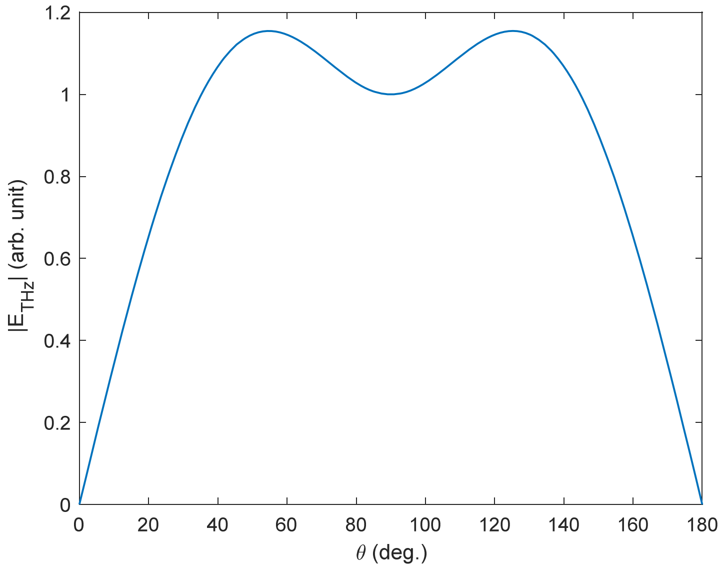

Fig. 2.3 Dependency of THz signal amplitude as a function of the polarization angle between the pump pulse and the optical axis of the (110) ZnTe crystal.

A similar procedure to compute the THz field $\boldsymbol{E}_{THz,111}$, induced in the (111) ZnTe can also be performed. In this case, a new set of transformation equation is defined as follows, **[3]**,

$$\begin{pmatrix} x' \\ y' \\ z' \end{pmatrix} = \frac{1}{\sqrt{6}} \begin{pmatrix} \sqrt{2} & -\sqrt{3} & -1 \\ \sqrt{2} & \sqrt{3} & -1 \\ \sqrt{2} & 0 & 2 \end{pmatrix} \begin{pmatrix} x \\ y \\ z \end{pmatrix} \tag{2-11}$$

As earlier, the modulus of the resulting THz electric field for the case of the (111) cut crystal is as follows,

$$\left|\boldsymbol{E}_{THz,111}\right| \propto |\boldsymbol{P}| = \epsilon_0\, \chi_{14}^{(2)}\, E_0^2 \tag{2-12}$$

For this cut orientation, the amplitude of the THz field is independent on θ'. It is also important to observe that, the maximum THz amplitude obtainable from the (110) cut crystal is by a factor of $\sqrt{\frac{4}{3}}$ higher than that obtained from the (111) cut crystal. This explains the reason behind its popular usage in the literature **[4-8].** In the rest of this manuscript, the discussion shall be restricted to only the (110) ZnTe crystal except otherwise mentioned. By maintaining a relative angle of 55° between the pump polarization and crystal z-axis, the (110) ZnTe crystal will generate THz pulse with the most maximum amplitude. This method of enhancing the THz amplitude by tuning the crystal angle is referred to as birefringent phase matching (a detailed treatment of other types of phase matching conditions shall be treated in subsequent sections). In the meantime, i.e., in the section that immediately follows, a description of the propagation effect of THz generation shall be studied by solving the nonlinear Maxwell's equation **[9]**.

2.2 THz field propagation

Following the optimization of the crystal orientation, it has been realized that a factor of $\sqrt{4/3}$ should be multiplied with P_i^{NL}. Next, the main concern becomes the shape of the THz following its generation. As the THz pulses are emitted, they will propagate until they exit the nonlinear crystal. The evolution of these THz pulses can be modelled by the solving the non-linear Maxwell propagation equation. Assuming that the conductivity of the crystal is neglected, the non-linear Maxwell equation simplifies to **[9-11],**

$$\left(\frac{\partial^2}{\partial z^2} + \omega^2 \frac{\varepsilon(\omega)}{c^2}\right) E_{THz}(\omega, z) = -\sqrt{\frac{4}{3}}\, \frac{4\pi}{c^2}\, \omega^2 P_i^{NL}(\omega, z) \tag{2-13}$$

Solving these equations is not trivial, but several simplifications can be made to make the problem easy to solve. The two main physical effects which will be considered are the following: (i) dispersion and absorption of the THz field, (ii) phase mismatch between the pump and the THz pulse. If the Rayleigh lengths of both the THz and laser fields are longer than the crystal thickness, one can reduce equation (2-13) to a one-dimensional equation. In a well-designed system, the Rayleigh length of the laser beam should be longer than the crystal length in order to benefit from the high laser intensity throughout the crystal's length.

In order to define the laser field $E(t, z)$, the effect of pump depletion and absorption will be neglected. By assuming a Gaussian pulse envelope one can conveniently write,

$$E(t, z) = \frac{E_0}{2} exp\left(\frac{\left(t - {}^{z}/_{v_g}\right)^2}{2\tau^2}\right). exp(i(\omega_0 t - k_0 z)) \tag{2-14}$$

where, v_g refers to the pump's group velocity, ω_0 is the center frequency, and τ is the pulse duration of the pump pulse and k_0 is the pump's wavenumber. By taking the Fourier transform of equation (2-14), and substituting into the equation (2-13), the following is obtained,

$$\left(\frac{\partial^2}{\partial z^2} + \omega^2 \frac{\varepsilon(\omega)}{c^2}\right) E_{THz}(\omega, z) = -\sqrt{\frac{4}{3}}\, \frac{\sqrt{2}\pi\, \chi^{(2)}(\omega)}{c^2}\, \tau\, exp\left(-\frac{\omega^2\tau^2}{4}\right) exp\left(\frac{i\omega z}{v_g}\right) E_0^2 \tag{2-15}$$

.

Assuming that THz field is not generated at the entrance of the crystal, the following sets of boundary condition are applied; $E_{THz}(\omega,0)=0$, $\frac{\partial E_{THz}(\omega,0)}{\partial z}=0$ so that the analytical solution of equation (2-15) becomes **[10],**

$$E_{THz}(\omega,z)=\frac{\chi^{(2)}_{ijk}(\omega)\,\pi\sqrt{2}}{(n^2_{THz}-n^2_g)}\tau\sqrt{\frac{4}{3}}\;e^{\left[\frac{-\omega^2}{4}\tau^2\right]}E_o^2\begin{bmatrix}\frac{1}{2}\left\{1+\frac{n_g}{n_{THz}}\right\}e^{i\omega n_{THz}z/c}\\+\frac{1}{2}\left\{1-\frac{n_g}{n_{THz}}\right\}e^{-i\omega n_{THz}z/c}-e^{i\omega n_g z/c}\end{bmatrix}\qquad(2\text{-}16)$$

Where n_g refers to the pump's group index defined as $n_g=c/v_g$, $n_{THz}=\sqrt{\varepsilon(\omega)}=n+ik$ is the index of refraction of the material in the THz spectral range; n is the real index of refraction and k is the complex index of refraction. As can be observed, the pump intensity dependence of the THz field in equation (2-9) and (2-12) is again recovered in equation (2-16). By increasing the pump intensity, the THz field strength is increased accordingly. However, there is a saturation limit beyond which this linearity is not obeyed in practice. According to equation (2-16), the resulting THz field is a sum of three terms: the first term is a forward propagating field, the third term is also a forward propagating field but with a different phase velocity

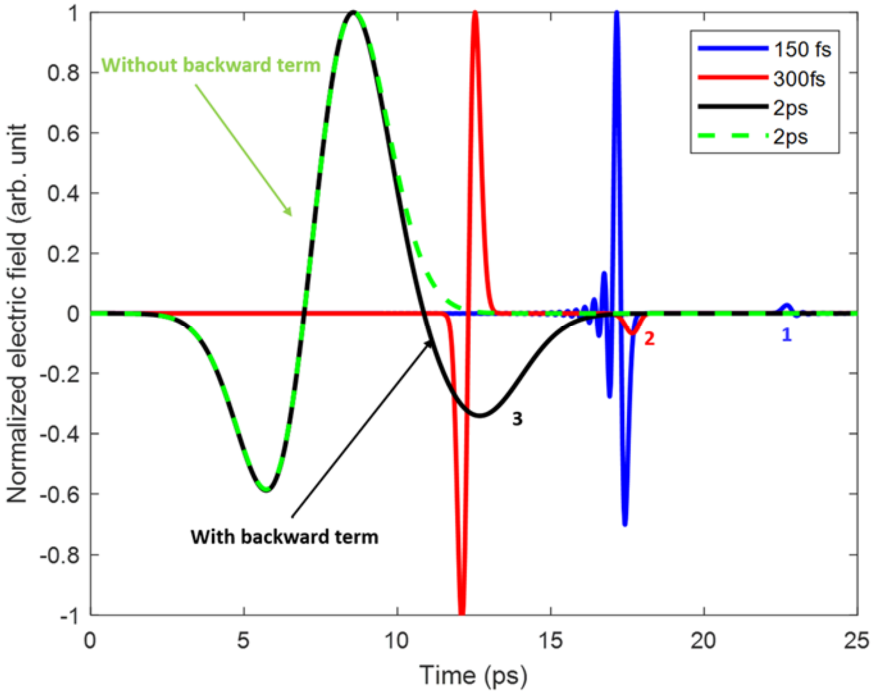

Fig. 2.4 Simulated effect of the contributory terms in a THz signal. There is usually a backward THz signal (labelled 1, 2 and 3) generated with the forward signal whose contribution depends on the pulse duration of the pump laser. Sub-picosecond laser sources such as 150 fs (blue) and 300 fs (red) generates an insignificant backward THz signal term. However, for a picosecond laser

pulse, this backward term has remarkable effects on the forward propagating THz signal (black line) when compared to only the forward term (dashed green line).

The second term is a backward propagating field but has a lower amplitude and are usually neglected. However, we have observed in some part of this work that this backward field does contribute significantly to the form of the overall THz field. By using the Fourier inverse transform of equation (2-16), a comparison between the THz field generated by different pump pulse duration are shown in Fig. 2.4. The plot illustrates the effect of the backward propagating THz pulse term on the overall THz field. By using a 2 ps long pump pulse, it is observed that the simulated THz field with the backward term (black line) and without the backward term (dashed green line) shows a significant discrepancy, such that the effect of this term cannot be neglected as in the case of shorter pump pulses. Another important term in equation (2-16) is $exp\,(-\omega^2\,\tau^2/4)$, which is a Gaussian term and acts as a low-pass filter. The shorter the transform-limited pump pulse duration τ, the wider the generated THz bandwidth. However, in most practical cases of generation, the achievable bandwidth is not infinitely wide, since it mostly depends on the response function of the crystal, as we will show later in subsequent sections. At the moment, assuming we do not exceed the limit of the crystal's response function, the influence of the propagation distance experienced by the generated THz field can influence both its bandwidth and amplitude. To illustrate this effect, the THz spectrum generated by a ZnTe crystal using an 800 nm laser and whose pulse duration is 100 fs will be used. By using equation (2-16), the simulated THz spectrum is plotted at two different propagation distances (which corresponds to two ZnTe crystals with different thickness). As shown in Fig. 2.5, the 0.1 mm thick crystal can generate a broader spectrum up to 4 THz but the THz amplitude will be comparatively lower than when a 1 mm crystal is used. By using the 1 mm thick crystal, higher THz amplitude is observed but the spectrum is narrowed to about 2. 5 THz.

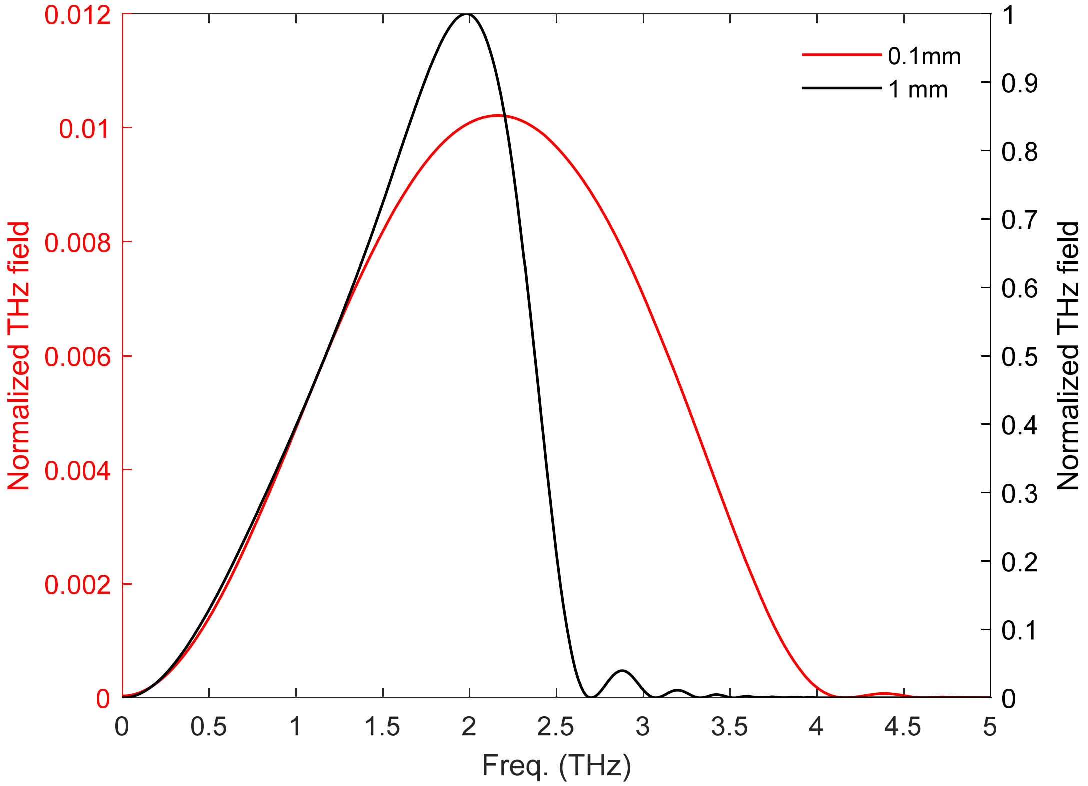

Fig. 2.5 Effect of crystal thickness on the generated THz spectrum. For thin crystal a broader bandwidth can be generated but at the expense of the THz amplitude.

Next, a treatment on certain linear and non-linear phenomena that competes with the THz optical rectification process will be investigated. These effects are namely diffraction, Two Photon Absorption (TPA) and Free Carrier Absorption (FCA) **[12-14]**.

2.3 Effect of diffraction, TPA and FCA on THz generation

In this section, certain effects that co-exist with optical rectification are studied. These effects compete with the scalable THz power. The presence of these effects typically leads to the breakdown of the THz quadratic power law. We shall begin the discussion with the role of the pump beam size as it does affect the diffraction of the THz beam. Then, the concept of TPA and FCA effects will be examined respectively in relation to the pump and THz pulses. The focusing of the pump pulse onto the crystal can be described by the Rayleigh diagram shown in Fig. 2.6.

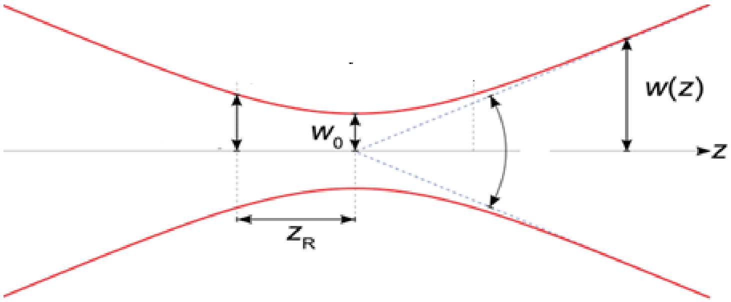

Fig. 2.6 The pump pulse Gaussian width as a function of propagation distance z, at the center of the crystal. w_0 is the beam waist, while z_R refers to the Rayleigh length.

As previously illustrated, the THz electric field varies linearly with the intensity I, of the pump pulse. The intensity of the pump pulse which in part depends on its beam size, can affect the extent to which the THz pulse can be diffracted **[15]**,

$$E_{THz}(t,z) \propto I \propto \frac{\varepsilon_{pump}}{\pi w^2(z)\,\tau} = \frac{P_{pump}}{\pi w^2(z)} \qquad (2\text{-}17)$$

Here ε_{pump} is the pump energy per pulse, P_{pump} is the peak pump power, $w(z) = w_0\sqrt{1+(z/z_R)^2}$ is the pump beam radius in the ZnTe crystal and z_R is the Rayleigh diffraction length of the pump beam. The position z = 0 is defined as the focal point of the pump beam. Here, our point of interest is the diffraction pattern of the THz beam. It has been reported that, the THz beam diffracts more than the pump beam, and as such, the Rayleigh law will not be suitable to define its diffraction length, rather the Bethe diffraction theory is used to obtain the THz diffraction length as follows **[16]**,

$$z_B = \frac{\omega^2 \, w_0^3}{4\sqrt{2}c^2} = \frac{2\pi^2 r_{THz}^3}{\lambda_{THz}^2} \tag{2-18}$$

Where, $r_{THz} = w_o/\sqrt{2}$, is the spot size of the THz pulse, and w_o describes the pump waist. It can be seen that for lower frequencies ω, the THz beam will diffract strongly, since it depends on the square of the frequency. However, for larger pump waist size, diffraction is practically negligible for the whole bandwidth **[17]**. On the other hand, an off-axis parabolic mirror is usually placed after the emitter crystal in order to collect the diffracted beam (THz and pump beam). The geometry of the mirror and the diffraction pattern of the THz beam are used to derive a diffraction transfer function T_{Diff}. The T_{Diff} which is used to model the effect of diffraction on the generated THz field is as follows **[10],**

$$T_{Diff}(\omega, \theta_{mir}) = \sqrt{1 - exp\left(-\frac{tan^2\theta_{mir} z_B^2}{r_{THz}^2}\right)} \tag{2-19}$$

Where, $\theta_{mir} = tan^{-1}\left(\frac{0.5D}{f}\right)$, refers to the semi-aperture, *D* is the diameter and *f* is focal length of the off-axis parabolic mirror.

Another process that competes with the optical rectification process is the absorption of the optical pulse. The differential intensity of the pump pulse is described by **[18-20]**,

$$\frac{dI}{dz} = \alpha - \beta . I^2(z, t) \tag{2-20}$$

Where α refers to the linear absorption coefficient of the pump pulse, β refers to the TPA coefficient which describes the nonlinear absorption of the pump pulse. This coefficient is responsible for saturation effect in the pump pulse intensity profile, and consequently leads to a frequency-dependent intensity profile. TPA are more significant at higher pump intensity than at lower intensities. Thus, limiting the THz field strength that can be achieved according to equation (2-16). As a consequence, the THz spectrum in the presence of TPA will be different from that affected only by a linear absorption. So, in the presence of TPA, the pump pulse intensity is represented as **[21]**,

$$I = \frac{I(z, t)}{1 + \beta I(z, t) S} \, e^{-\alpha z} \tag{2-21}$$

Where,

$$S = \frac{1 - e^{-\alpha z}}{\alpha}$$

One other important effect that limits process of optical rectification is the presence of free carriers in the emitter crystal. These carries which arises due to the effect of TPA, have been reported to contribute to the absorption of the generated THz pulses. The effect of THz absorption by these free carriers is called Free Carrier Absorption. It is described by an attenuation factor I_{FCA}, as follows **[22]**,

$$I_{FCA} = a.exp(-N_e(t).\ b) \tag{2-22}$$

Where, a and b are scaling factors that provides the best fit between theory and experiment. $N_e(t)$ describes the instantaneous electrons generated. The amount of attenuation is higher for high power and low pump pulses.

In the next section, we will study the underlining factors that favors the generation of efficient and spectrally broadened THz spectrum. These factors are namely; velocity phase matching (or simply called phase matching), crystal length as well as second-order nonlinear susceptibility coefficient.

2.4 Phase matching condition and coherence length

The generation of spectrally broadband THz pulses in nonlinear crystals can be determined by matching the THz phase velocity to the pump pulse group velocity. Given that, there is a perfect match between the two velocities, then there will be no restriction to the crystal length appropriate for the generation process. However, since a perfect matching condition is not possible in practice, then the choice of the crystal length can limit the phase matching condition. In this section, the relationship between phase matching and crystal length shall be examined. The study will begin with the investigation of inorganic nonlinear crystals, then followed by organic nonlinear crystals.

2.5 Phase matching criteria in inorganic crystals

Zinc blende structures namely, ZnTe, GaP and CdTe are principal sources of THz radiation among nonlinear crystals **[23-25]**. The refractive index properties of these crystals have an important effect on the magnitude of the THz frequencies that can be generated. In order to illustrate this concept, it has been shown that the THz spectrum can be approximated as a cardinal sinus function [**26**],

$$E_{THz}(\omega, z) \propto \frac{sin(\Delta kz/2)}{\Delta kz/2} \tag{2-24}$$

Where, $\Delta k = \frac{\omega}{c}\left(n_g - n_{THz}\right)$ describes the degree of phase mismatch between the pump and THz pulse. As $\Delta k \to 0$, E_{THz} in equation (2-24) will be optimum given that,

$$sinc(\Delta kz/2) = 1 \tag{2-25}$$

Thus, $\Delta kz = \pi$. So, the minimum corresponding length for which a phase mismatch can be tolerated, is thus

$$z = l_c = \frac{\pi}{\Delta k} \tag{2-26}$$

Where l_c refers to the coherence length needed for generation. This can be described as the minimum crystal length for which the THz pulse phase changes by π. It is important to highlight that the coherence length is a function of two variables namely; the pump pulse wavelength λ_{pump}, and the THz pulse frequency ω as depicted below **[26]**,

$$l_c\left(\lambda_{pump}, \omega\right) = \frac{\pi c}{\omega\left(n_g - n_{THz}\right)} = \frac{\pi c}{\omega\left[\left(n_o - \lambda_{pump}\frac{dn_o}{d\lambda}\Big|_{pump}\right) - n_{THz}\right]} \tag{2-27}$$

Where n_o refers to the optical refractive index of the crystal, and depends on the wavelength of the pump laser and c refers to the speed of light. By interposing n_g and n_{THz} it is possible to intuitively determine the extent of phase mismatch between the THz and pump pulse. Taking the case study of ZnTe, it's n_g and n_{THz} plots are interposed on the same figure as shown in Fig. 2.7. As can be seen, the value of n_g at 800 nm is around 3.25, and a similar match to this value for n_{THz} occurs at around 2.5 THz. Thus, the THz and optical pulse can only be phase matched at such THz frequencies giving rise to narrow band THz spectrum. It is important to observe that the n_{THz} value becomes high at around 5.3 THz. This value defines the phonon frequency of the material, beyond which it becomes extremely difficult to generate higher THz frequency components **[27]**. However, in the case of GaP, a phonon resonance occurs only at around 10 *THz* as shown in Fig. 2.8, as such it is possible to generate higher THz frequencies with GaP crystals than with ZnTe crystals. However, there is a severe mismatch when operated at 800 nm laser. This is because, the n_{THz} is higher than the n_g value at this wavelength. In order to take advantage of its wide spectral width, several methods **[28]** have been implemented to compensate for this phase mismatch which shall be treated in subsequent sections.

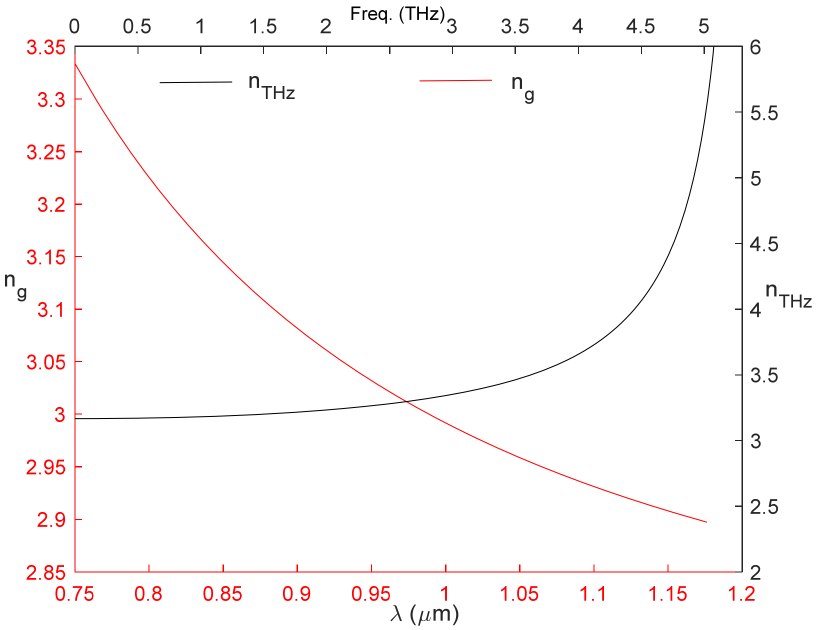

Fig. 2.7 Optical (n_g) and THz refractive index (n_{THz}) of ZnTe crystal in the wavelength region between 750 -1200 nm and 0- 5.3 THz respectively.

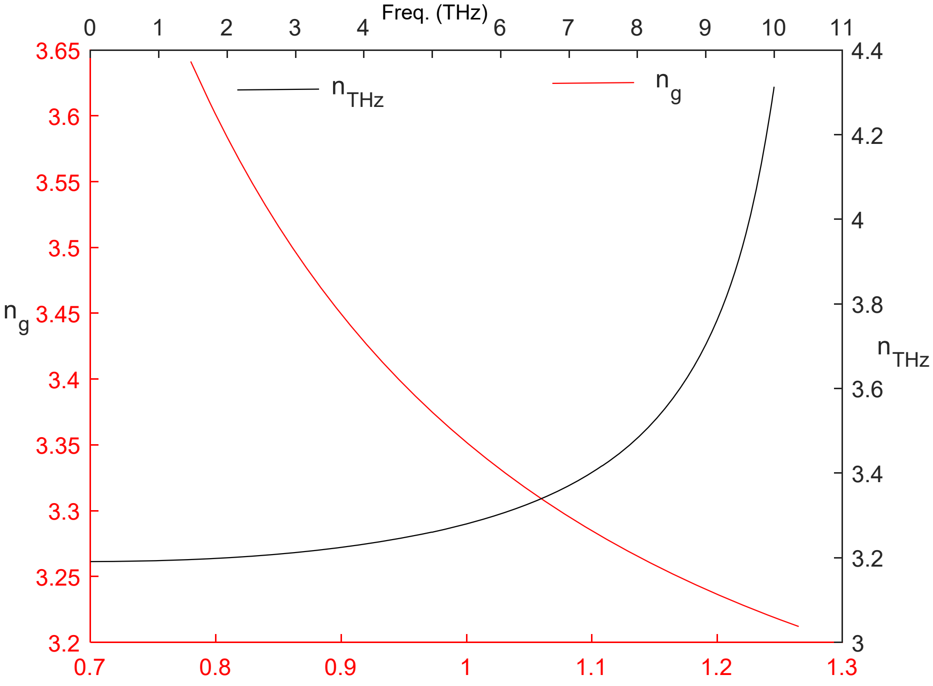

Fig. 2.8 Optical (n_g) and THz refractive index (n_{THz}) of GaP crystal in the wavelength region between 750 -1250 *nm* and 0- 10.5 *THz* respectively.

It is noted earlier, that for a ZnTe crystal, up to 5.2 THz bandwidth can be generated when the phase matching condition is satisfied with a 800 nm laser. However, this frequency value can in part be attainable if the thickness of the crystal is equal to or less than the coherence length. Fig. 2.9, represents the plot of coherence length at two different wavelengths namely 800 nm and 1030 nm. As can be observed, a 1 mm thick ZnTe crystal can generate up to 1 THz and 2.3 THz at 800 nm and 1030 nm respectively, while higher frequencies can be generated with thinner crystals. In the case of GaP crystals, much thinner crystals are required, and the coherence length curve of GaP are less stepper than ZnTe curve thus ensuring a much broader frequency generation.

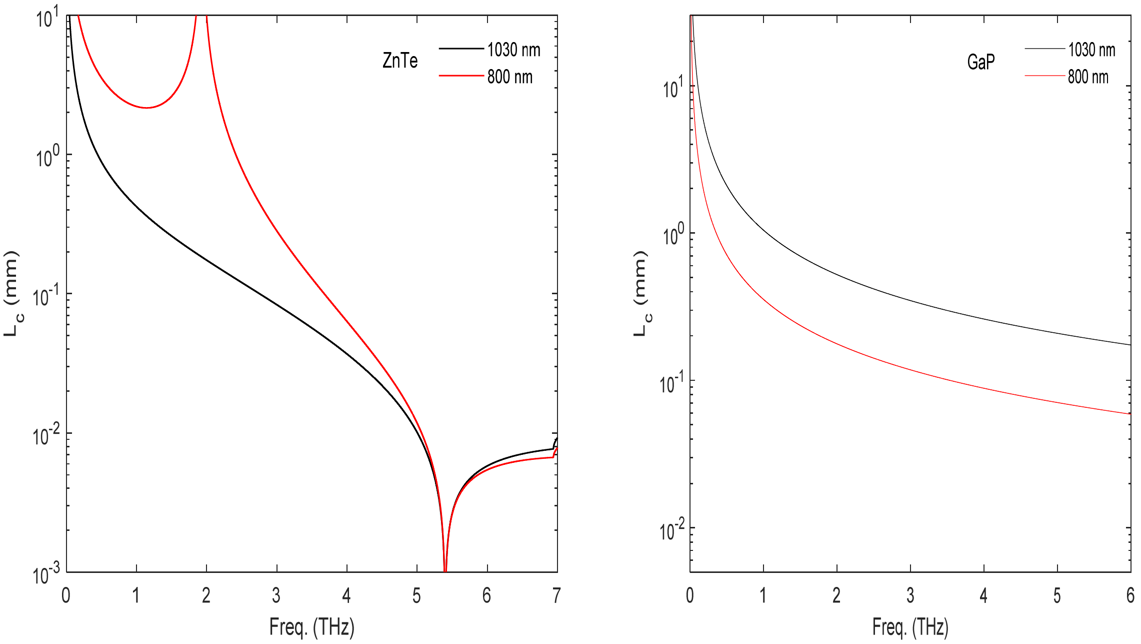

Fig. 2.9 The coherence length of ZnTe and GaP crystal at laser wavelength of 800 nm and 1030 nm.

Haven studied the crystal coherence length that corresponds to phase matching, next I shall examine the extent to which a particular crystal can emit varying bandwidth of THz frequencies. In that case, a new term is introduced which is commonly referred to as generation response function $R_{gen}(\omega)$ **[29-31]**,

$$R_{gen}(\omega) = \frac{2}{n_{THz} + 1} \, sinc \left[\omega z\left(n_g - n_{THz}\right)/c\right] \tag{2-28}$$

The generation response function is derived to include the influences of linear optics such as the mismatch between the THz phase velocity and the group velocity of the pump pulse, reflection losses at the emitter surface, and absorption. A plot of the generation response function for ZnTe and GaP crystals are shown in Fig. 2.10 for a laser wavelength of 800 nm. The plots were obtained by inserting the data in Fig. 2.7 and Fig. 2.8 into equation (2-28). The region in the plots where the value of the response function are maximal corresponds to the instance when the THz and pump are well phase matched. For values of the response function close to zero, the THz and the pump experiences severe mismatch.

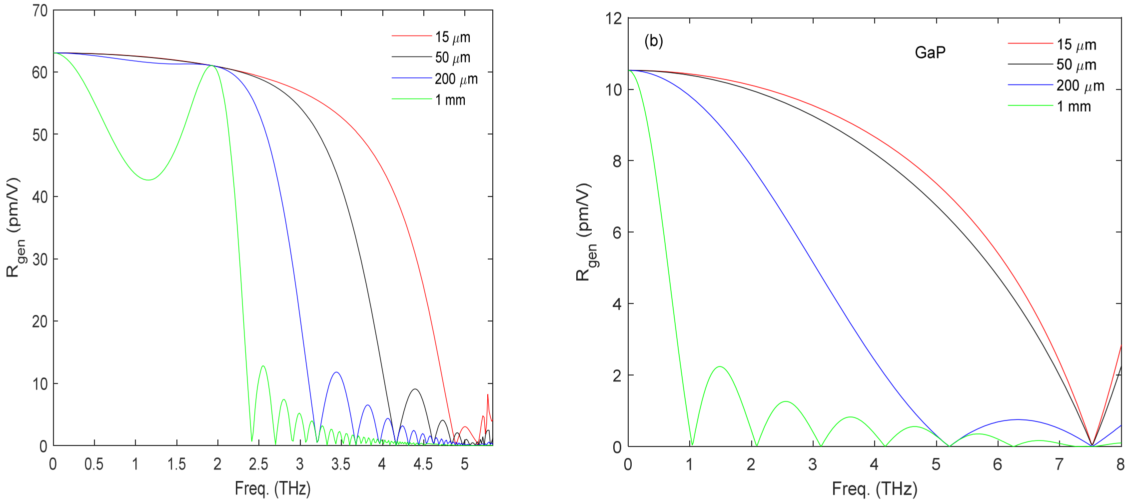

Fig. 2.10 The generation response function of ZnTe and GaP crystal (at 800 *nm*) for varying crystal thickness of 15 *μm*, 50 *μm*, 200 *μm* and 1 *mm*.

As can be seen in Fig. 2.10a, the broadest THz frequency that can be generated is up to 4.5 THz by using the thinnest crystal. Frequencies up to 3 THz can be generated by a ZnTe crystal thickness of 200 *μm*. Although 1 *mm* thickness can also generate up to 3 THz, however in the latter, the THz signal will be distorted and less effectively generated. Generally, the thinner the crystal, the broader the THz spectra and vice versa. In the case of the GaP crystal (Fig. 2.10b), the generation response shows a slightly different behavioral pattern but in generally, broader THz spectra are effectively generated by thinner crystals. Their response curve are less flattened (except for the 15 *μm* and 50 *μm* thickness) and the magnitude of the corresponding THz frequencies are less effectively generated.

In order to expand the scope of comparing the properties of various crystals, a list of the optical and THz refractive index of some inorganic crystals are tabulated in Table 2.1. In order to understand the results in the Table, I will quickly introduce the concept of Figure of Merit (FOM). FOM is used to compare the relative efficiency of optical rectification in different crystals. Depending on the effect of THz absorption in nonlinear crystals, two FOMs are defined respectively for a weakly absorbing and strongly absorbing crystal as follows **[32],**

$$FOM_{WA} = \frac{d_{eff}^2 L^2}{n_g^2 n_{THz}} \tag{2-29}$$

$$FOM_{SA} = \frac{4d_{eff}^2}{n_g^2 n_{THz} \alpha^2} \tag{2-30}$$

Where, $d_{eff=} n_g^4 \chi^{(2)}/4$ refers to the coefficient of nonlinear susceptibility, FOM_{WA} and FOM_{SA} refers to the FOM of a weakly and strongly absorbing crystal respectively and, while α refers to the absorption of THz by the crystal. As can be observed, crystals with large d_{eff} have a corresponding high FOM and are likely to be more efficient in the optical rectification process. A list of FOM values for different crystal is shown in Table 2.1.

Table 2.1 Optical and THz characteristics of some nonlinear inorganic crystals. The values in the table have been considered at 800 nm laser except for CdTe and GaAs crystal obtained between 1030-1060 nm. n_{THz} is measured at 1 *THz* **[33-35]**

	n_g	n_{THz}	$d_{eff}(pm/V)$	$FOM(pm^2cm^2/V^2)$	$\alpha(cm^{-1})$
ZnTe	3.13	3.17	68.5	7.27	1.3
GaP	3.67	3.34	24.8	0.72	0.2
CdTe	2.81	3.24	81.8	11.0	4.8
GaAs	4.18	3.93	65.6	4.21	0.5
$LiNbO_3$	2.25	4.96	168	48.6	17

By comparing the FOM values in Table 2.1, we realize that $LiNbO_3$ has the highest FOM followed by CdTe and ZnTe crystal. In practice, the efficiency of $LiNbO_3$ crystal are never as high as compared to ZnTe in collinear focusing. This difference can be understood based on the large difference between the n_g and n_{THz} values of $LiNbO_3$, in which n_{THz} is almost twice n_g, thus the THz and the pump pulse do not effectively interact during propagation through the crystal, thereby leading a much lower efficiency. Also, the THz absorption in $LiNbO_3$ absorption is about thirteen times higher than ZnTe crystal. In the case of ZnTe crystal, there is a better phase matching since n_{THz} and n_g do not widely differ, in addition to possessing a lower absorption effect on the THz pulse. Also, the effect of phase mismatch is high in GaAs. However, their d_{eff} is reasonably high. In other to fulfil the phase matching condition, and upgrade the efficiency in GaAs and $LiNbO_3$ crystals, certain modifications have already been proposed and implemented. In the next section, we shall briefly discuss the concept of Quasi-Phase Matching (QPM), tilted pulse front scheme and thermal cooling among commonly adopted strategies to augment the efficient of these crystals.

2.6 Compensating for phase mismatch

Compensating for phase mismatch basically involves optimizing the parameters that defines the coherence crystal length, l_c namely; the relative velocity of the pump (or THz pulse) and refractive index of the crystal **[36]**. In view of these, the geometry of the pump pulse and the intrinsic properties of the crystal are the main site of interest. We shall commence by treating these factors under the following headings; Quasi-Phase Matching (QPM), tilted pulse front scheme and cryogenic cooling.

2.6.1 Quasi-Phase Matching

Quasi-Phase Matching (QPM) is a complex technological process in terms of performing phase-matching for crystals that does not require birefringence to achieve phase matching. It is a reversal process that causes a periodic modulation in the nonlinear susceptibility phase of the crystal. This is so called because phase mismatch is not eliminated within each modulation period but it is compensated periodically. Since a phase mismatch leads to a change of the phase over the coherence length, then by periodically modulating $\chi^{(2)}$ such that an opposite phase is introduced, the phase, will then reset to its initial value so that the amplitude annihilation is prevented. This is essentially the principle of QPM. Practical methods for achieving QPM by the modulating nonlinear polarization phase include the stacking of crystalline plates with a periodic rotation of 180°, periodic poling, orientation-patterned epitaxial growth, among others **[37-39].** For example, the periods of the $LiNbO_3$ are periodically pooled by applying an external electric field. Following this ionic modification, better efficiencies have been recorded **[33]**. However, it is important to note that, the periodically poled crystals create a multiple-cycle THz pulse instead of a single cycle, and the efficiency cannot be as high as in the case of a true velocity matching since the THz components generated in the different domain pairs exit the crystal temporally separated, with no constructive interference **[33]**.

2.6.2 Tilted pulse front scheme

The arrival time of an incident pulse on a nonlinear crystal can be made to vary across the beam profile through tilted pulse scheme. By using a grating-lens system, the pump pulse front is tilted upon irradiating the crystal. The THz radiation excited by the tilted pulse front of the pump propagates perpendicularly to this front with a velocity v_{THz} . Consequently, the angle between the propagation direction of the THz radiation and the propagation direction of the pump pulse will be the same as the tilt angle γ of the pulse front relative to the phase front of the pump (which is perpendicular to its propagation direction). Because of this, the phase matching condition will be satisfied as follows **[33]**,

$$v_{gr} cos\gamma = v_{THz} \tag{2-31}$$

Equivalently,

$$n_{THz} cos\gamma = n_g \tag{2-32}$$

Thus, by tilting the pump pulse front appropriately, the otherwise huge refractive index of the THz field (for instance in $LiNbO_3$) becomes scalable to the optical refractive index of the pump pulse, thereby leading to an enhanced efficiency over QPM. However, this non-collinear focusing of the pump pulses is not easy to align **[40].** Certain photorefractive effects which also coexist and leads to the absorption of the THz pulses are mitigated by doping the $LiNbO_3$ crystals with Magnesium (Mg) **[41]**.

2.6.3 Cryogenic cooling

The irradiation of intense beam can result to TPA which can then lead to an increased absorption of the incident beam. As more power becomes absorbed in the crystal, it causes the crystal to heat up to temperature that causes dissociation in the molecular structure of the crystal, thus giving rise to thermo-optic effect. As an example, the crystal refractive index becomes temperature dependent. The reversal of this heating process otherwise called cryogenic cooling has been exploited in THz generation from GaP, PPLN of which higher THz efficiency were recorded compared to an uncooled crystal **[42-44]**. Thus, by controlling the temperature rise in the crystal with the aid of an external cooling system, the beams are less absorbed.

THz efficiency remains generally low for inorganic crystals than for organic crystals. In the following section, we shall discuss this effect with particular emphasis on the BNA crystals operated at around 800 *nm* and 1030 *nm* laser wavelength.

2.7 Phase matching effect in organic crystals

Organic crystals are important class of nonlinear crystals in the generation of THz pulse when the efficiency is considered. The presence of hydrogen bonds and Van Der Waals forces within these crystals forms the basis for their efficient performance. DAST, OH1, DSTMS, HMQ-TMS, CONAP and BNA are commonly used as organic crystals **[45-46]**. A list of some optical and THz properties at laser wavelength >1000 nm for some of these selected crystals are tabulated in Table 2.2. As can be seen, the second order nonlinear susceptibilities are between 160 – 234 pm/V, which are about ten times higher than that of inorganic crystals. As such, an increase in efficiency by one hundred times is expected according to equation (2-28). By using DSTMS for THz emission, a conversion efficiency of 3%, was achieved which led to an ultra-high THz pulse energy of 0.9 mJ at a laser repetition rate of 10 Hz **[47]**. For the organic crystal OH1, a conversion efficiency of 3.2% was also demonstrated at a low laser repetition rate of 10 Hz **[48]**. By pumping a DAST crystal with mid-IR pulses, a record value of 6% conversion efficiency and 1 mW of THz average power at a laser repetition rate of 20 Hz was achieved **[49]**. While pumping BNA at 1030 nm wavelength, 0.04% efficiency was achieved at a laser repetition rate of 13.3 MHz **[50]** and 0.6% at a repetition rate of 1 kHz **[51]**.

According to equation (2-28) and equation (2-29), the efficiency of optical rectification can be improved given that n_g and n_{THz} are low. By comparing the refractive indices of the inorganic and organic crystals in Table 2.1 and Table 2.2 respectively, it is thus expected that the latter will be more efficient that the former. Moreover, it can also be inferred from Table 2.2 that the dispersion of the refractive indices is intrinsically lower in organic crystals as compared to inorganic crystals, thereby guarantying a broad bandwidth THz spectrum generation.

Table 2.2 Optical and THz characteristics of some nonlinear organic crystals at 2 *THz*.

	n_g	n_{thz}	d_{eff} *(pm/V)*	Laser wavelength (*nm*)
DAST	2.26	2.24	242	1535
OH1	2.32	2.3	278	1319
DSTMS	2.12	2.2	167	1907
BNA	1.95	2.00	234	1060

In particular, THz signal bandwidth of more than 20 THz was obtained by using DSTMS pumped by 38 fs, 1250 nm laser pulses **[48].** The organic crystal HMQ-TMS was investigated with a compressed Yb-doped fiber to achieve 1.38 mW of THz average power in which the spectrum extended up to 6 THz at -30 dB **[52].** By using Ti:Saph laser followed by an Optical Parametric Amplifier at 65 fs, 1350 nm, THz pulses whose bandwidth extends up to 12 THz with an electric field of 0.06 GV/cm were generated **[53]**. The BNA crystals have also been operated with 1200 nm, 85 fs laser, in which the obtained spectral contents extend up to 7 THz and a nominal peak electric field of 0.01 GV/cm **[54]**.

To properly study the phase matching condition in BNA a plot of n_g and n_{THz} is shown in Fig. 2.11. It can be observed, that the refractive indices corresponding to phase matching between the optical and THz pulses are typically less than 2.2. In the wavelength region between 800 nm-1200 nm, the n_g and n_{THz} are similar, and as such leads to the generation of about 2-6 THz frequencies. It is important to note that, unlike in inorganic crystals where profound phonon frequency is present, this is not the case with BNA instead the refractive index decreased with frequency.

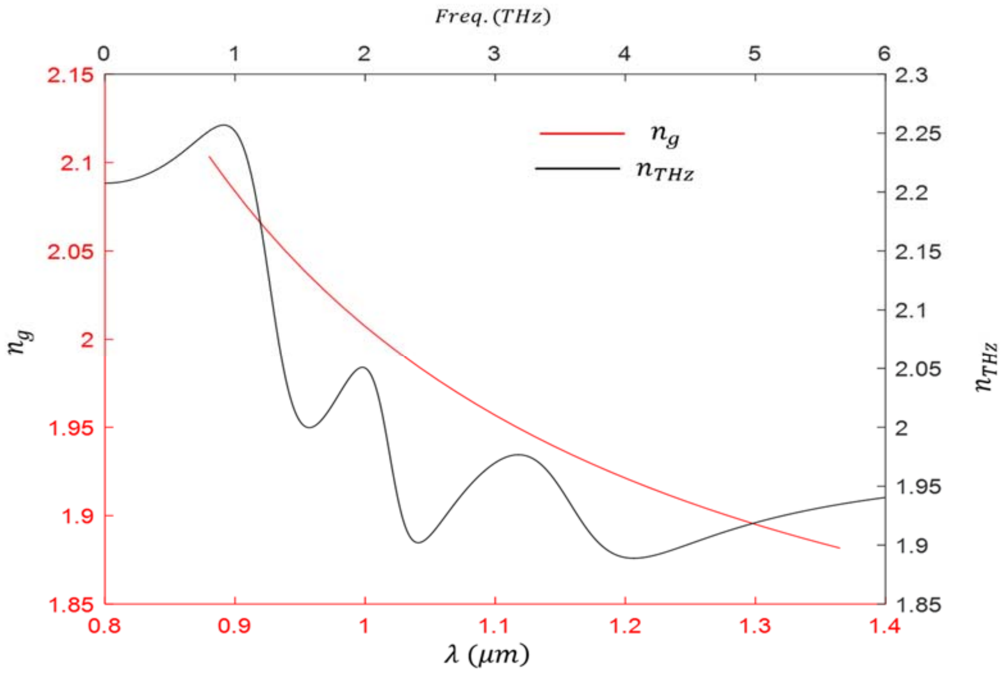

Fig. 2.11 Calculated optical (n_g) and THz refractive index (n_{THz}) of BNA crystal in the wavelength region between 750 -1250 nm and 0- 6 THz respectively.

In order to evaluate the crystal thickness that corresponds to the phase matching condition, the plot of coherence length for BNA crystal at 800 nm and 1030 nm laser wavelength is shown in Fig. 2.12. Generally, a crystal thickness less than 1 mm is ideal for higher THz frequency generation at both wavelength sources. It is easy to observe that, multiple THz frequencies can be generated for a particular crystal length. In practice these frequency components do not usually appear distinct, instead they are coalesced resulting to a broad bandwidth spectrum.

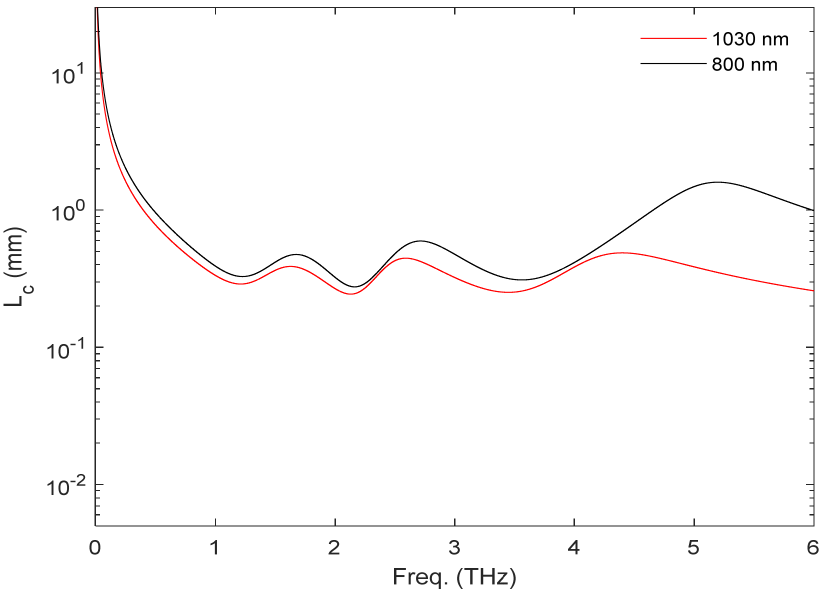

Fig. 2.12 The calculated coherence length of BNA crystal at laser wavelength of 800 nm and 1030 nm.

2.7.1 Fabrication and structure of BNA crystals

N-benzyl-2-methyl-4-nitroaniline (BNA) are single large crystals belonging to the point group of mm2 with an orthorhombic crystal structure. It has a melting temperature of 103°C, with a very high second order nonlinear coefficient of 234 pm/V in the near-infra red region **[55]**. They are fabricated from polycrystalline BNA granules. The *vertical-Bridgeman techniques* were the earliest methods employed in the production of BNA crystals. In this method, a moveable crucible is lowered into a furnace (consisting of different temperature sections in which a negative temperature gradient exists from the top to the bottom of the furnace). The BNA poly crystals are poured at the top of the furnace into the crucible. Since the temperature at the top of the furnace are often higher than the melting point of the crystals, a phase transition from solid to molten-solid occurs. So, as the crucible moves vertically downward through the furnace, the molten crystals become solidified into a single large crystal when it crosses into the temperature region lower than its melting point **[56]**. Another technique referred to as the *solution growth method* is now becoming more popular than the vertical-Bridgeman method for growing BNA crystals. In this method, the polycrystalline BNA granules are usually dissolved into a solvent of alcohol (ethanol or methanol). By increasing the temperature of the solution, more granules are dissolved. Subsequently, the solution are gradually cooled for several days resulting to the crystallization of pure BNA single crystal out of the solution. If required, the crystalized BNA are placed on a substrate, so that the BNA crystal are further grown on the substrate by further cooling down the solution. Eventually, a large yellow colored crystal will precipitate from the solution whose crystallographic axis are labelled *a, b, c*, where the *b*-axis direction corresponds to the propagation direction of the pump pulse and the generated THz radiation under the collinear phase-matching conditions of optical rectification **[55]**.

The performance efficiency of both the vertical-Bridgeman and ethanol solution grown BNA have previously been reported. The result showed that when the crystal is operated with a 1064nm, 100 Hz laser source, a damage threshold of 18 MW/cm^2 and 27 MW/cm^2 was recorded for the vertical-Bridgeman and ethanol solution grown BNA respectively **[57].** Hence, we have utilized the latter in our work.

2.7.2 Thermal-optical effect in BNA crystal.

Generally, BNA crystals possess relatively weak intermolecular binding compared to other organic crystals. The binding are even weaker in vertical-Bridgman than in solution grown crystals. Thus, in the presence of moderate power lasers, the crystals tend to produce defects and distortion. As a result of this thermal instability, they are usually glued to a substrate that possesses a good thermal conductivity. The substrate serves to conduct away the laser heat, so that a high damage threshold can be attained. Commonly utilized substrates are diamond and sapphire substrate. Table 2.3 summarizes some reported difference between substrate-BNA and pure-BNA **[50, 55, 58]**.

Table 2.3 Comparison among substrate-BNA and pure-BNA performance. A direct comparison cannot be made between [1] and [2] since a different repetition rate laser was used. However, the authors of the work highlighted that the diamond-BNA was more efficient than the Sapphire-BNA.

	Laser operating condition	**Max.THz power (mW)**	**THz field (kV/cm)**	**Damage threshold (mJ/cm^2)**
Pure-BNA	1 kHz, 800 nm		4.84	
Sapphire-BNA **[59]**	1 kHz, 800 nm		13.2	
Pure-BNA	13.3 MHz, 1030 nm	0.32		
Diamond-BNA **[60]**	13.3 MHz, 1030 nm	0.95		
[1]Diamond-BNA	13.3 MHz, 1030 nm	0.95		
[2]Sapphire-BNA **[61]**	540 kHz, 1030 nm	5.6		

Glass-BNA	2 kHz, 800 nm			3.7
Sapphire-BNA **[62]**	2 kHz, 800 nm			12
Pure-BNA	500 Hz, 800 nm			4
Pure-BNA **[63]**	1 kHz, 800 nm			2

From the table, it can be inferred that pure BNA crystals are less efficient for THz generation, owing to the poor conduction of the laser's thermal heat away from the crystal. In order to overcome this effect, the glued substrates which are often larger in dimensions are placed in the leading path of the pump pulse **[55]**. By comparing glass-BNA and sapphire-BNA under the same laser condition, the latter appears to be significantly higher in damage threshold. As can also be infer from Table 2.3, the repetition rate of the lasers plays a crucial role when operated with BNA crystals. Low rate repetition lasers are optimum for BNA crystals if one considers generating THz pulses **[64]**. Since these lasers are low in average power, the BNA crystals do not heat up quickly thus maintaining the structure of the otherwise fragile crystal. Lower the repetition rate of lasers have been reported to have achieved higher damaged threshold **[65-66]**. Though, the average power (for repetition rate between 10 Hz - 1 kHz) are low, however the energy per pulse which are often higher makes them the preferable candidates that offer high efficiency with a lower thermal effect on the crystal. Higher rate repetition lasers (in the order of several kHz to MHz) has certain drawbacks considering their application with BNA crystals **[50]**, in that the time between their pulses do not match the thermal relaxation time of the BNA crystals τ_r. τ_r gives an estimate of the time required to dissipate the laser's heat away from the BNA crystals. This value has been estimated at around 5-10 ms **[64]**. Taking the particular example of a 1 MHz laser source, the time between their laser pulses is 1 ns. As such, the BNA crystals does not have sufficient time to cool off before encountering subsequent pulses in the pulse train of the laser, thus heating up the crystal quickly. In order to circumvent this challenge, the use of controllable duty-cycle chopper was proposed and implemented **[50, 67]**. The duty-cycle of the chopper decides the ON/OFF time of the laser pulse energy which interacts with the crystal. With the use of low duty-cycle chopper wheels, BNA have been operated with high repetition rate laser, and improved efficiency obtained **[50]**. In this case, the 'burst pulses' controls the dynamics of the input laser rather than the 'single pulse'. Also, the longer off time (i.e. the time between the pulses) will provide a better match with the thermal relaxation of the crystal.

2.8 Conclusion

The optimization of THz generation in nonlinear crystals lies in the understanding of the theoretical framework governing optical rectification. For an efficient process, the group velocity of the optical pulse must be well matched to the phase velocity of the THz pulse for a given laser source. Even for an appropriate laser wavelength, the thickness of the EO crystal can limit the bandwidth of the THz spectrum. Generally, thinner crystals favor the phase matching condition at the expense of the strength of the generated THz field. If the conditions for phase matching are not satisfied certain techniques such as tilted pulse front scheme, cryogenic cooling and quasi phase matching are usually employed to compensate for the phase mismatch. With the use of short and intense pump pulses, broad and intense THz spectral can be generated in addition to other nonlinear effects such as FCA and TPA which may be detrimental to the overall efficiency of the process. In fact, the broadness of the THz spectrum is limited by the spectral response of the crystal.

2.9 Bibliography of Chapter 2

[1] Boyd R. W. Nonlinear Optics. Third edition, ISBN-978-0123694706

[2] Maeng I.; Kim, J.; Choi H. Ultrabroadband Terahertz Spectroscopy. Convergence of Terahertz Sciences in Biomedical Systems, 2012, 219–229. doi:10.1007/978-94-007-3965-9_12

[3] Chen Q.; Tani M.; Jiang Z.; Zhang X.C. Electro-optic transceivers for terahertz-wave applications. J. Opt. Soc. Am. B 2001, 18(6), 823–0. doi:10.1364/JOSAB.18.000823

[4] Rice A.;Jin, Y.; Ma X. F.; Zhang X. C.; Bliss D.; Larkin J.; Alexander, M. Terahertz optical rectification from <110> zinc-blende crystals. Appl. Phys. Lett. 1994, 64, 1324-1326. https://doi.org/10.1063/1.111922

[5] Fülöp J. A.; Tzortzakis S.; Kampfrath T. Laser-Driven Strong-Field Terahertz Sources. Adv. Optical Mater. 2020, 8, 1900681. https://doi.org/10.1002/adom.201900681

[6] Wei-Qiang H.; Chun-Ming G.; Wen-Zhong S. Direct evidence of Kerr-like nonlinearity by femtosecond Z-scan technique. Opt. Express, 2006, 14, 5476-5483

[7] Dong L.;Guohong M. Pump-wavelength dependence of terahertz radiation via optical rectification in (110)-oriented ZnTe crystal. Journal of Applied Physics, 2008, 103, 123101. https://doi.org/10.1063/1.2938847

[8] Blanchard F.; Razzari L.; Bandulet H.C.; Sharma G.; Morandotti R.; Kieffer J. C.; Ozaki T.; Reid M.; Tiedje H. F.; Haugen H. K. Generation of 1.5 µJ single-cycle terahertz pulses by optical rectification from a large aperture ZnTe crystal. Optics express, 2007, 15, 13212–0.doi:10.1364/OE.15.013212

[9] Ravi K.; Huang W. R.; Carbajo S.; Nanni E. A.; Schimpf D. N.; Ippen E. P.; Kärtner F. X. Theory of terahertz generation by optical rectification using tilted-pulse-fronts. Optics Express, 2015, 23, 5253. doi:10.1364/oe.23.005253

[10] Faure J.; Van T. J.; Kaindl R. A.; Leemans W. P. Modelling Laser-Based Table-Top THz Sources: Optical Rectification, Propagation and Electro-Optic Sampling. Optical and Quantum Electronics, 2004, 36, 681–697.doi:10.1023/b:oqel.0000039617.85129.c2

[11] He, G. S. Terahertz Nonlinear Photonics. Nonlinear Optics and Photonics (Oxford, 2014, Oxford Academic, 18 Dec. 2014). https://doi.org/10.1093/acprof:oso/9780198702764.003.0017.

[12] Gaivoronsky V. Y.; Nazarov M. M.; Sapozhnikov D. A.; Shepelyavyi Y. V.; Shkel'nyuk S. A.; Shkurinov A. P.; Shuvaev A. V. Competition between linear and nonlinear processes during generation of pulsed terahertz radiation in a ZnTe crystal. Quantum Electronics, 2005, 35, 407–414. doi:10.1070/QE2005v035n05ABEH002805

[13] Ku S. A.; Tu C. M.; Chu W.C.; Luo C. W.; Wu K. H.; Yabushita A.; Chi C. C.; Kobayashi T. Saturation of the free carrier absorption in ZnTe crystals. Optics Express, 2013, 21, 13930. doi:10.1364/OE.21.013930

[14] Vidal S.; Degert J.; Tondusson M.; Oberlé J.; Freysz E. Impact of dispersion, free carriers, and two-photon absorption on the generation of intense terahertz pulses in ZnTe crystals. Applied Physics Letters, 2011, 98, 191103–.doi:10.1063/1.3588411

[15] Qirong X.; Liying L.; Zhen T.; Ning Z.; Shuxin L.; Kai W.; L.; Chai.; Qingyue W. The effect of two-photon absorption and optical excitation area on the generation of THz radiation. Optics Communications, 2006, 267, 422-426. https://doi.org/10.1016/j.optcom.2006.06.051

[16] Tomasino A.; Parisi A.; Stivala S.; Livreri P.; Cino A. C.; Busacca A. C.; Peccianti M.; Morandotti R. Wideband THz Time Domain Spectroscopy based on Optical Rectification and Electro-Optic Sampling. Scientific Reports, 2013, 3. doi:10.1038/srep03116

[17] Xu J. Z.; Zhang X. C. Optical rectification in an area with a diameter comparable to or smaller than the center wavelength of terahertz radiation. Optics letters 2002, 27, 1067–0. doi:10.1364/OL.27.001067

[18] Bechtel J. H.; Smith W. L. Two-photon absorption in semiconductors with picosecond laser pulses. Physical Review B 1976, 13, 3515–3522. doi:10.1103/physrevb.13.3515

[19] Dakovski G. L.; Kubera B.; Shan Jie. Localizedterahertz generation via optical rectification in ZnTe. J. Opt. Soc. Am. B 2005, 22(8), 1667.doi:10.1364/JOSAB.22.001667

[20] Zhao Z.Y.; Hameau S.; Tignon J. THz Generation By Optical Rectification And Competition With Other Nonlinear Processes. AIP Conference Proceedings, 2007, 893, 503–504. doi:10.1063/1.2729986

[21] Sheik-Bahae M.; Said A. A.; Wei T. H.; Hagan D. J.; Van Stryland E. W. Sensitive measurement of optical nonlinearities using a single beam. IEEE Journal of Quantum Electronics, 1990, 26, 760-769. doi: 10.1109/3.53394.

[22] Harrel S. M.; Milot R. L.; Schleicher J. M.; Schmuttenmaer C. A. Influence of free-carrier absorption on terahertz generation from ZnTe(110). Journal of Applied Physics 2010 107. doi:10.1063/1.3296064

[23] Lewis R .A. A review of terahertz sources Journal of Physics D: Applied Physics, 2014, 47, 374001. DOI 10.1088/0022-3727/47/37/374001

[24] Xu X.; Jingzhou X.; Zhang X.-C. Terahertz wave generation and detection from a CdTe crystal characterized by different excitation wavelengths, Opt. Lett. 2006, 31, 978-980

[25] Li Z.; Wang M.; Wang S. Investigation on terahertz generation from zinc-blende crystal waveguide at polariton resonance. J Opt 2019, 48, 31–35. https://doi.org/10.1007/s12596-018-0500-z

[26] Schneider A.; Neis M.; Stillhart M.; Ruiz B.; Khan R. U. A.; Günter P. Generation of terahertz pulses through optical rectification in organic DAST crystals: theory and experiment. J. Opt. Soc. Am. B 2006, 23, 1822-1835. doi:10.1364/JOSAB.23.001822

[27] Gorelik V. S.; Katyba G. M. Generation of terahertz radiation in cubic non-centrosymmetric crystals. Bulletin of the Lebedev Physics Institute 2014, 41, 127–134. doi:10.3103/S1068335614050030.

[28] Q. Wu and X.-C. Zhang , Terahertz broadband GaP electro-optic sensor", Appl. Phys. Lett. 1997, 70, 1784-1786. https://doi.org/10.1063/1.118691

[29] Brunner F. D. J.; Schneider A.; Günter P. Velocity-matched terahertz generation by optical rectification in an organic nonlinear optical crystal using a Ti:sapphire laser. Applied Physics Letters, 2009, 94, 061119. doi:10.1063/1.3080214.

[30] Leitenstorfer A.; Hunsche S.; Shah J.; Nuss M. C.; Knox W. H. Detectors and sources for ultrabroadband electro-optic sampling: Experiment and theory", Appl. Phys. Lett. 1999 74, 1516-1518 https://doi.org/10.1063/1.123601.

[31] Mamedov A. M.; Ozbay E. Mechanism of the electro-optic effect and nonlinear optical susceptibilities of some ferroelectrics: abinitio calculation. arXiv preprint arXiv:1112*.585,1* 2011. https://arxiv.org/abs/1112.5851.

[32] Mossman S.; Lytel R.; Kuzyk M. G. Fundamental limits on the electro-optic device figure of merit. Optical Society of America B, 2016, 33. doi:10.1364/josab.33.00e109.

[33] Hebling J.; Yeh K.; Hoffmann M. C.; Bartal B.; Nelson K.A. Generation of high-power terahertz pulses by tilted-pulse-front excitation and their application possibilities. J. Opt. Soc. Am. B, 2008, 25,doi:10.1364/JOSAB.25.0000B6

[34] Hebling J.; Stepanov A.G.; Almási G.; Bartal B.; Kuhl J. Tunable THz pulse generation by optical rectification of ultrashort laser pulses with tilted pulse fronts. Appl. Phys. 2004, 78, 593 599. doi:10.1007/s00340-004-1469-7.

[35] Pradarutti B.; Matthäus G.; Riehemann S.; Notni G.; Nolte S.; Tünnermann A. Highly efficient terahertz electro-optic sampling by material optimization at 1060nm.Optics comm. 2008, 281, 5031–5035. doi:10.1016/j.optcom.2008.06.055.

[36] Liu P.; Niu C.; Qi F.; Li W.; Li W.; Fu Q.; Guo L.; Li Z. Phase-Matching in Nonlinear Crystal-Based MonochromaticTerahertz Wave Generation. Crystals, 2022,*12*, 1231. https://doi.org/10.3390/cryst12091231.

[37] Tomita I.; Suzuki H.; Ito H.; Takenouchi H.; Ajito K.; Rungsawang R.; Ueno Y. Terahertz-wave generation from quasi-phase-matched GaP for 1.55 μm pumping. Applied physics letters, 2006, 88, 71118. doi:10.1063/1.2174832.

[38] Schaar J. E.; Vodopyanov K. L.; Kuo P. S.; Fejer M. M.; Xiaojun Y.; Lin A.; Harris J.S.; Bliss D.; Lynch C.; Kozlov V.G.; Hurlbut W. Terahertz Sources Based on Intracavity Parametric Down-Conversion in Quasi-Phase-Matched Gallium Arsenide. IEEE journal of selected topics in quantum electronics, 2008, 14, 354–362. doi:10.1109/jstqe.2008.917957.

[39] Vodopyanov K. L.; Fejer M. M.; Yu X.; Harris J. S.; Lee Y.S.; Hurlbut W. C.; Kozlov V. G.; Bliss D.; Lynch C. Terahertz-wave generation in quasi-phase-matched GaAs.Applied Physics Letters, 2006, 89, 141119. doi:10.1063/1.2357551.

[40] Janos H.; Gabor A.; Ida K.; Jurgen K. Velocity matching by pulse front tilting for large area THz-pulse generation. Optics express, 2002, 10, 1161–1166.doi:10.1364/OE.10.001161.

[41] Unferdorben M.; Szaller Z.; Hajdara I.; Hebling J.; Pálfalvi L. Measurement of Refractive Index and Absorption Coefficient of Congruent and Stoichiometric Lithium Niobate in the Terahertz Range. Infrared, Millimeter, and Terahertz Waves, 2015, 36, 1203–1209. doi:10.1007/s10762-015-0165-5.

[42] Hekmat N.; Vogel T.; Wang Y.; Mansourzadeh S.; Aslanib F.; Omar A.; Hoffmann M.; Meyer F.; Saraceno C. Cryogenically cooled GaP for optical rectification at high excitation average powers. Opt. Mater. Express, 2020, 10, 2768-2782. https://doi.org/10.1364/OME.402564.

[43] Xiaojun W.; Koustuban R.; Wenqian R. H.; Chun Z.; PeterZ.; Giulio M.; Giovanni C.; Oliver D. M.; Franz X.K. Half-percent terahertz generation efficiency from cryogenically cooled lithium niobate pumped by Ti:sapphire laser pulses. https://arxiv.org/ftp/arxiv/papers/1601/1601.06921.pdf.

[44] Wu, X.; Zhou C.; Huang W. R.; Ahr F.; Kärtner F. X. Temperature dependent refractive index and absorption coefficient of congruent lithium niobate crystals in the terahertz range. Optics Express, 2015, 23, 29729doi:10.1364/OE.23.029729.

[45] Jazbinsek, M.; Puc, U.; Abina, A.; Zidansek, A. Organic Crystals for THz Photonics. Appl. Sci. 2019, 9, 882. https://doi.org/10.3390/app9050882.

[46] Andrea G. M.; Daniel M. M. Perspective on Terahertz Applications in Bioscience and Biotechnology. ACS Photonics, 2022, 4. https://doi.org/10.1021/acsphotonics.2c00228.

[47] Vicario C.; Ovchinnikov A. V.; Ashitkov S. I.; Agranat M. B.; Fortov V. E.; Hauri C. P. Generation of 0.9-mJ THz pulses in DSTMS pumped by a Cr:Mg2SiO4 laser. Opt. Lett. 2014, 39, 6632-6635.

[48] Vicario C.; Jazbinsek M.; Ovchinnikov A. V.; Chefonov O. V.; Ashitkov S. I.; Agranat M. B.;. Hauri C. P. High efficiency THz generation in DSTMS, DAST and OH1 pumped by Cr:forsterite laser. Opt. Express, 2015, 23, 4573-4580.

[49] Claudia G.; Mostafa S.; Corinne B.; Ignas A.; Rokas J.; Evan C.; Lorenz B.; Andrius B.; Audrius P. Highly efficient THz generation by optical rectification of mid-IR pulses in DAST. APL Photonics, 2021, 6, 046105. https://doi.org/10.1063/5.0037235.

[50] Samira M.; Tim V.; Mostafa S.; Frank W.; Clara J. S. Milliwatt average power, MHz-repetition rate, broadband THz generation in organic crystal BNA with diamond substrate," Opt. Express, 2021, 29, 38946-38957.

[51] Gollner C. Efficient Broadband Terahertz Generation in BNA Organic Crystals at Ytterbium Laser Wavelength," 2020 45th International Conference on Infrared, Millimeter, and Terahertz Waves (IRMMW-THz), Buffalo, NY, USA, 2020, pp. 1-2, doi: 10.1109/IRMMW-THz46771.2020.9370510.

[52] Buchmann T.O.; Railton K.E. J.; Jazbinsek M.; Zhou B.; Seok J.; Kwon O.; Rotermund F.; Jepsen P. U. High-power few-cycle THz generation at MHz repetition rates in an organic crystal. APL Photonics, 2020, 5, 106103.doi:10.1063/5.0022762.

[53] Shalaby M.; Hauri C. P. Demonstration of a low-frequency three-dimensional terahertz bullet with extreme brightness. Nature Communications, 2015, 6, 5976. doi:10.1038/ncomms6976.

[54] Hang Z.; Yong T.; Tong W.; Gunther S.; Yan Z.; Cunlin Z.; Liangliang Z.; Mostafa S. Efficient broadband terahertz generation from organic crystal BNA using near infrared pump. Appl. Phys. Lett. 2019, 114, 241101. https://doi.org/10.1063/1.5098855.

[55] Zachary B. Z.; Isaac C. T.; Gabriel A. V-B.; Charles B. B.; Karissa C. K.; Claire R.; Matthew J. L.; Brittan P. H.; David J. M.; Jeremy A. J. Enabling high-power, broadband THz generation with 800-nm pump wavelength. Opt. Express, 2021, 29, 38084-38094.

[56] Masazumi F.; Kazuhiro Y.; Minoru M.; Mitsuru S.; Kazuyoshi K.; Hironori T.; Shin-ichiro A.; Yutaka T.; A.; Hideki H. Second Order Nonlinear Optical Properties of the Single Crystal of N-Benzyl 2-methyl-4-nitroaniline: Anomalous Enhancement of the d333 Component and Its Possible Origin. Jpn. J. Appl. Phys. 2006, 45, 8676. DOI 10.1143/JJAP.45.8676

[57] Notake T.; Nawata K.; Kawamata H.; Matsukawa T.; Minamide H. Solution growth of high-quality organic N-benzyl-2-methyl-4-nitroaniline crystal for ultra-wideband tunable DFG-THz source. Optical Materials Express, 2012, 2, 119. doi:10.1364/OME.2.000119.

[58] Samira M.; Tim V.; Alan O.; Mostafa S.; Mirko C.; Clara J. S. Broadband, high power THz source at 540 kHz using organic crystal BNA. APL Photonics, 2023, 8, 011301. https://doi.org/10.1063/5.0126367.

[59] Zaccardi Z.; Tangen I.; Valdivia-Berroeta G.; Bahr C.; Kenney K.; Rader C.; Lutz M.; Hunter B.; Michaelis D.; Johnson J. Enabling high-power, broadband THz generation with 800-nm pump wavelength. Opt. Express 2021, 29, 38084-38094. https://doi.org/10.1364/OE.437421

[60] Mansourzadeh S.; Vogel T.; Shalaby M.; Wulf F.; Saraceno C. Milliwatt average power, MHz-repetition rate, broadband THz generation in organic crystal BNA with diamond substrate. Opt. Express 2021, 29, 38946-38957. https://doi.org/10.1364/OE.435344

[61] Samira M.; Tim V.; Alan O.; Mostafa S.; Mirko C.; Clara J. S. Broadband, high power THz source at 540 kHz using organic crystal BNA. APL Photonics 2023, 8, 011301 https://doi.org/10.1063/5.0126367.

[62] Swiss THz. Conversion efficiency at room temperature of BNA crystal. https://www.swissterahertz.com/bna

[63] Tangen I.; Valdivia-Berroeta G.; Heki L.; Zaccardi Z.; Jackson E.; Bahr C.; Ho (.; Michaelis D.; Johnson J. Comprehensive characterization of terahertz generation with the organic crystal BNA. J. Opt. Soc. Am. B 2021, 38, 2780-2785. https://doi.org/10.1364/JOSAB.420597

[64] Roeder F.; Shalaby M.; Beleites B.; Ronneberger F.; Gopal A. THz generation by optical rectification of intense near-infrared pulses in organic crystal BNA. Opt. Express, 2020, 28, 36274-36285.

[65] Tangen I. C.; Valdivida-Berroeta G. A.; Heki L. K.; Zaccardi Z. B.; Jackson E.; Bahr C. B.; Michaelis D. J.; Johnson J. A. Comprehensive characterization of terahertz generation with the organic crystal BNA J. Opt. Soc. Am. B. 2021, 38, 2780-2785.

[66] Shalaby M.; Vicario C.; Hauri C. P. Intense THz source based on BNA organic crystal pumped at conventional Ti:Sapphire wavelength. 41st International Conference on Infrared, Millimeter, and Terahertz waves (IRMMW-THz), Copenhagen, Denmark, 2016, pp. 1-1. doi: 10.1109/IRMMW-THz.2016.7758840.

[67] Vimal R.; Jithin J.; Swapna M .S.; Sankararaman S. Effect of duty cycle on photothermal phenomenon-A thermal lens study. Optik, 2019, 186, 20.https://doi.org/10.1016/j.ijleo.2019.04.117.

Chapter 3

Electro-optic THz Pulse Characterization Techniques

This chapter deals with the electro-optic detection of THz pulse in a non-linear crystal. There are two commonly used electro-optic techniques namely Electro-Optic Sampling (EOS) and single shot detection. This chapter will begin by first treating the theory and experimental configuration of the EOS scheme, and followed by the single shot scheme. Though, the latter scheme reduces the acquisition time of the THz characterization process, however they are limited by temporal resolution. As such, the different variations of the single shot scheme which are available in literature to help address the lapses of this scheme shall be highlighted.

Typically, EOS involves overlapping the THz pulse and a short optical pulse (otherwise referred to as probe pulse) in an electro-optic crystal. By varying the temporal delay of the probe pulse with respect to the THz pulse, the full waveform of the THz signal can be determined over time. At the same time, the convolution of the THz pulse shape is measured with the spectral response function of the crystal **[1-2].** In order not to distort the THz signal, it is recommended that the response function of the crystal should extend beyond the measured THz frequency. Therefore, it makes sense to use a crystal that is well phase matched in addition to possessing low absorption effect within the range of the measured THz frequencies.

3.1 Phase mismatch and absorption in electro-optic crystals

In this section, the effect of phase mismatch (i.e. the different propagation velocities of the THz and the probe pulse) will first be discussed using the specific examples of ZnTe and GaP because these crystals are popularly operated with 800 nm and 1030 nm laser. Furthermore, the frequency-dependent absorption of THz radiation in ZnTe and GaP are discussed while emphasizing on the prerequisites for efficient phase matching and lower losses of the measured THz signal.

In the context of this work, the propagation of two types of electromagnetic pulses is of interest. The first of these electromagnetic pulses are the probe pulse, for which the following description is used **[3, 4]**:

$$E_{pr}(z,t) = E'_{pr}(z,t) * exp\left(i\omega_{pr}\left(t - \frac{n_{gr}(\omega_{pr})z}{c}\right)\right) \tag{3-1}$$

The first term $E'_{pr}(z,t)$, describes the temporal envelope of the probe pulse, while the second term describes the carrier wave of the pulse oscillating with the frequency ω_{pr}. The associated group velocity v_{gr}, by which the envelope propagates through the crystal is given by **[5, 6]**,

$$v_{gr} = \frac{c}{n_{gr}} \tag{3-2}$$

Where,

$$n_{gr}(\omega_{pr}) = n_0(\omega_{pr}) + \omega_{pr}\frac{dn_0(\omega_{pr})}{d\omega_{pr}}$$

or,

$$n_{gr}(\lambda_{pr}) = n_o(\lambda_{pr}) - \lambda_{pr}\frac{dn_o(\lambda_{pr})}{d\lambda}\bigg|_{\lambda_{pr}}$$

Where $n_{gr}(\omega_{pr})$ and $n_{gr}(\lambda_{pr})$ are the probe group refractive indices in terms of frequency ω_{pr}, and wavelength λ_{pr} respectively. When considering the propagation of the probe pulse, only this group velocity v_{gr} and the associated group refractive index n_{gr} are relevant.

The second type of electromagnetic pulse is the generated THz pulse. They generally consist of only few half-waves, implying that the THz pulse has a high spectral bandwidth relative to the probe pulse. In spite of this fact, the refractive index of the THz pulses does not remain constant within a dispersive material **[7]**.

For the electro-optical detection scheme used in this work, one is particularly interested in adjusting the propagation velocity of the probe and the THz pulse. The difference in the propagation velocity between the optical and the THz pulse can determine the minimum crystal length that can be used for detection. This is referred to as the detection coherence length l_{det}, $[\mathbf{8-10}]$

$$l_{det} = \frac{\pi}{\Delta k} = \frac{\pi\, c}{\omega_{THz}(n_{gr} - n_{THz})} \tag{3-3}$$

Where, Δk, describes the difference between the probe and THz velocity. It is used to quantify the phase mismatch between the THz and probe pulse. n_{THz} describes the phase refractive index of the THz pulse. A large coherence length is usually preferable for detection, because a long spatial interaction between the THz and optical pulse makes the detection process more efficient **[11-12]**.

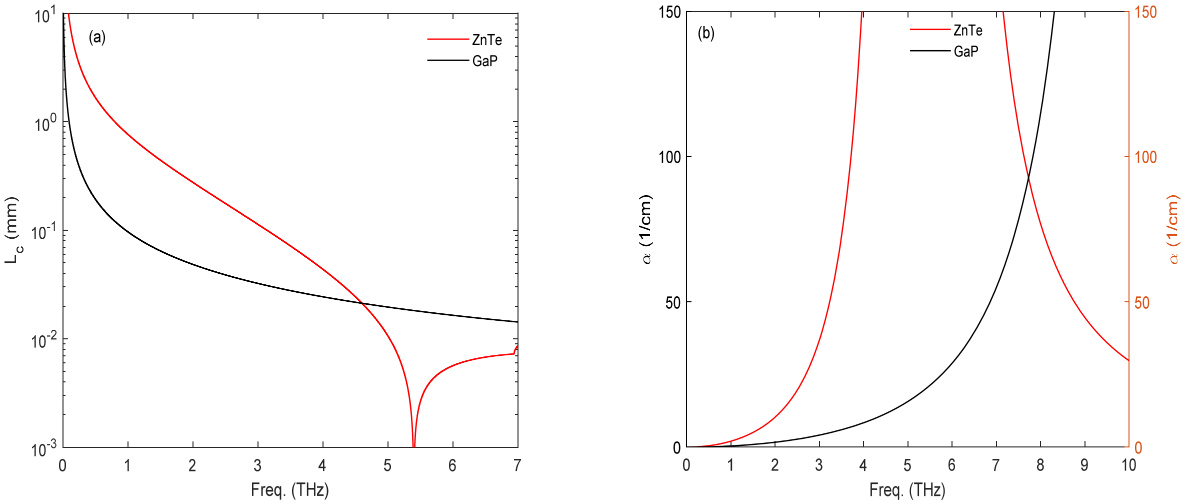

Fig. 3.1 Comparison between the coherence length (a), and (b) log-scale absorption coefficient of two common electro-optic crystals namely ZnTe and GaP crystals when operated with 1030 nm laser.

ZnTe, GaP and CdTe are among the most popular crystals that are used for the detection of THz pulse **[13-21]**. The choice of selecting either crystals depend on the configuration of the experimental set-up. Since in certain part of this work, EOS is performed with the ytterbium-based laser sources operating at a wavelength of 1030 nm, it is therefore important to study the coherence length of ZnTe around this wavelength range. A comparative plot between the coherence length of ZnTe and GaP crystals at 1030 nm laser wavelength is shown in Fig.3.1a. A long coherence length is observed with the ZnTe crystals at low THz frequencies. The coherence length of the ZnTe crystal fall between 1- 0.2 mm within the corresponding THz spectral range of 1-2 THz. Considering the same frequency range, the coherence length of the GaP crystal are about five times shorter than that of ZnTe crystal. Since long coherence length are favourable for EOS, the ZnTe crystal have become popular for detecting THz frequencies typically around 2 THz. For some experimental set-up in which broadband THz spectral are generated, it is often observed that the usage of GaP is preferable to ZnTe crystal **[20]**. The properties of the GaP crystal support a favorable phase matching between the detected THz and the probe pulse when the wavelength of the probe pulse is centered around 1000-1030 nm. At this wavelength value, the probe and the detected THz pulses can travel long distance within the crystal before there arises a walk-off in their velocities. In order to quantify the amount of THz absorbed $\alpha(cm^{-1})$, the following relation is used **[22]**,

$$\alpha(cm^{-1}) = \frac{\pi f}{c} k \qquad (3\text{-}4)$$

Where k refers to the imaginary THz refractive index and f describes the THz frequencies. A plot of the THz absorption coefficient is shown in Fig. 3.1b. As seen from the plot, GaP crystals generally have a lower absorption coefficient at THz frequencies less than 7 THz, while ZnTe crystals are low in absorption coefficient only at THz frequencies less than 2 THz.

3.2 Linear Pockels effect in ZnTe crystal

The quasi static nature of the electric field of a THz pulse is capable of inducing a change in the refractive index of a nonlinear crystal **[23]**. The refractive index n, induced by any given Electromagnetic (EM) field can be modelled by the following equation **[24]**,

$$n = n_o + n_2 I \qquad (3\text{-}5)$$

Where, I is the intensity of the applied field, n_0 and n_2 are the corresponding linear and nonlinear refractive indices of the crystal respectively. The n_2 terms are higher-order terms that lead to a quadratic dependency on the applied electric field of the EM wave. For the particular case of the THz field strength obtainable in a table top experimental set-up, their electric field are weak in strength, and thus are unable to cause a nonlinear change in the refractive index of the EO crystal. As such, the relationship between n and the intensity of the applied field is linear, and this phenomenon is referred to as the Pockels effect **[24]**.

In general, the refractive index of an electro-optical crystal subjected to the electric field of a THz wave can be described by the refractive index ellipsoid. If $x, y,$ and z define the principal coordinate axes in the crystal, then prior to the presence of the THz field, the refractive index is described by a spheroid equation **[25]**,

$$\left(\frac{1}{n_x^2}\right) x^2 + \left(\frac{1}{n_y^2}\right) y^2 + \left(\frac{1}{n_z^2}\right) z^2 = 1 \qquad (3\text{-}6)$$

Where $n_x, n_y, n_z,$ are the respective principal refractive index in the x, y, z coordinates. It should be noted that the x-axis is the [100]-axis, the y-axis is the [010]-axis and the z- axis corresponds to the [001] axis of the crystal. In this present work, where a ZnTe crystal has been used, the principal refractive indices are identical because the refractive index of an isotropic crystal is direction-independent (this is true only in the absence of the THz field). However, during the electro-optic detection, their refractive index will no longer be equal, in addition to modification in their coordinates. Generally, the refractive index ellipsoid in the presence of the THz field $E = (E_x, E_y, E_z)$ is given below **[25],**

$$\left(\frac{1}{n^2}\right) x^2 + \left(\frac{1}{n^2}\right) y^2 + \left(\frac{1}{n^2}\right) z^2 + 2r_{41}E_x yz + 2r_{41}E_y xz + 2r_{41}E_z xy = 1 \qquad (3\text{-}7)$$

where r_{41} is the coefficient used in the r_{im}matrix (6 X 3) referred to the electro-optical tensor with i=1,2,3 while, m=1,2,3,…6. For the ZnTe cubic crystal with point group 43m, the only nonzero coefficient of the electro-optic tensor are $r_{41} = r_{52} = r_{63}$ **[26],** thus,

$$r_{im} = \begin{pmatrix} 0 & 0 & 0 \\ 0 & 0 & 0 \\ 0 & 0 & 0 \\ r_{41} & 0 & 0 \\ 0 & r_{41} & 0 \\ 0 & 0 & r_{41} \end{pmatrix} \tag{3-8}$$

According to equation (3-7), it can be observed that the presence of the THz field causes the appearance of mixed terms in the equation of the ellipsoid. These refers to the terms with xy, xz, yz. This means that the major axes of the ellipsoid with THz field applied are no longer parallel to the x, y, and z crystal axes. It becomes necessary then, to find the directions of the new axes (x', y', z') and the magnitude of the refractive indices ($n_{x'}, n_{y'}, n_{z'}$) due to the presence of E so that one can determine the effect of the field due to its propagation.

Two kinds of geometries have commonly been reported in the literature, which considers the relative polarization direction of the THz field as it travels through the electro-optic crystal **[27-28]**. In the first geometry, the THz field is oriented at 45 degree with respect to the probe polarization. While in the case of the second geometry, both the THz and probe polarization are parallel to each other. In both geometries the optical axis of the ZnTe crystal is adjusted such that it lies perpendicularly to the travel direction of the two pulses. In the following sections, these two geometries will be presented.

3.3 Detection in ZnTe with 45° polarization difference between the THz and probe pulse

In this geometry, the angle between the THz and probe pulse polarization is set at 45° as shown in Fig. 3.2. The electric field of the THz pulse is aligned along the z-axis of the crystal,

$$E = E_{THz} \begin{pmatrix} 0 \\ 0 \\ 1 \end{pmatrix} \tag{3-9}$$

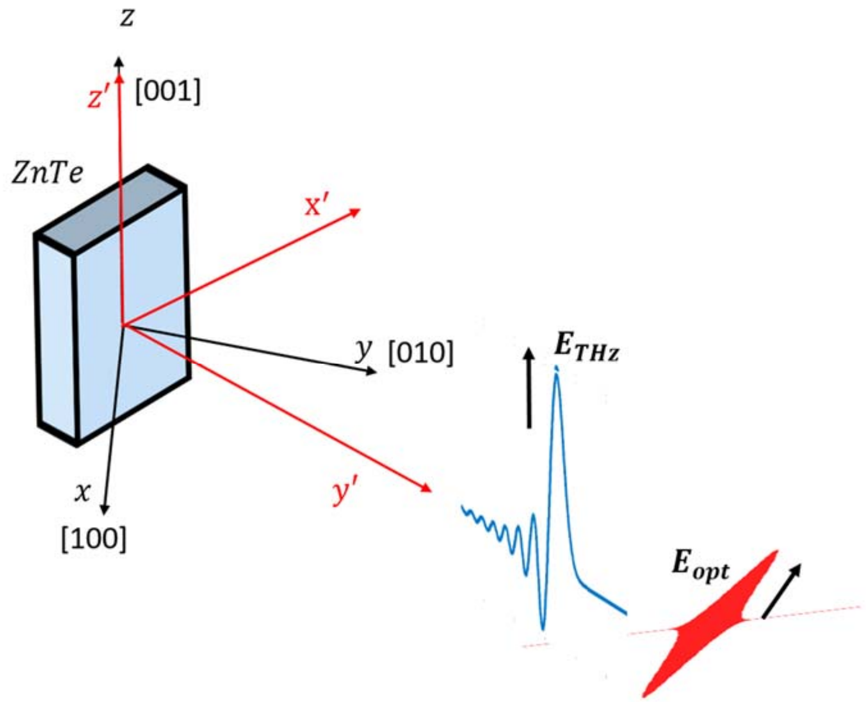

Fig. 3.2 The 45° polarization geometry for detecting THz pulse. The THz pulse is aligned along the optical axis of the crystals and oriented at 45° with respect to the probe pulse polarization.

From equation (3-9), it follows that there exists no THz field component in the y and x direction, i.e. $E_x = E_y = 0$, as such the results for the refractive index ellipsoid is given by **[29],**

$$\left(\frac{1}{n^2}\right) x^2 + \left(\frac{1}{n^2}\right) y^2 + \left(\frac{1}{n^2}\right) z^2 + 2r_{41}E_{THz}xy = 1 \quad (3\text{-}10)$$

A laboratory coordinate system (x', y', z') needs to be chosen in order to transform the measurement in the crystal frame to a form that can be visualized. With these coordinate systems, the mixed term xy will thus vanish. These required coordinate transformation can be defined as follows **[30]**,

$$\begin{pmatrix} x' \\ y' \\ z' \end{pmatrix} = \begin{pmatrix} -1/\sqrt{2} & 1/\sqrt{2} & 0 \\ 1/\sqrt{2} & 1/\sqrt{2} & 0 \\ 0 & 0 & 1 \end{pmatrix} \cdot \begin{pmatrix} x \\ y \\ z \end{pmatrix} \quad (3\text{-}11)$$

The x'-axis of the laboratory coordinate system lies in the crystal surface, while the y'-axis was chosen parallel to the (110) crystal direction (or to the direction of propagation). Using the sets of equation in equation (3-11) to transform the ellipsoid in equation (3-10), one obtains,

$$x'^2\left(\frac{1}{n^2}-r_{41}E_{THz}\right)+y'^2\left(\frac{1}{n^2}+r_{41}E_{THz}\right)+z'^2\left(\frac{1}{n^2}\right)=1 \tag{3-12}$$

By comparing the transformed ellipsoidal equation with the original ellipsoid, it can be shown that, the refractive index in the x' direction is thus;

$$\frac{1}{n_{x'}^2}=\frac{1}{n^2}-r_{41}E_{THz} \tag{3-13}$$

By rearranging and applying the Taylor expansion up to the first order, one finally obtains

$$n_{x'}=n+\frac{n^3}{2}r_{41}E_{THz}, \tag{3-14}$$

while the refractive index remains unchanged in the z'-direction:

$$n_{z'}=n \tag{3-15}$$

Since the optical probe beam is polarized at 45° to the x′ and z' axes, then the refractive index change between the x' and z' axis induced by the THz pulse is simply

$$\Delta n=n_{x'}-\ n_{z'}=\frac{n^3}{2}r_{41}E_{THz} \tag{3-16}$$

In summary, the geometry shown above is relatively clear and easy to calculate, which probably explains why they are mostly appreciated in the literature **[31]**. However, the results to be obtained in the next subsection, will indicate that this geometry does not achieve the maximum possible refractive index change.

3.4 Detection in ZnTe with 0° polarization difference between the THz and probe pulse

In the geometry shown in Fig. 3.3, the polarization of the THz and probe pulse are parallel to each other. Also, both polarizations are perpendicular to the z-axis of the crystals. In general, this geometry ensures the largest possible refractive index change per induced electric field applied **[17]**. To illustrate this argument, we proceed by defining the electric field of THz pulse as **[32]**

$$E=E_{THz}\begin{pmatrix}1/\sqrt{2}\\-1/\sqrt{2}\\0\end{pmatrix} \tag{3-17}$$

The corresponding refractive index ellipsoid due to the THz field is represented as,

$$\left(\frac{1}{n^2}\right)x^2 + \left(\frac{1}{n^2}\right)y^2 + \left(\frac{1}{n^2}\right)z^2 + \sqrt{2}r_{41}E_{THz}yz - \sqrt{2}r_{41}E_{THz}xz = 1 \tag{3-18}$$

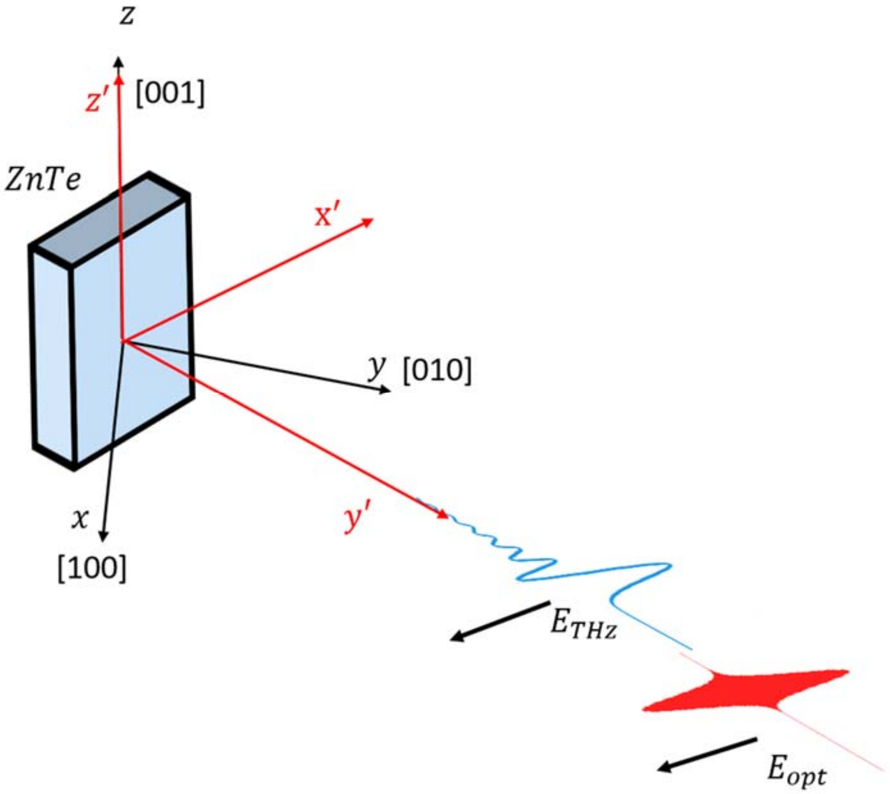

Fig. 3.3 The 0° polarization geometry for detecting THz pulse. The THz pulse is aligned perpendicularly to the optical axis of the crystals and oriented parallel with respect to the probe pulse polarization.

As earlier, the coordinate axes (x', y', z') are chosen so as to transform the measurement from the crystal frame into the laboratory frame **[32]**. It leads to the transformed refractive index ellipsoid in the laboratory frame given by,

$$\left(\frac{y'^2}{n^2}\right) + x'^2\left(\frac{1}{n^2} - r_{41}E_{THz}\right) + z'^2\left(\frac{1}{n^2} + r_{41}E_{THz}\right) = 1 \tag{3-19}$$

By comparing the transformed ellipsoidal equation with the original ellipsoid, it can be shown that the refractive indices in the y' and z' direction are thus;

$$\frac{1}{n_{z'}^2} = \frac{1}{n^2} + r_{41}E_{THz} \tag{3-20}$$

And,

$$\frac{1}{n_{x'}^2} = \frac{1}{n^2} - r_{41}E_{THz} \tag{3-21}$$

By rearranging and applying the Taylor expansion up to the first order, one finally obtains

$$n_{z'} = n - \frac{n^3}{2}r_{41}E_{THz} \tag{3-22}$$

And similarly,

$$n_{x'} = n + \frac{n^3}{2}r_{41}E_{THz} \tag{3-23}$$

Since the probe beam is polarized at 45° to the *x'* and *z'* axes, then the refractive index change between the x' and z' axis induced by the THz pulse is simply

$$\Delta n = n_{x'} - n_{z'} = n^3 r_{41}E_{THz} \tag{3-24}$$

In comparison to Δn obtained when there exist a 45° polarization difference, we conclude that there is a factor of 2 between these two geometries. The 0° polarization difference induces a higher refractive index change, as such we shall henceforth restrict our discussion to this particular geometry except otherwise stated. At the same time, this is popularly utilized particularly for the (110) ZnTe crystal.

3.5 Measurement of induced phase by ellipsometry

The refractive index change in the ZnTe crystal induced by the presence of the THz field will affect the phase of the probe pulse. So, as the probe pulse travels through the *y'*-direction, it will encounter a different refractive index in the different crystal's axis. This difference in refractive index is what have been derived in the previous section. In practice, it is not possible to directly detect this acquired phase since optical detectors such as photodiodes can only measure the intensity and not the phase of a pulse. The option available in order to circumvent this challenge is to introduce a $\lambda/4$-plate at the exit of the electro-optic crystal **[33-34].** The $\lambda/4$-plate converts the polarization of the probe pulse from linear to circular polarization. With the aid of a polarizer, the main polarization components (i.e. the vertical and horizontal polarization) are then separated, and the difference in their intensity is measured by a balanced photodiode. In what follows, we shall show that this differential intensity is proportional to the phase induced on the probe beam by the THz pulse.

In order to compute the detectable intensity difference, resulting from the ordinary and the extraordinary axis of the λ/4 plate, it is best to use the Jones matrix. To begin, we first neglect the effect of the THz pulse on the probe pulse. It then follows that, the complex field amplitude of the input probe with an assumed phase difference Δφ in the *x'y'z'*- coordinate frame is [**32**],

$$\boldsymbol{E}_{in}^{0} = \begin{pmatrix} E_{in,x'}^{0} \\ E_{in,z'}^{0} \end{pmatrix} = \frac{E_{abs}^{0}}{\sqrt{2}} \begin{pmatrix} e^{i\frac{\Delta\varphi}{2}} \\ e^{-i\frac{\Delta\varphi}{2}} \end{pmatrix}, \tag{3-25}$$

where E_{abs}^{0} is the complex field amplitude of the corresponding linearly polarized probe pulse. The $\lambda/4$ plate gives rise to a 45° rotation about the y'-axis. A transfer matrix $\mathbf{M}_{45}$ can be used to model this rotation as follows,

$$\boldsymbol{M}_{45} = \frac{1}{\sqrt{2}}\begin{pmatrix} 1 & -1 \\ 1 & 1 \end{pmatrix} \cdot \begin{pmatrix} e^{-i\frac{\pi}{4}} & 0 \\ 0 & e^{i\frac{\pi}{4}} \end{pmatrix} \cdot \frac{1}{\sqrt{2}}\begin{pmatrix} 1 & -1 \\ 1 & 1 \end{pmatrix} \tag{3-26}$$

$$= \frac{1}{\sqrt{2}}\begin{pmatrix} 1 & -i \\ -i & 1 \end{pmatrix}$$

The resulting complex field amplitude at the exit of the $\lambda/4$ plate is then derived as follows:

$$\boldsymbol{E}_{out}^{0} = \begin{pmatrix} E_{out,x}^{0} \\ E_{out,z}^{0} \end{pmatrix} = \boldsymbol{M}_{45} \ . \ \boldsymbol{E}_{in}^{0}$$

$$= \frac{1}{\sqrt{2}}\begin{pmatrix} 1 & -i \\ -i & 1 \end{pmatrix} \cdot \frac{E_{abs}^{0}}{\sqrt{2}} \begin{pmatrix} e^{i\frac{\Delta\varphi}{2}} \\ e^{-i\frac{\Delta\varphi}{2}} \end{pmatrix} = \frac{E_{abs}^{0}}{2} \begin{pmatrix} e^{-i\frac{\pi}{4}} e^{i\frac{\Delta\varphi}{2}} - e^{i\frac{\pi}{4}} e^{-i\frac{\Delta\varphi}{2}} \\ -e^{i\frac{\pi}{4}} e^{i\frac{\Delta\varphi}{2}} + e^{-i\frac{\pi}{4}} e^{-i\frac{\Delta\varphi}{2}} \end{pmatrix}$$

$$= E_{abs}^{0} e^{i\frac{\pi}{4}} \begin{pmatrix} cos\left(\frac{\Delta\varphi}{2} + \frac{\pi}{4}\right) \\ -sin\left(\frac{\Delta\varphi}{2} + \frac{\pi}{4}\right) \end{pmatrix} \tag{3-27}$$

The above expression indicates that the output beam at this point is circularly polarized, consisting of a vertical and horizontal component. In the case, that the THz pulse interacts with the probe, the initial probe phase will become modified (because the crystal's refractive indices will change by different amount in different axes), consequently equation (3-28) will become elliptically polarized. With the help of a polarizer, the output beam is then separated into the components polarized in the *y'* and *z'* direction. A pair of photodiodes placed in the path of the output beam then measures the respective intensities $\left(I_{x'} = \frac{1}{2}\epsilon_0 c\left|E^0_{out,x'}\right|^2 \; and \; I_{z'} = \frac{1}{2}\epsilon_0 c\left|E^0_{out,z'}\right|^2\right)$ of each polarization. The difference in their intensity becomes amplified by an amplifier system. Often times, the diodes and the amplifier are integrated within as a single system referred to as balanced photodiode device. The output difference is then detected by a phase locked lock-in-amplifier. By assuming a linear relationship between the lock-in signal U_{det}, and the intensity difference ($I_{y'} - I_{z'}$), we can then write the following **[35-37]**,

$$U_{det} \propto \Delta I = I_{x'} - I_{z'}$$

$$= \frac{1}{2}\epsilon_0 c_0\left(\left|E^0_{out,x'}\right|^2 - \left|E^0_{out,z'}\right|^2\right)$$

$$= \frac{1}{2}\epsilon_0 c_0\left|E^0_{abs}\right|^2 sin(\Delta\varphi)$$

$$= \left(I_{y'} + I_{z'}\right)sin(\Delta\varphi)$$

$$= K_{det}sin(\Delta\varphi) \qquad (3\text{-}28)$$

For very small values of $\Delta\varphi$, i.e. $\Delta\varphi \ll 1$, it follows that $\Delta I \approx K_{det}\Delta\varphi$, where, K_{det}, represents the scaling factor of the electro-optic system **[38-39]**. Thus, we realize that, the induced probe phase change can be indirectly measured by, first converting the probe's output signal into an elliptically polarized beam, then spatially splitting the two polarization components, and thereafter computing the differential intensity.

3.6 Spectral bandwidth of electro-optic detection

Until now, we have only discussed the retrieval process for the induced phase difference in the probe pulse (due to the THz field). Other than the effect the THz pulse has on the magnitude of the induced phase $\Delta\varphi$, there are certain characteristics such as the crystal's electro-optic coefficient and phase mismatch that limits the detection bandwidth of the electro-optic process **[34, 40]**. In order to study these effects, the detection response function needs to be considered. To begin, an approximate expression to calculate the induced phase is given as follows **[41]**,

$$\Delta\varphi = \frac{2\pi}{\lambda_{opt}}\Delta n.z = \frac{2\pi}{\lambda_{opt}}n^3 r_{41}E_{THz}\, z \qquad (3\text{-}29)$$

During electro-optic detection, the probe pulse scans through the entire length of the THz pulse within the crystal, while the THz pulse position is kept fixed. This scanning is achieved by including a delay stage in the path of the probe pulse. As such a time lag is introduced between the two pulses. At each point in the scanning process, the probe pulse overlaps with the THz field at different position as shown in the Fig. 3.4.

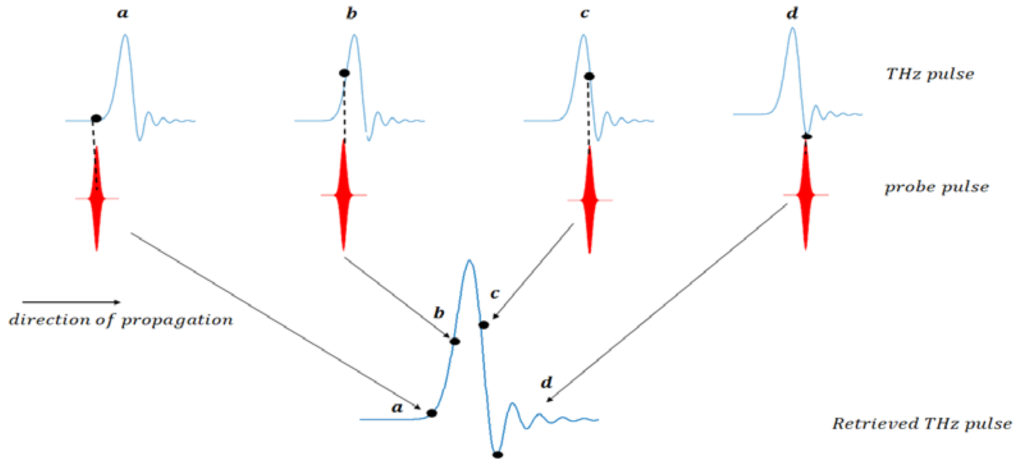

Fig. 3.4 The convolution scheme between the THz and probe pulse. A preset time delay between these pulses is created by a delay stage in the path of the probe pulse.

Mathematically, a convolution function $C(t, \tau, z)$, between the THz and probe pulse can better describes this process **[2, 42],**

$$E_{THz} \rightarrow C(\tau, z) \sim \int_{-\infty}^{\infty} dt \; E_{THz}(t+\tau, z) \,.\, I'_{pr}(t, z) \tag{3-30}$$

Where I'_{pr} corresponds to the intensity of the probe pulse defined in equation (3-1). By considering the convolution function, the induced phase in equation (3-30) can now be written as,

$$\Delta\varphi(t) \sim \frac{2\pi}{\lambda_{opt}} n_0^3 r_{41} \, z \int_{-\infty}^{\infty} dt \; E_{THz}(t+\tau, z) \,.\, I'_{pr}(t, z) \tag{3-31}$$

In practice, the detected THz frequency obtained from $\Delta\varphi$, is limited by the detection spectral response G, of the crystal **[43-44**]. By including the effect of G in equation (3-31), it follows that the induced phase is,

$$\Delta\varphi(t) \sim \frac{2\pi}{\lambda_{opt}} n_0^3 r_{41} \, z \int_{-\infty}^{\infty} dt \; \left(E_{THz}(t+\tau, z) * \; FT[G]\right) .\, I'_{pr}(t, z) \tag{3-32}$$

It can be observed in equation (3-32) that the induced phase is proportional to the thickness of the crystal. This implies that, in thicker EO crystals the amplitude of the detected THz signal is higher than in thinner crystals. The detection spectral response is an intrinsic property of the electro-optic crystal that determines the bandwidth of the detectable THz pulse. It considers, the interaction between the THz and probe pulse. Similar to the generation response spectral (see chapter 2), the detection spectral response will approach a maximum value if the velocities between these two pulses are well matched while it drops to a zero value when there exist a large walk-off between the two pulses. In essence, the detection spectral response would depend on the probe's wavelength and the crystal length according to [**44**],

$$G(\lambda,\ \omega,\ z) = \frac{2}{n_{THz}+1}\, sinc\left[\omega z\left(n_g - n_{THz}\right)/c\right] \qquad (3\text{-}33)$$

The term n_{THz} can be derived from the complex dielectric function ε(ν) and it describes the refractive index encountered by the THz pulse within the crystal. It is defined as **[45-46]**,

$$\varepsilon(\nu) = \left(n_{THz} + ik\right)^2 = \varepsilon_\infty + \frac{\varepsilon_{st} f_{TO}^2}{f_{TO}^2 - \nu^2 + 2i\zeta\nu} \qquad (3\text{-}34)$$

Where ε_∞ describes the electronic contribution, ε_{st} represents the oscillatory strength, ν_{T0} represents the transverse optical phonon mode, and ζ represents the damping constant of the transverse optical phonon mode, and *k* refers to the imaginary refractive index of the THz field. A brief summary of the experimentally reported coefficients used for determining the THz refractive index of ZnTe, GaP and CdTe crystal is found in Table 4.1

Table 3.1 The parameters commonly utilized for the calculation of the complex dielectric function of ZnTe, GaP and CdTe crystals **[45, 47-48]**.

PARAMETERS CRYSTAL	$\boldsymbol{\varepsilon_\infty}$	$\boldsymbol{\varepsilon_{st}}$	$\boldsymbol{\nu_{TO}(THz)}$	$\boldsymbol{\gamma}$
ZnTe	7.44	2.58	5.32	0.025
GaP	8.46	1.72	10.9725	0.033
CdTe	6.8	3.008	4.361	0.0505

The behavior of the optical refractive index n_o, can be modelled by the Sellmeier equation as follows **[47]**.

$$n_o(\lambda_{pr}) = \sqrt{A + B\frac{\lambda_{pr}^2}{\lambda_{pr}^2 - C}} \tag{3-35}$$

Where, *A*, *B* and *C* are parameters that fits the experimental data. There are several values of these parameters that are obtainable in the literature. In this work, we have chosen the parameters obtained within the optical wavelength range relevant to our laser source. For this purpose, we have selected the parameters within a wavelength region of $580 - 2500\ nm$ for both the ZnTe and GaP crystals. The corresponding values of the parameters are listed in Table 4.2 **[26].**

Table 3.2 The Sellmeier parameters for the determination of the optical refractive index of ZnTe and GaP crystal **[49-51]**.

PARAMETER / **CRYSTAL**	**A (μm)**	**B (μm)**	**C (μm)**
ZnTe	4.27	3.01	0.142
GaP	2.68	6.40	0.0903

We shall now discuss an extension of the detection response function called the effective response function. It takes into account the frequency dependency of the crystal's electro-optic coefficient.

3.7 Effective spectral response function

In order to achieve a comprehensive treatment of the response function, it is a good practice to consider the effect of the frequency-dependent electro-optic coefficient, $\gamma_{41}(\nu)$. Thus, a new term referred to as the effective response function is defined as follows **[52]**,

$$G_{eff} = G(\lambda_p, \omega_{THz}, l_{det}) \cdot \gamma_{41}(\nu) \tag{3-36}$$

The effective response function G_{eff}, allows the accurate estimation of the detection bandwidth of the crystal, with respect to the probe's wavelength. $\gamma_{41}(f)$ which is used to describe the motion of the bound electrons and lattice oscillations in the electro-optic crystals can be express as follows **[48]**,

$$\gamma_{41}(f) = d_e\left(1 + \frac{\xi f_{T0}^2}{f_{T0}^2 - f^2 - i\Gamma_0 f}\right) \tag{3-37}$$

Where, d_e represents the electronic influence on the electro-optical coefficient, ξ which is called the Faust-Henry coefficient gives a measure of the ratio between the electronic and ionic part of the electro-optical coefficient at zero frequency and Γ_0 represents the damping constant of the transverse optical phonon mode. The magnitude of each of these parameters have been tabulated for ZnTe and GaP crystals in Table 4.3**.** It can be noted that, there are small differences in the magnitude of these parameters in different articles, but I have adopted the results obtained from experimental set-up similar to mine.

Table 3.3 Electro-optic crystal parameters for the determination of the electro-optic coefficient of ZnTe and GaP crystals **[53-54]**.

PARAMETERS CRYSTAL	$d_e(pm/V)$	ξ	$f_{TO}(THz)$	$\Gamma_0(THz)$
ZnTe	4.25	- 0.07	5.3	0.09
GaP	8.46	-0.53	10.98	0.02

By using equation (3-37) and the parameters in Table 3.3, a comparison between the electro-optic coefficient of ZnTe and GaP crystals is shown in Fig. 3.5. As can be observed, ZnTe has a coefficient of about 4 pm/V. This value remains fairly constant until it drops off to 0 pm/V at around 5 *THz*. Beyond this point, it's γ_{41} rapidly decreases to 5.3 THz. This observation can be explained by the presence of transverse optical phonon resonance that restricts the detection limit of the crystal to less than 5.3 *THz*. However, a broader detection limit is achievable with GaP crystal. It’s detection range which is set at around 7 *THz*, is about one-half times broader than that of ZnTe crystals. Though, the phonon resonance occurs at around 10.9 THz, but it is impossible to detect frequencies above 7 THz due to a negative γ_{41} value.

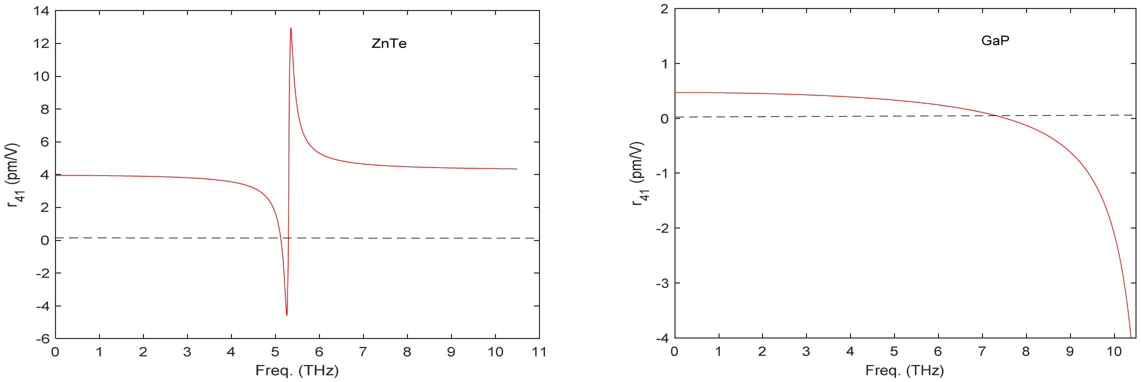

Fig. 3.5 Comparison of the real electro-optical coefficient for ZnTe and GaP for the THz frequency range from 1 to 11 THz. The respective transverse optical phonon resonances is obvious at around 5 and 11 THz.

The plot of the effective response function at different laser wavelength is shown in Fig. 3.6 and Fig. 3.7 for ZnTe and GaP crystals respectively. I have chosen wavelengths of 800 nm and 1030 nm since my experiment was performed with Ti:Saphhire and ytterbium lasers. For ZnTe crystal, a spectral range of less than 2.5 THz is investigated while, a spectral range up to 5 THz is investigated for GaP crystal. Considering the GaP crystal, it can be observed that within each subfigure, the thinner crystals result in a broader detection bandwidth. A maximum detectable bandwidth up to 5 THz is observed with the 0.2 mm crystal length operated at 1030 nm laser while a narrower spectral of up to 1.8 THz can be detected with the use of 800 nm laser. In the case of ZnTe crystal, narrower detection bandwidth are generally observed. The detection limit is broadest extending up to 3.2 THz when operated at 800 nm laser, while it is narrowest when operated at 1030 nm laser. It is equally important to note that, the effective response function shows a rapid fall off towards the phonon resonance at 5.3 THz for the 0.2 mm thick ZnTe crystal.

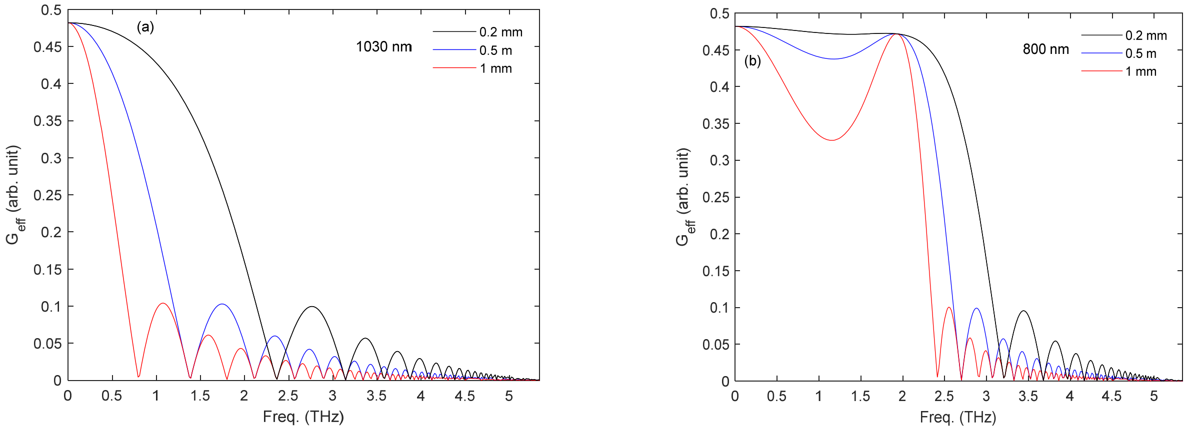

Fig. 3.6 Comparison of the ZnTe effective spectral response function for different crystal thicknesses and at laser wavelengths of (a) 1030 nm and (b) 800 nm.

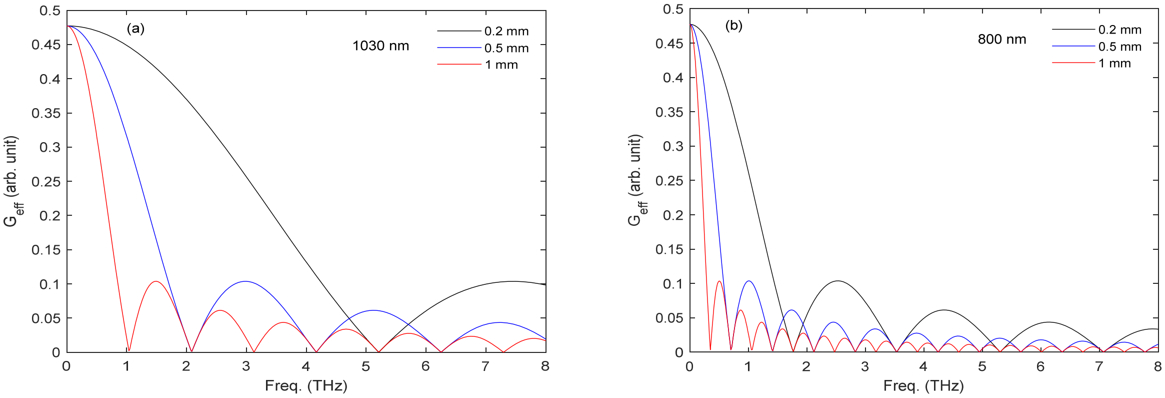

Fig. 3.7 Comparison of the GaP effective spectral response function for different crystal thicknesses and at laser wavelengths of (a) 800 nm and (b) 1030 nm.

EO detection can also performed in variety of other ways by modifying the probe pulse profile. These modifications gives rise to either a chirped probe or series of beamlets. Different orientations for overlapping the THz and these modified probe have already been studied in the literatures. In particular, the use of a chirped probe for EO detection usually limits the time required to characterize the THz pulse, hence this technique is generally referred to as single shot detection. Contrary to EOS in which a short probe scans the THz pulse, the single shot detection can sample the THz with a single pulse or in some cases by averaging over the single pulse measurement. All the EO factors (such as phase mismatch, coherence length, and spectral response function) that limits the EOS also apply in single shot detection. In what follows, I shall discuss the principle of the single shot detection while leaving out the EO effects for the sake of simplicity.

3.8 Single shot electro-optic detection

Single shot electro-optic detection involves overlapping the THz pulse with a long-chirped probe. In this scheme, there is no need to scan the probe. In this section we will treat the general scheme of the single shot electro-optic detection.

The temporal profile of the probe beam used in single shot EO detection is markedly different from those in EOS. In the single shot detection scheme, the probe beam is first dispersed by a material medium for example to produce a chirped and temporally broadened pulse. The probe pulse can be defined as the product of an envelope and carrier frequencies function as shown in Fig. 3.8

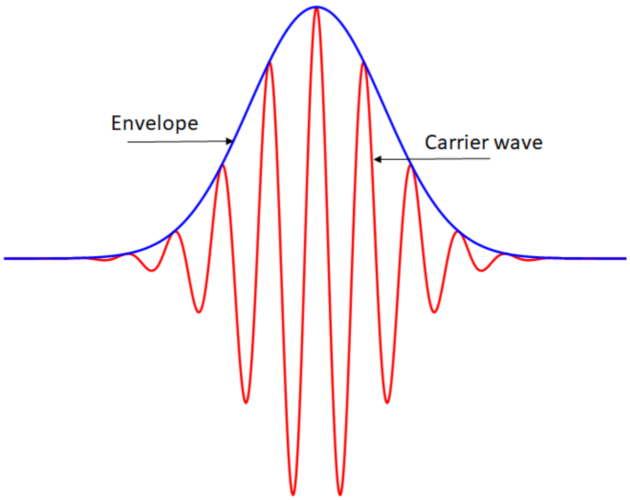

Fig. 3.8 The envelope and carrier wave of a pulse.

During dispersion through the material medium, the envelope becomes temporally stretched, while the carrier waves are either positively or negatively chirped. The probe pulse is said to be positively or negatively chirped if the temporal spacing increases or decreases linearly with time. A simple expression for describing the undispersed and dispersed pulse can be written as follows **[55]**,

$$E_{ud} \propto exp\left(\frac{t^2}{T_o^2} - i\omega t\right) \tag{3-38}$$

And,

$$E_d \propto exp\left(\frac{t^2}{T_c^2} - i\omega t - i\sigma t^2\right) \tag{3-39}$$

Where E_{ud} describes the undispersed probe, whose original length is T_o, and E_d refers to the dispersed probe which have been chirped and stretched to a new length T_c, σ refers to the chirp rate. In practice, a chirped and temporally stretched pulse can be obtained by passing the probe beam through a prism, pair of diffraction grating, or dispersion blocks. **[56]**. Since the entire length of the THz pulse is not scanned in the single shot detection, a different time scaling is adopted **[57]**. The time scaling involves an indirect retrieval process (which shall be discussed later in details) in which frequency is being mapped to time. In order to facilitate the easy retrieval of time information, a linear frequency-time mapping is beneficial**.** Creating a linear chirp over the probe pulse is possible if the change of refractive index ($dn/d\lambda$) over the bandwidth of the pulse is constant. In reality this is not achieved and higher order dispersion effects need to be considered.

A general approach to the dispersion introduced by a material is based on the group velocity dispersion GVD, which is defined as **[57],**

$$GVD = \frac{1}{c}\left(2\frac{dn}{d\omega} + \omega\frac{d^2n}{d\omega^2}\right) \tag{3-40}$$

Where *GVD* is expressed in the unit of fs^2/mm.The group velocity dispersion takes the first and second order dispersion effects into account. In order to achieve a large linear chirp over the probe pulse, the contribution of the first parameter needs to be much larger than the contribution of the second parameter. A large contribution of the second order effect will limit the linear range and therefore the usable temporal window (temporal window is defined as the minimum length of THz pulse that can be measured by the probe). The dispersive material used in this work is SF6. After the probe has been chirped, both the THz and the chirped probe pulses will then be collinearly overlapped in the electro-optic crystal. Both a spatial and temporal overlap must be maintained between the pulses. The different frequency components of the chirped probe will be rotated by the THz pulse by different amount. The degree and direction of rotation is proportional to the THz field strength. The induced polarization in the probe beam is then sent through a polarizer. The polarizer helps to convert the probe's modulated polarization into an intensity modulation **[58]**. The electric field of the intensity modulated probe beam E_m, can be expressed as **[59-60]**,

$$E_m(t) = E_d(t-\tau)\,[1 + kE_{THz}(t)] \tag{3-41}$$

Where k is a modulation constant with $k << 1$, $E_{THz} \propto exp\left(-\frac{t^2}{\Delta T^2}\right)$, and ΔT refers to the THz pulse duration. Then, another dispersive element (for instance a grating) within an optical spectrometer will be used to disperse the modulated beam onto a CCD-chip. The spectrally modulated probe will then be spatially separated on the CCD pixel. Therefore, *a frequency to spatial mapping* is realized. The resulting THz electric waveform can be computed by performing a background subtraction as follows **[60]**,

$$E_{THZ}^{retrieved}(\omega) \propto \frac{[g * |E_m|^2](\omega) - [g * |E_d(\omega)|^2](\omega)}{[g * |E_d(\omega)|^2](\omega)} \tag{3-42}$$

Where, $g(\omega) = e^{-[(\omega-\omega_1)/\Delta\omega_s]^4}$, $E_m(\omega) = \left|\int_{-\infty}^{\infty} E_m(t)\,.\,exp(i\omega t)\,dt\right|^2$ (3-43)

$g(\omega)$ describes the response function of the optical spectrometer. $\Delta\omega_s$ refers to the spectral resolution of the optical spectrometer. As can be observed from equation (3-42), the recovery of the THz waveform occurs in two distinct steps; first of which is the registration of the chirped pulse spectrum in the absence of the THz pulse i.e. $[g * |E_d(\omega)|^2](\omega)$, and followed by the measurement of the THz modulated-probe spectrum $[g * |E_m|^2](\omega)$. The ratio of the difference between these signals to the probe spectrum is proportional to the electric field of the THz pulse. As in the case of EOS, the crystal thickness and spectral response sets the limit to the detectable THz bandwidth. Until now, the retrieved THz field is represented as a function of the CCD pixel. So, there is a need to calibrate the CCD pixel in terms of ps time scale in order to determine the THz pulse duration. To achieve this, a *spatial to time mapping* is carried out by adjusting the temporal overlap between the probe and THz beam. As seen in equation (3-43), a temporal delay is inserted in the probe beam. By adjusting the position of the delay stage, the positioning of the modulated probe on the pixel will be shifted accordingly and recorded. In order to represent the position of the delay stage in time, the following transformation is performed, $T_{sc} = \frac{2x}{c}$, where T_{sc} describes the temporal scaling of the THz pulse, *c* represents the speed of light, and *x* is the length traveled by the delay stage. Thus, by plotting T_{sc} against the recorded CCD pixel, the time information of the THz pulse can be retrieved. However, in this work, a simpler and different approach involving the use of Frequency Resolved Optical Gating (FROG) characterization was performed (details of these technique are found in chapter 4).

In terms of measurement reliability, there are two important points of interest to note about the single shot detection which are namely; the temporal resolution and time window of the measurement. The temporal resolution of this measurement is principally affected by both the spectral width of the unchirped pulse and the spectral resolution of the optical spectrometer. Considering the situation where the spectral resolution of the optical spectrometer is very high, the temporal resolution of the single shot measurement can then be represented as **[60]**,

$$\tau_{res} = \sqrt{T_o T_c} \tag{3-44}$$

given that $T_c \gg \Delta T$.

Where T_c gives a measure of the temporal window. As can be observed, when T_c is increased (i.e. the time window is elongated), the THz field will be imprinted onto a narrower range of frequency components thereby degrading the temporal resolution. For example, a 100 fs transform-limited input pulse that is chirped to 10 ps provides a temporal resolution of 1 ps, while for a 3 ps chirped pulse, it results to a temporal resolution of 0.5 ps leading to a much better resolution but at the expense of the time window **[57]**. In order to improve the resolution of this detection scheme, a short read out pulse is introduced to in order to overlap with the modulated probe **[57]**. The temporal resolution in this case, is set by the pulse width of the short read out pulse, while the time window is given by the pulse width of the chirped pulse. As a result, this method has provided a 10 ps time window with 100 fs temporal resolution, making it as a better diagnostic tool in terms of time resolution compared to the absence of the read-out pulse **[59]**. However, given that $T_c \approx \Delta T$, then in the absence of the read out pulse, a better resolution independent on T_c can be realized as follows, **[60]**

$$\tau_{res} = \sqrt{T_o \Delta T} \tag{3-45}$$

In this case, the parameter that can be adjusted is T_o . This implies that the duration of the chirped pulse has no influence on the resolution of the measurement. Thus, high temporal resolution can be achieved by shortening T_o. In this work, the resolution of the single shot measurement followed the definition in equation (3-45).

So far, we have discussed the single shot measurement in the unbalanced mode. This means that, the modulated probe beam was analyzed without splitting the beam into its vertical (s) and horizontal (p) polarization components, as in the case of the EOS where the probe beam is first elliptically polarized, then separated into its polarization by a polarizer (wollaston prism). As a way to suppress noise and increase the dynamic range of the single shot measurement, a balanced detection scheme is usually utilized. The implementation of the balanced detection scheme is similar to the configuration in the EOS except that the balanced photodiodes are being replaced with sets of Charge Coupled Device (CCD) systems. Usually, two sets of grating-spectrometer-CCD systems are each used in place of the balanced photodiodes, and are synchronized to each other. Usually, it is recommended to also replace the Wollaston beam splitter with a wire grid-based polarizer. These wire grid polarizers guarantee higher and uniform extinction ratio, and also are capable of minimizing additional dispersion. By subtracting the s and p signal, the noise is sufficiently suppressed **[61]**.

3.8.1 Variations of the single shot electro-optic detection

Other than the *frequency-time* encoding scheme discussed in previous section, there are two other methods of encoding the THz pulse. These methods are *angle to time encoding* and *space to time encoding*. We shall examine these variations and their sub-variations in this section.

The angle-to-time encoding method uses a non-collinear geometry. In this method, the readout probe samples the THz field when they spatially overlap in the detection crystal at different times. The mapping between the spatial and time coordinates is calculated geometrically and depends only on the non-linear crossing angle. As a result, the time window T is determined as, $T = w.\tan(\theta)/c$, where, w is the beam width and c is the speed of light in vacuum. While this method is relatively easier to implement as there is minimal modification to the conventional EO sampling method, there are limitations to the time window, as a large beam width is required. In addition, to achieve a large crossing area, the readout and THz pulses are not focused at the detection crystal significantly reducing SNR compared to other techniques **[62-64]**. Another variance of the space to time encoding involves the use of a second harmonic cross correlation. The THz is first mapped onto a chirped pulse profile; however, the temporal profile of the pulse is measured by crossing it with a short readout pulse in a β-Barium Borate (β-BBO) crystal to produce a second-harmonic signal. Different frequencies of the chirped pulse, and thus different parts of THz waveform, are projected onto different spatial locations on the BBO crystal. The spatial profile of the second harmonic (SH) signal is recorded on a CCD array which is represented as an intensity cross-correlation of the two pulses at the detection crystal. This method does not suffer from significant time resolution degradation from the chirped pulse, however it requires a second nonlinear process, SHG, in addition to the EO effect, which significantly effects the signal intensity and SNR.

Increasing the temporal window is achieved by larger beam widths which inherently lowers SHG efficiency and measurement sensitivity **[65-66]**.

The space-to-time encoding is achieved using transmissive dual echelons. This single-shot technique is built around a complementary pair of custom-made transmission-mode echelons, optics that look like glass stairways. When the readout beam passes through a pair of echelons, each with *m* steps, it splits into an array of beamlets incrementally delayed in time. The more the glass the beamlet passes through, the longer the time delay associated with it. The time window is determined by the total beamlet delay time of all *m* steps and the temporal resolution is the larger of the readout pulse duration and the time delay introduced by the smallest time increment. This method requires minimal modification to the probe arm in a conventional EOS setup and achieves high temporal resolution and wide time windows with relative ease **[67-68]**.

In summary, the electro-optic detection of THz pulse which can be carried out in a nonlinear crystal can either be performed by sampling the THz pulse with a short probe or typically overlapping the THz pulse with a chirped probe. The latter case typical have faster acquisition rate of detection than the former. In both cases, the thickness and detection spectral response of the crystal sets the limit of the detectable THz spectral bandwidth.

3.9 Conclusion

The Pockels effect forms the basis by which EO detection can be achieved with the use of either a short or chirped probe (as well as a combination of both a short and chirped probe). Other than the difference in the acquisition time between the EOS and single shot detection, the EO conditions for efficient detection is essentially similar. Conditions such as large spectral response, high nonlinear EO coefficient and phase matching in the crystal must be satisfied for an efficient broadband detection. The useable spectral response of the crystal is limited by the thickness of the crystal. With the use of thinner crystals, the entire width of the response function can be utilized, however, the intensity of the measured THz signal will be compromised and vice versa. For this reason, a crystal with a high nonlinear EO coefficient are preferable.

3.10 Bibliography of chapter 3

[1] Wu Q.; Zhang X.C. Free space electro optic sampling of terahertz beams, Appl. Phys. Lett. 1995, 67, 3523–0. doi:10.1063/1.114909.

[2] Zhiping .J.; Xi-Cheng .Z. Measurement of spatio-temporal terahertz field distribution by using chirped pulse technology, IEEE journal of quantum electronics 2000, 36, 0–1222. doi:10.1109/3.880663.

[3] Träger .F. Springer Handbook of Lasers and Optics Volume 633 Short and Ultrashort Laser Pulses. 2012, (Chapter 12), 1047–1094. doi:10.1007/978-3-642-19409-2_12.

[4] Rylyuk .V. M. Tunneling and multiphoton ionization of atoms in two-color linear and circular laser fields and possibility of coherent polarization control of terahertz waves. International Journal of Modern Physics B. 2020, 2050275. doi:10.1142/S0217979220502756.

[5] Dmitriev V. G.; Gurzadyan G. G.; Nikogosyan D. N. Handbook of Nonlinear Optical Crystals. Springer Series in Optical Sciences, 1999, 64. doi:10.1007/978-3-540-46793-9.

[6] Schneider A.; Stillhart M.; Günter P. High efficiency generation and detection of terahertz pulses using laser pulses at telecommunication wavelengths. Optics express, 2006, 14, 5376–0. doi:10.1364/OE.14.005376.

[7] Stone M.; Goldbart P. Mathematics for Physics, a guided tour for graduate students. Department of Physics, University of Illinois at Urbana-Champaign, 1110 West Green Street, Urbana, Illinois 61801-3080, U.S.A.

[8] Tomasino A.; Parisi A.; Stivala S.; Livreri P.; Cino A. C.; Busacca A. C.; Peccianti M.; Morandotti R. Wideband THz Time Domain Spectroscopy based on Optical Rectification and Electro-Optic Sampling. Scientific Reports, 2013, 3. doi:10.1038/srep03116.

[9] Jazbinsek M.; Puc U.; Abina A.; Zidansek A. Organic Crystals for THz Photonics. Applied Sciences, 2019, 9, 882. doi:10.3390/app9050882.

[10] Yi M.; Lee K. H.; Maeng I.; Son J.; Averitt R. D.; Ahn J. Tailoring the Spectra of Terahertz Emission from CdTe and ZnTe Electro-Optic Crystals. Appl. Phys 2008 47. doi:10.1143/JJAP.47.202.

[11] Bang W.; Lei C.; Qiang F.; Ping T.; Yongqian X. Comparison of the detection performance of three nonlinear crystals for the electro-optic sampling of a fel-thz source. 5th international particle accelerator conference, 2014, 978-3-95450-132-8. doi:10.18429/JACoW-IPAC2014-THPRO017.

[12] Redkin R. A.; Bereznaya S. A.; Korotchenko Z. V.; Sarkisov S. Yu. A comparison of terahertz electro-optic sampling in ZnTe, ZnSe, GaP and GaSe crystals. 2015, 1–3. doi:10.1109/SIBCON.2015.7147189.

[13] Pradarutti B.; Matthäus G.; Riehemann S; Notni G.; Nolte S.; Tünnermann A. Highly efficient terahertz electro-optic sampling by material optimization at 1060nm.Optics Communication, 2008, 281, 5031–5035. doi:10.1016/j.optcom.2008.06.055.

[14] Du L.; Roeder F.; Li Y.; Shalaby M.; Beleites B.; Ronneberger F.; Gopal A. Organic crystal-based THz source for complex refractive index measurements of window materials using single-shot THz spectroscopy. Appl. Phys. A, 2021, 846. https://doi.org/10.1007/s00339-021-04948-1.

[15] Guiramand L.; Ropagnol X.; Blanchard F. Time-frequency analysis of two-photon absorption effect during optical rectification in a ZnTe crystal pumped at 1.024 μm Opt. Lett. 2021, 46, 6047-6050. https://doi.org/10.1364/OL.441231.

[16] Mansourzadeh S.; Vogel T.; Omar A.; Shalaby M.; Cinchetti M.; Saraceno C. J. Broadband, high power THz source at 540 kHz using organic crystal BNA APL Photonics, 2023, 8, 011301. https://doi.org/10.1063/5.0126367.

[17] Vidal S.; Degert J.; Tondusson M.; Freysz E.; Oberlé J. Optimized terahertz generation via optical rectification in ZnTe crystals. Journal of the Optical Society of America B. 2014, 31, 149. doi:10.1364/josab.31.000149.

[18] Degert J.; Cornet M.; Abraham .E; Freysz .E. Simple and distortion-free optical sampling of terahertz pulses via heterodyne detection schemes. Journal of the Optical Society of America B. 2016, 33, 2045.doi:10.1364/JOSAB.33.002045.

[19] Xie X.; Jingzhou X.; Zhang X.C. Terahertz wave generation and detection from a CdTe crystal characterized by different excitation wavelengths. Optics letters. 2006, 31, 978–0. doi:10.1364/OL.31.000978.

[20] Veronese M.; Danailov M.; Ferianis M.; Sincrotrone T.; Trieste, Filippetto D.; Frascati, Jamison S.P. Laboratory characterization of electro optical sampling (EOS) and thz diagnostics for fermi bymeans of a laser drivenpulsed thz source. 2009. https://accelconf.web.cern.ch/FEL2009/papers/tupc12.pdf.

[21] Hebling J.; Stepanov A.G.; Almási G.; Bartal B.; Kuhl J. Tunable THz pulse generation by optical rectification of ultrashort laser pulses with tilted pulse fronts. Appl. Phys. B 2004, 78, 593–599. doi:10.1007/s00340-004-1469-7.

[22] Susa M.; Li F.; Nagata K. Determination of refractive index and absorption coefficient of iron- oxide-bearing slags. Metall Mater Trans B 23, 331–337 (1992). https://doi.org/10.1007/BF02656289

[23] Planken P. C. M.; Nienhuys H. K; Bakker H. J.; Wenckebach T. Measurement and calculation of the orientation dependence of terahertz pulse detection in ZnTe. Journal of the Optical Society of America B 2001, 18, 313–317. doi:10.1364/JOSAB.18.000313.

[24] Boyd R. W. Nonlinear Optics. Third edition, ISBN-978-0123694706.

[25] Yariv A. Quantum Electronics, third edition. California institute of technology, 1989. John Wiley and sons, Inc.

[26] Narasimhamurty T. S. Photoelastic and Electro-Optic Properties of Crystals (chapter 3). ISBN 978-1-4757-0027-5, https://doi.org/10.1007/978-1-4757-0025-1.

[27] Casalbuoni S.; Schlarb H.; Schmidt B.; Schmüser P.; Steffen B.; Winter A. Numerical studies on the electro-optic detection of femtosecond electron bunches. Physical Review Special Topics - Accelerators and Beams, 2008, 11, 072802. doi:10.1103/PhysRevSTAB.11.072802.

[28] Bell G.; Hilke M. Polarization Effects of Electro-optic Sampling and Over-rotation for High Field THz Detection. Journal of Infrared, Millimeter, and Terahertz Waves, 2020. doi:10.1007/s10762-020-00724-z.

[29] Chen Q.; Tani M.; Jiang Z.; Zhang X. C. Electro-optic transceivers for terahertz-wave applications. Opt. Soc. Am. B, 2001, 18, 823–0. doi:10.1364/JOSAB.18.000823.

[30] Amnon Y. Pochi Y. Optical Waves in Crystals: Propagation and Control of Laser Radiation. 2002, ISBN: 978-0-471-43081-0.

[31] Winnewisser C.; Jepsen P. U.; Schall M.; Schyja V.; Helm H. Electro-optic detection of THz radiation in LiTaO, LiNbO and ZnTe. Applied Physics Letters, 1997, 70, 3069. doi:10.1063/1.119093.

[32] Van der Valk N. C. J.; Wenckebach T.; Planken P. C. M.. Full mathematical description of electro-optic detection in optically isotropic crystals. J. Opt. Soc. Am. 2004, 21, 622–0. doi:10.1364/JOSAB.21.000622.

[33] Parc Y. W.; Ko I. S.; Postech J. Y.; Kim C.; PAL. A study of detection schemes in electro-optic sampling. Proceedings of FEL 2007, 790-784. https://accelconf.web.cern.ch/f07/PAPERS/MOPPH040.PDF.

[34] Sinyukov A. M.; Hayden. L. M. Efficient Electro-optic Polymers for THz Applications. The Journal of Physical Chemistry B. 2004, 108, 8515–8522. doi:10.1021/jp036644l .

[35] Brunkena M.; Genza H.; Gottlicherb P.; Hesslera C.; Huningb M.; Loosa H.; Richtera A.; Schlarbb H.; Schmuserc P.; Simrockb S.; Suetterlind D.; Tonuttie M.; Turk D. Electro-Optic Sampling at the TESLA Test Accelerator: Experimental Setup and First Results. TESLA Report 2003.

[36] She W.L.; Lee W.K. Wave coupling theory of linear electro-optic effect. Optics Communications, 2001, 195, 303–311. doi:10.1016/s0030-4018(01)01345-1.

[37] Schneider A.; Biaggio I.; Gunter P. Terahertz-induced lensing and its use for the detection of terahertz pulses in a birefringent crystal. Appl. Phys. Lett. 2004, 84, 2229–0. doi:10.1063/1.1688986.

[38] Williams P. A.; Rose A. H.; Lee K. S.; Conrad D. C.; Day G. W.; Hale P. D. Optical, thermo-optic, electro-optic, and photoelastic properties of bismuth germanate (Bi_4Ge_3O_12). Applied optics, 1996, 35, 3562–0. doi:10.1364/AO.35.003562.

[39] Bakker H. J.; Cho G. C.; Kurz H.; Wu .Q.; Zhang, X.C. Distortion of terahertz pulses in electro-optic sampling. Bakk1998, 15. doi:10.1364/JOSAB.15.001795.

[40] Hattori. T.; Homma Y.; Mitsuishi A.; Tacke M. Indices of refraction of ZnS, ZnSe, ZnTe, CdS, and CdTe in the far infrared. Optics communications, 1973, 7, 229–232. doi:10.1016/0030-401890015-1.

[41] Schneider A.; Neis M.; Stillhart M.; Ruiz B.; Khan R. U. A.; Günter P. Generation of terahertz pulses through optical rectification in organic DAST crystals: theory and experiment. Opt. Soc. Am. 2006, 23, 1822–0. doi:10.1364/JOSAB.23.001822.

[42] Faure J.; Van T. J.; Kaind R. A. l; Leemans W. P. Modelling Laser-Based Table-Top THz Sources: Optical Rectification, Propagation and Electro-Optic Sampling. Optical and Quantum Electronics, 2004, 36, 681–697. doi:10.1023/b:oqel.0000039617.85129.c2.

[43] Kuroyanagi .K; Fujiwara .M; Hashimo.H; Takahashi .H; Aoshima .S; Tsuchiya .Y. .All Organic Terahertz Electromagnetic Wave Emission and Detection Using Highly Purified N-Benzyl-2-methyl-4-nitroaniline Crystals. Japanese Journal of Applied Physics 2006, 45, 4068–4073.doi:10.1143/JJAP.45.4068

[44] Han P Y; Zhang X.C. Free-space coherent broadband terahertz time-domain spectroscopy. Measurement Science and Technology, 2001, 12, 1747–1756. doi:10.1088/0957-0233/12/11/301.

[45] Leitenstorfer A.; Hunsche S.; Shah J.; Nuss M. C.; Knox W. H. Detectors and sources for ultrabroadband electro-optic sampling: Experiment and theory. Appl. Phys. Lett. 1999, 74, 1516–0.doi:10.1063/1.123601.

[46] Schall M.; Helm H.; Keiding S. R. Far Infrared Properties of Electro-Optic Crystals Measured by THz Time-Domain Spectroscopy. International Journal of Infrared and Millimeter Waves, 1999, 20, 595–604. doi:10.1023/a:1022636421426.

[47] Marple D. T. F. Refractive Index of ZnSe, ZnTe, and CdTe. Journal of Applied Physics, 1964, 35, 539. doi:10.1063/1.1713411.

[48] Nahata. A; Weling .A S.; Heinz .T .F. A wideband coherent terahertz spectroscopy system using optical rectification and electro optic sampling. Appl. Phys. Lett, 1996, 69, 2321–0. doi:10.1063/1.117511.

[49] Madarasz F. L.; Dimmock J. O.; Dietz N.; Bachmann K. J. Sellmeier parameters for ZnGaP2 and GaP. Journal of Applied Physics, 2000, 87. https://doi.org/10.1063/1.372050

[50] Ward L. Handbook of Optical Constants of Solids II (Academic Press, Boston, 1991), p. 737.

[51] Dietze D.; Unterrainer K.; Darmo J. Dynamically phase-matched terahertz generation. Opt. Lett. 37, 2012, 1047-1049.

[52] Faust W. L.; Henry C. H.; Eick.R. H. Dispersion in the Nonlinear Susceptibility of GaP near the Reststrahl Band. Physical Review, 1968, 173, 781–786. doi:10.1103/physrev.173.781.

[53] Barker A. S. Dielectric Dispersion and Phonon Line Shape in Gallium Phosphide. Phys. Rev. 1968, 917-922. doi:10.1103/PhysRev.165.917.

[54] Li H. H. Refractive Index of ZnS, ZnSe, and ZnTe and Its Wavelength and Temperature Derivatives. Journal of Physical and Chemical Reference Data 13, 103-150 (1984) https://doi.org/10.1063/1.555705

[55] Sun F. G.; Zhiping J.; Zhang X. C. Analysis of terahertz pulse measurement with a chirped probe beam. Appl. Phys. Lett. 73, 1988, 2233-2235. https://doi.org/10.1063/1.121685.

[56] Wollenhaupt M.; Assion A.; Baumert T. Short and Ultrashort Laser Pulses. In: Träger, F. (eds) Springer Handbook of Lasers and Optics. Springer Handbooks. Springer, Berlin, Heidelberg. 2012. https://doi.org/10.1007/978-3-642-19409-2_12.

[57] Teo S. M.; Ofori-Okai B. K.; Werleya C. A.; Nelson K. A. Invited Article: Single-shot THz detection techniques optimized for multidimensional THz spectroscopy. Review of Scientific Instruments, 2015, 86, 051301 https://doi.org/10.1063/1.4921389.

[58] Zhiping J.; Zhang X. C. Electro-optic measurement of THz field pulses with a chirped optical beam. Appl. Phys. Lett. 1998, 72, 1945-1947 https://doi.org/10.1063/1.121231

[59] Matlis N. H.; Plateau G. R.; Van T.J.; Leemans W. P. Single-shot spatiotemporal measurements of ultrashort THz waveforms using temporal electric-field cross correlation. J. Opt. Soc. Am. B. 2011, 28, 23-27.

[60] Zhiping J.; Xi C. Z. Measurement of spatio-temporal terahertz field distribution by using chirped pulse technology. IEEE Journal of Quantum Electronics, 2000, 36, 1214-1222. doi: 10.1109/3.880663.

[61] Brandon K. R.; Benjamin K. O.; Zhijiang C.; Matthias C. H.; Ying Y. T.; Siegfried H. G. Self-referenced single-shot THz detection. Opt. Express, 2017, 25, 16140-16150

[62] Jie S.; Aniruddha S.W.; Ernst K.; Ludwig B.; Mischa B.; Ajay N.; Georg A. R.; Tony F. H. Single-shot measurement of terahertz electromagnetic pulses by use of electro-optic sampling. Opt. Lett. 2000, 25, 426-428.

[63] Yoichi K.; Takashi Y.; Atsushi N.; Koichiro A.; Hironori T. Single-shot terahertz spectroscopy using pulse-front tilting of an ultra-short probe pulse. Opt. Express, 2011, 19, 11228-11235.

[64] Yoichi K.; Takashi Y.; Hironori T.; Shin-ichiro A. Real-time measurement of temporal waveforms of a terahertz pulse using a probe pulse with a tilted pulse front. Opt. Lett. 2008, 33, 180-182.

[65] Steven P. J.; Jingling S.; MacLeod A.M.; Gillespie W. A.; Jaroszynski D. A. High-temporal-resolution, single-shot characterization of terahertz pulses. Opt. Lett. 2003, 28, 1710-1712.

[66] Salin F.; Georges P.; Roger G.; Brun A. Single-shot measurement of a 52-fs pulse. Appl. Opt. 1987, 26, 4528-4531.

[67] Wekaham G. P.; Nelson K. A. Dual-echelon single-shot femtosecond spectroscopy. Opt. Lett. 2000, 25, 505-507.

[68] Kim K. Y.; Yellampalle B.; Taylor A. J.; Rodriguez G.; Glownia J. H. Single-shot terahertz pulse characterization via two-dimensional electro-optic imaging with dual echelons. Opt. Lett. 2007, 32, 1968-1970.

Chapter 4

Generation and Detection of Narrow Bandwidth THz Spectrum

This chapter discusses the experimental results on THz generation and detection. The results are based on optical rectification processes in ZnTe and BNA crystals. These results can be broadly divided into two parts. In the first part, the THz pulses generated by the nonlinear crystals are characterized by EOS. Then in the second part, a modified single shot detection is performed in a ZnTe crystal. The uniqueness of this single shot, is that the generated THz is characterized in the same crystal used for detection. This scheme will be referred to as *single crystal configuration*.

4.1 EOS of THz pulse emitted by ZnTe crystal

The efficiency of optical rectification is strongly dependent on the phase matching condition between the laser pulse and the THz pulse. For a Ti:Sapphire laser centered at 800 nm, the phase matching condition (in a ZnTe crystal) is well satisfied for a broad range of THz frequencies **[1-3]**. Other than the Ti:Sapphire laser source, the ytterbium (Yb) doped fiber lasers has emerged in a wide range of scientific and industrial applications, offering advantages such as stability, low maintenance, high average power in its regenerative amplification section and a tunable repetition rate up to several tens of megahertz **[4-6]**. However, its application is limited to certain nonlinear crystals, in which ZnTe crystal is an exemption. It is because, at this wavelength the phase-matching conditions in the ZnTe crystal are not optimal.

Nevertheless, the phase mismatch condition has been advantageously used for the generation of radially polarized THz beams with 300 fs, 120 MHz Yb lasers. In this case, the induced nonlinear polarization radiates into a Cherenkov cone and it is manifested in the far field as a radially polarized terahertz beam. By increasing the Cherenkov radiation angle through creating a larger velocity mismatch, the emitted power of the radially polarized terahertz beam was improved **[7]**.

ZnTe has a bandgap energy of 2.3 eV at 300 K. So, the effect of TPA cannot be neglected when the crystal is pumped with laser sources whose photon energy are lower than 2.3 eV. Generally, the effect of TPA in (110) ZnTe is more severe at 800 nm than at higher wavelengths. The TPA coefficient of ZnTe measured at 800 nm laser is around 5.6-15 cm/GW **[8-12]**, while the TPA coefficient at 1060 nm is around 4.2 cm/GW **[13].** Following this comparison, it has be suggested that this effect of strong TPA at 800 nm can ultimately limit the terahertz scaling power **[7]**.

On one hand, the TPA effect at 1030 nm has been favorably harnessed. By using a 280 fs with a repetition rate of 25 kHz, the ultrafast charge carrier dynamic arising from TPA filtered the out-of-phase components of the THz signal, thus enabling the recovery of broadband THz pulse generations at the expense of lower efficiency. It was also highlighted that the effect of TPA tends to be significant in thicker crystals. As such a 1mm thick ZnTe crystal yielded more efficiently than 2 mm thickness **[14].** In this work, I also will utilize an Yb-based laser but with a longer pulse duration at 500 fs and operated at moderately high repetition rate to irradiate a 1 mm thick ZnTe crystal.

4.1.1 Experimental design for the EOS in ZnTe/BNA

An Ytterbium laser source centered at 1030 nm with a repetition rate of 42 kHz was used as the input beam for the experimental set-up shown in Fig. 4.1. At the output of the laser source, the beam size is 2024 µm in diameter and the duration is at 500 fs FWHM and it is linearly polarized. The pulse duration was measured with an autocorrelation device and found to be 500 fs, while the maximum average power was recorded as 380 mW. The set-up is mainly divided into two arms namely; the detection and generation arm. A beam splitter (BS) is placed in the path of the laser source in order to reflect 35 percent of the input laser power to the detection arm, while the remaining 65 percent is transmitted to the generation arm of the set-up. I will refer to the reflected and transmitted beams as the probe and pump pulses respectively. The pump pulse is then focused onto the non-linear crystal by using a lens of 500 mm focal length. As the pump pulse propagates through the non-linear crystal, THz pulses are radiated out in a conical form. In order to efficiently collect the radiated beam (i.e. the optical and THz pulse), a 2" inch diameter off axis parabolic mirror (PM_1) is placed at the exit portion of the non-linear crystal such that it collimates the radiated beam. To achieve this, the distance between the PM_1 and non-linear crystal is adjusted to fit the PM_1 focal length. The pump pulse is filtered out if the radiated beam by placing a 2 mm thick silicon filter in the path of the collimated beam. Thus, the beam at the exit of the filter is mainly the THz pulse. A second off axis parabolic mirror PM_2 is used to focus the collimated THz pulse on to a ZnTe crystal that is used as the electro-optic crystal.

As the THz pulse is focused on the electro-optic crystal, the probe pulse overlaps with it spatially and temporally with the aid of a computerized delay stage. In order to ensure the overlap between the THz and the pump pulse, the overlap position was initially determined by overlapping the probe and pump pulses in the absence of the silicon filter. By doing this, one can only have an estimate of the possible overlap position between the THz pulse and the probe pulse. However, when the filter is in place, the overlap between the THz and probe pulse is realized by optimizing the orientation of PM_2. It is important to note that, the Half Wave Plate (HWP) placed in the path of the probe pulse is used to influence of the polarization of the probe such that the polarization are optimized for detection. Also, the probe is collinear focused by passing it through a hole in PM_2.

In the absence of the THz field, no phase will be induced in the probe pulse. As such, the probe pulse will be circularly polarized upon passing through the Quarter Wave Plate (QWP). To verify this assumption, the THz is cut off so that only the probe goes through the electro-optic crystal. At the exit of the QWP the probe pulse becomes equally polarized in two directions (i.e. circularly polarized). A Wollaston prism (WP) is used to separate the individual polarization by transmitting one of the components while reflecting the other component. The difference between these components was observed to be negligible. However, in the presence of the THz field, a refractive index change occurs in the electro-optic crystal. This results to a change in the phase of the probe pulses as it passes through the crystal (see chapter 3). In order to measure the amount of the induced phase change, the probe beam is initially elliptically polarized by passing through the QWP. Then the WP is used to separate the individual polarization by transmitting one of the components while reflecting the other component. With the aid of the balanced photodiode, the difference between the two polarization components is recorded. In order to suppress the effect of noise, and to improve the signal-to-noise ratio of the balanced photodiode, the output of the balanced photodiode is connected to a Lock-In-Amplifier (LIA).

The LIA uses a phase-sensitive detection technique to single out the component of the signal at a specific reference frequency. The noise occurring at frequencies other than the reference frequency are filtered out and do not affect the measurements. In our case this frequency is 400 Hz and it is given by the chopper frequency which is transmitted to the LIA by BNC cable. Then, a LabVIEW code is used to record the data from the LIA as the delay stage is translated. At the same time, the spatial position of the delay stage is recorded. Thus, the LIA signal is measured as a function of the delay stage position. The spatial position is then converted to time.

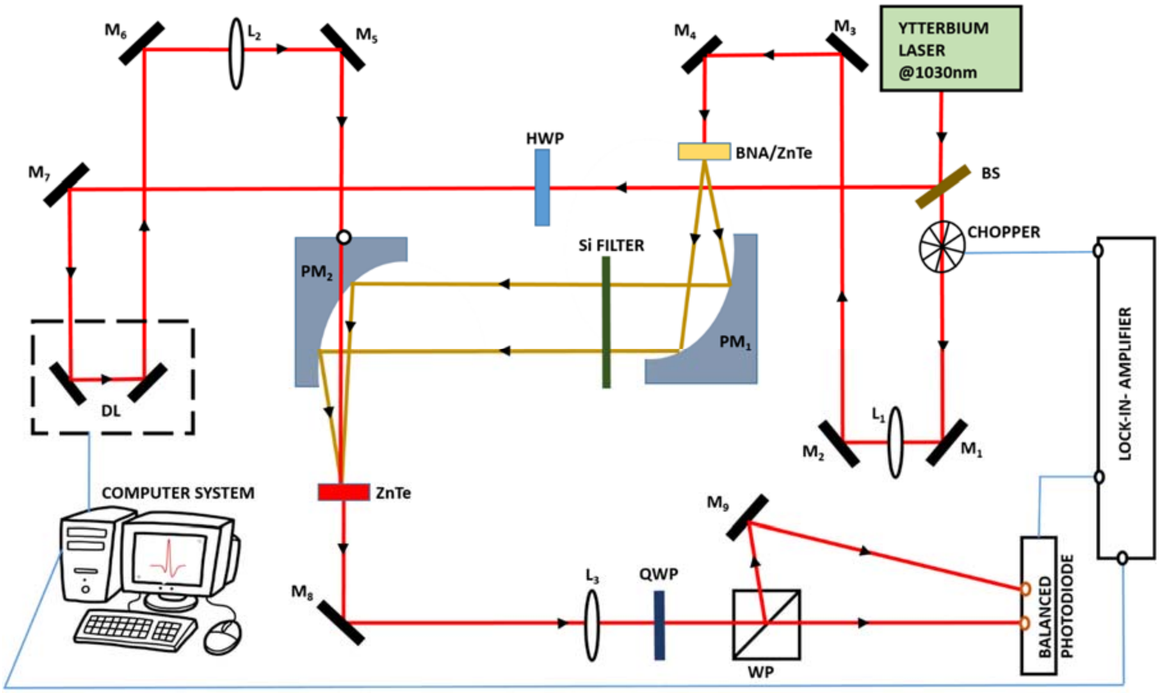

Fig. 4.1 The experimental set-up for the generation and detection of THz pulse using ZnTe or BNA crystals as emitters. The THz pulse is characterized by EOS in ZnTe crystal. The beam path of the

optical and THz pulse is indicated in red and brown color respectively. Mirrors; $\mathrm{M_1 - M_9}$, Off-Axis Parabolic Mirror; $\mathrm{PM_1}$-$\mathrm{PM_2}$; Lens; $\mathrm{L_1 - L_3}$; Half Wave Plate; HWP, Quarter Wave Plate; QWP; Beam Splitter; BS; Delay line; DL.

4.1.2 Results and discussion (using ZnTe as the THz emitter)

The experimental result of the EOS shows that a 1 ps (FWHM) long THz pulse was sampled, whose electric field is bipolar in shape as shown in Fig. 4.2a. A comparison between this pulse and the simulated pulses is performed in order to understand the profile of the experimentally observed THz pulse. The emitted and detected pulse in Fig. 4.2a which are simulation results correspond to the THz pulse without and with EO effect respectively. Equation (2-16) equation (3-32) and equation (3-36) were used for the simulation. The result of the simulation shows that, the experimentally observed THz pulse (blue) is shorter than the simulated-detected pulse (red) which has a pulse duration of about 2 ps. Without considering EO effect, the simulated-emitted pulse (dashed black) tends to be similar to the experimentally observed THz pulse.

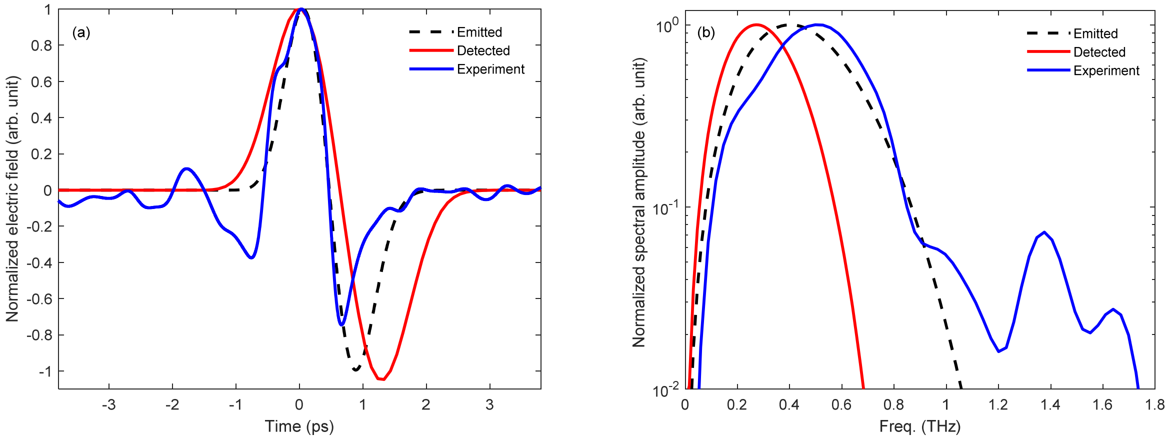

Fig. 4.2 Experimental (blue) and simulation result (red) of the THz pulse emitted by the ZnTe crystal. (a) The simulated electric field is broader than the experimentally observed field. (b) The experimental spectral is unexpectedly broader than the simulated spectral.

The marked difference between the experimentally observed and simulation-detected pulse arises from the narrowed dip towards the positive time axis, as well as the winged pattern towards the negative time axis in Fig.4.2a. In order to resolve these features more clearly, a log plot of the corresponding THz spectral is shown in Fig.4.2b. As shown, the spectral width of the experimentally observed spectrum (blue line) extends up to about 1.7 THz, and the simulated-emitted spectrum (dash black) extends up to 1.1 THz, whereas, the simulated-detected spectrum (red) has a narrower cut off at about 0.68 THz. It can be noted that, spectral width which extends from 0.8 - 1.7 THz cannot be detected by the 1 mm thick electro-optic ZnTe crystal. This argument follows from the spectral response shown in Fig 4.3a. The curve of the response function (cyan) is plotted by using equation (3-33) and it indicates a cutoff at 0.8 THz. As such, higher THz frequency components cannot be detected in practice. The emitted THz spectrum (black) which have been simulated without considering the EO effect is overlaid on the detection response function.

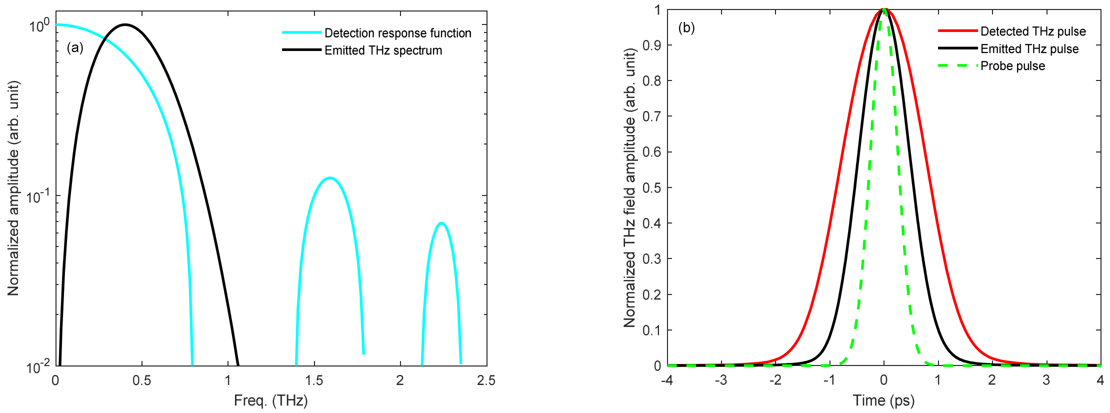

Fig. 4.3 Effect of spectral response of the 1 mm thick detector crystal and phase mismatch. (a) Simulation of the emitted THz spectrum (black) extends beyond the cutoff frequency of the 1 mm thick detector (cyan). (b) The probe (dash green) may not have been properly phase matched with the emitted THz pulse (black line), thereby leading to an extrapolation in the pulse duration of the detected THz pulse (red).

The right side of the emitted THz spectrum extends out of the response function. So, the result of multiplying the response function and THz spectrum may lead to a falsified extension of the spectral width as observed in the experiment. The discrepancy between experiment and simulation-emitted, refer to Fig. 4.2b) which sets in at around 0.6 THz corresponds to point where the response function begins to roll-off to zero. Thus, the frequency component between 0.6 – 1.7 THz cannot be interpreted as part of the experimentally emitted frequencies. So, the narrowed dip in the time domain is probably an artifact. Moreover, the discrepancy between simulation and experimental result can be illustrated by simulating the pulse duration of the emitted and detected THz pulse. To do this, a plot of their respective THz intensity is shown in Fig.4.3b. The pulse duration of the detected THz pulse (red line) is 2 ps long whereas the pulse duration of the emitted THz pulse (black) is 1 ps. The detected THz pulse is simulated by considering EO effect. i.e. by including equation (3-32) and (3-33). The result reveals that, the detected THz pulse is longer than the emitted THz pulse. This may be due to the usage a long probe pulse to sample the THz pulse or the poor phase matching that is inherent in the usage of ZnTe at 1030 nm laser.

A slight narrowing of the experimental THz spectrum occurs at frequencies less than 0.4 THz. This might be due to the effect of diffraction. By using equation (2-19), a plot of the diffraction function is plotted as shown in Fig. 4.4. The result indicates that THz frequencies less than 0.4 THz are more prone to diffraction effect than higher frequencies. Since the wavelength equivalent of the experimentally measured THz spectrum is 600 Um, which is LONGER than the pump beam size (324 µm), then the effect of diffraction cannot be neglected. This diffraction effect has also been confirmed by **[15]**. Thus, it appears that the winged pattern in the time domain might have originated from the effect of diffraction.

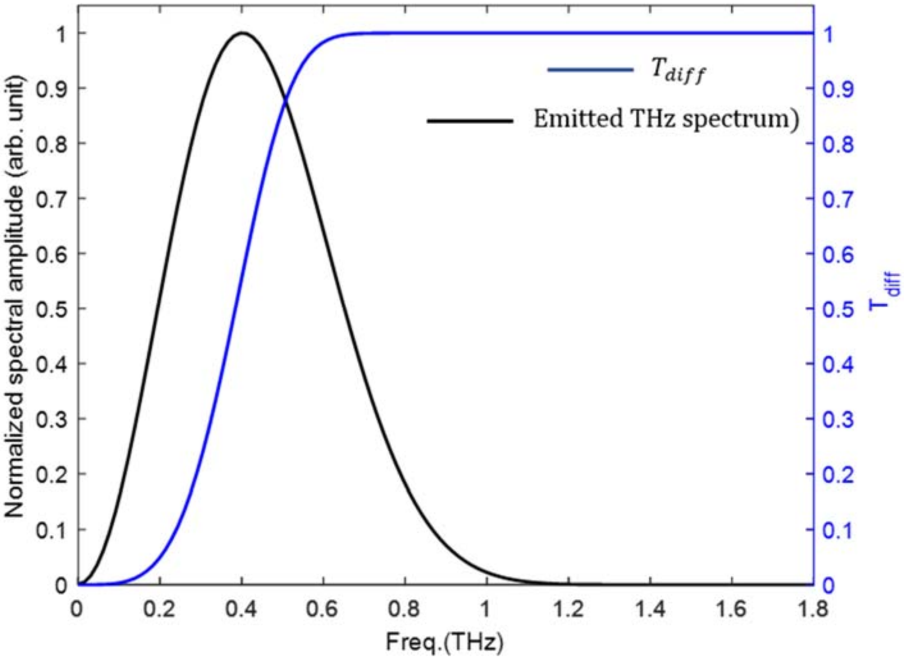

Fig. 4.4 Effect of diffraction on sub-THz frequencies. The diffraction curve (blue line) shows that at frequencies below 0.3 THz the diffraction effect is obvious, and less significant at higher frequencies.

The aforementioned spectral discrepancy between 0.6 – 1.7 THz can be further studied in relation to the thickness of the detector crystal. Assuming that a 200 µm is used for detection, it can be observed that the THz spectrum is situated away from the cutoff (see Fig. 4.5). As such, it will be possible to perform detection without distortion. So, I remark that the distortion and discrepancy observed may be overcome by the use of thinner crystal, because there will be a better compensation for phase mismatch between the probe and THz pulse (refer to chapter 3).

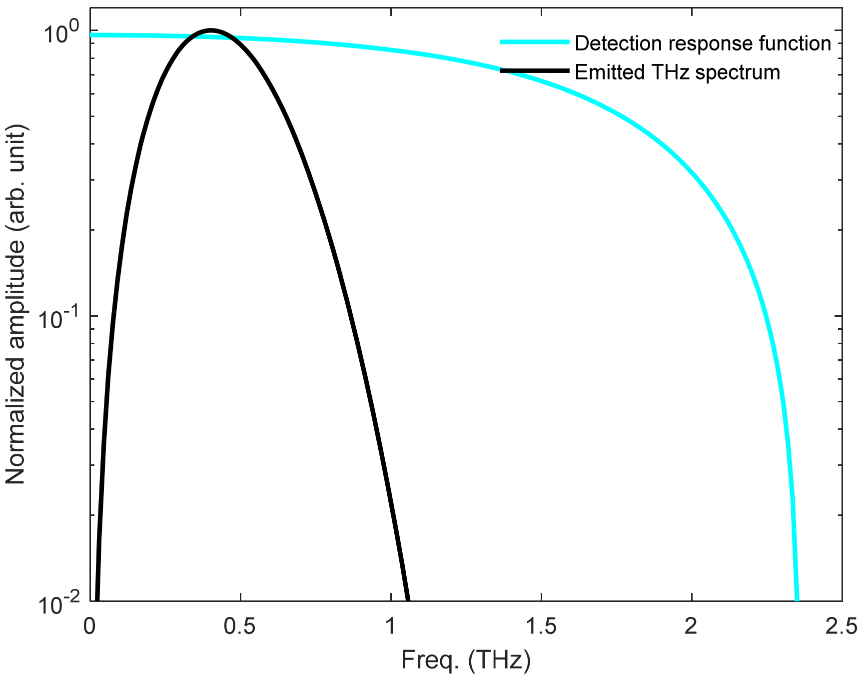

Fig. 4.5 Effect of spectral response of a 200 µm thick detector. The detection response function (cyan) is broader than the spectrum of the emitted THz spectrum (black).

Next, the power of the experimentally generated THz pulse (measured as the absolute squared of the detected signal) is studied with respect to the intensity of the pump pulse. The probe pulse intensity is fixed while the pump intensity is varied with the help of neutral density filters. The plot of the outcome is as shown in Fig. 4.6. The experimental data (brown circles) indicates that, at the instance the pump intensity is below 2 X 10^{13} W/m^2, the measured THz power slowly. However, at intensity levels beyond 3 X 10^{13} W/m^2, the THz power rises quickly and attain a maximum value at about 13 X 10^{13} W/m^2.

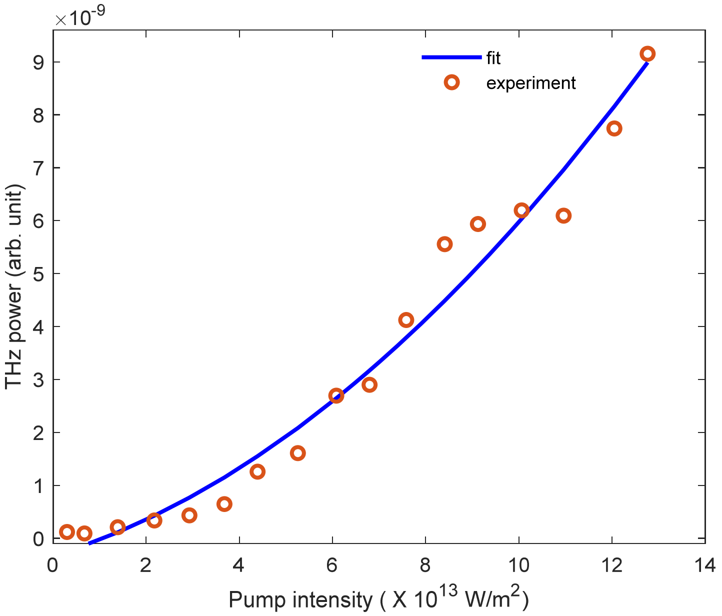

Fig. 4.6 The quadratic dependency of the ZnTe THz power as a function of pump pulse intensity. The experimental data (brown circles) is fitted by a quadratic curve (blue)

A fit (blue) for the experimental data shows that the variation of the THz power can be modelled by a quadratic law. This finding obeys the theoretical dependency of the THz power on the pump intensity given as $P_{THz} \propto I_0^2$. I highlight that, since this scaling law have been recovered experimentally, then the effect of the nonlinear absorption of the pump intensity is insignificant. Usually, this nonlinearly absorption gives rise to both TPA and FCA effect that absorb the useable pump and THz pulse power respectively. It does appear that, in this work, the nonlinearities are inherently suppressed. Moreover, it was possible to obtain a quadratic fit because the pump energy is low (10 μJ). However, saturation effect of the pump pulse can lead to linear fit at higher pump pulse energy **[4]**.

4.1.3 Conclusion (using ZnTe as the THz emitter)

A 1 ps long bipolar THz field has been generated by a 1 mm thick ZnTe crystal via optical rectification. A corresponding narrow THz spectrum was realized whose frequency is centered at 0.5 THz. The detection was performed by EOS in a 1 mm thick ZnTe crystal. The experiment which was performed in ambient air was carried out using an ytterbium-based laser whose center wavelength is at 1030 nm, with a 42 kHz repetition rate and a pulse duration of 500 fs.

It is observed that, nonlinear effects such as TPA may have been negligible since there is a quadratic dependency of the THz power on the pump pulse intensity. In addition to other factors, this may be because the energy per pulse of the laser is less than 10 μJ. As such, saturation effect on the pump pulse may not have been significant. The consequence of this result is that the strength of the THz signal may be weak, although no characterization of the THz strength was performed.

In the same vein, the effect of phase mismatch between the THz and optical pulses which limits the scalable THz frequency may not have been severe as compared to other effects. Other effects such as the crystal thickness and the diffraction of the THz beam seems to better explain the discrepancy between the simulated and experimental THz signal. As a way to optimize the experimental set-up, I suggest that a thinner crystal should be used for the EOS so that the full spectral width of the THz pulse can be faithfully recovered. Though, the effect of diffraction may not be completely eliminated at low THz frequencies, the use of a large semi-aperture parabolic mirror may limit diffraction effect.

4.2 EOS of THz pulse emitted by BNA crystal

In chapter 2, it was highlighted that, the usability of BNA crystals is limited by two important factors. These are namely, the repetition rate of the incident laser and the presence of a bonded substrate on the BNA crystals. In what follows, I shall briefly discuss the impact of the incident laser wavelength on the performance efficiency of BNA crystals.

4.2.1 Brief state of the art

Recently, BNA crystal are gaining attention in the THz community. They have the potentiality to emit broad THz spectrum. In the literature, several laser wavelengths ranging from 800 -1550 nm have been used to generate THz pulses from the BNA crystals. A summary of these wavelengths sources is tabulated in Table 4.1. The results are particular to the substrate-BNA crystals. For a clear understanding, I shall group the results into two main parts depending on the wavelength characteristics of the incident laser. Accordingly, the shaded portion are obtained from the use of 1 µm lasers while the unshaded part is from 0.8 µm laser. At the earliest stage in the use of BNA, it was initially irradiated by 800 nm, 50 fs laser, and this led to the generation of up to 3 THz **[16].** Later on, by using 1150-1550 nm, 35 fs laser, an extended THz spectrum up 7 THz was realized at an improved efficiency of 0.8 % with the use of longer crystal length **[17]**. In a bid to predict the THz yield from BNA as function of laser repetition rate, a 10 Hz repetition rate laser pulse centered at 800 nm with 100 fs pulse duration was used to irradiate a 650 µm thick BNA resulting to the generation of up to 2.5 THz **[18]**, and with an approximate efficiency equal to the earliest result but much lower than that obtained from the 1150-1550 nm laser. After the publications of the afore cited references, several other groups have conducted experimental works in the past few years with either a 0.8 µm or a 1 µm laser **[19-24]**. In the strict sense, though, it is difficult to compare the results from different experiments that were performed in different conditions. However, there seems to be a consistent trend with the results of the 1 µm laser in relation to the 0.8 µm laser. Broader THz spectral up to 6-7 THz are generated from 1 µm laser compared to a narrower spectral of 2.5-4 THz generated from the 0.8 µm laser. This is possibly due to the favorable phase matching occurring at 1 µm wavelength. Recently, a laser pulse duration of 85 fs and centered at 1030 nm was used to irradiate the BNA crystals, and this resulted to the generation of broad THz spectrum up to 7 THz with a measured efficiency of 0.12% **[24]**.

Table 4.1 Incident laser characteristics of the emitted THz pulses from BNA crystals

Laser parameters	**Crystal thickness (μm)**	**THz bandwidth (THz)**	**Efficiency (%)**
800 nm, 50 fs, 100 Hz **[16]**	680	3	0.26
1150-1550 nm, 35 fs, 1kHz **[17]**	1100	7	0.8
800 nm, 100 fs, 10 Hz **[18]**	650	2.5	0.2
800 nm, 100 fs, 1 kHz **[19]**	183	4	-
1250 nm, 100 fs, 1 kHz **[20]**	700	6	-
800 nm, 100 fs, 500 Hz **[21]**	300-400	4	-
960 nm, 35 fs, 1 kHz **[22]**	300	7	0.6
1030 nm, 85 fs, 13.3 MHz **[23]**	305	6	0.04
1030 nm, 45 fs, 540 kHz **[24]**	650	7	0.12

In my experimental work on BNA crystal, a long pump pulse measuring 500 fs FWHM and with a center wavelength of 1030 nm, was used in order to investigate the form of the THz pulse that can be generated with a long pulse. The photograph of the BNA crystal used in this work is shown in Fig. 4.7. The crystal size along the *a, b* and *c* axis respectively are 4 mm X 2 mm X 0.38 mm. For the experimentation, the same experimental set-up in Fig. 4.1 is adopted in which the ZnTe crystal is replaced by the BNA crystal.

Fig. 4.7 Image of the 0.38 mm thick single BNA crystal fabricated by Swiss THz technology, which was used in this work. It has a damage threshold of 3.7 mJ/cm^2.

4.2.2 Results and discussion (using BNA as the THz emitter)

The resolution of an EO measured signal depends directly on the experimental time window. A longer window leads to better spectral resolution, but extends the experimental scan time, and thus finding an optimum time window to balance this trade-off is preferred. As a result, a longer delay stage was used to replace the initial delay stage in Fig. 4.1.

A long range scan of the THz signal emitted by the BNA crystal is shown in Fig. 4.8. It spans 40 ps with a temporal step of 133 fs. An obvious feature in the long range scan is the appearance of multiple terahertz pulses. After the initial THz pulse, attenuated waveforms equally spaced by 10 ps can be seen. This observation which is commonly referred to as etalon effect is a Fabry-Pérot like effect. It is very important to note here, that these pulses will add oscillation features to the Fourier spectra. Thus, the time-domain waveforms need to be time-windowed numerically in order to eliminate the multiple pulse reflections. On the other hand, these reflections may be eliminated by using a thinner misaligned piece of the silicon filter.

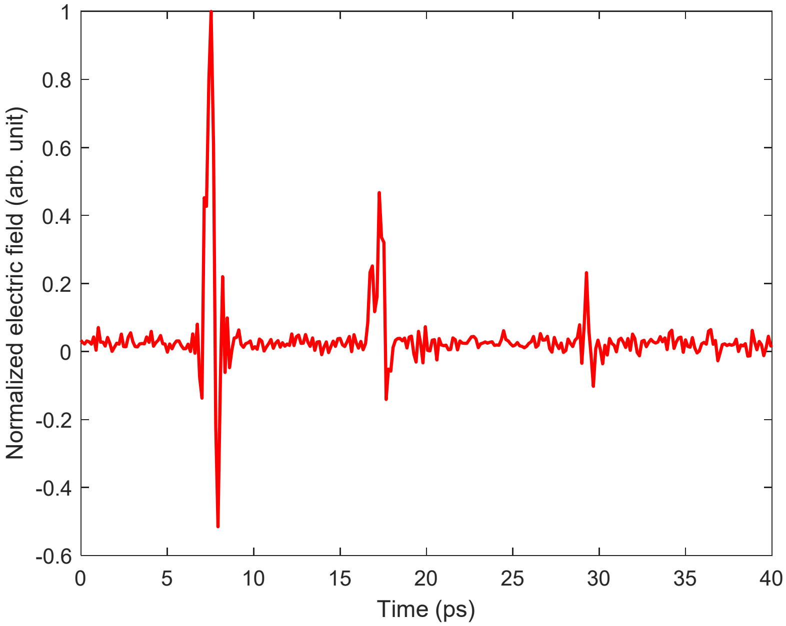

Fig. 4.8 Long range sampling of BNA THz pulses offered by a 150 mm delay stage. Multiple pulse reflections are observed at a consistent spacing of 10 ps. These features may be attributed to the nature of the pump pulse filter used in this work.

When BNA crystal is used as the emitter crystal, less than 1 ps long THz pulse was detected by EOS as shown in Fig. 4.9a. The THz pulse is multicycled, consisting of up to three cycles. Similar multicycle pulses have also been observed in literatures **[16-24]**. The THz pulse is recovered with a high temporal resolution, thanks to the long scanning range provided by the long delay stage. This has made it possible to adequately resolve the oscillatory pattern in the THz pulse. The corresponding Fourier transform of Fig.4.9a is depicted in log scale as shown in Fig 4.9b.

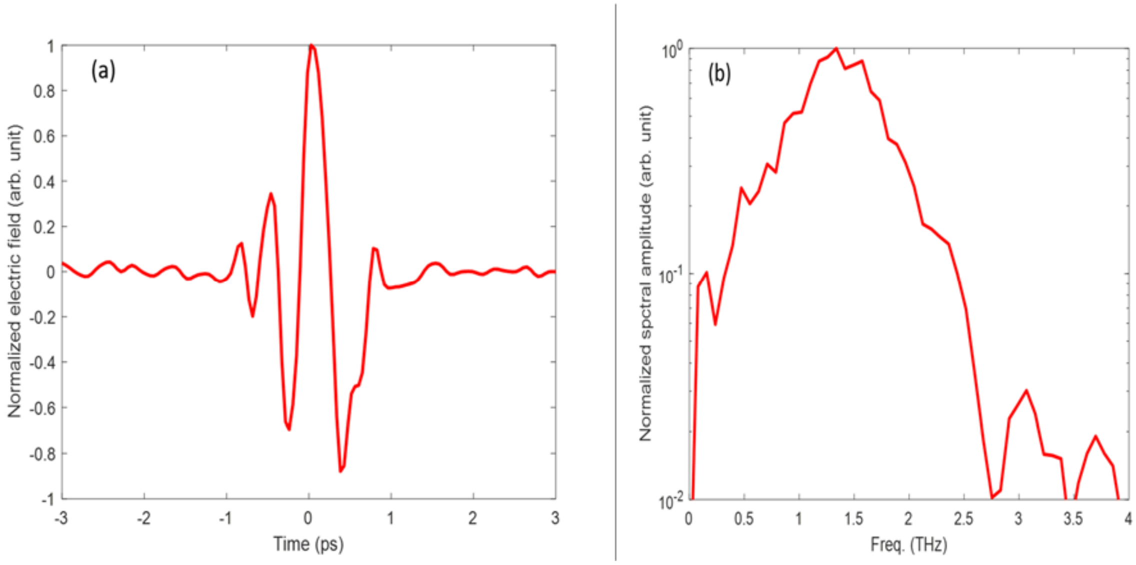

Fig. 4.9 Experimental result of the THz pulse emitted by the BNA crystal, and sampled in 1mm thick detector. (a) The electric field is multi-cycled and has a pulse duration less 1 ps. (b) The spectrum is centered at 1.3 THz.

It has a spectral bandwidth of about 1 THz. Lower frequency components below 1 THz are lower in spectral amplitude, while the highest spectral amplitude occurred at around 1.3 THz. Beyond 1.5 THz, the spectral amplitude rollsoff until a cut off occured at around 2.7 THz. In order to understand this spectral pattern, a typical THz absortpion plot in BNA crystal is shown in Fig. 4.10a. It is simulated by using equation (3-4).

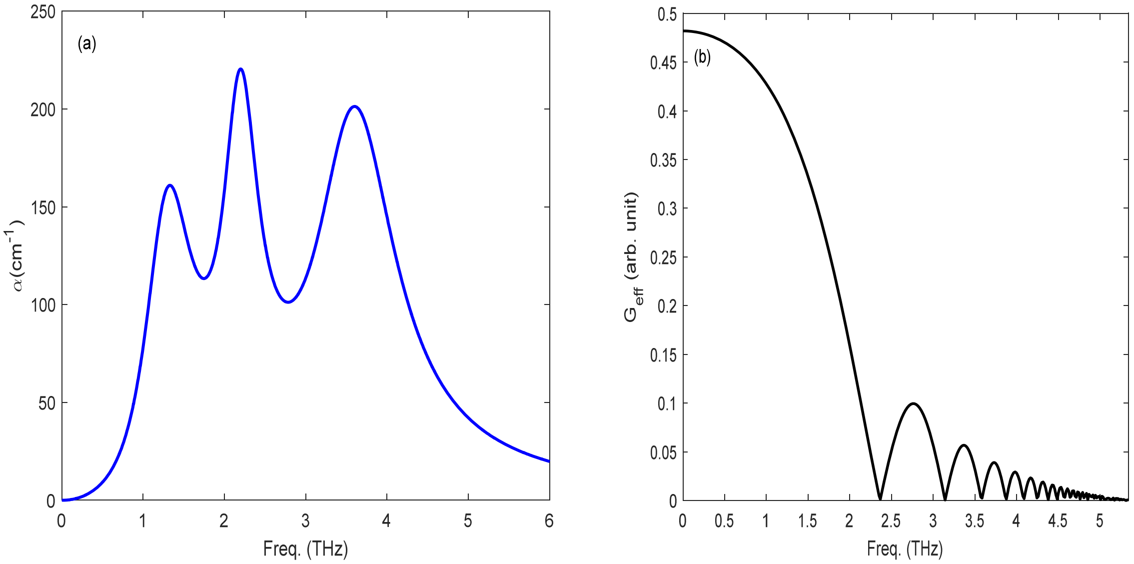

Fig. 4.10 BNA absorption coefficient and ZnTe response function. (a) BNA absorption coefficent at THz frequencies. (b) Response function of the detector crystal at 200 µm thickness.

There are notably three absorption peaks occurring at 1.3 THz, 2.2 THz and 3.6 THz. In between these peaks the absorption is minimal (i.e. at around 1.7 THz and 2.7 THz). So, it is expected that the spectral amplitude of the generated THz pulse at the former frequency values will be low compared to the latter values. However, this is not exactly the case in our experimental result. Instead, the THz frequency is centered at around 1.3 THz. To further the analysis, it is observed that the detection response function of the detector crystal has a cutoff frequency at 0.8 THz (see Fig. 4.3a). As such, the response function corresponding of the 1 mm thick detector is only effective to detect frequencies not higher than 0.8 THz. According to this argument, it is therefore surprising to have been able to detect frequency components higher than 0.8 THz.

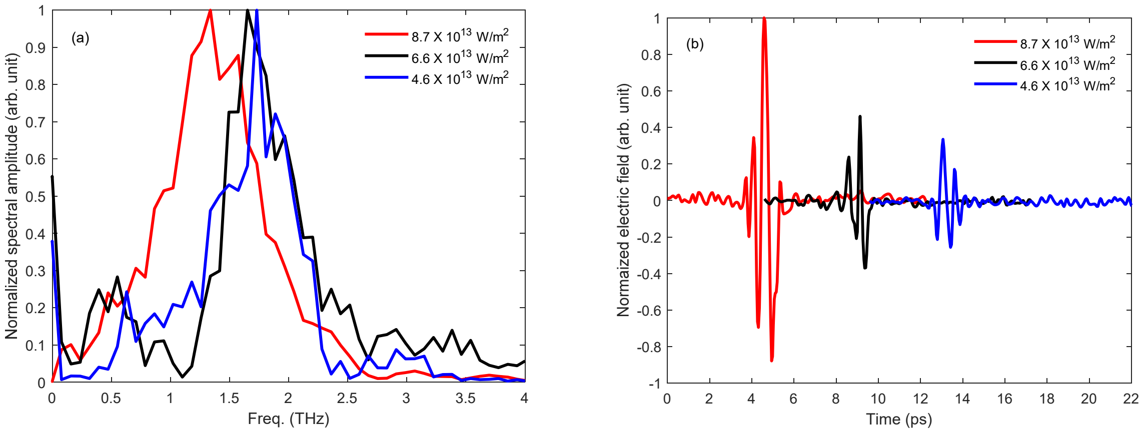

Fig. 4.11 BNA THz pulses emitted at several pump intensity, and sampled in 1 mm thick detector. (a) The spectrum is centered at 1.5 THz for the maximum pump intensity, and at 1.7 THz for other intensities. (b) The electric field are multi-cycled and each have a pulse duration of 0.5 ps.

As a way to check the consistency in our measurement, several THz spectral and their corresponding electric field are shown in Fig. 4.11a and 4.11b. Less than 1 ps multicycle THz pulses are obtained at different pump intensities. The electric fields in Fig. 4.11b have been shifted for clear viewing. The fields obtained at lower intensities (i.e. at 4.6 X 10^{13} and 6.6 X 10^{13} W/m^2) shows more resemblance to each other and are a bit different from that obtained at high intensity (i.e. at 8.7 X 10^{13} W/m^2. In the spectral domain, a central frequency of about 1.7 THz is obtained at pump intensities of 4.6 X 10^{13} and 6.6 X 10^{13} W/m^2. This center frequency is a bit wider than that obtained with 8.7 X 10^{13} W/m^2 pump intensity, although the cutoff is narrower and occurred at around 2.2 THz. As earlier noted, the detector response function may not have guaranteed the possibility of detecting such broader spectral. Generally, these frequency values are higher than that obtained detected from the ZnTe emitter. It does seem that broader THz spectral which is broader than the detection limit must have been emitted. In order to confirm the presence of the broadly emitted spectrum, a thinner detector of 200 µm is used to replace the 1 mm crystal. The detected spectrum by using this thinner crystal is shown in Fig.4.10b.

With the use of thinner crystal it is expected that the detected spectrum will be relatively lower in spectral amplitude. This follows from our discussion in chapter 3, that thinner crystals are able detect broader spectrum at the expense of the signal amplitude. As such, the dynamic range in Fig. 4.12 is expected to be lower than in Fig. 4.11, thereby resulting to a noisy detection. The frequency of the detected pulse is centered around 2 THz, and has a spectral bandwidth of 1 THz. The corresponding THz electric field has a pulse duration close to 0.5 ps, which is shorter compared with the result of the thicker detector crystal. Based on the detection response function plot of a 200 µm thick crystal shown in Fig 4.10b, it indicates that up to 2 THz can be detected. Close to 2.2 THz frequency (which corresponds to an absorption peak (see Fig. 4.10a)), the THz spectrum in Fig. 4.12a rapidly rolls off to zero, possibly due to the effect of THz absorption. On the other hand, it may also be due to the use a long pump pulse.

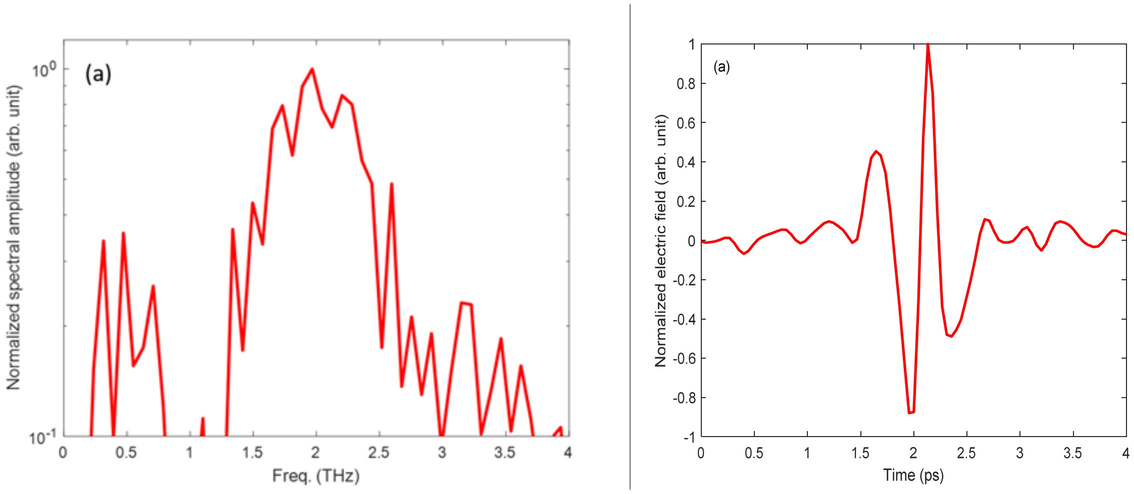

Fig. 4.12 Sampling of BNA THz pulses in 200 µm thick detector. (a) The spectrum is centered at 2 THz. (b) The electric field is multi-cycled and has a pulse duration of 0.5 ps.

The THz power is graphed in Fig. 4.13 as a function of the pump intensity. The measured power gradually increases at pump intensity beyond 3.0 X 10^{13} W/m^2 and rapidly peaks beyond 9 X 10^{13} W/m^2 as shown by the experimental data (red circles). The corresponding fit (blue) is found by a quadratic curve. This observation suggests the exclusion of the TPA and FCA effect that competes with optical rectification.

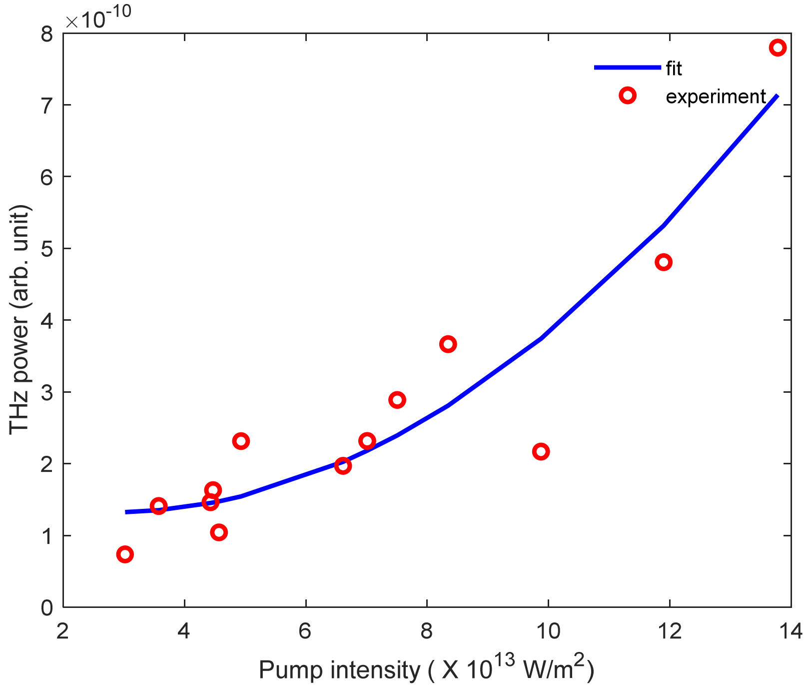

Fig. 4.13 The quadratic dependency of the BNA THz power as a function of pump pulse intensity. The experimental data (red circles) is fitted by a quadratic curve (blue line)

In order to emphasize the multicyle nature of the BNA THz pulse, a comparison with the ZnTe THz pulse is shown in Fig. 4.14. The thickness of the detector crystal is 1 mm for both crystals. A THz spectrum centered at 0.5 THz is detected in the case of ZnTe while, a spectrum centered at 1.3 THz is observed in the case of BNA crystal. Though, it is not possible to detect frequencies as high as 1.3 THz by using a 1 mm thick ZnTe crystal, it can be observed that the BNA THz pulse is multicycled as compared to the bipolar form of the ZnTe THz field.

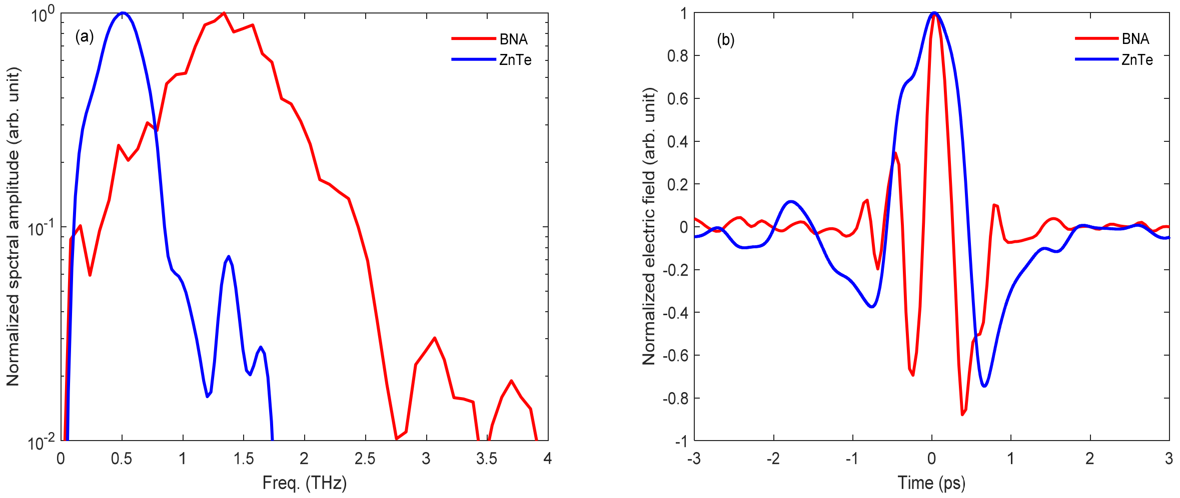

Fig. 4.14 Comparison between the THz pulses generated from BNA (red) and ZnTe (blue) crystals. (a) The THz spectrum of the BNA has a peak central frequencies at 1.3 THz while that of ZnTe has a center frequency at 0.5 THz. (b) The electric field of the BNA is multi-cycled and shorter than that of the ZnTe crystal.

4.2.3 Conclusion (using BNA as the THz emitter)

Multicycle THz pulse has been generated by a 390 µm thick BNA crystal via optical rectification. The detection was performed by EOS in a 1 mm and 0.2 mm thick ZnTe crystal. The experiment which was performed in ambient air was carried out using an Ytterbium-based laser whose center wavelength is at 1030 nm, with a 42 kHz repetition rate and a pulse duration of 500 fs.

The result of the THz signal sampled in the different ZnTe crystal, indicated obvious differences in terms of the signal spectral component and dynamic range. When the 1 mm ZnTe crystal is used as the detector, the sampled THz pulse had a duration less than 1 ps and a center frequency of around 1.3 THz, while a shorter pulse duration with an extended center frequency was realized with the use of the thinner crystal. To understand the discrepancy in these results, the detection response function of the two crystals were compared to the detected THz spectrum. It was inferred from the comparison that it is surprising to detect frequencies higher than 0.8 THz when the 1 mm crystal is used. As such, a thinner crystal was used which had a cut-off frequency at 2.4 THz. A THz spectrum centered at 2 THz with a pulse duration of 0.5 ps was measured by this thinner crystal. These results indicate that the bandwidth of the generated THz signal is broader than the detection response function of the 1mm ZnTe crystal, as such it was inadequate to characterize the THz pulse. Replacing the thicker crystal with the thinner crystal broadened the detection limit, however the noise level severely affected the signal.

The power of the THz signal (measured by taking the integral square of the THz electric field) was observed to vary as the squared pump intensity which in part supports the claim of the exclusion of TPA and FCA effects that competes with the optical rectification process. It is noted that the maximum pump fluence of our laser source is lower than the crystal damage threshold. As such, it is likely that our measurement did not extend up to the pump's saturation region. By comparing the BNA and the ZnTe THz signal it was realized that the BNA THz pulses are multi-cycled, while the ZnTe THz pulses are bipolar. In conclusion, I suggest that, a different EO crystal, for example, a GaP crystal can be used as the detector crystal. Since phase matching is well optimized for such crystal and that the effect of THz absorption is lesser, then broader THz spectrum free from artifacts may be measured.

4.3 Single crystal configuration.

Oftentimes, two nonlinear crystals are needed in typical experimental set-up for THz emission and detection respectively. In this set-up, the THz pulse being radiated by one of the crystal is detected at the other crystal by either a collinear or non-collinear interaction with a weak probe beam. Due to the usage of the weak probe beam in the detection arm, there are usually no other observed processes other than the linear electro-optic (EO) effect. However, in the case where the generation occurs alongside with the detection in the same crystal, in what I shall refer to as *single crystal configuration*, the EO effect may coexist with other nonlinear processes such as two photon absorption (TPA) and free carrier absorption (FCA), which competes with the generated THz pulse **[25, 26]**. In order to have a close look into these nonlinear effects, *Caumes et. al.* in their heterodyne Kerr experimental set-up, have observed optical Kerr effect and Kerr-like effect in certain zinc blend structures that modifies the form of the detected THz pulse **[27]**. The Kerr-like effects are cascaded nonlinear signal induced by the generated THz pulse. Few years later, other researchers adopted the single crystal configuration as a tool to study and evaluate these additional nonlinear effects in the ZnTe crystals. *He et. al.* confirmed the observation of *Caumes et. al.* in the (111) ZnTe in which the measured nonlinear refractive index, was dominated by Kerr and Kerr-like effects, whereas, only the Kerr effect was more significant in the (110) ZnTe **[28]**. Furthermore, the effect of the Kerr signal which usually appears at the onset of the THz waveform because the optical group velocity is lower than the THz phase velocity, was minimized by creating a temporal shift **[29-30]**. In a bid to distinguish the presence of either effects, *Xiaoshu. et. al.* included a phase sensitive time-resolved z-scan in their experiment. By moving the crystal along a defined direction, they evaluated the contribution of each effects **[31]**.

As can be observed in the previous paragraph, the single crystal configuration is a great tool to study the response of ZnTe crystal. Additionally, they are useful for application purposes in integrated THz devices. *Chen et. al.* has demonstrated the possibility of this configuration to be applied in tomography, in which they used a ZnTe to transmit pulsed signal which was detected in the same crystal upon being reflected **[32, 33]**. Thus, it appears there will be a need to minimize the nonlinearities in the single crystal configuration in order to boost their applications. Being temporally stretched, chirped laser pulses are less powerful than their Fourier transformed limited pulse duration. However, their higher pulse-energy can be used to reach the same power, thus leading to an increase of the THz yield due to many photons present. Previously, efficient THz yield have been reported using a pre-chirped pump pulse in air-plasma THz based sources **[34]**. *Erschens et. al.* extended this concept to nonlinear crystal-based sources **[35-37]**. Usually, chirped pump laser sources are capable of generating tunable and narrow-band THz frequencies **[38-39],** which have been used to selectively excite phonon in certain mediums by some research groups **[40-41]**. In this manuscript, I will introduce the idea of adding a chirp to the pump pulse in the single crystal configuration **[46]**.

4.3.1 Experimental design for the single layout configuration.

The experimental set-up for the single ZnTe crystal is shown in Fig. 4.15. The laser source used for this experiment is the Coherent Libra Ti-sapphire laser. The output beam from the laser is coupled to a Chirped Pulse Amplifier (CPA) to generate a beam centered at a wavelength of 796 ± 2 nm, with a repetition rate of 1 kHz and ~0.6 mJ of energy per pulse. The distance between the compressor's gratings in the CPA was adjusted to initially chirp the pulse. This resulted to the generation of 3.6 ps long pulses as measured by a Frequency Resolved Optical Gating (FROG) device. A beam splitter is placed in the path of the output pulse to transmit 50 percent and reflect the other 50 percent of the total laser power. The reflected beam is used as the pump pulse, while the transmitted beam is used as the probe pulse. The probe beam is additionally chirped by repeated passage through an assembly of dispersion blocks made up of SF6 material. A total of twenty-four (24) passes was realized in the 52 mm long blocks and the probe pulse finally broadens to 5.2 ps due to material-dispersion.

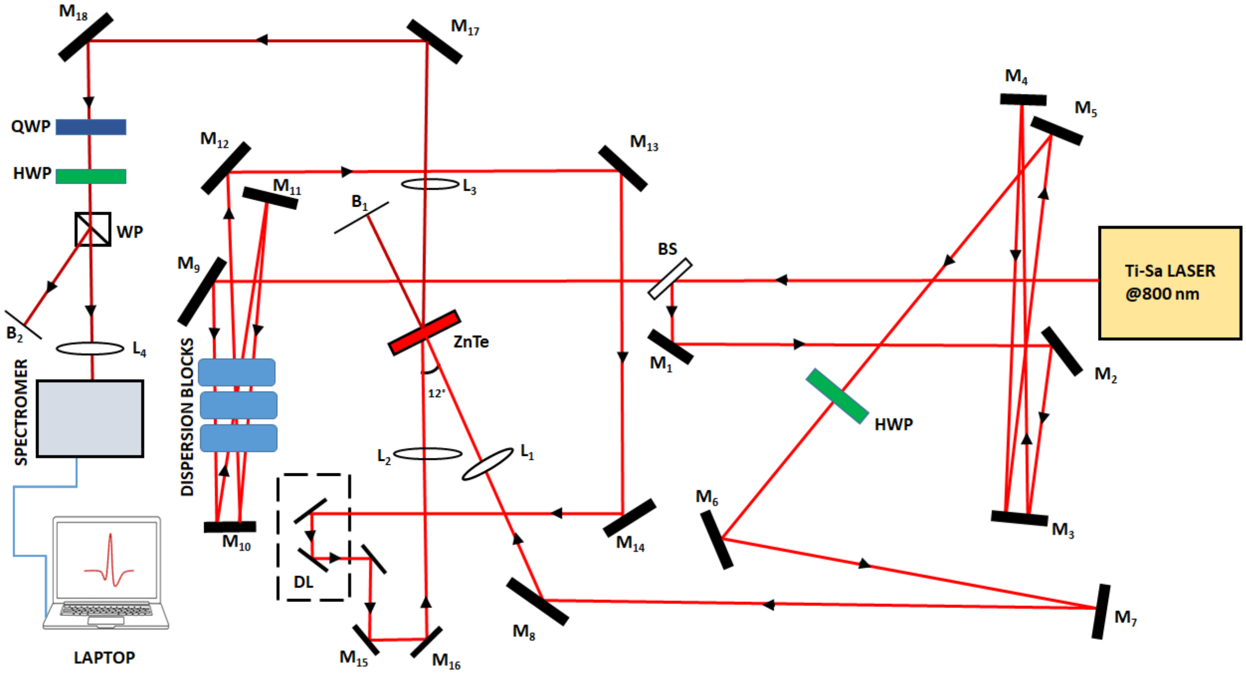

Fig. 4.15 Single layout configuration for the generation and detection of THz pulse, in which the pre-chirped pump and chirped probe beam crosses the ZnTe crystal at an angle of 12°. The pump being spatially broader overlaps with the probe by appropriately adjusting the translational delay stage. The beam path of these pulses and the THz modulated-probe beam are indicated in red and brown color respectively. For the sake of simplicity, the FROG characterization unit is not included. Mirrors; $M_1 - M_{18}$, Lens: $L_1 - L_4$, Half Wave Plate; HWP, Quarter Wave Plate; QWP. Beam splitter; BS, Delay line; DL, Wollaston prism; WS.

The pre-chirped 3.6 ps pump beam is focused on the 0.6 mm thick (110) ZnTe crystal with few tens of μJ. Due to the inherent complexity to simultaneously optimize the crystal angle for efficient emission and detection in the single layout configuration, there is certainly an unarguably tradeoff between these two phenomena. To this regard, an optimum angle of 26° (relative to the (001) axis) has been proposed and explored **[32]**. In this present work, the crystal angle is adjusted to maximize the detected THz signal, in that the 5.2 ps horizontally polarized chirped probe overlaps temporally and spatially with the vertically polarized pre-chirped pump beam on the crystal at a crossing angle of ~12°. The two beams were focused independently on the crystal, with the inclusion of a manual delay stage in the arm of the chirped probe. The diameter of the pump and probe beam at the crystal position were 570 µm and 125 µm respectively. It is straight forward to see that the beam size of the THz pulse given by $r_{THz} = r_p/\sqrt{2}$, is larger than the probe size, where r_p denotes the pump size. Thus, I have assumed that the THz pulse has a constant intensity profile around the probe, as such E_{THz} is spatially independent in the simulation.

In this single crystal configuration, the THz pulse is generated in a first part of the crystal by the incident pre-chirped pump beam, then it induces a phase change on the incoming chirped probe beam. The overlap length between the THz pulse and the probe depends on the crossing angle and crossing point. This probe-THz beam is collimated by lens L_3, and subsequently circularly polarized by a QWP of which the vertical and horizontal polarized components exit the polarizer with a slight deviation from each other. The HWP located between the QWP and polarizer switches between the beam paths of the polarization components. Since a gating-based optical spectrometer is sensitive to polarization, then with the aid of the HWP, the appropriate polarization component can be injected into the spectrometer. In this work, the p polarization was injected into the spectrometer.

The choice of the optical spectrometer is such that, its spectral resolution is effectively high in order to effectually resolve the frequency components of the measured signal. The recovery of the THz waveform occurs in two steps. (1) First the probe spectrum is recorded in the absence of the pre-chirped pump pulse. (2) Then the probe spectrum is measured with the THz (i.e in the presence of the chirped pump pulse. (3) Finally, the ratio of the difference between these signals to the chirped pulse spectrum is calculated. This ratio is proportional to the electric field of the THz pulse, since it has been established that the EO retrieved THz in equation (3-44) is identical to the measured electric waveform of the THz spectrum in equation (2-16). Prior to performing the THz field retrieval, the chirped probe is characterized once at the beginning of the experiment by a FROG device. This is important to determine the spectral phase $\phi(\omega)$ of the probe, from which the frequency-time calibration is obtained. Since each temporal slice of the THz field is projected onto different frequency components in the chirped probe, the THz field can be reconstructed from the direct mapping of frequency to time.

4.3.2 Results and discussion (using the single layout configuration)

There are two posssibilities to calibrate the time-frequency distribution in order to retrieve the duration of the THz signal. This involves analyzing the FROG measurement of the chirped probe or by displacing the relative position of the THz pulse with respect to the chirped probe. The latter is a simple technique, and involves translating the manual delay stage in order to observe a shift in the position of the ridge-like pattern seen on top of the chirped probe being due to the presence of the THz signal. However, the high order terms of the spectral term cannot be effectively estimated leading to a loss of accuracy. Instead, the former was adopted to calibrate the THz signal.

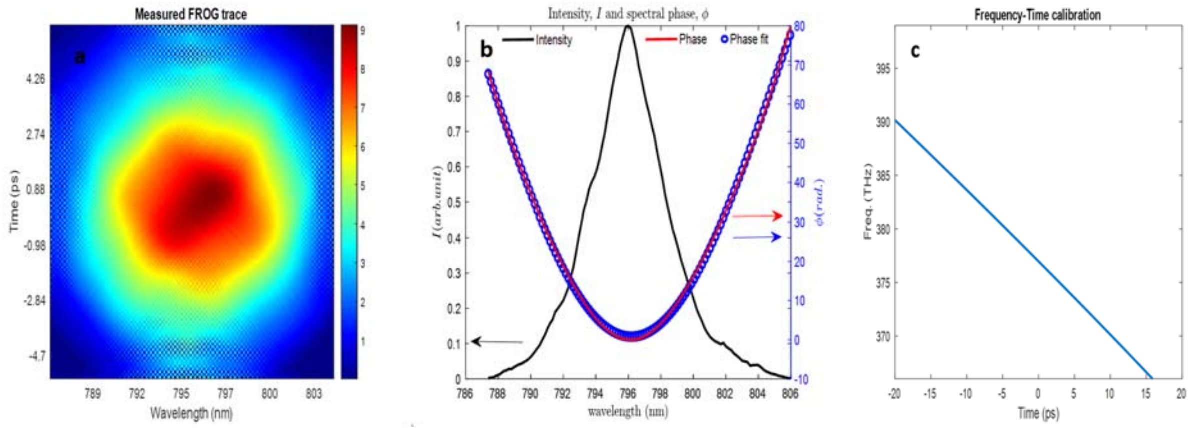

Fig. 4.16 FROG trace of the 800 nm chirped probe pulse, spectral phase fit $\phi(\omega)$, spectrum and group delay derivation T_g. (a) the spectrogram of the retrieved FROG trace has well defined regions. (b) The data from the retrieved FROG trace phase (red lines), is used to create the third order polynomial phase fit (blue circles). The bandwidth of the chirped probe spectrum (black line) is wide enough to accommodate THz signal. (c) The frequency to time calibration is extracted from the first order derivative of the phase fit in which the cubic term in T_g, is ignored.

This involved characterizing the chirped probe by using a FROG technique to determine its spectral phase. In this technique, a replica of the chirped pulse is produced and subsequently delayed with the use of an interferometer. The replica is then used to gate the main pulse in an Second Harmonic Generation (SHG) nonlinear crystal. So, a second harmonic of the chirped pulse is created whose spectrogram is as follows **[42]**,

$$I_{FROG}^{SHG}(\omega,\tau) = \left| \int_{-\infty}^{\infty} E_d(t)\, E_d(t-\tau)\, exp(-i\omega t)\, dt \right|^2 \qquad (4\text{-}1)$$

Where $E_d(t)$ refers to the main chirped pulse, $E_d(t-\tau)$ refers to the replica of the chirped pulse and $I_{FROG}^{SHG}(\omega,\tau)$ refers to the spectrogram of the SHG signal. The information about the spectrogram is sufficent to essentially characterize the chirped probe (only that the sign of its spectral phase can not be determined, which of course is not of interest in this work). The information about its spectral phase is then used to associate each of its frequency component to a time scale. During the THz-chirped probe interaction, the THz signal overlaps on the chirped probe, so that by mapping out the frequency region on which the THz signal lies, the corresponding time scale for the THz signal was constructed. The retrieved spectrogram of the chirped probe pulse as measured by the FROG device is shown in Fig. 4.16a. A *3rd* order polynomial curve fit (red line) was performed for the spectral phase of the chirped probe (blue circles) as shown in Fig. 4.16b. The group delay expression T_g, is then constructed from the coefficients of the fitted spectral phase.

$$T_g = \tau = \frac{\partial \phi(\omega,\tau)}{\partial \Delta\omega} \tag{4-2}$$

Where,

$$\phi(\omega,\tau) = \sum_{i=0}^{3} \phi_i \Delta\omega^i$$

As such, a cubic fit was obtained in which there is an observed linearity behaviour within the spectral bandwidth of the chirped probe as shown in Fig. 4.16c. It was observed that, it was possible to retrieve the THz signal by analyzing only one out of the two polarization beams from the polarizer. Hence, an unbalanced detection was utilized to reconstruct the spectrally encoded THz signal. The optical spectrometer records the chirped probe signal in two sequences. The first measurement is taken in the absence of the pre-chirped pump to give rise to the unmodulated probe signal. This unmodulated probe which serves as the reference signal is subtracted from the measurement taken afterwards in the presence of the pre-chirped pump. The result of this substraction is proportional to the product of the THz signal and the reference beam. To extract only the THz signal shown in Fig. 4.17b, I normalized accordingly. In a way to verify the reproducibility of the spectrometer signals, several shots were recorded and a resemblance was observed among the shots from which the average signals of these shots are shown in Fig. 4.17a. As can be seen, the intensity of the chirped probe spectrum increased due to the overlapping THz signal that was emitted by the presence of the pre-chirped pump.

In the data analysis, only the *s* polarization of both the modulated probe and unmodulated probe were analyzed and presented. The measured THz pulse has a FWHM duration of 6.5 ps and exhibits few cycles of oscillations. The corresponding spectrum is centered at 100 GHz with a width of 100 GHz. The narrow bandwidth is due to the long pulse duration of the pump. This THz pulse is generated with significant contribution of the backward THz component.

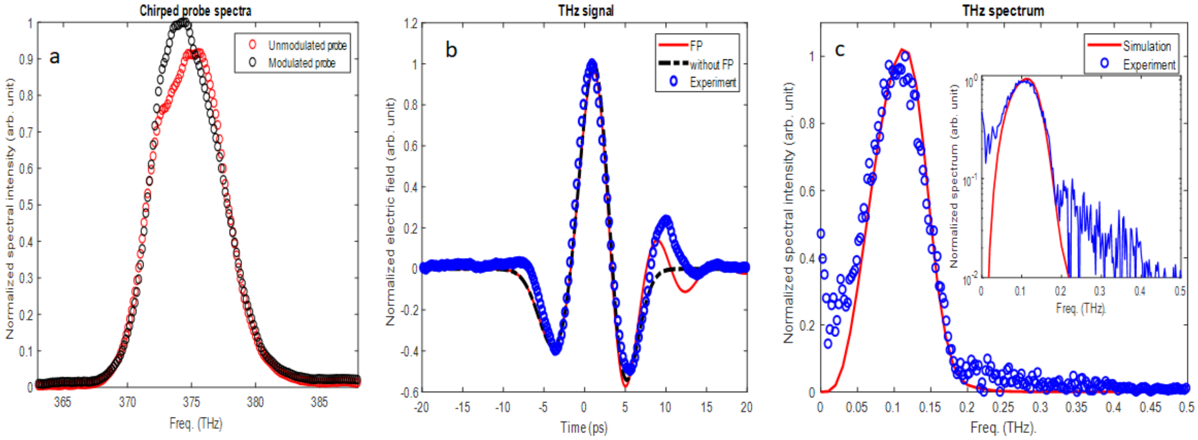

Fig. 4.17 (a) Signal of the modulated and unmodulated chirped probe spectra recorded by the spectrometer in the presence and absence of the pump beam respectively. The consistency in the

spectra profile was confirmed by recording one hundred shots of each spectrum. The presence of the THz on top of the chirped probe tends to skew up the tip of the chirped probe. (b) The duration of the retrieved THz pulse is about 6.5 ps FWHM. The form of its shape is impacted by certain contributions. At the tail end of the field, there exists an amplitude difference between the experimental data (red circles) and simulation (blue line) been due to Fabry Pérot which that gave rise to faster oscillations (c) The corresponding low frequency narrow bandwidth spectrum is centered at 0.1 THz. The inset corresponds to the spectrum plotted in the log-scale.

The comparison between the experimentally retrieved and the simulated THz pulse do not fit well. This dissimilarity which is essentially due to Fabry-Pérot effect can be observed in both Fig. 4.17b and inlet of Fig. 4.17c. The Fabry-Pérot effect in this case is due to the reflection of the THz pulse at the boundary of the crystal. In fact, the effect of multiple reflection cannot be neglected since the round-trip time of the THz pulse within the crystal is shorter than its pulse duration. By considering the bouncing of the THz pulse between the opposite faces of the crystal, a transfer function for the Fabry-Pérot effect is defined as per **[43]**,

$$T_{FP} = \frac{1}{1 - r^2 exp\left(\frac{2in_{thz}\omega_{thz}}{c}L\right)} \tag{4-3}$$

Where, $r = (n_{thz} - 1)/(n_{thz} + 1)$, corresponds to the amplitude of the reflected THz pulse, and L represents the effective length of the crystal for THz generation, n_{thz} refers to the TH refractive index, c refers to the speed of light and ω_{thz} refers to the THz frequency. As the THz pulse bounces off from the crystal-air interface with successively decreasing amplitude, it encounters the chirped probe in the last part of the crystal length. The THz pulse that have been generated in the first-part of the crystal length and modified by the Fabry-Pérot effect, becomes coalesced on to the chirped probe. Though, the duration of the chirped pulse is not long enough to reveal the entire oscillation length of the Fabry-Pérot effect, yet the calculated magnitude of the maximum reflected pulse is around 25 percent which agrees with our experimental plot.

Generally, there is an observed uncertainty around 5-20 % percent between the one hundred measured signal. The comparison between the root mean squared (rms) error and the 100 signal shots indicates two maxima values around the edges and central position of the signal (see Fig. 4.18). Generally, this fluctuation is mostly due to the laser fluctuation. On the other hand, this can be traced to the pulse duration of the chirped pulse.

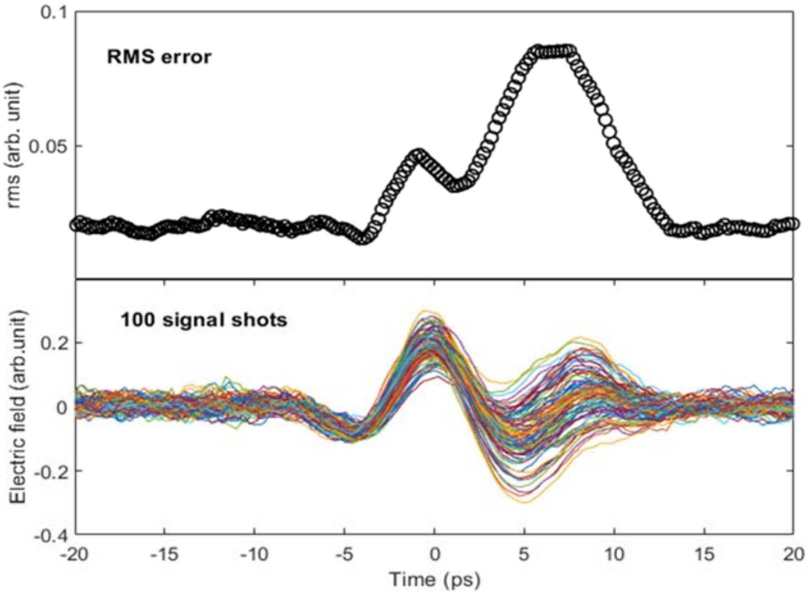

Fig. 4.18 Estimation of the experimental uncertainty. In a bid to verify the consistency in the form of the retrieved THz signal, one hundred shots of these signals were recorded in a total time of 8 *s*. The corresponding root rms (that represents the deviation of the average signal from each signal) has low uncertainty values except at regions corresponding to the right edges and central area of the chirped probe.

A comparison between the chirped probe (red line) and THz pulse (black line) is shown in Fig. 4.19. Since both pulses are temporally overlaped, it can easily be observed that part of the fast oscillations in the THz pulse protrudes out of the edges of the chirped probe. Thus, the high rms value at the right side edges of the THz causes the chirped probe to fluctuate rapidly at their edges. As such the probe's chirp rate may have been insufficient to provide a wide temporal window leading to inaccuracies in regions farther from its FWHM.

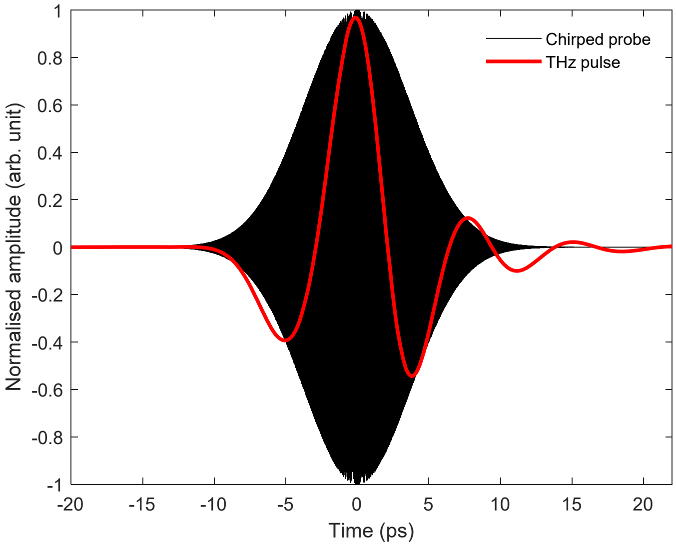

Fig. 4.19 Simulation of the pulse duration of the chirped probe and THz pulse. The THz and chirped probe nearly overlap at the zero delay thanks to their similar refractive index value which ensures that they propagate with more or less equal speed. However, the limited temporal window made some part of the THz pulse extends out of the probe's spectral.

It is most likely that an increase in the intensity of the pump pulse will increase the THz signal strength and highten the effect of TPA on the chirped probe, which in turn will decrease the amplitude of the measured THz pulse, however this was contrary to our observation in that the THz signal increased in magnitude (see Fig. 4.20). As such, there is a reported negligible TPA effect that co-exist with the retrieved signal. Since the effect of TPA is negligible on the chirped probe, the huge number of photons in the pre-chirped pump freely participates in the Difference Frequency Generation (DFG) process thus facilitating the optical-THz conversion efficiency. In this work, the Kerr signal could not be isolated contrary to the case of other works, where a temporally short pump pulse was used for pumping, and in which the Kerr signal was situated around the overlap position between the probe and pump pulse, and lags the generated THz signal, making it possible to identify and isolate the Kerr signal to certain extent **[27, 29]**. I remark that, since the presence of THz Kerr-like effect induced by the generated THz signal is less dominant in (110) ZnTe crystal as observed by *He et. al.,* **[28]**. Coupled with the fact that our experiment and theory are in good agreement with no significant deviation that warrants the skepticism about the presence of other effects, I believe that such cascaded nonlinear effects and Kerr effect are minimally present. The corresponding narrow bandwith THz spectral in Fig. 4.17c has a peak frequency at around 0.1 THz, and a cut-off at 0.2 THz. The high frequency features in the spectrum correspond to the oscillatory part of the THz time domain signal. In the overall, the simulation and experimental data are in close agreement with only minor differences because the chirped probe is not long enough to properly retrieve the edges of the THz signal.

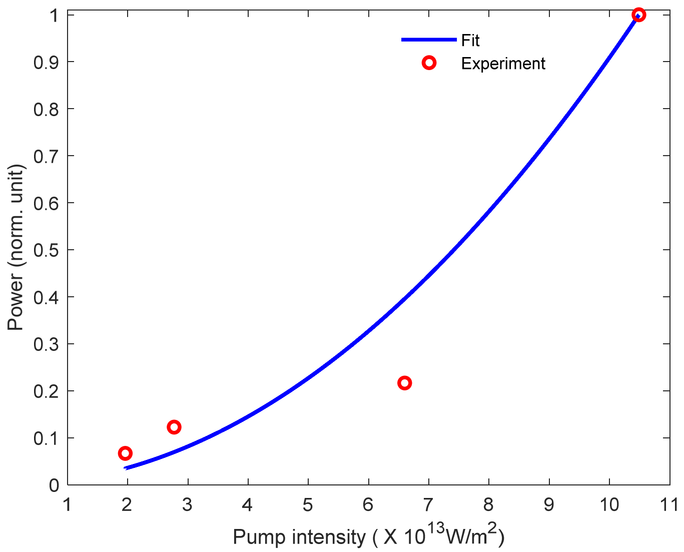

Fig. 4.20 Influence of the pump pulse intensity on the THz signal power. The power law of the THz signal is a quadratic polynomial in terms of the pump intensity. Though the experimental data points (red circles) are few due to certain constraints, they tend follow the theoretical prediction (blue line).

The relationship between the pre-chirped pump intensity and THz power is as shown in Fig. 4.20. The fit (blue line) is a quadratic plot that follows the experimental data (red circles). I noted that due to certain technical difficulties that arose in the laser source only few data points could only be accurately illustrated.

4.3.3 Conclusion on the single crystal configuration

I have investigated the response of ZnTe crystal in the presence of a pre-chirped pump pulse. The results indicate the feasibility of both generating and detecting few picosecond THz pulse in the same crystal. The THz pulse was characterized via the single shot EO scheme with an accompanied high resolution. The experimental data conformed well to the predictions of optical rectification theory and Fabry Pérot effect with a negligible contribution of nonlinear effects such as TPA, Kerr, and Kerr-like effects. The polarization components of the THz-probe modulated beam were independently recovered, thanks to the simplicity and flexibility of the set-up. Although, I have generated narrow band THz spectrum at low frequency (without focusing on the tunability of their spectrum), their frequencies can be tuned by adjusting the pump chirp rate via the separation distance between the gratings in the laser source. The choice between the selection of the bandwidth and chirp rate of the chirped probe used in this detection scheme is a compromise between the temporal window and resolution of our measurement.

This scheme may be harnessed for practical application in various ways as follow; Firstly, the results of our findings further supports the possibility of realizing photonic THz integrated systems **[44]** with the use of ZnTe crystals. Usually, the set-up for THz sources and detection been huge and complex do not facilitate their affordability and mobility for outdoor applications. So, there is often times a need for an integrated system that combines the generation and detection in a miniature device. The quest for such compact THz spectroscopy system has previously been realized by the use of THz integrated systems. Secondly, our findings can also find favorably application in condensed matter physics, since with the use of tunable narrow band THz spectrum, the excitation of selective phonon modes has been achieved previously **[41]**. Lastly, since the conventional single shot detection scheme have previously been used to monitor molecular dynamics occurring on a fast time scale such as laser induced material damage, chemical reactions, and phase transformations **[45],** then our experimental set-up may be adapted to serve as a time resolved spectroscopy set-up if certain modifications in the pump pulse path is considered.

4.4 Bibliography of chapter 4

[1] Nahata A.; Weling A.S.; Heinz T. F. A wideband coherent terahertz spectroscopy system using optical rectification and electro-optic sampling. Appl. Phys. Lett, 1996, 69, 2321–0. doi:10.1063/1.117511

[2] Löffler T.; Hahn T.; Thomson M.; Jacob F.; Roskos H. G.. Large-area electro-optic ZnTe terahertz emitters. Optics express, 2005, 13, 5353–0. doi:10.1364/OPEX.13.005353

[3] Blanchard F.; Razzari L.; Bandulet H.C.; Sharma G.; Morandotti R.; Kieffer J. C.; Ozaki T.; Reid M.; Tiedje H. F.; Haugen H. K.. Generation of 1.5 µJ single-cycle terahertz pulses by optical rectification from a large aperture ZnTe crystal. Optics express, 2007, 15, 13212–0. doi:10.1364/OE.15.013212

[4] Hoffmann M. C.; Yeh K.L.; Hebelin J.; Nelson K. A. Efficient terahertz generation by optical rectification at 1035 nm. Optics express, 2007, 15, 11706–0. doi:10.1364/OE.15.011706

[5] Nagai M.; Matsubara E.; Ashida M.; Takayanagi J.; Ohtake H. Generation and detection of THz pulses with a bandwidth extending beyond 4 THz using a subpicosecond Yb-doped fiber laser system. IEEE Transactions on Terahertz Science and Technology 2014, 4, 440–446. doi:10.1109/TTHZ.2014.2327377

[6] Ropagnol X.; Matoba M.; Nkeck J. E.; Blanchard F.; Isgandarov E.; Yumoto J.; Ozaki T. Efficient terahertz generation and detection in cadmium telluride using ultrafast ytterbium laser. Applied Physics Letters, 2020, 117, 181101–. doi:10.1063/5.0024112

[7] Chang G.; Divin C.J.; Liu C.H.; Williamson S. L.; Galvanauskas A.; Norris T.B. Generation of radially polarized terahertz pulses via velocity-mismatched optical rectification. Optics letter 2007, 32, 433–0. doi:10.1364/OL.32.000433

[8] Bechtel J. H.; Smith W. L. Two-photon absorption in semiconductors with picosecond laser pulses. Physical Review B, 1976, 13, 3515–3522. doi:10.1103/physrevb.13.3515

[9] Zhao Z.; Hameau S.; Voos M.; Tignon J. THz generation by optical rectification and competition with other nonlinear processes. International Symposium on Space-Terahertz Technology, 2006, Paris, France. hal- 00109941. https://hal.science/hal-00109941/document

[10] Volodymyr G.; Maxim M. N.; Dmitrii A. S.; Yevgenii V S.; Svetlana A S.; Shkurinov A.P.; Aleksandr V S. Competition between linear and nonlinear processes during generation of pulsed terahertz radiation in a ZnTe crystal. Quantum Electronics 2005, 35, 407. doi:10.1070/QE2005v035n05ABEH002805

[11] He W.Q.; Gu C.M.; Shen W.Z. Direct evidence of Kerr-like nonlinearity by femtosecond Z-scan technique. Optics Express 2006, 14, 5476–0. doi:10.1364/OE.14.005476

[12] Zhai D.; Hérault E.; Garet F.; Coutaz J. Terahertz generation from ZnTe optically pumped above and below the bandgap. Opt. Express, 2021, 29, 17491-17498. https://doi.org/10.1364/OE.421282

[13] Said A. A.; Sheik B.M.; Hagan D. J.; Wei T. H.; Wang J.; Young J.; Stryland E. W. V. Determination of bound-electronic and free-carrier nonlinearities in ZnSe, GaAs, CdTe, and ZnTe. J. Opt. Soc. Am. B 1992, 9, 405–0. doi:10.1364/JOSAB.9.000405

[14] Guiramand L.; Ropagnol X.; Blanchard F. Time-frequency analysis of two-photon absorption effect during optical rectification in a ZnTe crystal pumped at 1.024 µm. Opt. Lett. 2021, 46, 6047-6050. https://doi.org/10.1364/OL.441231

[15] Qirong X.;Liying L.; Zhen T.; Ning Z.; Shuxin L.; Kai W.; Lu C.; Qingyue W. The effect of two-photon absorption and optical excitation area on the generation of THz radiation. , Optics Communications, 2006, 267, 422–426. doi:10.1016/j.optcom.2006.06.051

[16] Shalaby M.; Vicario C.; Thirupugalmani K.; Brahadeeswaran S.; Hauri C. P. Intense THz source based on BNA organic crystal pumped at Ti:sapphire wavelength. Optics Letters 2016, 41, 1777–. doi:10.1364/OL.41.001777

[17] Zhao H.; Tan Y.; Wu T.; Steinfeld G.; Zhang Y.; Zhang C.; Zhang L.; Shalaby M. Efficient broadband terahertz generation from organic crystal BNA using near infrared pump. Applied Physics Letters, 2019, 114, 241101. doi:10.1063/1.5098855

[18] Roeder F.; Shalaby M.; Beleites B.; Ronneberger F.; Gopal A. THz generation by optical rectification of intense near-infrared pulses in organic crystal BNA. Opt. Express 2020, 28, 36274-36285.https://doi.org/10.1364/OE.404690

[19] Elchin Isgandarov. Development of ytterbium laser based THz sources and systematic study of THz radiation enhancement of PCA on nanodecorated surfaces, PhD thesis, 2023

[20] Tangen I.; Valdivia-Berroeta G.; Heki L.; Zaccardi Z.; Jackson E.; Bahr C. Sin-Hang H.; Michaelis D.; Johnson J. Comprehensive characterization of terahertz generation with the organic crystal BNA. J. Opt. Soc. Am. B 2021, 38, 2780-2785. https://doi.org/10.1364/JOSAB.420597

[21] Zaccardi Z.; Tangen I.; Valdivia-Berroeta G.; Bahr C.; Kenney K.; Rader C.; Lutz M.; Hunter B.; Michaelis D.; Johnson J. Enabling high-power, broadband THz generation with 800-nm pump wavelength. Opt. Express 2021, 29, 38084-38094. https://doi.org/10.1364/OE.437421

[22] Gollner G.; Lee H.;Jiaqi X.; Weber C.; Sollinger E.; Stummer V.; Baltuska A.; Zhang Y. Efficient Broadband Terahertz Generation in BNA Organic Crystals at Ytterbium Laser Wavelength . 2020, 45th International Conference on Infrared, Millimeter, and Terahertz Waves (IRMMW-THz). doi:10.1109/irmmw-thz46771.2020.9370510

[23] Mansourzadeh S.; Vogel T.; Shalaby M.; Wulf F.; Saraceno C. Milliwatt average power, MHz-repetition rate, broadband THz generation in organic crystal BNA with diamond substrate. Opt. Express 2021, 29, 38946-38957. https://doi.org/10.1364/OE.435344

[24] Samira M.; Tim V.; Alan O.; Mostafa S.; Mirko C.; Clara J. S. Broadband, high power THz source at 540 kHz using organic crystal BNA. APL Photonics 2023, 8, 011301 https://doi.org/10.1063/5.0126367.

[25] Ku S. A.; Tu C. M.; Chu W. C.; Luo C. W.; Wu K. H.; Yabushita A.; Chi C. C.; Kobayashi T. Saturation of the free carrier absorption in ZnTe crystals. Opt. Express 2013, 21, 13930-13937.

[26] Vidal S.; Degert, J.; Tondusson M.; Oberlé J.; Freysz E. Impact of dispersion, free carriers, and two-photon absorption on the generation of intense terahertz pulses in ZnTe crystals. Appl. Phys. Lett. 2011, 98, 191103. https://doi.org/10.1063/1.3588411

[27] Caumes J. P.; Videau L.; Rouyer C.; Freysz E. Kerr-like nonlinearity induced via terahertz generation and the electrooptical effect in zinc blende crystals. Phys. Rev. Lett. 2002, 89. doi: 10.1103/PhysRevLett.89.04 7401.

[28] Wei-Qiang H.; Chun-Ming G.; Wen-Zhong S. Direct evidence of Kerr-like nonlinearity by femtosecond Z-scan technique. Opt. Express 2006, 14, 5476-5483

[29] Dong L.; Guohong M. Pump-wavelength dependence of terahertz radiation via optical rectification in (110)-oriented ZnTe crystal. Journal of Applied Physics. 2008, 103, 123101. https://doi.org/10.1063/1.2938847

[30] Zhen T.; Changlei W.; Qirong X.; Jianqiang G.; Yanfeng L.; Mingxia H.; Lu C.; Qingyue W. Quantitative analysis of Kerr nonlinearity and Kerr-like nonlinearity induced via terahertz generation in ZnTe. Appl. Phys. Lett. 2008, 92, 041106. https://doi.org/10.1063/1.2838446

[31] Xiaoshu C.; Shan H.; Zhen S.; Fu L. Z.; Xu K.Y.; Gang W.; Reng W.; Ning, D. Influence of nonlinear effects in ZnTe on generation and detection of terahertz waves. Journal of Applied Physics. 2009, 105, 023106. https://doi.org/10.1063/1.3068480

[32] Niessen K. A.; Xu M.; Markelz A.G. Terahertz optical measurements of correlated motions with possible allosteric function. Biophysical reviews (2015), 7, 201–216. doi: 10.1117/12.2519878

[33] Chen Q.; Zhiping J.; Tani M.; Zhang X.-C. ‘Electrooptic terahertz transceiver. Electron. Lett. 2000, 1298–1299. https.//10.1049/el:20000945

[34] Tie-Jun W.; Yanping C.; Claude M.; Francis T.; Marc C.; Jacques D.; See L. C. High energy terahertz emission from two-color laser-induced filamentation in air with pump pulse duration control. Appl. Phys. Lett. 2009, 95, 131108. https://doi.org/10.1063/1.3242024

[35] Erschens D. N.; Turchinovich D.; Jepsen P. U. Optimized Optical Rectification and Electro-optic Sampling in ZnTe Crystals with Chirped Femtosecond Laser Pulses. J. Infrared Milli. Terahz Waves, 2011, 32, 1371–1381. https://doi.org/10.1007/s10762-011-9829-y

[36] Vidal S.; Degert J.; Tondusson M.; Freysz E.; Oberlé J. Optimized terahertz generation via optical rectification in ZnTe crystals. J. Opt. Soc. Am. B. 2014, 31, 149-153.

[37] József A. F.; László, P.; Matthias C. H.; János H. Towards generation of mJ-level ultrashort THz pulses by optical rectification. Opt. Express. 2011, 19, 15090-15097.

[38] Weling A. S.; Auston D. H. Novel sources and detectors for coherent tunable narrow-band terahertz radiation in free space. J. Opt. Soc. Am. B 1996, 13, 2783–2791

[39] Silaev A. A.; Romanov A. A.; Vvedenskii N. V. Generation of tunable mid- and far-infrared pulses during gas ionization by a chirped two-color laser field. Opt. Lett. 2020, 45, 4527-4530.

[40] Chefonov O. V.; Ovchinnikov A. V.; Hauri C. P.; Agranat M. B. Broadband and narrowband laser-based terahertz source and its application for resonant and non-resonant excitation of antiferromagnetic modes in NiO. Opt. Express 2019, 27, 27273-27281.

[41] Vicario C.; Trisorio A.; Allenspach S.; Rüegg C.; Giorgianni F. Narrow-band and tunable intense terahertz pulses for mode-selective coherent phonon excitation. Appl. Phys. Lett. 2020, 117. https://doi.org/10.1063/5.0015612

[42] Rick T.; Delong K. W.; David N.; John S.; Marco K. Measuring ultrashort laser pulses in the time-frequency domain using frequency-resolved optical gating. Review of Scientific Instruments, 1997, 68, 3277-3295. DOI:10.1063/1.1148286

[43] Faure J.; Van T. J.; Kaind R.A.; Leemans W.P. Modelling Laser-Based Table-Top THz Sources: Optical Rectification, Propagation and Electro-Optic Sampling. Optical and Quantum Electronics. 2004, 36, 681–697. https://doi.org/10.1023/B:OQEL.0000039617.85129.c2

[44] Dekorsy T. and Auer H. and Waschke C. and Bakker, H. J. and Roskos, H. G. and Kurz, H. and Wagner, V. and Grosse. Emission of Submillimeter Electromagnetic Waves by Coherent Phonons. Phys. Rev. Lett, 1995, 74, 738-741. https://link.aps.org/doi/10.1103/PhysRevLett.74.738

[45] Zhao-Hui Z.; Sen-Cheng Z.; Jun Li.; Li-Guo Z.; Kun M.; Jiang L.; Qiao L.; Qi-Xian P.; Ze-Ren L.; Jian-Heng Z. Time-resolved single-shot terahertz time-domain spectroscopy for ultrafast irreversible processes. Review of Scientific Instruments. 2016, 87, 095101. https://doi.org/10.1063/1.4961494

[46] Ojo M. E.; Fauquet F.; Mounaix P.; Bigourd D. THz Pulse Generation and Detection in a Single Crystal Layout. Photonics, 2023, 10, 1-11. https://doi.org/10.3390/photonics10030316

Chapter 5

Optical Analysis of Oil Shales

Following the generation and detection of THz radiation in the preceding chapter, a concentration on the application perspective will be discussed in this current chapter. This chapter is dedicated to explore the application of THz radiation on some oil shale samples. Oil shales have shown to be very responsive to THz radiation. This is due to the presence of an organic constituent referred to as kerogen. Their response in the presence of THz radiation have previously been studied in relation to their oil yielding capacity. Parameters such as the refractive index and absorption coefficient of the oil shales have previously been examined. In what follows, a brief review on the THz-Time Domain Spectroscopy (THz-TDS) on oil shales shall be examined, and this will be followed by presenting the experimental results obtained from the analysis of Lopkanta oil shales. Subsequently, two other optical measurements namely Scanning Electron Microscope-Electron Dispersive X-ray (SEM-EDX) and Laser Induced Breakdown Spectroscopy (LIBS) shall be performed to supplement the oil shale THz spectroscopy/imaging results.

5.1 THz spectroscopy generality

We consider that a THz pulse travels through an oil shale sample at normal incidence. In order to investigate the effect of the sample on the THz pulse, the THz signal is recorded firstly without the sample, then with the sample. The signal obtained in the former and latter cases are respectively termed reference and sample signals. The waveform of these two signals often indicates obvious differences. The sample signal is both delayed i.e. propagating at a lower speed and reduced in amplitude due to absorption and reflection at interfaces within the sample, as compared to the reference signal. In practice, the signals are represented in the frequency domain in relation to each other as per **[1]**,

$$T(\omega) = \frac{S_{sam}(\omega)}{S_{ref}(\omega)} = |T(\omega)|\, e^{-i\Delta\varphi(\omega)} \qquad (5\text{-}1)$$

where, ω is the THz frequencies, $\Delta\varphi(\omega)$ is the phase difference between the sample and reference signal. $|T(\omega)|$ is the transmission coefficient, and $T(\omega)$ is the complex transmission signal. Afterwards, $T(\omega)$ is analyzed, from which important optical properties of the oil shale (such as refractive index and absorption coefficient) can be deduced. Assuming the THz pulse is incident at an angle away from normal incidence, the complex reflectance signal, $R(\omega)$ instead can be obtained. Using this reflection geometry, *Miao et al.* have observed subsurface images of the

Hudian oil shale, by representing the peak amplitudes of the spectra obtained at different positions from the oil shale on a contrast image plot **[2]**.

The refractive index $n(\omega)$, is obtained by comparing the experimental result, $T(\omega)$ with its theoretical form $T_{theo}(\omega)$ given by **[3]**,

$$T_{theo}(\omega) = \frac{4n}{(n+1)^2} \cdot\ e^{-i(n-1)\frac{\omega d}{c}} .FP \tag{5-2}$$

Where the first term in equation (5-2) is the transmission coefficient which considers the effect of amplitude decreases due to absorption. The second term is responsible for the time delay, and represents the phase acquired by the pulse on its passage through the oil shale whose thickness and refractive index are d and n respectively. The Fabry Pérot (FP) term, accounts for the reflections of the pulse within the oil shale. Similarly, in the reflection mode, the theoretical complex reflectance signal $R_{theo}(\omega)$, is given by

$$R_{theo}(\omega) = \frac{n-1}{n+1} \cdot \left(1 - \ e^{-2i\frac{\omega n d}{c}}\right) \tag{5-3}$$

Solving for $n(\omega)$, involves performing the following operations: $T(\omega) = T_{theo}(\omega)$ or $R(\omega) = R_{theo}(\omega)$.The foregoing equation is an inverse value problem that can be solved analytically by assuming an initial guess solution. The fixed-point iteration, Newton Raphson and Nicolson-Ross-Weir method have been so far used to obtain $n(\omega)$ which has been shown to exhibit good correlation with oil yield of oil shales **[4]**. By considering the results of different literatures, it has been found experimentally that, oil shales with lower $n(\omega)$ usually exhibits a negative correlation with oil yields, i.e. high-oil yielding oil shales have lower $n(\omega)$ and vice versa **[1, 5-6]**. It is worth mentioning that the experimental techniques employed in preparing the samples, have impact on the outcome of the measured $n(\omega)$. *Li et al.* observed that using pulverized over bulk oil shale samples possessed no true correlation with oil yield. Due to the complex heterogeneity of the oil shale, their properties were altered upon mechanical processing **[5]**. Thus; it is usually preferable to work with the bulk samples, in which case the original form is preserved.

Oil shale has shown to possess anisotropy, in which their optical properties differ in different plane. The presence of lamination, i.e. alternating layers with varying organic matter content in the oil shale is a possible reason for anisotropy. As such, during field extraction, it is recommended to cut through the earth crust at specific plane, preferably at the bedding plane of deposition. *Miao et al.* **[6]** investigated the anisotropy of some oil shale in relation to oil yield. In their procedure, they used oil shales cut at a direction parallel to the bedding plane. The refractive index was measured when the incoming THz pulse was incident parallel to the bedding plane of the oil shale, to obtain n_0, then the oil shale is rotated up to 90° to obtain the minimum refractive index, n_{90}. They observed a symmetric behaviour in $n(\omega)$ at every 180°, such that the anisotropy in the refractive index is given by,

$$\Delta n(\omega) = n_0(\omega) - n_{90}(\omega) \qquad (5\text{-}4)$$

A strong positive correlation between $\Delta n(\omega)$ and oil yields from different oil shales was observed. I.e. the higher the refractive index anisotropy, the higher the oil yield and vice versa **[6]**.

The absorption coefficient α (cm^{-1}), which measures the magnitude of absorbed THz pulse, have also been used as an indicator tool to assess the oil yield potential of some oil shales. This quantity is proportional to the imaginary component of the complex refractive index **[3]**,

$$\alpha(cm^{-1}) = \frac{2\omega}{c} Im[n(\omega)] \qquad (5\text{-}5)$$

Typically, α (cm^{-1}) increases with THz frequency and falls between 400-1800 cm^{-1}. A comparison between the absorption plots of different oil shales analysis has indicated that, higher α (cm^{-1}) corresponds to higher oil yield, and vice versa. However, when the refractive index in equation (5-5) is replaced by $\Delta n(\omega)$, the value of the new absorption coefficient $\Delta\alpha$ (cm^{-1}), have been observed to be lower for oil shales with higher oil yields, and vice versa **[6-8]**. In order to reveal detailed information about the bulk samples of the Hudian oil shale, *Yi et al.* **[9]** made several absorption plots at different pyrolysis temperature, to determine the T_{max} for useful oil yields. The T_{max} value corresponded to the maximum recorded temperature just before inconsistency in the absorption plot begins to appear; possibly due to THz absorption by metallic oxides in the pyrolyzed oil shale.

The inorganic constituent of oil shale comprises of minerals and water. Quartz, calcite, dolomite, and pyrite has been identified as been among the principal mineral constituent of oil shales **[10-12]**. During a THz-TDS at room temperature, THz pulse are mainly absorbed by the kerogen content, due to the fact, that kerogen are large macromolecules whose aromatic compounds typically have vibration modes in the THz region around 0.5 - 4 THz. When the THz-TDS is performed with a pyrolyzed oil shale sample, there are generally two major stages in the optical response of the kerogen to the THz pulse. The first stage occurring at lower temperature, involves the evaporation of moisture from the oil shale thereby resulting to an increase in the strength of the transmitted THz signal. The second stage is typically characterized by a decrease in the strength of the THz signal, due to absorption of the pulses at high temperature **[5, 9, 13]**. At such high temperature, the minerals are dissolved in water, then become generally conductive, and subsequently absorbing the THz pulse. The comparison between the first and second stages as well at room temperature signifies that the absorption of THz pulse is an interplay between the water, kerogen and mineral constituent. At high temperature, the kerogen macromolecules decompose into lighter molecules mostly with short chains alkanes, while the minerals are decomposed into metals and metallic oxides. At this stage, the absorption of THz pulse is reversed, and mainly dominated by the metallic components **[5, 14]**. Also, at such high temperatures, oil shale with significant pyrite composition decomposes to elemental Iron (Fe) and Sulphur (S), whose ferromagnetic response to an external magnetic field can also be studied to reveal the nature of the constituent minerals. Unfortunately, this has not been investigated in the oil shale.

Moreover, investigation has been carried out on the transmitted THz signal of an oil shale under increasing temperature up to 1000 °C, and a different trend was observed. The plot of the maximum electric peak E_p, of the THz signal obtained at each pyrolysis temperature made by *Honglei et al.* [**1**], revealed four stages of oil shale decomposition. These four stages are grouped under four different temperature ranges. For the temperature range between 25 − 200 °C, E_p increased and then stabilized around 200 − 300 °C. Following this stabilization, E_p gradually increased from 300 − 500 °C until a maximum is reached, then a sharp decrease between 500 − 600 °C was observed. During the first stage, the initial increase in E_p was due to moisture loss and become stabilized during the second stage after the moisture content was at minimum. During the third stage, the macromolecules of the kerogen were broken down, resulting to an unexpected increase in E_p possibly due to the loss of more moisture. During the fourth stage, THz pulses were absorbed due to the decomposition of the minerals to their respective metallic oxides resulting to decrease in E_p nearly up to the same magnitude at 25°C. In a recent work, *Honglei et.al* investigated the absorptive behavior of oil shales at temperature beyond 600 °C, and observed that, E_p at 1000°C, was much lesser than at 25°C, due to metallic (semi-coke) formation. On the other hand, THz subsurface imaging of oil shales has been achieved via the reflection mode of the THz-TDS [**1**]. The reflected THz amplitude from different regions of the oil shale was employed to reconstruct the non-uniform distribution of organics on the oil shale surface. Three regions corresponding to high kerogen, low kerogen and mineral regions were observed based on the intensity distribution. Their THz contrast image showed good with results obtained from optical micrographs and micro-Raman spectra.

5.2 THz Spectroscopy and Imaging Measurement

In our study on oil shales, the THz pulse used for spectroscopy and imaging were provided by two commercial systems namely, the TPS spectra 3000 and the TPS spectra 4000 both from TeraView. The latter was used in the reflection mode, while the former was used in the transmission mode. The system photograph and the sketch of the set-up in both transmission and reflection geometry are shown in Fig. 5.1 and Fig. 5.2.

The TPS spectra 3000 uses GaAs Photoconductive Antennas (PCA) as both THz emitter and detector. An incoming 80 fs Ti:Sa laser operated at 800 nm with a repetition rate of 76 MHz is first passed through a beam splitter in order to reflect and transmit the beam in different proportions. The transmitted beam (pump beam) is then used to illuminate the PCA emitter, while the reflected beam (probe beam) is sent through a delay line and later injected into the PCA detector. As the THz pulse is emitted, it is collimated and focused at normal incidence onto the sample as shown in Fig. 5.1. Both the emitter, sample and detector are contained in a chamber. Prior to detection, the chamber, is purged with dry air to eliminate water vapor, in order to avoid undesired absorption bands in the spectral window under study.

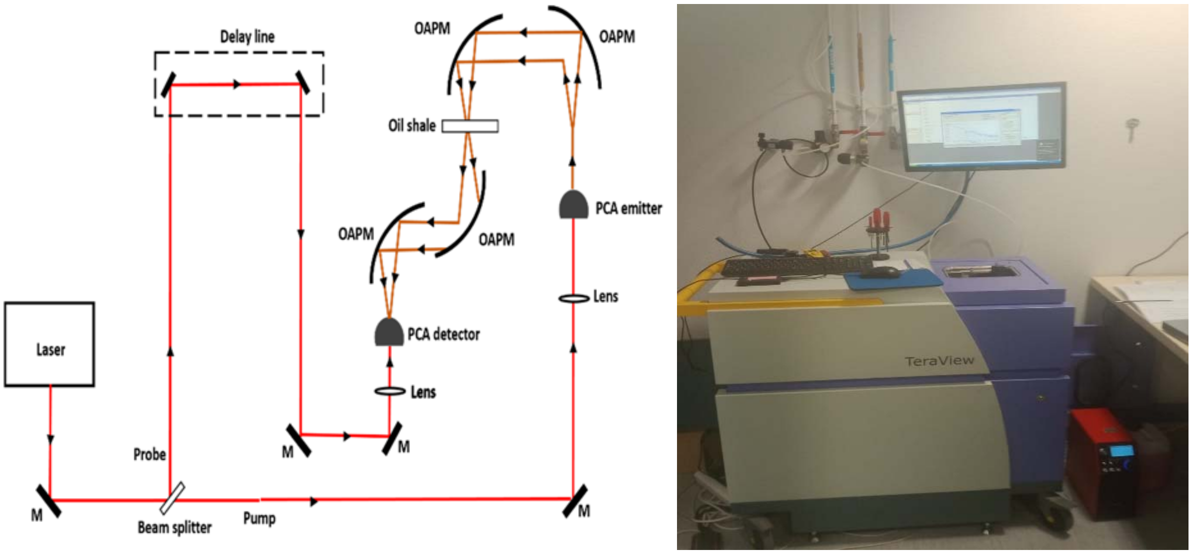

Fig. 5.1 Schematic set-up and photograph of the TPS 3000 Teraview in transmission mode. The emitted THz pulse irradiates the oil shale sample at normal incidence. Off Axis Parabolic Mirror; OAPM, Mirror; M.

An x-y translating stage is positioned in the plane of the sample to allow a raster scanning. The obtained data set is three-dimensional with time as the third axis. The time axis corresponds to the scanning delay provided by the probe beam. So, each point in the x-y plane is associated with a time scale. Thus, the THz electric field of the THz pulse can be reconstructed. Each THz temporal trace is averaged to reduce noise and artifacts thereby stabilizing the signal fluctuation. In order to provide an image of the sample, a fast Fourier transform (FFT) is applied to the temporal trace according to equation (5-2). This TDS system offers a useful frequency range 0.06 – 6 THz with a maximum dynamic range around 85 dB, a spectral resolution of 0.06 THz and a rapid scan mode at the rate of 30 scans/second.

The TPS spectra 4000 is similar to the TPS spectra 3000 except that the sample is not placed in a chamber and that the generated THz pulses are not normally incident on the sample, instead it irradiates the sample at about 30° to the normal as shown in Fig.5.2. The first pair of OAPM collimate and focus the THz pulse onto the sample, while the reflected THz pulse emanating from the sample were re-collimated and re-focused (using another pair of OAPM) onto the PCA detector. A reference signal is obtained by first by irradiating a metal slab, thereafter the oil shale sample is placed on the metal slab. By sweeping the delay line through the entire THz pulse, the time domain THz waveforms were obtained. By keeping the sample position fixed, the THz pulse was raster scanned in the x-y plane to form an image. The reflection mode offered a useful frequency range of 0.06 – 4.5 THz with a maximum dynamic range around 80dB.

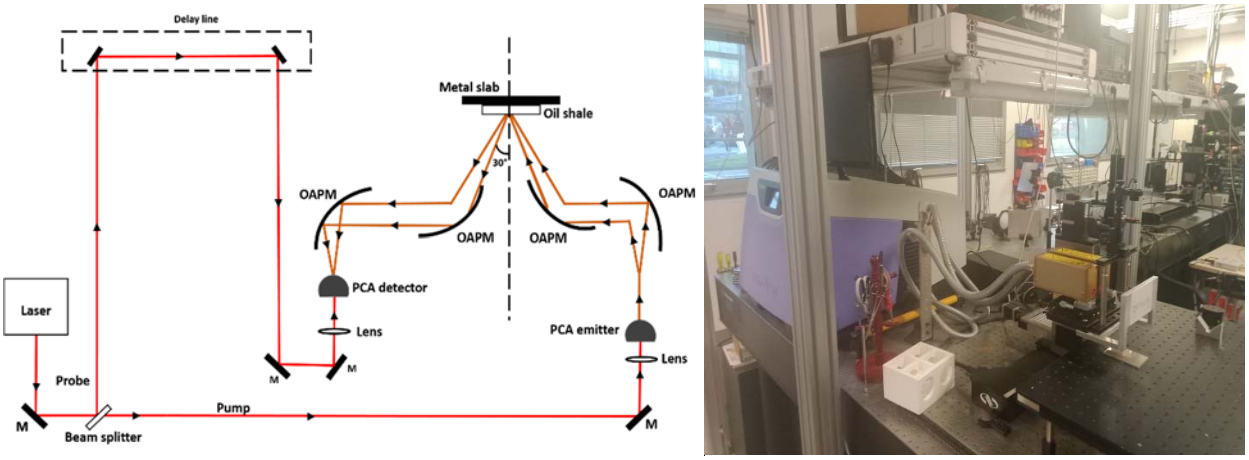

Fig. 5.2 Schematic set-up and photograph of the TPS 4000 Teraview in reflection mode. The emitted THz pulse irradiates the oil shale sample at 30° to the normal axis. Off Axis Parabolic Mirror; OAPM, Mirror; M.

5.2.1 Sample and surface morphology inspection

The oil shales used in this work are referred to as Lokpanta oil shales. With the aid of geological tools (fossil hammers), the oil shales were excavated from several different geological locations in Lokpanta, Nigeria. The oil shale samples were originally large mass in size when they were extracted from the earth. Prior to analysis, thin slices with an average thickness of 2 mm were prepared from the large masses, and thereafter polished in order to maintain plain surfaces on the samples. The photograph of all the different samples prepared are shown in Fig. 5.3. Depending on the location of extraction, the samples are labelled as L3S2, L3S3, L3S4, L5S1, L5S2, L5S3, L7S1 and L9S2.

Fig.5.3 Photographic images of the oil shale samples

In order to examine the surface layer of the samples, an ultra-magnification view of the samples were performed using a numerical microscope whose spatial resolution is 200 µm. It was revealed that the thickness across the sample surfaces varied slightly. For example, the 3D microscope image of L3S4 sample as shown in Fig. 5.4a indicated three levels of layers. The distance between the first and second level is 208 µm, while the distance between the second and third layer is 106 *µm*. The varied thickness is due to the fissile nature of oil shales. And since the oil shales are made up of slates stacked together, then slight pressure applied on the samples may cause depressions on the surface as clearly seen in the colored image in Fig.5.4b

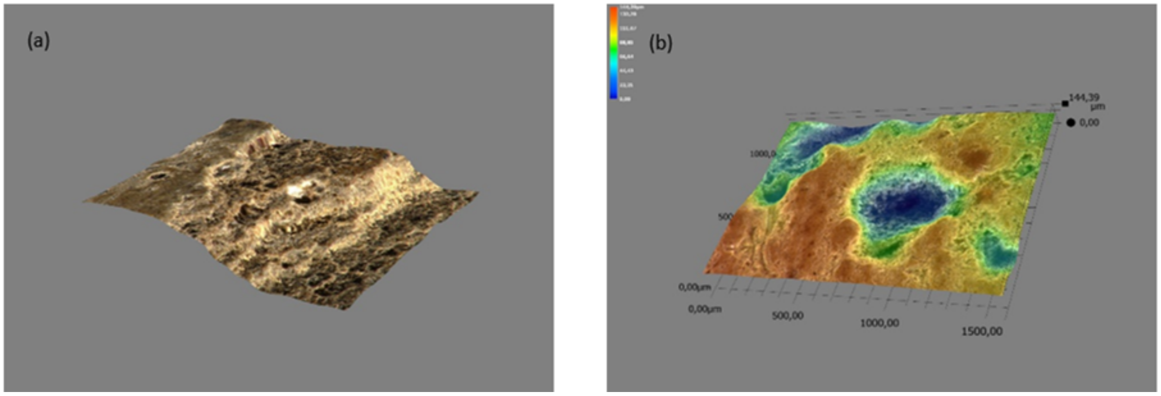

Fig. 5.4 3D view of the L3S4 sample using a numerical microscope.

By zooming in on the second layer, a shallow pattern was observed as shown in Fig. 5.5a. As can be observed, the sample is generally grey-colored with whitish and dark spots. By considering the central position, the grey-whitish-dark color is better resolved in Fig.5.5b. A localized view on the middle of Fig.5.5b was performed in which the result shows a dark hollow region (see Fig. 5.5c). Generally, the surface at difference locations consists of varying shades of grey-whitish dark color. Next, THz spectroscopy is performed at some specific positions in the samples.

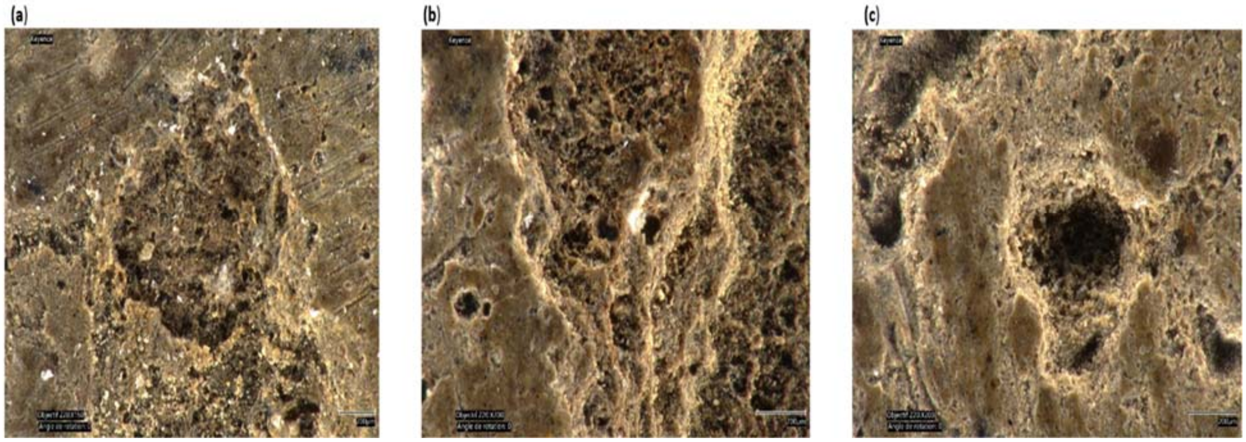

Fig. 5.5 Ultra high magnifcation of the surface view of L3S4 sample.

5.2.2 THz Spectroscopy of Lokpanta Oil Shales

THz spectroscopy was performed by recording the temporal profile and the spectrum was obtained through a Fast Fourier Transform (FFT) to obtain the index of refraction and absorption coefficient in the frequency domain. The transmission measurements were achieved at three to four different points in some selected samples. The transmitted THz signal as well as the retrieved absorption coefficient and refractive index will be discussed for samples L7S1, L5S1, L9S2 and L3S2. In Fig. 5.6, the results of the spectroscopy measurements are shown for L7S1. A significant decrease in the transmitted THz signal (inlet) is observed in Fig.5.6a as compared to the reference signal. Though, the absorption coefficient tends to be similar as seen in Fig.5.6b, the sample variation at the different points was clearly shown by the refractive index in Fig. 5.6c. It varied from 2.1-2.2.

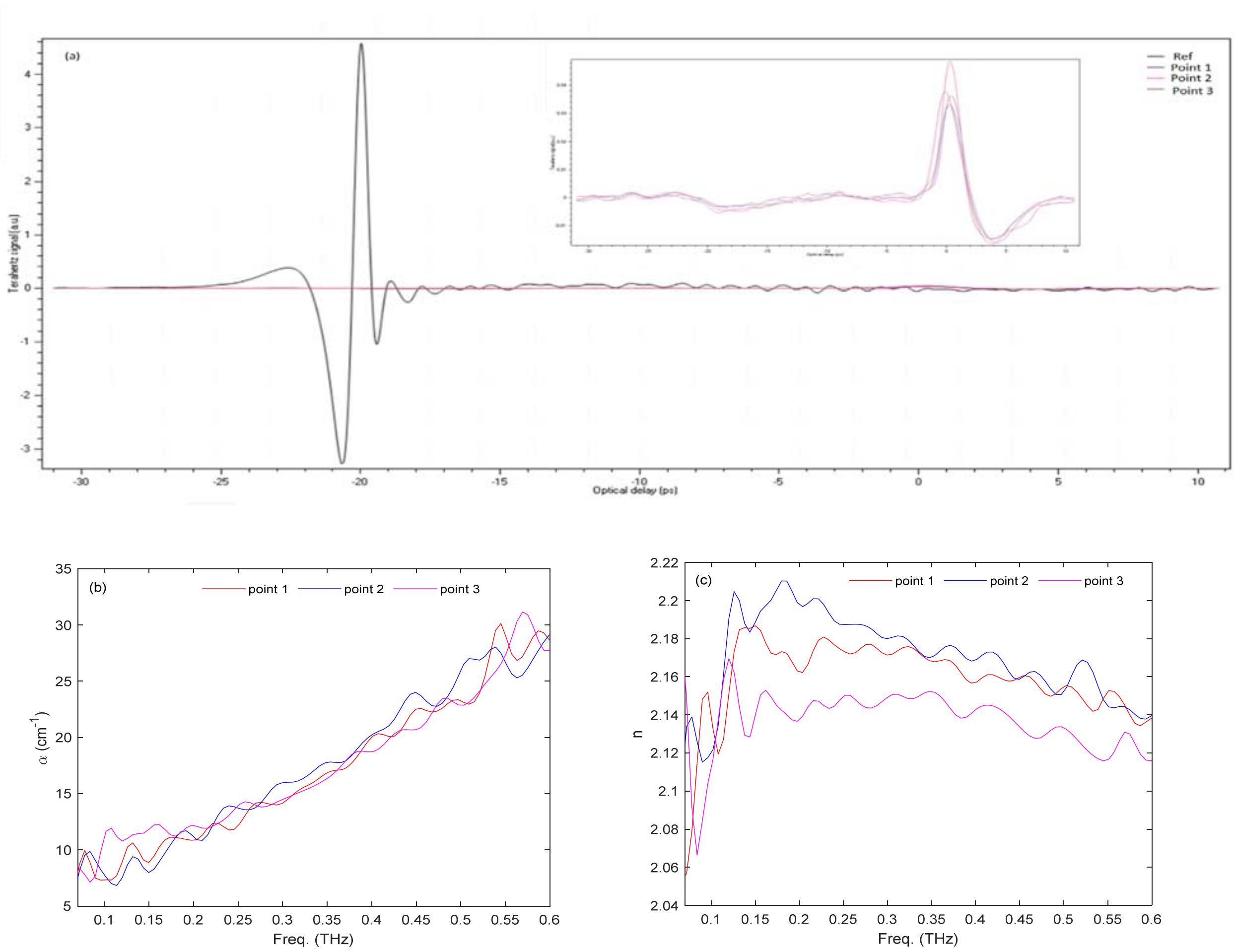

Fig. 5.6 THz spectroscopy of the L7S1 sample showing the (a) time domain signal, (b) absorption coefficient and (c) refractive index. The sample thickness is ~2.98 mm.

Similarly, the spectroscopy measurement with the L5S1 sample shows a decrease in the transmitted THz signal (see Fig. 5.7). In this sample, the absorption coefficient showed variations at different locations. An obvious variation is seen in their refractive index which varied between 2.05- 2.3.

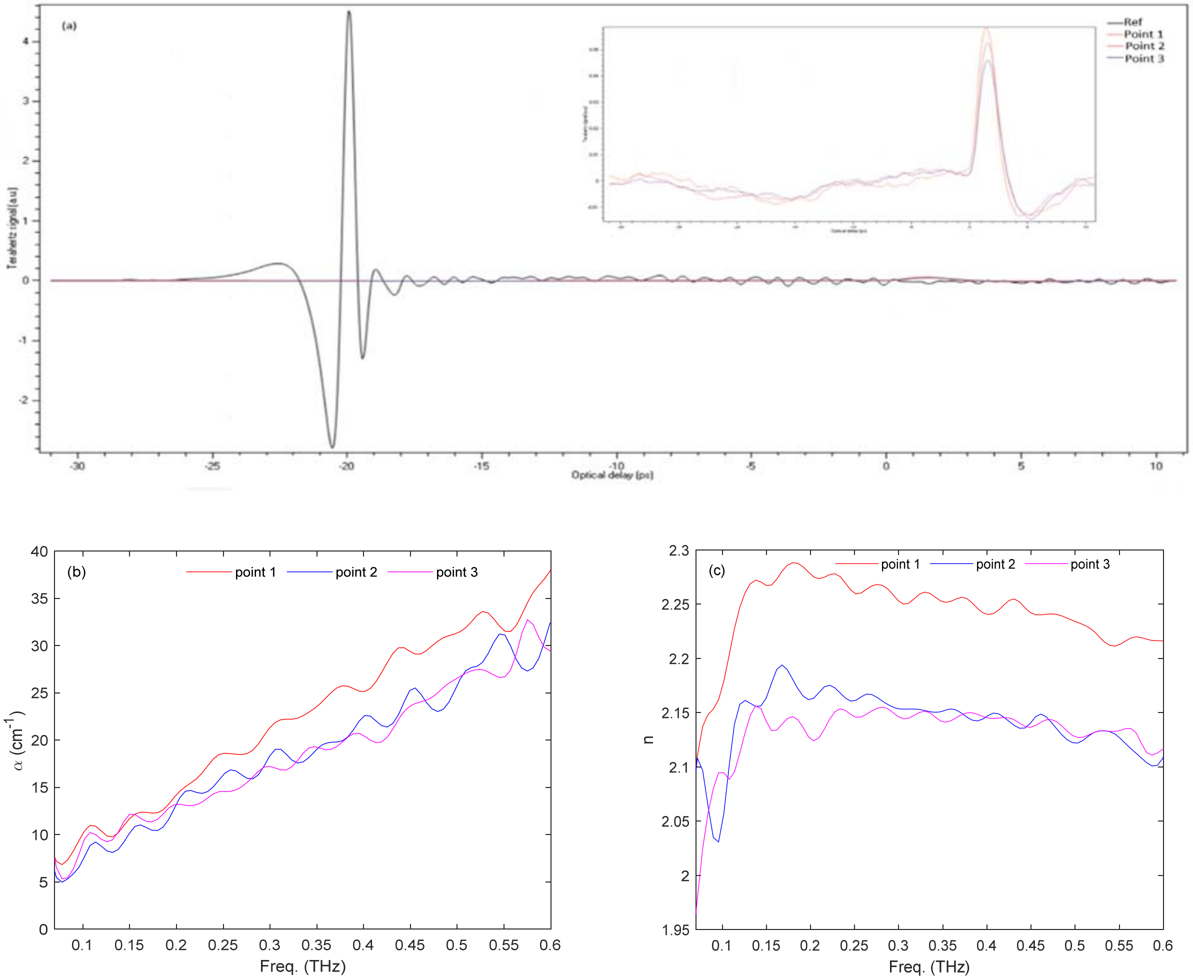

Fig. 5.7 THz spectroscopy of the L5S1 sample showing the (a) time domain signal, (b) absorption coefficient and (c) refractive index. The sample thickness is $\sim 2.50 - 2.76\ mm$.

The same spectroscopy measurement is repeated on the L9S2 sample, and the results are shown in Fig. 5.8. Variations in the absorption coefficient was observed, as well as in the refractive index which ranged from 2.02-2.12.

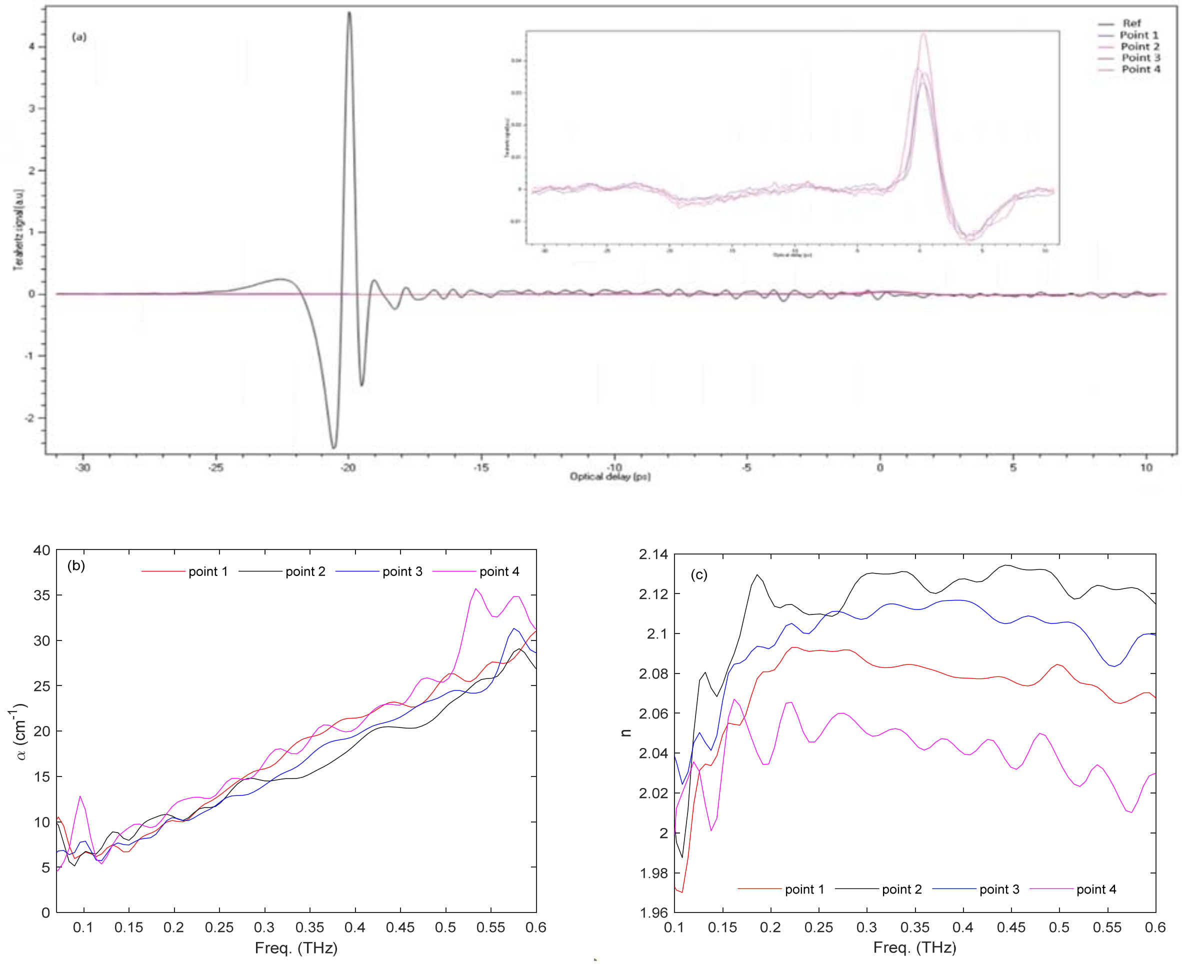

Fig. 5.8 THz spectroscopy of the L9S2 sample showing the (a) time domain signal, (b) absorption coefficient and (c) refractive index. The sample thickness is ~2.43 mm.

For the case of the L3S2 sample whose results are as shown in Fig. 5.9, the spectroscopic measurement generally showed a slight deviations. The amplitude of the transmitted THz signal was less absorbed. The absorption coefficient shows certain difference in the different points. A wide variation in the refractive index from 1.8-2.1 was observed since the local thickness could vary significantly.

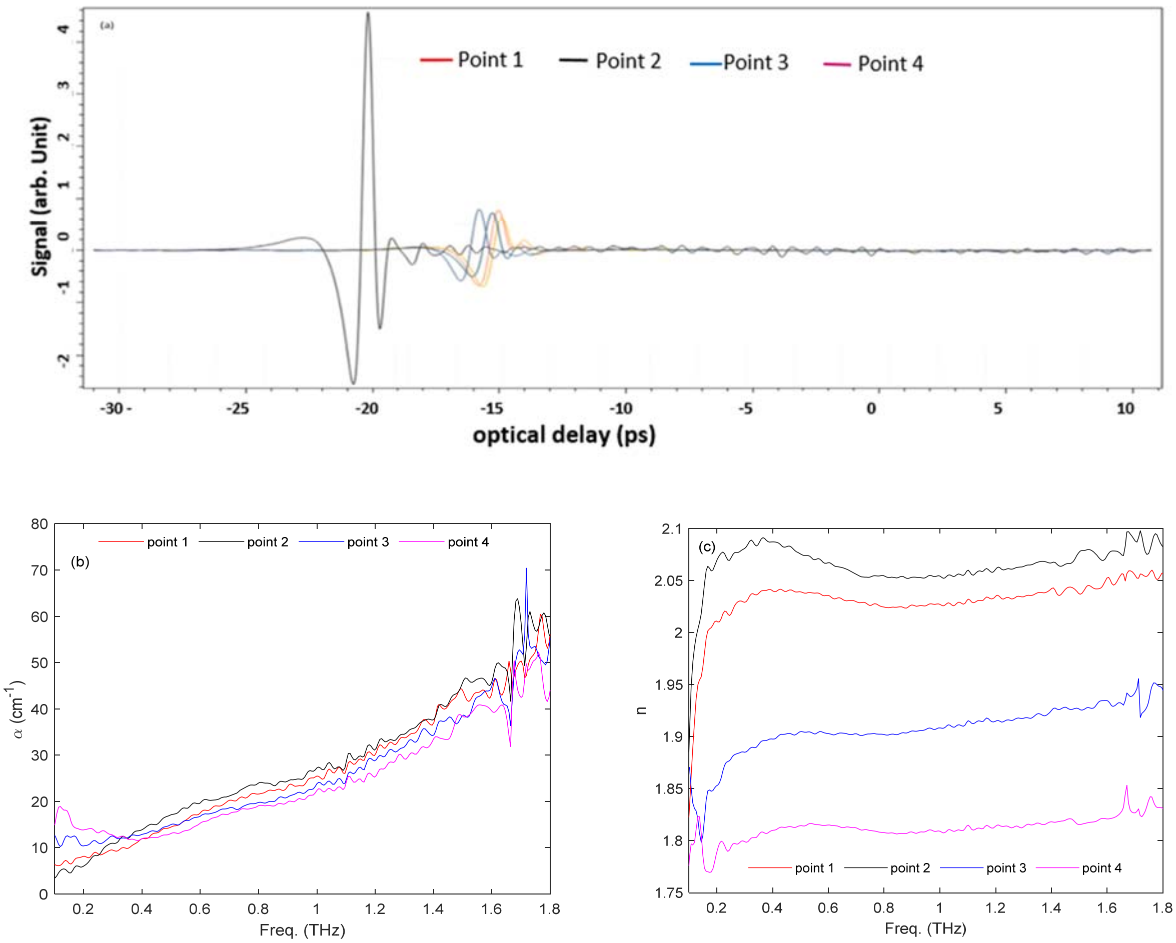

Fig. 5.9 THz spectroscopy of the L3S2 sample showing the (a) time domain signal, (b) absorption coefficient and (c) refractive index. The sample thickness is $\sim 1.48 - 1.61\ mm$.

Based on the forgoing results, it can be clearly observed that the oil shale samples exhibit inhomogeneity at different points in the samples. The variation in the absorption coefficient and refractive clearly illustrated this attribute. In particular, the variation in the refractive index was more pronounced. This result is in agreement with the surface morphology images that indicated varying surface features such as color and heights. In the next line of action, an entire mapping of two selected samples will be performed to check the sample inhomogeneous state.

The transmission spectroscopy map of the L3S3 sample is shown in Fig.5.10. The photograph of the sample is placed along side with the measurements. The spectroscopic analysis was carried out at two selected frequencies; 400 GHz and 500 GHz. The absorption pattern shows remarkable differences. Certain features that are not obvious in the 400 GHz were observed in the 500 GHz. Similarly, the spectroscopic map of sample L5S2 exhibited different degree of absorption particularly at the central portion of the sample at 190 GHz and 400 GHz as shown in Fig. 5.11.

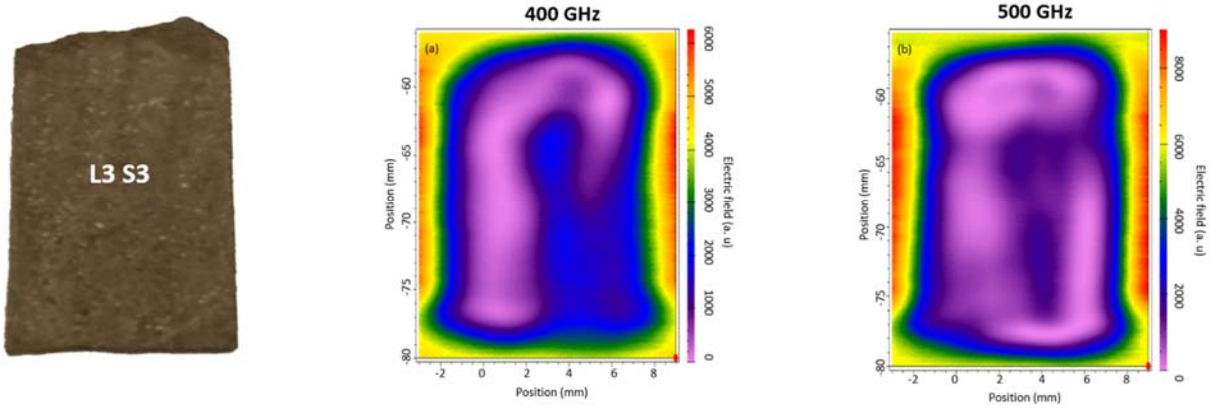

Fig. 5.10 Transmission spectroscopy of L3S3 sample at (a) 400 GHz and (b) 500 GHz.

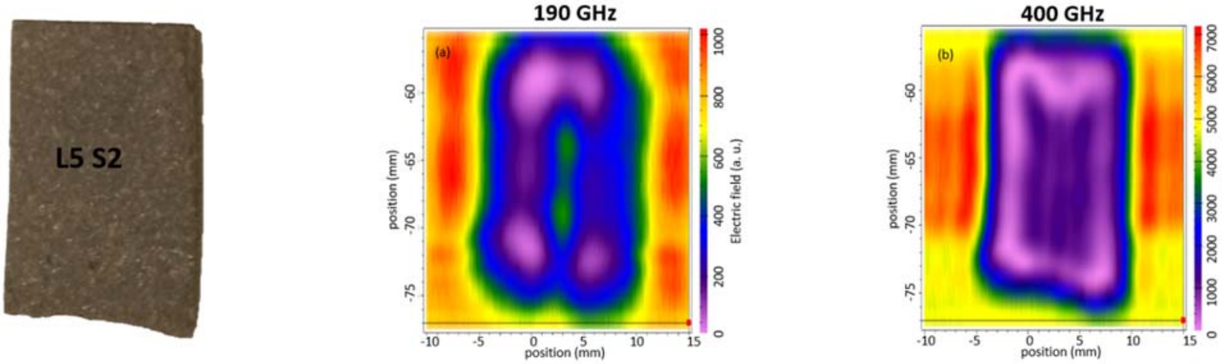

Fig. 5.11 Transmission of spectroscopy L5S2 at (a) 190 GHz and (b) 400 GHz.

5.2.3 THz reflection imaging of Lokpanta oil shales

Owing to the fact that the spectroscopy measurement have demontrated the heteroegrnous nature of the samples, THz imaging is carried out to identify any spatial variataion on the sample surfaces. The image of three selected samples are shown in Fig.5.12, Fig.5.13, and Fig.5.14. Distinct images were obtained in sample L3S3 and L3S4 at different frequencies. Only sample L7S2 had slight variations at the different frequency of analysis.

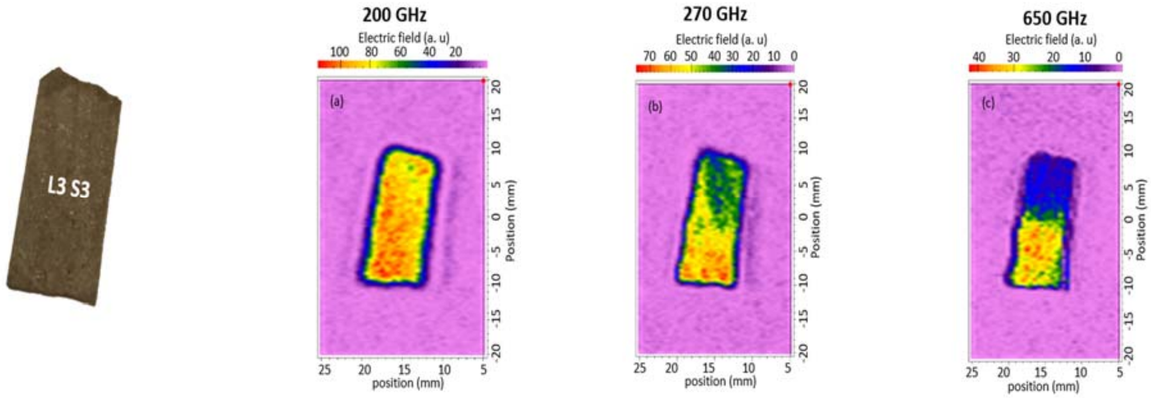

Fig. 5.12 reflection imaging of L3S3 sample at (a) 200 GHz, (b) 270 GHz and (c) 650 GHz.

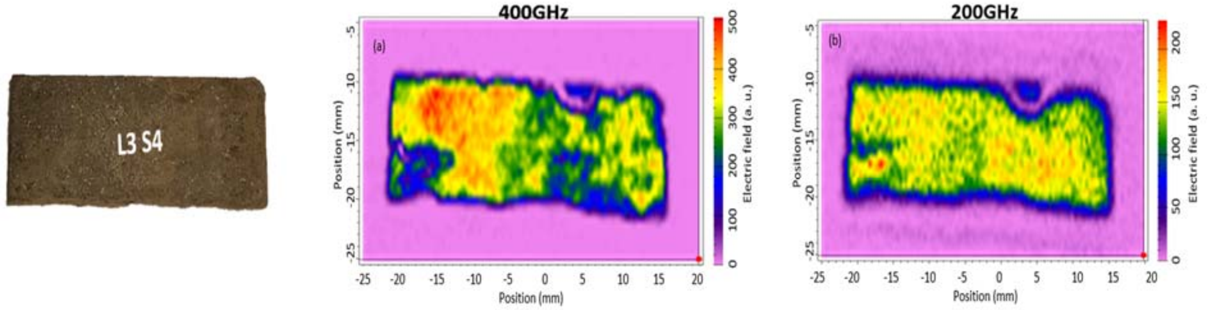

Fig. 5.13 Reflection imaging of L3S4 sample at (a) 400 GHz and (b) 200 GHz.

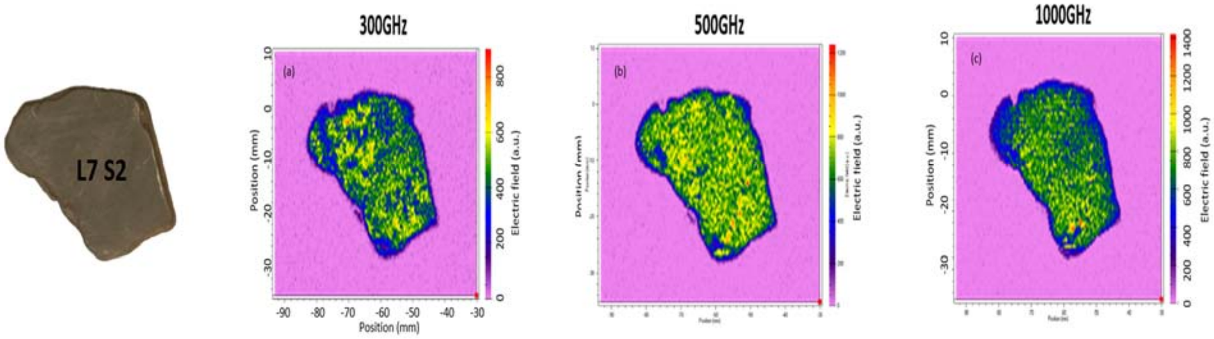

Fig. 5.14 Reflection imaging of L7S2 sample at (a) 300 GHz, (b) 500 GHz and (c) 1000 GHz.

5.2.4 Conclusion on THz spectroscopy/imaging results

Based on the present THz spectroscopy and imaging measurement, it appears to be fairly impossible to associate the absorption patterns to the presence of organics owing to the large imhomogenous pattern observed. Moreover, due to the inhomogeneous nature of this material, variariation of the rugosity , the mixing of different chemical element , the correlation between the dielectric response of the material and the presence of kerogen is utopic. For future work, I suggest the incorporation of pyrolytic technique in the THz spectroscopy and imaging measurement. In this technique, the oil shales will be heated above room temperature in stepwise manner. For example, at every 50°C interval in the heating process, spectroscopy of samples but also of reclaimed gazes and imaging can be performed after cooling the sample. Since, the constituent of oil shales are decomposed during pyrolysis, then a relationship between the transmitted/reflected THz signals can be plotted as a function of the pyrolytic temperature to reveal varying absorption patterns on the THz signal amplitude. In the result to be obtained, it may be possible that the different stages of pyrolysis (i.e. moisture loss, decomposition of macromolecules (organics) and mineral decomposition) may be linked to the strength of the transmitted THz signal. As such, a reasonable conclusion may be drawn with respect to relative presence of moisture, inorganics or organics.

On the other hand, the THz analysis in this work were supplemented with SEM-EDX and LIBS measurements for the sole aim to verify the imhomogeneous nature in the samples and to determine their elemental composition. The operation principle of SEM-EDX will first be discuseed and the results will be presented. Then the LIBS measurement will be presented too.

5.3 SEM-EDX Measurements

SEM has a variety of applications in a number of scientific and industry-related fields especially where characterization of solid materials is beneficial **[15-17]**. In addition to topographical, morphological information, a SEM can reveal spatial variations in chemical composition. Broad range of elements, i.e., from Boron to Uranium can be examined synchronously. To facilitate this measurement, an EDX is attached to SEM to provide information about the quantitative presence of elements in the material **[18-20]**.

The basic principle involve in SEM-EDX is that a beam of electron is generated by a source and used to irradiate the sample. The photograph of the SEM-EDX equipment is shown in Fig. 5.15. It consists of a SEM unit (made up of a vertical chamber and sample chamber), EDX unit and the data analysis unit. The components in SEM are housed in a vacuum environment so that the electron beams do not encounter interference from air particles in the atmosphere. An electron gun located at the top of the SEM emits the electron beam when thermally (or electrically) driven. As the electrons are released, they follow a downward vertical path through the column of the microscope. Condenser lens made up of magnets are placed in the column of the microscope. They are used to focus and control the directions of the electron beam towards the sample chamber. By using a user selectable aperture, the size of the electron beam is suitably adjusted to the desired beam size as it reaches the sample chamber. The surface of the sample is cleaned to remove dust and then placed in the sample chamber. The sample is mounted in a motorized stage so that the electron beam scans the entire surface. X-ray radiations in addition to various kinds of radiations (backscattered electrons, Auger electrons, secondary electrons) are emitted from the sample by the action of the scanning electron beam. The emission of the X-ray can be explained based on electronic transition between energy levels in the atoms of the sample. As the incoming electron beam hits the sample, electrons from the inner shell are released and a positively charged hole is created. Due to the displaced electron, the hole attracts another electron from an outer shell to fill the vacancy. As the electron moves from the outer higher-energy to the inner lower-energy shell of the atom, an amount of energy is released in the form of an X-ray. The energy of this X-ray is unique to the specific element and transition. Only the emitted X-rays are collected by a suitably positioned EDX detector that converts the photon into an electronic signal. The energy of the emitted X-rays can be obtained from the Moseley's relation **[21]**,

$$E\ (eV) = \frac{hc(Z-C)^2}{eB} \tag{5-6}$$

Where *B*, *C* are constant depending on the X-ray transition line. *Z* refers to the atomic number, *e* refers is the electron charge, *c* is the speed of light and *h* is Planck's constant. The characteristic of the X-ray energy from the different positions in the sample is used to perform a 2-dimensional elemental map distribution. By comparing the result to standard X-ray data, the qualitative and quantitative nature of the present elements are determined.

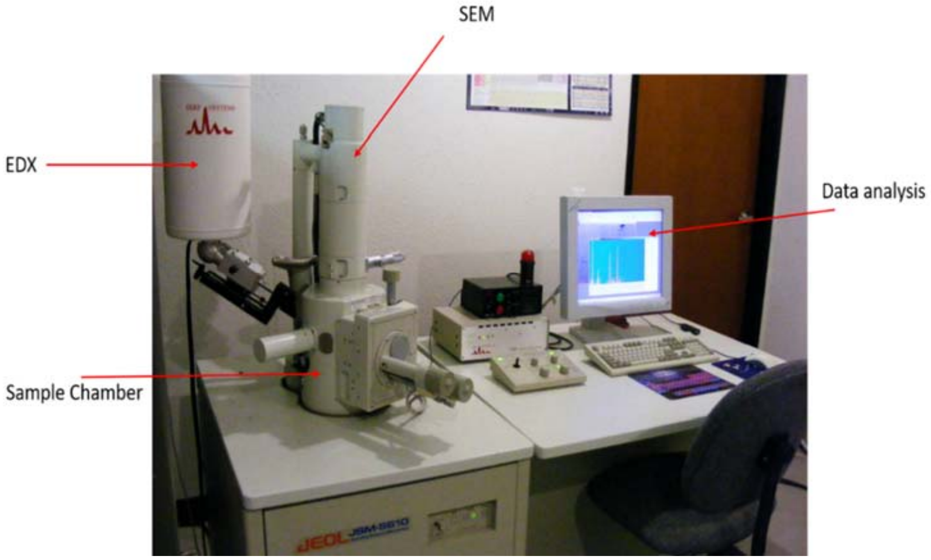

Fig.5.15 SEM-EDX equipment. The electron beam is generated at the top of the SEM and released vertically downward to the sample chamber. The emitted X-rays are collected by the EDX and the results of the analysis are displayed on a system monitor.

For the SEM-EDX analysis, three samples were analyzed. The measurements were performed on a small area in the samples. The SEM global images for the three selected samples; L5S2, L3S2 and L5S3 are shown in Fig. 5.16. Generally, the result of the analysis confirmed the presence of various elements including Al, Si, Ca, O, K, C, Fe, Mg, Mn, Ti, S, C and Na.

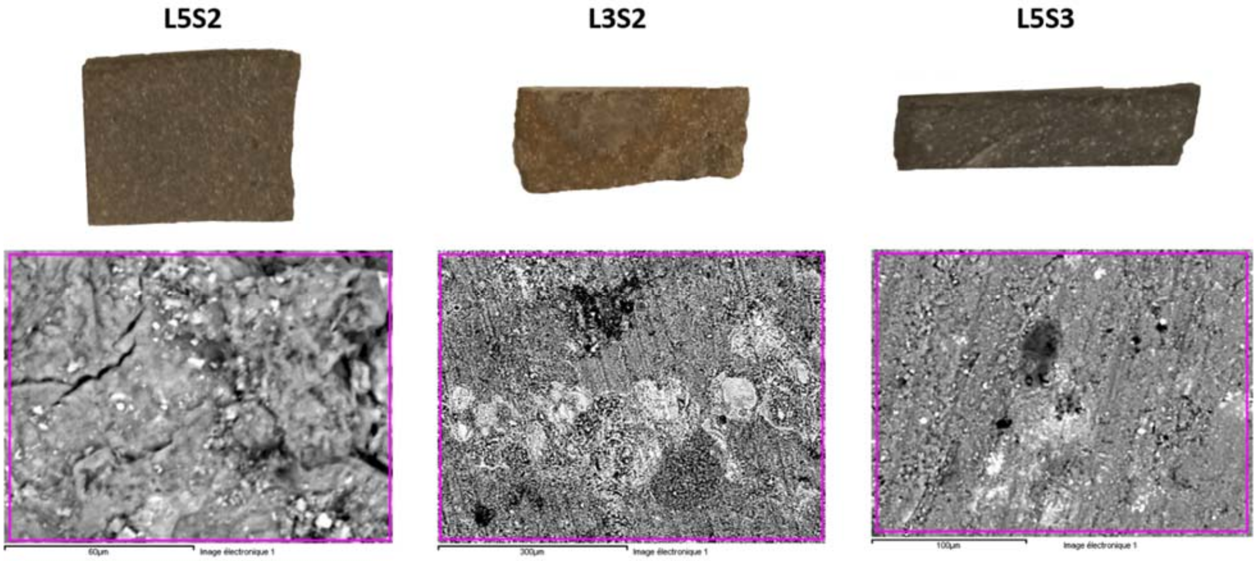

Fig.5.16 SEM global images of L5S2, L3S2 and L5S3 samples taken at a certain selected point.

The element analysis for each of the SEM global images in Fig.5.16 are presented in Fig. 5.17, Fig. 5.18, and Fig. 5.19. The presence and varying amount of the elements are represented by the intensity of the shades. In Fig. 5.17, the analysis revealed that the L5S2 sample consists of C in addition to other principal elements like Al, O and Si. The presence of these elements (Al, O and Si) indicates the presence of kaolinite mineral. This agrees with previous works on the mineral composition of Lopkanta oil shales **[22-23]**.

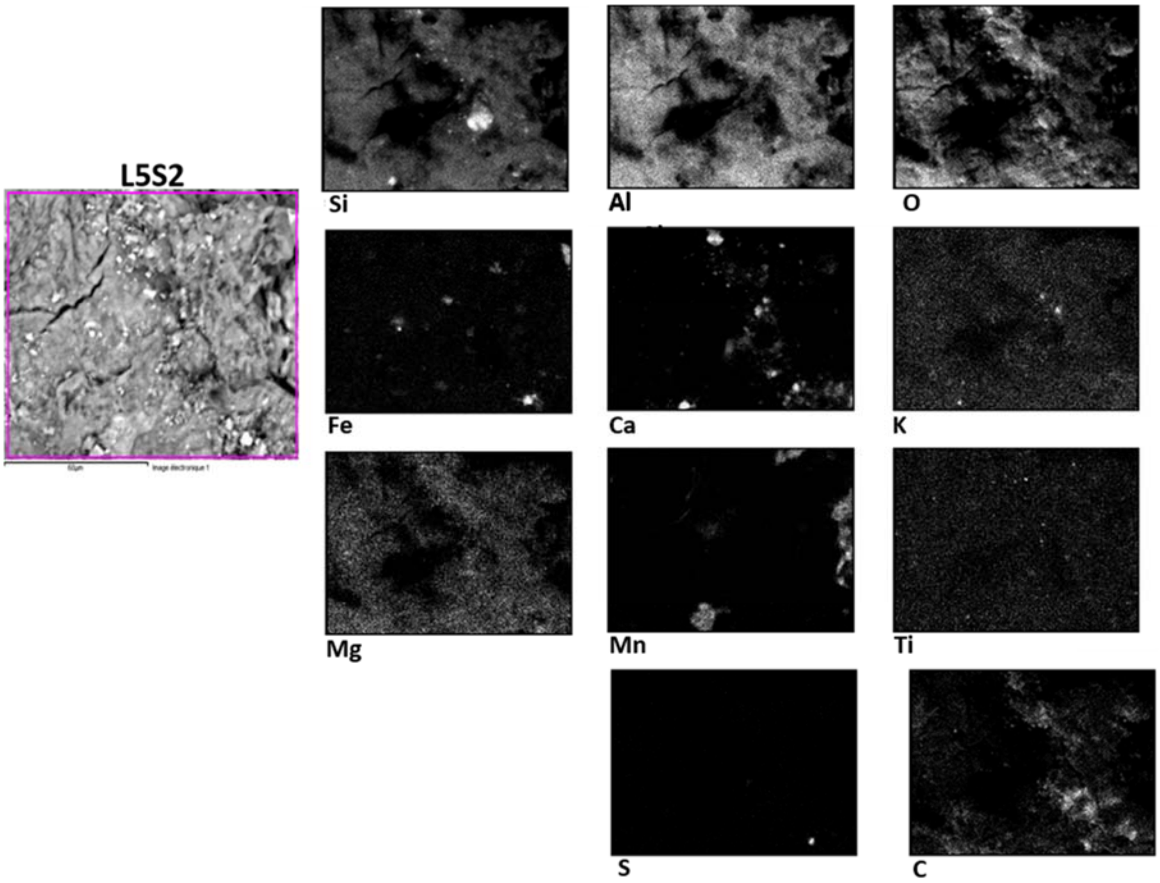

Fig. 5.17 SEM-EDX images of L5S2 sample.

In Fig.5.18, the L5S3 sample consists primarily of Ca, Al, Fe, C and other elements. The dominancy of Ca and Al is a possible indication of the presence of feldspar mineral which is also in agreement with the mineral constituent of Lopkanta oil shale **[22-23]**.

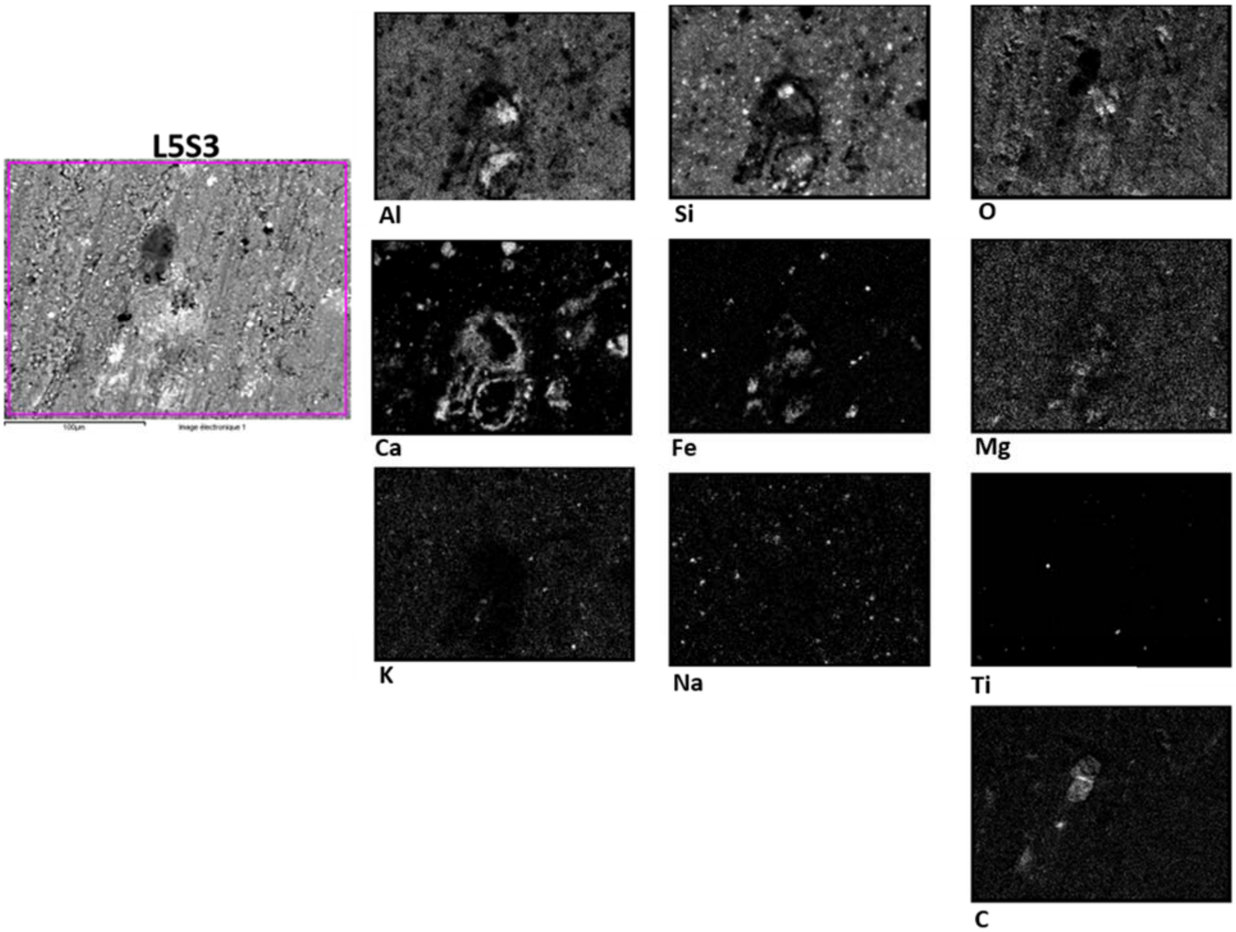

Fig. 5.18 SEM-EDX images of L5S3 sample.

In Fig. 5.19, it is observed that the L3S2 consists of tiny traces of C, and mostly dominated by Ca and Si. Since calcite mineral consists of Ca in addition to other elements, the results indicates that calcite may be present in the sample. Quartz may also be dominant due to the presence of silicon. This result follows closely to the typical mineral composition of Lokpanta oil shale since quartz and calcite have initially been identified as part of the Lopkanta oil shale constituent **[22-23]**.

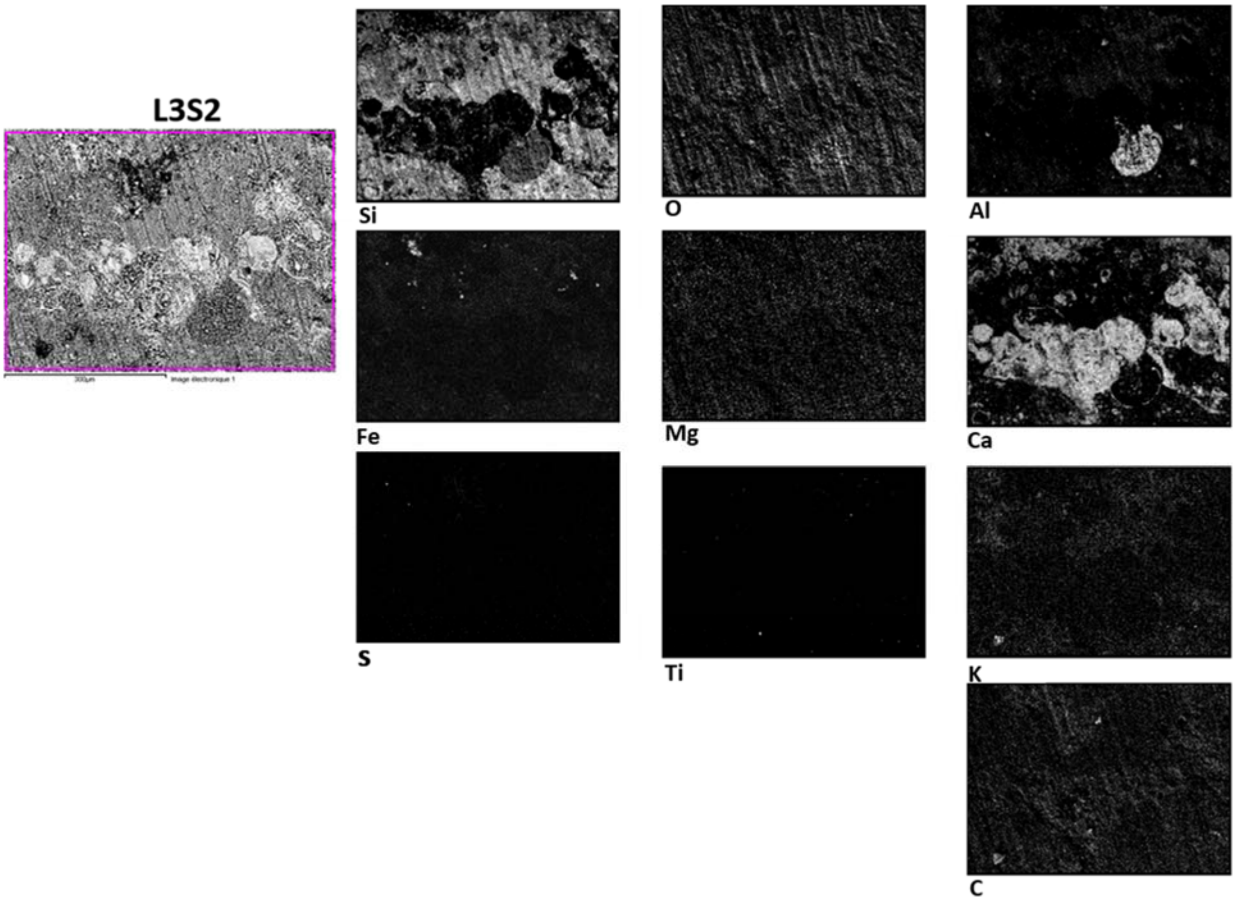

Fig. 5.19 SEM-EDX images of L3S2 sample.

Conclusion on SEM-EDX results

The elemental composition of the Lopkanta oil shales on selected areas on the samples have been performed by SEM-EDX analysis. Though, there is a slight variation in the composition between the different oil shale samples, they generally consist of a combination of more than one of the following elements; Al, Si, Ca, O, K, C, Fe, Mg, Mn, Ti, S, C and Na. Based on the relative composition in the detected elements, certain minerals such as quartz, calcite, feldspar may be present. The results agree well with previous works on the Lokpanta oil shales. In all the SEM-EDX analysis, C was detected but in low proportion. However, the typical elemental mineral composition of the Lopkanta oil shale was faithfully ascertained.

In order to verify the SEM-EDX results, a LIBS measurement was conducted on the samples. In what follows, the principle of LIBS technique will be discussed briefly and it will be followed by the results.

5.4 LIBS Measurements

Laser-induced breakdown spectroscopy (LIBS) is a reliable and versatile form of atomic emission spectroscopy that has broad capability for rapid in situ elemental detection in solid, liquid, or gaseous materials **[24-26].**

In LIBS, a high-intensity pulsed laser beam is focused onto the surface of a sample to create a high-temperature plasma. With the use of a short-pulse laser beam, a small volume of the sample mass is ablated (i.e. removed via thermal mechanisms) — in a process known as Laser Ablation. Usually, the ablated mass ranges from hundreds of nanograms to a few micrograms. The maximum amount of ablated mass, M that can be evaporated by a laser pulse can be calculated as follows **[27]**,

$$M = \frac{E(1-R)}{C_p(T_b - T_o) + L_v} \tag{5-7}$$

Where R refers to the surface reflectivity, C_p refers to the specific heat, T_b refers to the boiling point, T_o refers to the room temperature, E refers to the energy of the laser pulse and L_v refers to the latent heat of vaporization. This ablated mass will further interact with a trailing portion of the laser pulse to form a highly energetic plasma that contains free electrons, excited atoms and ions at high energy state E_p. When the laser pulse terminates, the plasma starts to cool. During the plasma cooling process, the electrons of the atoms and ions at the excited electronic states fall down into natural ground states E_k, thus, causing the plasma to emit light with discrete spectral peaks according to **[28]**,

$$E_p - E_k = \frac{hc}{\lambda} \tag{5-8}$$

Where, h refers to Planck's constant, c refers to the speed of light, while, E_p and E_k refer to the high energy and ground state. In the simplest set-ups, the emitted light from the plasma is collected and sent into a wide spectral range spectrometer. Because all elements emit in the 200–900 *nm* spectral range, a LIBS emission intensity spectrum will consist of unique finger prints of spectral emission lines. LIBS is especially sensitive to the light elements (H, He, Li, Be, B, C, N, O, Na, and Mg) that can be present in high abundance within natural materials but are difficult to determine by many other analytical techniques **[29-30]**. Monitoring the wavelength and intensity of the emission lines in the LIBS plasma will provide information on both the chemical species present and their abundance. The spectral line wavelength documents the identity of an element, whereas its intensity is proportional to the number of atoms of the element present. One particularly attractive attribute of this technique, is that it is highly spatially resolved. As the plasma forms over a limited spatial area of only tens to hundreds of microns on the sample surface, only a small amount of material (typically picograms to nanograms) is sampled by each laser pulse. This allows for in situ analysis of individual particles **[31]** and the fine-scale compositional mapping of a complex sample **[32-33].**

The LIBS measurement in my work was performed with Z-903 LIBS handheld gun manufactured by SCIAP. The photograph of this analyzer is shown in Fig. 5.20. This handheld LIBS analyzer consists of a Nd-YAG laser with an energy of 6 mJ, 6 ns FWHM pulse duration. The spot size of the laser is around 80 µm.

Fig. 5.20 Front and back view of the SciAps Z-903 handheld laser-induced breakdown spectroscopy analyzer.

The LIBS measurements were carried out by placing the nose of the instrument against the samples and then pulling the trigger. As a result high temperature intense plasma are generated. The radiations emitted by samples as they cool off are collected and sent to an internal spectrometer within the analyzer. The spectrometer is time-gated to allow the rejection of background Bremsstrahlung radiation emitted during the plasma creation. The analyzer is equipped with a user-selectable XYZ stage to enable beam rastering. A 4 X 3 array of locations were rastered in which ten laser shots were performed at each point. This was necessary in order to increase the sensitivity of the measurement and to reduce the standard deviation in the recorded data. The data were then collected and analyzed by averaging all the data points. In what follows, the LIBS measurement shall be presented.

The LIBS measurement taken on the L5S4 sample (as shown in Fig. 5.21) revealed distinct spectral peaks in the range of 380 -770 nm. It indicates the presence of a wide list of elements including Ca, Al, Na, K, Ti, Si, Mg and Fe. These results are in accordance with the SEM-EDX measurements. In addition, trace elements such as Sr, Rb and Ba were identified in the sample.

Since these trace elements have previously been identified as among the principal constituent of Lopkanta oil shale **[23]**, the LIBS measurement appears to be reliable.

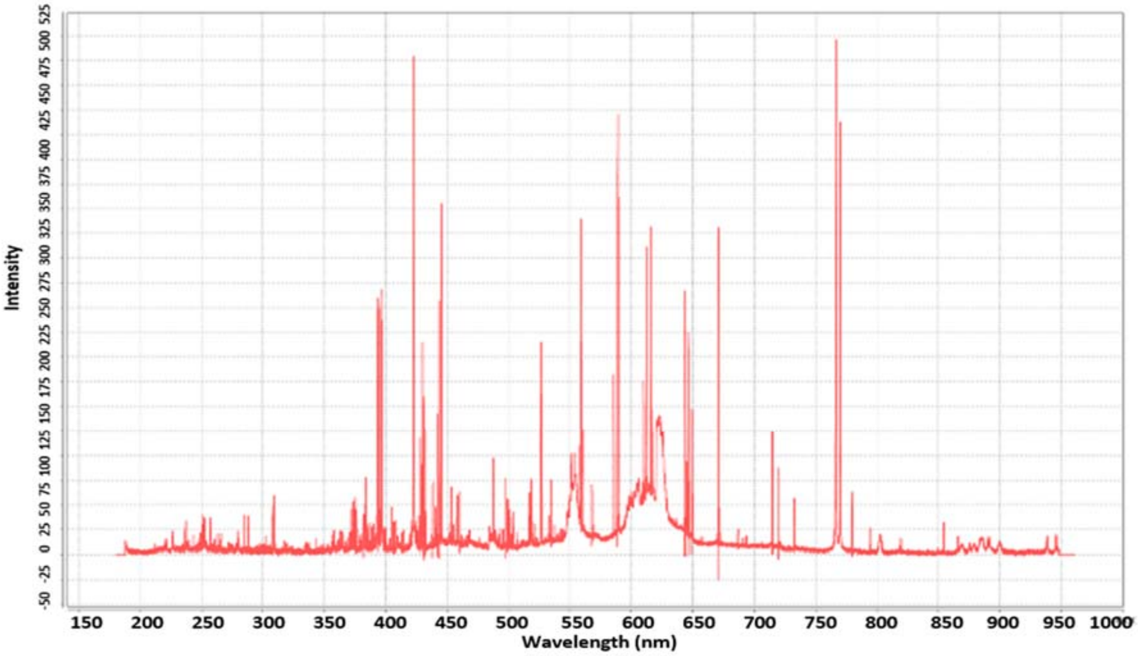

Fig. 5.21 LIBS spectrum of L5S4 sample.

By performing LIBS measurement under a strict experimental condition, the presence of elemental carbon was confirmed in the L7S2 sample as shown in Fig. 5.22. The sample spectrum (red) is overlaid on the spectrum of a sample containing Carbon (blue). An identical spectral peak at around 193 nm unique to carbon element was found.

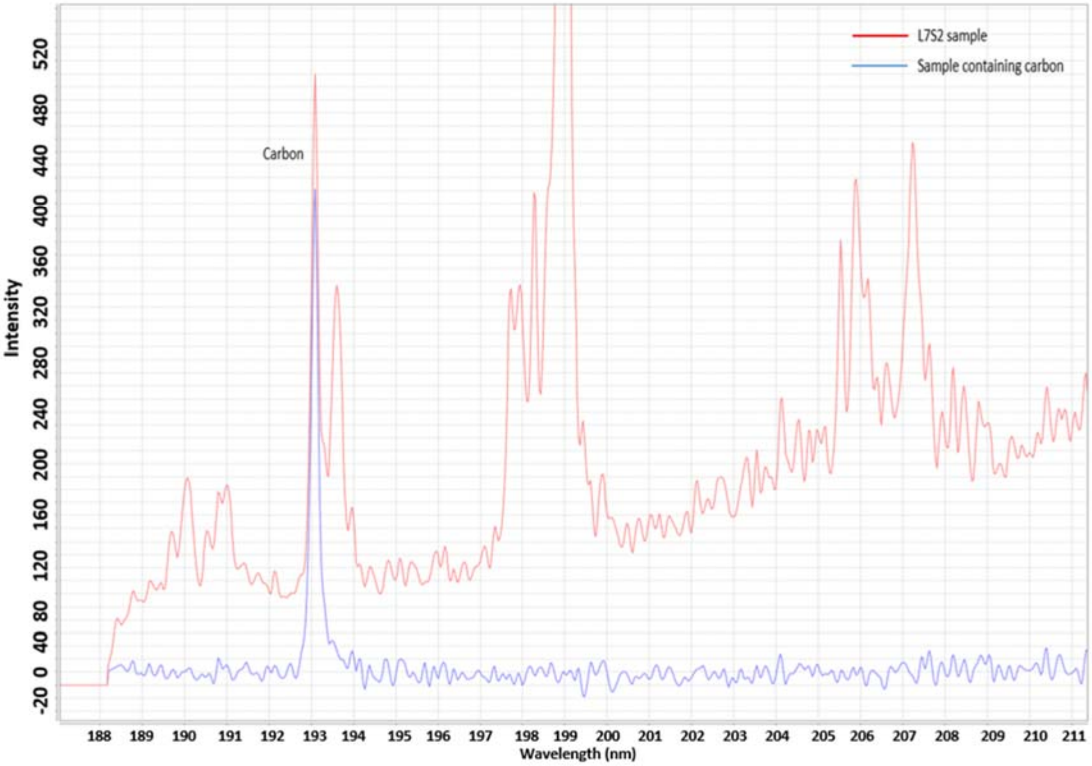

Fig.5.22 LIBS Measurement on the L7S2 sample (red) and a sample containing Carbon (blue). Both samples have an identical peak at around 193 nm and thus, indicating the presence of elemental carbon in the L7S2 sample.

A comparative measurement was performed between samples L1S2, L3S1, L3S3, L3S4, L5S4, L7S2 and L9S1 as shown in Fig.5.23. Generally, the results indicates that the L3 and L5 samples show the highest spectral peaks, followed by L9S1 sample. L1 and L7 samples have the lowest spectral peaks. These differences on the spectral intensities are due to the relative quantity of the detected elements presents in the samples. Thus, L3 and L5 samples contain the highest amount of elements, while L1 and L7 samples have the least amount of elements.

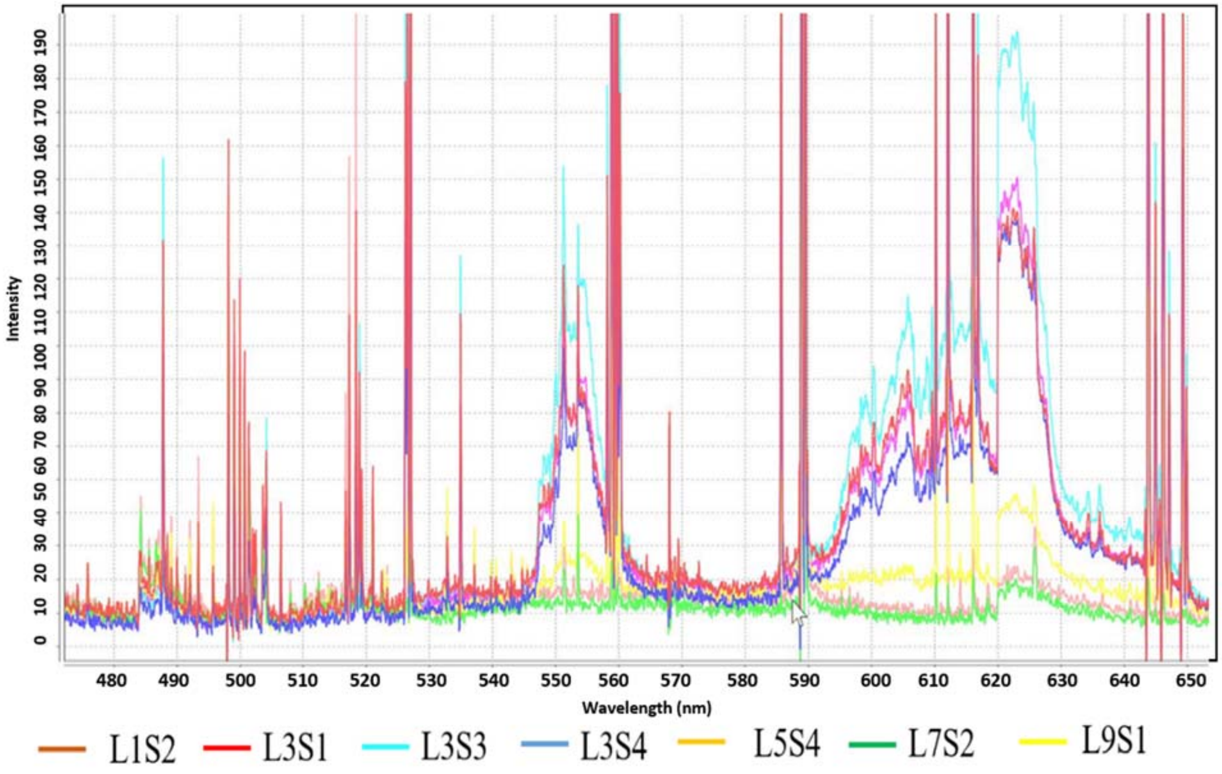

Fig. 5.23 LIBS measurement of L1S2, L3S1, L3S3, L3S4, L5S4, L7S2 and L9S1 samples.

The anomalies around 550 nm and 600-620 nm (shoulder shape) are still under investigation. It could be very important since Hα lines shows strongly broadened Hα line at 656.28 nm together. The other hydrogen shows expressively that effects in hydrogen line intensity caused by moisture could obscure the differences caused by the different content of organics: there is almost no difference between the intensities of Hα line in dry oil shale and in moistened lime-stone spectra **[36]**.

Conclusion on LIBS results

The LIBS results confirmed the presence of a wide list of elements including Ca, Al, Na, K, Ti, Si, Mg and Fe in addition to trace elements such as Sr, Rb and Ba. The results of the experimental procedure which are in close agreement to previous work on the Lopkanta oil shales could not have been able to detect C under the same experimental condition. Since the presence of C was only detected under a strict condition (experiment was performed in an inert environment), it may be that the percentage of C in the sample is comparatively weak which is in agreement to the SEM-EDX results. It is important to note that, in all the LIBS results Nitrogen was not detected. This also agrees with the SEM-EDX result.

5.5 Bibliography of chapter 5

[1] Hangyo H.; Tani M.; Nagashima T. Terahertz Time-Domain Spectroscopy of solids; A review. International Journal of Infrared and Millimeter. Waves, 2005, 26, 1661–1690. https://doi.org/10.1007/s10762-005-0288-1a

[2] Miao X.; Chen M.; Li Y.; Zhan H.; Zhao K.; Yue W. Simultaneous determination of organic distribution and content in oil Shale by Terahertz imaging. Energy Fuels, 2020, 34, 1664−1668.

[3] J. Roux, F. Garet, J. Coutaz. Physics and applications of terahertz radiation. Chapter 8 (Principles and applications of THz Time domain spectroscopy), 2014, pp 203-231.

[4] Motlep R. ; Kirsimae K. ; Talviste P. ; Puura E. ; Jurgenson J. Mineral composition of Estonian oil shale semi-cokes sediment. Oil Shale, 2007, 24, 405–422.

[5] Li Y.; Miao X.; Zhan H.; Wang W.; Bao, R.; Leng W.; Zhao K. Evaluating oil potential in shale formations using Terahertz time domain spectroscopy. Journal of Energy Resources Technology, 2018, 140, 034501.

[6] Miao X.; Zhan H.; Zhao K.; Li Y.; Sun Q.; Bao R. Oil yield characterization by anisotropy in optical parameters of the oil shale. Energy and Fuels, 2016, 301, 10365–10370. https://doi.org/10.1021/acs.energyfuels.6b02443

[7] Li Y.; Wu S.; Yu X.; Bao R.; Wu Z.; Wang W.; Zhan H.; Zhao K.; Ma Y.; Wu J.; Liu S.; Li S. Optimization of pyrolysis efficiency based on optical property of semi coke in terahertz region. Energy, 2017, 126 202-207

[8] B. Rima, L. Zhang, Z. Lei, Z. Kun, W. Wei, M. Yue, W. Xun, L. Hua, L. Yuan, X. Zhi. Probing the oil content in oil shale with terahertz spectroscopy. Science China Physics Mechanics and Astronomy, 2015, 58, 114211.

[9] Mai Y.; Li S. The mechanism and kinetics of oil shale pyrolysis at the presence of water. Carbon Resources Conversion, 2018, 1, 160-164.

[10] Roux J.; Garet F.; Coutaz J. Physics and applications of terahertz radiation. Chapter 8 (Principles and applications of THz Time domain spectroscopy) 2014, 203-231.

[11] Ozturk T.; Güneşer M. Electrical and electronics properties of materials, chapter 5 (Measurement, methods, and extraction techniques to obtain the dielectric properties of materials). 2018.

[12] Miao X.; Zhan H.; Zhao K.; Li Y.; Sun Q.; Bao R. Oil yield characterization by an isotropy in optical parameters of the oil shale. Energy and Fuels, 2016, 30, 10365–10370.

[13] Zhan V.; Chen M.; Zhang Y.; Chen R.; Zhao K.; Yue W. Utilization of oil shale as an electromagnetic wave absorbing material in the terahertz range. IEEE Access, 2020, 8, 46795-46801

[14] Rima B.; Zhang L.; Lei V.; Kun Z.; Wei W.; Yue M.; Xun W.; Hua L.; Yuan L.; Zhi X. Probing the oil content in oil shale with terahertz spectroscopy. Science China Physics Mechanics and Astronomy, 2015, 58, 114211.

[15] Falisi G.; Foffo G.; Severino M.; Di Paolo C.; Bianchi S.; Bernardi S.; Pietropaoli D.; Rastelli S.; Gatto R.; Botticelli G. SEM-EDX Analysis of Metal Particles Deposition from Surgical Burs after Implant Guided Surgery Procedures. Coatings 2022, 12, 240. https://doi.org/10.3390/coatings12020240

[16] Tobias K.; Egbert B.; Carl G. F. A Review of Scanning Electron Microscopy in Transmission Mode and Its Applications (Chapter 6). Advances in Imaging and Electron Physics. 171, 2012, pp 297-356. https://doi.org/10.1016/B978-0-12-394297-5.00006-4.

[17] Azad M.; Avin A. Scanning Electron Microscope (SEM): A review. International Conference on Hydraulics and Pneumatics Romania. 2018

[18] Tarik S.; Qingyang L.; Branko B.; Martin J. B. Microstructural imaging and characterization of oil shale before and after pyrolysis. Fuel, 197, 2017, pp 562-574. https://doi.org/10.1016/j.fuel.2017.02.030.

[19] Zhou S.; Xue H.; Guo W. A mineral analysis method for shale based on SEM and X-ray EDS. China Petroleum Exploration, 2017, 22(6): 27-33. 10.3969/j.issn.1672-7703.2017.06.004

[20] Rodriguez R.; Crandall D.; Song X.; Verba, C.; Soeder D. Imaging Techniques for Analyzing Shale Pores and Minerals. NETL Technical Report Series, 2014.

[21] Compton A. H.; Allison S.K. X-Rays in Theory and Experiment, 2nd Edition Hardcover – January 1, 1967

[22] Oluwadayo O. S.; Dorrit E. J.; Colin R. W.; Stephen F. F. Mineral and trace element composition of the Lokpanta oil shales in the Lower Benue Trough, Nigeria. Fuel, 90, 2011, 2843-2849. https://doi.org/10.1016/j.fuel.2011.04.037.

[23] Ofili, S.; Soesoo A. Oil Shale; Tallinn. General geology and geochemistry of the Lokpanta Formation oil shale, Nigeria. Oil shale, 38, 2021.DOI:10.3176/oil.2021.1.01

[24] Singh J.; Thakur S. (Eds.) Laser-Induced Breakdown Spectroscopy; Elsevier: Amsterdam, the Netherlands, 2007.

[25] Musazzi S.; Perini U. (Eds.) Laser-Induced Breakdown Spectroscopy, Theory and Applications; Springer: Berlin, Germany, 2014.

[26] Rusak D.; Castle B.; Smith B.; Winefordner J. Fundamentals and applications of laser-induced breakdown spectroscopy. Crit. Rev. Anal. Chem. 1997, 27, 257–290. https://doi.org/10.1080/10408349708050587.

[27] Cremers D.; Radziemski L. Handbook of Laser-Induced Breakdown Spectroscopy. John Wiley & Sons, 2006

[28] Ayed M. B. Application of laser-induced breakdown spectroscopy (LIBS) to the expansion of strontium (Sr) analysis options and engine oil. PhD thesis, 2021.

[29] Harmon R. S.; Lawley C. J. M.; Watts J.; Harraden C. L.; Somers A. M.; Hark R. R. Laser-Induced Breakdown Spectroscopy-An Emerging Analytical Tool for Mineral Exploration. Minerals, 2019, 9. https://doi.org/10.3390/min9120718

[30] Jolivet L.; Leprince M.; Moncayo S.; Sorbier L.; Lienemann C.P.; Motto-Ros V. Review of the recent advances and applications of LIBS-based imaging. Spectrochimica Acta Part B: Atomic Spectroscopy, 2091, 151, 41-53. https://doi.org/10.1016/j.sab.2018.11.008.

[31] Fabre C.; Devismes D.; Moncayo S.; Pelascini F.; Trichard F.; Leocmte A.; Bousquet B.; Cauzid J.; Motto-Ros V. Elemental imaging by laser-induced breakdown spectroscopy for the geological characterization of minerals. J. Anal. At. Spectrom, 2018, 33, 1345–1353. https://doi.org/10.1039/C8JA00048D.

[32] Kim T.; Lin C.; Yoon Y. Compositional mapping by laser-induced breakdown spectroscopy. J. Phys. Chem. B. 1998, 102, 4284–4287. https://doi.org/10.1021/jp980245m.

[33] Novotný K.; Kaiser J.; Galiová M.; Konečna V.; Novotný J.; Malina R.; Liška M.; Kanický V. Mapping of different structures on large area of granite sample using laser-ablation based analytical techniques, an

exploratory study. Spectrochim Acta Part B. 2008, 63, 1139–1144. https://doi.org/10.1016/j.sab.2008.06.011.

[34] Sweetapple M.; Tassios S. Laser-induced breakdown spectroscopy (LIBS) as a tool for in situ mapping and textural interpretation of lithium in pegmatite minerals. Mineral, 2015, 100, 2141- 2151. https://doi.org/10.2138/am-2015-5165.

[35] Jinesh J.; Daniel H.; Dustin M.; Johnathan M.; Dustin C. Laser induced breakdown spectroscopy: An emerging spectroscopic technique for shale rock characterization. Unconventional resources technology conference, colorado, USA, 2019.10.15530/urtec-2019-389.

[36] Paris P.; Piip K.; Lepp A.; Lissovski A.; Aints M.; Laan M. Discrimination of moist oil shale and limestone using laser induced breakdown spectroscopy. Spectrochimica Acta Part B: Atomic Spectroscopy, 2015, 107, 61-66, https://doi.org/10.1016/j.sab.2015.02.017.

General Conclusion in English

Since the early days of Physics, scientists have been fascinated by the interaction of electromagnetic waves with matter. Rich information about the matter can be explored by spectroscopy techniques using the optical and mm waves. While the development of electromagnetic sources at microwave and optical frequencies have rapidly advanced in the last century, Terahertz (THz) technology is relatively new, and has only seen significant progress in the last three decades. This progress was facilitated by the invention of the Ti: Sapphire laser which are capable of supplying intense short and high energy pulses. On the other hand, considerate effort to develop THz sources using Yb-based laser sources are currently emerging owing to its stability, low maintenance, high average power in its regenerative amplification section and a tunable repetition rate up to several tens of megahertz. In this work, both laser sources have been explored for use in nonlinear crystals namely ZnTe and BNA crystals.

In the first part of this work, an Yb-laser source centered at 1030 nm with a repetition rate of 42 kHz and with a 500 fs FWHM was used as the input beam to pump the ZnTe and BNA crystals. The particular interest was to study the form of the THz spectrum that can be generated with such a long pulse duration. With the use of the ZnTe as THz emitter, a narrow bandwidth of 0.5 THz was generated with a center frequency of 0.5 THz. It was observed that, nonlinear effects such as TPA may have been negligible since there was a quadratic dependency of the THz power on the pump pulse intensity. In the same vein, multicycle THz pulses were generated by replacing the ZnTe emitter with a 390 µm thick BNA. In this case, the detection was performed by electro-optic sampling in a 1 mm and 0.2 mm thick ZnTe crystal. The result of the THz signal obtained from the different thickness of the ZnTe crystal, indicated obvious differences in terms of the signal spectral component and signal amplitude. When the 1 mm ZnTe crystal is used for detection, the sampled THz pulse had a duration of 1 ps and a center frequency of 1.3 THz, while a shorter pulse duration with an extended center frequency was realized with the use of the thinner crystal. To understand the discrepancy in these results, the effective response function of the two crystals were compared to the detected THz spectrum. It was inferred from the comparison that it is surprising to detect frequencies higher than the 0.7 THz when the 1 mm crystal is used. As such, a thinner crystal was used whose cut-off frequency was at 2.4 THz. A THz spectrum centered at around 2 THz with a pulse duration of 0.5 ps was measured by this thinner crystal, however, the dynamic range were compromised. The replacement of the ZnTe detector with a GaP is suggested since the GaP have a more suitable phase matching condition at 1030 nm and possess less absorptive effect on the detected THz pulse. As regards the etalon effect observed during the long scanning range, they may be eliminated by using a thinner misaligned piece of the silicon filter.

In the second part of this work, a Ti: Sapphire laser centered at 800 nm and pre-chirped to 3.6 ps was focused onto a ZnTe crystal in order to demonstrate the feasibility of both generating and detecting few picosecond THz pulse in the same crystal. The THz pulse was characterized via the single shot electro-optic scheme. The experimental data conformed well to the predictions of optical rectification theory and Fabry Pérot effect with a negligible contribution of nonlinear effects such as TPA, Kerr, and Kerr-like effects. The polarization components of the THz-probe modulated beam were independently recovered, thanks to the simplicity and flexibility of the set-up. Although, narrow band THz spectrum at low frequency were generated (without focusing on the tunability of their spectrum), their frequencies may be tunable by adjusting the pump's chirp rate via the separation distance between the gratings in the laser source. The choice between the selection of the bandwidth and chirp rate of the chirped probe used in this detection scheme is a compromise between the temporal window and resolution of the measurement. In line with the advent of compact THz systems, the results of this findings supports the possibility of realizing photonic THz integrated systems with the use of ZnTe crystals. These findings can find favorably application in condensed matter physics, since with the use of tunable narrow band THz spectrum, the excitation of selective phonon modes have been achieved previously. With regards to other application purposes, it was noted that since the conventional single shot detection scheme have previously been used to monitor molecular dynamics occurring on a fast time scale such as laser induced material damage, chemical reactions, and phase transformations**,** then the experimental set-up may be adapted to serve as a time resolved spectroscopy set-up if certain modifications in the pump pulse path is considered.

It is clear that crude oil reserves are declining due to heavy demands to meet the energy need of the society. In Nigeria, the end of crude oil supply has been projected to occur by the year 2057. As such, the quest to find an alternative fuel source are currently ongoing. Oil shales in widespread deposit have previously been identified as unconventional fuel sources. A prior characterization of oil shales are necessary to determine the degree of their potentiality to yield oil. In the third part of this work, preliminary investigation of oil shales by THz spectroscopy were performed to demonstrate its capability to probe oil shales. A clear inhomogeneity in the samples was revealed by the different refractive index and absorption coefficient at some selected points in the sample, cause by the strong inhomogeneity of the stones. The result of the spectroscopic images obtained both in the reflection and transmission mode also revealed marked differences in the absorption pattern at different THz frequencies that must be correlated to other quantitative measures. Supplementary analysis namely LIBS and SEM-EDX were carried out to better examine the samples. Both analysis confirmed the presence of C, Fe, Mg, Si, Ti, K, Al and Ca. For future work, I suggest the incorporation of pyrolytic technique in the THz-TDS. In this technique, the oil shales are heated above room temperature in stepwise manner. For example, at every 50°C interval in the heating process, THz-TDS can be performed after cooling the sample. Since, the constituent of oil shales are decomposed during pyrolysis, then a relationship between the transmitted THz signals can be plotted as a function of the pyrolytic temperature to reveal varying absorption patterns on the THz signal amplitude. In the result to be obtained, it may be possible that the different stages of pyrolysis (i.e. moisture loss, decomposition of macromolecules (organics) and mineral decomposition) may be linked to the strength of the transmitted THz signal. As such, a reasonable conclusion may be drawn with respect to relative presence of moisture, inorganics or organics. Since THz-TDS is only a supplementary technique in the analysis, then for a firm assertion of the investigation, geochemical analysis such as the rock Eva pyrolysis must be carried out in order to quantitatively determine the amount of extractable oil in the oil shales.

Conclusion Générale en Français

Depuis les débuts de la physique, les scientifiques sont fascinés par l'interaction des ondes électromagnétiques avec la matière. Des informations riches sur la matière peuvent être explorées par des techniques de spectroscopie utilisant les ondes optiques et mm. Alors que le développement des sources électromagnétiques aux fréquences micro-ondes et optiques a rapidement progressé au cours du siècle dernier, la technologie Terahertz (THz) est relativement nouvelle et n'a connu des progrès significatifs qu'au cours des trois dernières décennies. Ce progrès a été facilité par l'invention du laser Ti : Saphir qui est capable de fournir des impulsions intenses courtes et de haute énergie. D'autre part, des efforts considérables pour développer des sources THz utilisant des sources laser à base d'Yb émergent actuellement en raison de sa stabilité, de sa faible maintenance, de sa puissance moyenne élevée dans sa section d'amplification régénérative et d'un taux de répétition accordable jusqu'à plusieurs dizaines de mégahertz. Dans ce travail, les deux sources laser ont été explorées pour une utilisation dans des cristaux non linéaires, à savoir des cristaux de ZnTe et de BNA. Dans la première partie de ce travail, une source laser Yb centrée à 1030 nm avec un taux de répétition de 42 kHz et avec une FWHM de 500 fs a été utilisée comme faisceau d'entrée pour pomper les cristaux de ZnTe et de BNA. L'intérêt particulier était d'étudier la forme du spectre THz qui peut être généré avec une durée d'impulsion aussi longue. Avec l'utilisation du ZnTe comme émetteur THz, une bande passante étroite de 0,5 THz a été générée avec une fréquence centrale de 0,5 THz. Il a été observé que les effets non linéaires tels que le TPA peuvent avoir été négligeables car il y avait une dépendance quadratique de la puissance THz sur l'intensité de l'impulsion de pompe. Dans le même ordre d'idées, des impulsions THz multicycles ont été générées en remplaçant l'émetteur ZnTe par un BNA de 390 µm d'épaisseur. Dans ce cas, la détection a été réalisée par échantillonnage électro-optique dans un cristal de ZnTe de 1 mm et 0,2 mm d'épaisseur. Le résultat du signal THz obtenu à partir des différentes épaisseurs du cristal de ZnTe a indiqué des différences évidentes en termes de composante spectrale du signal et d'amplitude du signal. Lorsque le cristal ZnTe de 1 mm est utilisé pour la détection, l'impulsion THz échantillonnée avait une durée de 1 ps et une fréquence centrale de 1,3 THz, tandis qu'une durée d'impulsion plus courte avec une fréquence centrale étendue a été réalisée avec l'utilisation du cristal plus fin. Pour comprendre l'écart entre ces résultats, la fonction de réponse effective des deux cristaux a été comparée au spectre THz détecté. Il a été déduit de la comparaison qu'il est surprenant de détecter des fréquences supérieures à 0,7 THz lorsque le cristal de 1 mm est utilisé. Ainsi, un cristal plus fin a été utilisé dont la fréquence de coupure était à 2,4 THz. Un spectre THz centré à 2 THz avec une durée d'impulsion de 0,5 ps a été mesuré par ce cristal plus fin, cependant, la plage dynamique a été compromise. Le remplacement du détecteur ZnTe par un GaP est suggéré puisque le GaP a une condition d'accord de phase plus appropriée à 1030 nm et possède moins d'effet d'absorption sur l'impulsion THz détectée Dans la deuxième partie de ce travail, un laser Ti: Saphir centré à 800 nm et pré-chirpé à 3,6 ps a été focalisé sur un cristal de ZnTe pour démontrer la faisabilité de générer et de détecter à la fois une impulsion THz de quelques picosecondes dans le même cristal. L'impulsion THz a été caractérisée via le schéma électro-optique monocoup. Les données expérimentales étaient bien conformes aux prédictions de la théorie de la rectification optique et de l'effet Fabry Pérot avec une contribution négligeable des effets non linéaires tels que sous forme d'effets d'absorption à deux photons et Kerr. Les composantes de polarisation du faisceau modulé par la sonde THz ont été récupérées indépendamment, grâce à la simplicité et à la flexibilité de la configuration. Bien que des spectres THz à bande étroite à basse fréquence aient été générés (sans se concentrer sur l'accordabilité de leur spectre), leurs fréquences peuvent être réglées en ajustant le taux de dérive de fréquence de la pompe via la distance entre les réseaux de diffraction dans la source laser. Le choix des paramétres de la sonde optique (bande passante spectrale et le taux de dérive de fréquence) utilisée dans ce schéma de détection est un compromis entre la fenêtre temporelle et la résolution. Conformément au avancée des systèmes THz compacts, les résultats de ces découvertes soutiennent la possibilité de réaliser des systèmes intégrés photoniques THz avec l'utilisation de cristaux de ZnTe. Habituellement, la configuration des sources et de la détection THz est relativement complexe et il est souvent nécessaire d'intégrer le système en combinant la génération et la détection. Notre étude peut également déboucher sur une application en physique de la matière condensée pour exciter les modes de phonons excités par un spectre THz à bande étroite accordable. Enfin, en tirant profit de schéma de détection monocoup, ce type de montage peut être implémenter pour étudier la dynamique moléculaire sur une échelle de temps ultra-rapide par spectroscopie résolue en temps pour les réactions chimiques et les transformations de phase.

Du côté applicatif de ce travail, nous avons étudié le potentiel des ondes THz pour analyser le schiste bitumeux. Il est clair que les réserves de pétrole brut diminuent en raison de la forte demande pour répondre aux besoins énergétiques de la société. Au Nigéria, la fin de l'approvisionnement en pétrole brut devrait se produire d'ici 2057. Ainsi, la recherche d'une source de carburant alternative est actuellement en cours. Les schistes bitumineux dans des gisements étendus ont déjà été identifiés comme des sources de combustibles non conventionnelles. Une caractérisation préalable des schistes bitumineux est nécessaire pour déterminer le degré de leur potentialité à produire du pétrole. Dans la troisième partie de ce travail, une étude préliminaire des schistes bitumineux par spectroscopie THz a été réalisée pour fournir ou démontrer sa capacité à détecter les schistes bitumineux. Une nette inhomogénéité dans les échantillons a été révélée par la différence d'indice de réfraction et de coefficient d'absorption à certains points sélectionnés de l'échantillon, causée par la forte inhomogénéité des pierres. Le résultat des images spectroscopiques obtenues à la fois en mode réflexion et transmission a également révélé des différences marquées dans le schéma d'absorption à différentes fréquences THz qui doivent être corrélées à d'autres mesures quantitatives. Des analyses supplémentaires, à savoir LIBS et SEM-EDX, ont été effectuées pour mieux examiner les échantillons. Les deux analyses ont confirmé la présence de C, Fe, Mg, Si, Ti, K, Al et Ca. Pour les travaux futurs, je suggère l'incorporation de la technique pyrolytique dans le THz-TDS. Dans cette technique, les schistes bitumineux sont chauffés au-dessus de la température ambiante de manière progressive. Par exemple, à chaque intervalle de 50 °C dans le processus de chauffage, une mesure THz-TDS peut être effectuée après refroidissement de l'échantillon. Puisque, les constituants des schistes bitumineux sont décomposés lors de la pyrolyse, alors une relation entre les signaux THz transmis peut être tracée en fonction de la température pyrolytique pour révéler des modèles d'absorption variables sur l'amplitude du signal THz. Il est alors possible que les différentes étapes de la pyrolyse (c'est-à-dire la perte d'humidité, la décomposition des macromolécules (organiques) et la décomposition minérale) soient liées à l'amplitude du signal THz transmis. Ainsi, une conclusion raisonnable pourrait être tirée en ce qui concerne la présence relative d'humidité, de matières inorganiques ou organiques.

Appendix: Publications

photonics

MDPI

Article

THz Pulse Generation and Detection in a Single Crystal Layout

Moses Eshovo Ojo *, Frederic Fauquet, Patrick Mounaix and Damien Bigourd

Laboratoire IMS, Université de Bordeaux, UMR CNRS 5218, 33400 Talence, France
* Correspondence: moses-eshovo.ojo@u-bordeaux.fr

Abstract: The THz pulse of a few picosecond durations have been generated and detected via optical rectification and electro-optic effect within the same ZnTe crystal. An unbalanced single-shot detection scheme was performed to characterize the signal. As a result, a multicycle signal was obtained, in which two-photon absorption and other associated nonlinear effects were reportedly negligible. The experimental set-up is compact, economical, easy to build and has the added simplicity of facilitating an independent analysis of the horizontal or vertical polarization arm of the THz-modulated chirped probe beam. This work finds a useful application in integrated THz devices, narrow-band THz phonon spectroscopy and spectroscopic investigation of fast-occurring processes.

Keywords: THz pulse; ZnTe crystal; chirped pulse; single crystal configuration; nonlinear effects

1. Introduction

The science of THz pulse technology is a growing field of interest in fundamental research, security surveillance, pharmaceutical industries, the biomedical sector, telecommunications, spectroscopy and imaging applications [1–3]. THz technology has gained wide attention in the study of various materials. In particular, its research and spectroscopic application stems from the signature response of electrons, spins, phonons and the rotational modes of molecules in the THz spectral range [4–6]. THz pulses have been generated in various forms regarding their polarization states, vorticity, spectral bandwidth and signal amplitude, in which the characteristics of the generated pulses determine their suitability for certain specific applications [7,8]. These characteristics can be modified based on the emitter sources. Among the table-top sources, nonlinear crystals can generate intense THz pulse amplitude in either time-resolved (pump-probe) or time-domain spectroscopy. ZnTe crystal is commonly used owing to its favorable phase-matching condition and its transparency in the optical and THz region [9,10]. These crystals, which are cut in either the (100), (111) or (110) plane, generate THz pulses with varying efficiency via optical rectification (OR) upon normal incidence with femtosecond laser sources [11,12]. OR can be explained in terms of Difference Frequency Generation (DFG), in which the spectral components within the bandwidth of the laser pulses interact to generate low-frequency signals within the THz region. Often, two crystals are needed in a typical experimental set-up for THz source and detection. Here, the THz pulse radiated by one crystal is detected at the other crystal by either a collinear or non-collinear interaction with a weak beam. Due to the usage of a weak laser pulse in the detection arm, there are usually no other observed processes other than the linear electro-optic (EO) effect. However, in the case where the generation occurs alongside the detection in the crystal, in what we shall refer to as single crystal configuration, the EO effect may coexist with other nonlinear processes such as two-photon absorption (TPA) and free carrier absorption (FCA), which competes with the generated THz pulse [13,14]. In order to have a close look into these nonlinear effects, Caumes et al., in their heterodyne Kerr experimental set-up, have observed the optical Kerr effect and Kerr-like effect in certain zinc blend structures that modify the form of the detected THz pulse [15].

check for updates

Citation: Ojo, M.E.; Fauquet, F.; Mounaix, P.; Bigourd, D. THz Pulse Generation and Detection in a Single Crystal Layout. *Photonics* **2023**, *10*, 316. https://doi.org/10.3390/photonics10030316

Received: 19 January 2023
Revised: 20 February 2023
Accepted: 8 March 2023
Published: 15 March 2023

The Kerr-like effects are cascaded nonlinear signals induced by the generated THz pulse. A few years later, other researchers adopted the single crystal configuration as a tool to study and evaluate these additional nonlinear effects in the ZnTe crystals. He et al. confirmed the observation of Caumes et al. in the (111) ZnTe in which the measured nonlinear refractive index, was dominated by Kerr and Kerr-like effects, whereas only the Kerr effect was more significant in the (110) ZnTe [16]. Furthermore, the effect of the Kerr signal, which usually appears at the onset of the THz waveform because the optical group velocity is lower than the THz phase velocity, was minimized by creating a temporal shift [17,18]. In a bid to distinguish the presence of either effect, Xiaoshu et al. included a phase-sensitive time-resolved z-scan in their experiment. Furthermore, by moving the crystal along a defined direction, they evaluated the contribution of each effect [19].

A single crystal configuration is a great tool not only to study the response of ZnTe but also for application purposes in integrated THz devices. Chen et al. demonstrated the possibility of this configuration being applied in tomography. They used a ZnTe to transmit a pulsed signal detected in the same crystal upon being reflected [8,20]. Thus, it appears there will be a need to minimize the nonlinearities in the single crystal configuration in order to boost their applications. Temporally stretched, chirped laser pulses are less powerful than their Fourier-transform-limited pulse duration. However, their higher pulse energy can be used to reach the same power, thus leading to an increase in the THz yield due to the many photons present. Previously, efficient THz yields have been reported using a pre-chirped pump pulse in air-plasma THz-based sources [21]. Erschens et al. extended this concept to nonlinear crystal-based sources [22–24]. In our manuscript, we will introduce the idea of adding a chirp to the pump pulse in the single crystal configuration. Usually, chirped pump laser sources are capable of generating tunable and narrow-band THz frequencies [25–27], which have been used to selectively excite phonons in certain mediums by some research groups [28,29].

One of the bases that form the framework of this research is the methodology commonly adopted for detecting THz pulses. Identical crystals are both used for the generation and detection scheme. Since appreciable success has been realized with the use of EO detection in this regard, it likely would have influenced the emergence of photonic THz compact devices. The EO detection route, which can be carried out by either the sampling or single-shot technique, has consequences on the form of the retrieved THz signal. In certain THz spectroscopy measurements involving fast and transient processes, the single-shot detection scheme is unarguably necessary. In particular, Murakami et al. and Zhao-Hui et al. have illustrated the performance of the single-shot measurement in time-resolved THz spectroscopy [30,31]. However, this technique has the drawback of reproducing a potentially deformed signal. There has been some progress in the single-shot geometries to address this challenge [32], with an exception in the single crystal configuration, in which there has been no result until now, to the best of our knowledge. This research investigates the feasibility of a coupled and reliable system for THz generation and detection through a study based on the single crystal configuration involving a single-shot EO detection scheme in a ZnTe crystal.

To begin with, this work is a recall of the THz pulse generation theory ensuing from the chirped pump propagation in the crystal, apace with a contributory linear effect. It is followed by highlighting the consequence of the detection scheme on the form of the retrieved THz pulse. Afterward, the functions of the optical elements in the experimental scheme are indicated, with an explanatory note on the retrieval algorithm of the THz pulse. Subsequently, by discussing the observed results based on the theoretical predictions, a conclusion is drawn to spotlight the relevance of the work.

2. Principle and Theory

The generation of the THz pulse is initiated by irradiating a ZnTe crystal with an infra-red laser beam. Consider a pre-chirped pump pulse propagating along the z-direction of the crystal, with group velocity v_g, whose Fourier-transform-limited pulse duration and second-order dispersion term are denoted by T and φ_2, respectively. As in the following, the crystal is relatively thin (600 μm), and the optical pulse is long (3.6 ps); the dispersion due to the crystal is ignored. By neglecting pump depletion and absorption within the crystal, we can write the form of the pre-chirped pump pulse centered at ω_0 and propagating along the z-direction as

$$E(t,z) = \frac{E_0}{2}\frac{1}{\gamma^{\frac{1}{4}}}\exp\left(\frac{\left(t-\frac{z}{v_g}\right)^2}{\beta\cdot\gamma}\right)\cdot\exp\left(i\left(a\left(t-\frac{z}{v_g}\right)^2+\varepsilon\right)\right)\cdot\exp(i(\omega_0 t - k_0 z)) \quad (1)$$

$$\beta = T^2,\ \gamma = 1+\frac{\varphi_2^2}{\beta^2},\ a = \frac{\varphi_2}{\beta^2\gamma},\ \epsilon = -\arctan\left(\frac{\varphi_2}{2T^2}\right)$$

where k_0 is the wave vector and E_0 is the amplitude of the pulse. The pre-chirped pulse induces a total polarization in the crystal in which the nonlinear polarization term P_{NL} is the most relevant for optical rectification. In this case, any two frequency components E_j, E_k within the spectral bandwidth of the incident pulse interact to generate low-frequency pulses in the THz region by the DFG process [33,34].

$$P_i(\omega) = \varepsilon_0\int_{-\infty}^{+\infty}\sum_{j,k=1}^{3}\chi_{ijk}^{(2)}E_j(\omega_0)E_k(\omega_0-\omega)\,d\omega_0 \quad (2)$$

where $\chi_{ijk}^{(2)}$ is the frequency-dependent second-order susceptibility of the crystal. The evolution of the generated THz pulse at normal incidence is modeled by the nonlinear Maxwell equation, in which the conductivity of the crystal has been neglected [35],

$$\left(\frac{\partial^2}{\partial z^2}+\omega^2\frac{\varepsilon(\omega)}{c^2}\right)E_{THz}(\omega,z) = -\frac{4\pi}{c^2}\,\omega^2\,P_{NL}(\omega,z) \quad (3)$$

Assuming the absence of THz field at the beginning of the crystal and neglecting the Fabry–Pérot effect, we set the boundary condition as $E_{THz}(\omega,\,0)=0$, $\frac{\partial E_{THz}(\omega,\,0)}{\partial z}=0$, so that the analytical solution to Equation (3) upon substituting Equation (1) into the second term of Equation (2) is,

$$E_{THz}(\omega,z) = \frac{\chi_{ijk}^{(2)}\,\pi\sqrt{2}}{4(n_{THz}^2-n_g^2)}T\,e^{\{\frac{-\omega^2}{4}\beta\cdot\gamma\}}E_0^2\begin{bmatrix}\frac{1}{2}\left\{1+\frac{n_g}{n_{THz}}\right\}e^{i\omega n_{THz}z/c}\\ +\frac{1}{2}\left\{1-\frac{n_g}{n_{THz}}\right\}e^{-i\omega n_{THz}z/c}-e^{i\omega n_g z/c}\end{bmatrix} \quad (4)$$

where $\chi_{ijk}^{(2)}$ is assumed to be constant i.e., frequency independent since the THz frequency is well below the optical phonon resonance in our set-up. Three terms exist in Equation (4) corresponding to the carrier waves of the THz and pump pulses. The coefficient of the second term has a lower amplitude compared to the other terms. This second term propagating in the opposite direction to the first and last term contributes significantly to the waveform of the THz pulse if T is in the order of picosecond. The interaction between these terms adds up to the THz efficiency when chirped pump pulses irradiate the nonlinear crystal. In other words, the differences in the value of the group refractive index n_g (n_g = 3.2 at 800 nm) and the frequency dependent-n_{THz} (n_{THz}~3.2 at 1 THz) experienced by the optical pulse and generated THz respectively leads to an insignificant temporal walk-off, thus making the generation process efficient. The plot in Figure 1 illustrates the effect of backward propagating the THz pulse term in the profile of the THz field. By considering an incident 2 ps long laser pulse, the simulated THz with the backward term (black line) and without the backward term (dashed green line) shows a significant contribution, such that the effect of this term cannot be neglected as in the case of shorter incident pulses.

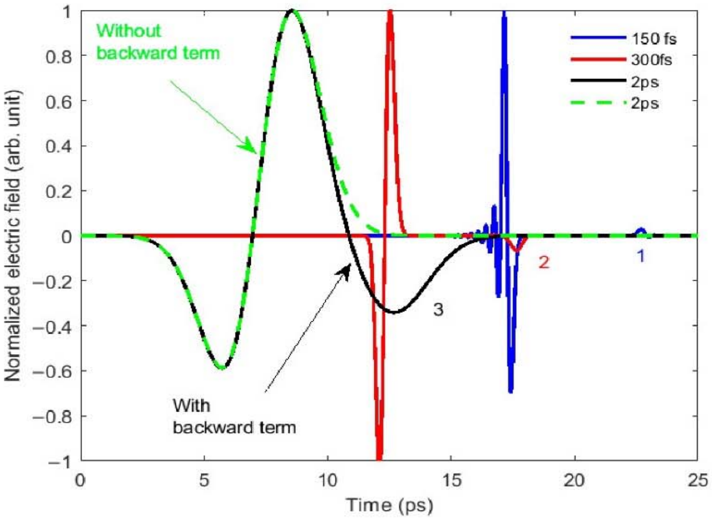

Figure 1. Simulated effect of the contributory terms in a THz signal. There is usually a backward THz signal (labeled 1, 2 and 3) generated alongside their forward propagating THz signal, whose contribution depends on the pulse duration of the pumping laser source. Subpicosecond laser sources such as 150 fs (blue) and 300 fs (red) generate an insignificant backward THz signal term. However, for a picosecond laser pulse, this backward term has remarkable effects on the forward propagating THz signal (black line) compared to the forward term (dashed green line).

The round trip time of the THz pulse within the crystal is shorter than the THz pulse duration, implying that the effect of multiple reflections cannot be neglected. By considering the bouncing of the THz pulse between the opposite faces of the crystal, a transfer function for the Fabry–Pérot effect is defined as per [35],

$$\mathrm{T_{FP}} = \frac{1}{1 - \mathrm{r}^2 \mathrm{e}^{\frac{2\mathrm{i}\mathrm{n_{thz}}\omega}{\mathrm{c}}\mathrm{L}}} \tag{5}$$

where $\mathrm{r} = (\mathrm{n_{thz}} - 1)/(\mathrm{n_{thz}} + 1)$, corresponds to the amplitude of the reflected THz pulse, and L represents the effective length of the crystal for THz generation. For a given THz spectrum, the spectral modulation appears with a lower spacing for a thicker crystal. As the THz pulse bounces off from the crystal–air interface with successively decreasing amplitude, it encounters the chirped probe in the last part of the crystal length. The THz pulse generated in the first part of the crystal length and modified by the Fabry–Pérot effect becomes coalesced onto the chirped probe.

Using a chirped pulse to probe the THz pulse, the different portions are overlaid onto different sections in the chirped probe. It makes achieving a single-shot measurement for a fixed position of the chirped probe's delay stage possible. This form of encoding the THz pulse onto the chirped pulse is different from the conventional EOS in that the THz pulse is not sampled by the probe pulse. Due to the orientation of the chirped probe with respect to the principal axis of the crystal, the impact of the overlapping THz pulse can result in either a rotation in the chirped probe polarization, a temporally varying phase shift or a combination of these two phenomena [36]. In the case relevant to the design of our set-up, the chirped probe polarization is rotated, and this change is converted by a polarizer into an amplitude modulation $\mathrm{f(t)}$ as per;

$$\mathrm{f(t)} = \mathrm{E_{cp}}[1 + \mathrm{kE_{THz}}] \tag{6}$$

where the modulation parameter due to the EO effect is given by $k \ll 1$, and E_{cp} is the chirped probe electric field with a 10 nm FWHM spectral bandwidth and a duration of 5.2 ps. The recovery stage for this EO single-shot encoded THz pulse is achieved using the standard THz spectral interferometry technique. Denoting $g(\omega)$ as the spectral response of the optical spectrometer, the retrieved THz field, $E_{THZ}^{retrieved}$ is represented from the convolution between the optical spectrum and $g(\omega)$ as in [37],

$$E_{THZ}^{retrieved}(\omega) \propto \frac{\left[g * |F|^2\right](\omega) - \left[g * |E_{cp}(\omega)|^2\right](\omega)}{\left[g * |E_{cp}(\omega)|^2\right](\omega)} \tag{7}$$

where $F(\omega)$ is the Fourier transform of Equation (6), $g(\omega) = e^{-[(\omega-\omega_1)/\Delta\omega]^4}$. ω_1 and $\Delta\omega$ are the frequency of the signal recorded on one pixel and the resolution of the spectrometer. Given that $\Delta\omega$ is effectively low, the retrieved THz pulse will not be affected by the spectrometer resolution. Our detection scheme excluded the inclusion of a read-out pulse to probe the THz-modulated chirped pulse, as in the case of other works [38,39]. The read-out pulse, which improves the temporal resolution of the THz pulse, is often needed where a large temporal window degrades the temporal resolution [40]. Since we have utilized a chirped probe with a short temporal window, we expect that the temporal resolution is not adversely affected. The temporal resolution τ_{res}, derived by comparing the form of the generated and detected THz signal in the case where $T_c \sim T_{THz}$ [37] is,

$$\tau_{res} = \sqrt{T_{THz} T} \tag{8}$$

In the next section, we used Equations (4) and (6) to simulate the THz pulse with a crystal length of 350 µm for the detection. In fact, the length used for the emission or the detection section does not significantly modify the shape of the THz pulse but mostly the amplitude.

3. Experimentation Section

The laser source for the experiment is a Ti-sapphire laser beam centered at a wavelength of 796 ± 2 nm, with a repetition rate of 1 kHz and ~0.6 mJ of energy. The distance between the compressor's gratings at the output of the chirped pulse amplifier was adjusted to generate 3.6 ps long pulses as measured by a Frequency Resolved Optical Gating (FROG) device [41]. A beam splitter is placed in the path of the output pulse to separate the pulse into a pump and probe beam (Figure 2). The probe beam was additionally chirped by repeated passage through an assembly of dispersion blocks made up of SF6 material. A total of twenty-four (24) passes are realized in the 52 mm long blocks, and the probe pulse is broadened to 5.2 ps due to the material dispersion. The experimental set-up illustrated in Figure 1 consists of the pre-chirped 3.6 ps pump beam focused on the 0.6 mm thick <110> ZnTe crystal with few tens of µJ. Due to the inherent complexity of simultaneously optimizing the crystal angle for efficient emission and detection in the single layout configuration, there is an unarguable tradeoff between these two phenomena. In this regard, an optimum angle of 26° (relative to the (001) axis) has been proposed and explored [8]. In this experiment, the crystal angle was adjusted to maximize the detected THz signal. The 5.2 ps horizontally polarized chirped probe overlaps temporally and spatially with the vertically polarized pre-chirped pump beam on the crystal at a crossing angle of ~12°. The two beams were focused independently in the crystal. The diameter of the pump and probe beam at the crystal position was 570 µm and 125 µm, respectively. It is straightforward to see that the beam size of the THz pulse given by $r_{THz} = r_p/\sqrt{2}$ is larger than the probe size, where r_p denotes the pump size. Thus, we have assumed that the THz pulse has a constant intensity profile around the probe; as such, E_{THz} is spatially independent in our simulation. The polarization of the beam is horizontal, while the pump one is rotated vertically.

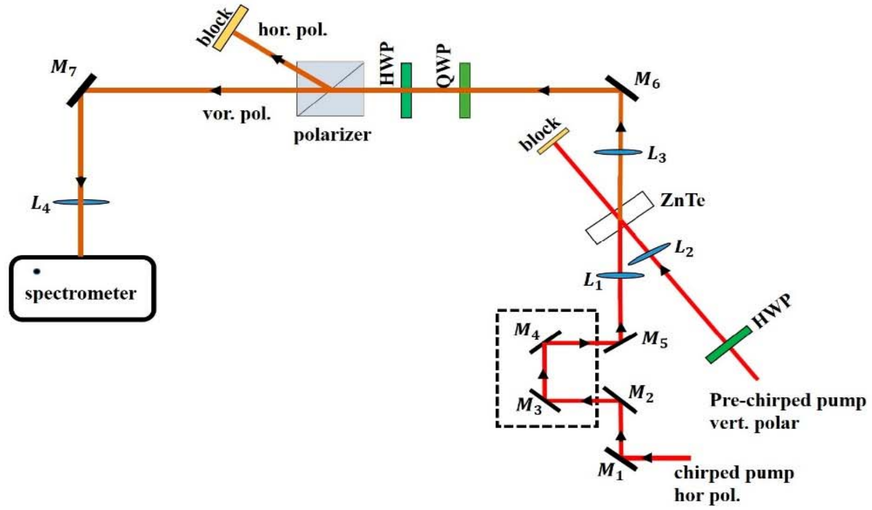

Figure 2. Single layout configuration for generating and detecting THz pulse, in which the pre-chirped pump and chirped probe beam cross the ZnTe crystal at an angle of 12°. The pump being spatially broader, overlaps with the probe by appropriately adjusting the translational delay stage. The beam path of these pulses and the THz-modulated probe beam are indicated in red and brown, respectively. For the sake of simplicity, the FROG characterization unit is not included. Mirrors: $M_1 - M_7$, Lens: $L_1 - L_4$. Half Wave Plate—HWP, Quarter Wave Plate—QWP.

In this single crystal configuration, the THz pulse is generated in the first part of the crystal by the incident pre-chirped pump beam; then, it induces a phase change on the incoming chirped probe beam. The overlap length between the THz pulse and the probe depends on the crossing angle and crossing point. This probe THz beam is collimated and subsequently circularly polarized by a quarter wave plate (QWP). The vertical and horizontal polarized components exit the polarizer with a slight deviation from each other. The HWP located between the QWP and polarizer switches between the beam paths of polarization components, such that the same optical spectrometer, sensitive to the P polarization, detects the different polarization. The choice of the optical spectrometer is such that its spectral resolution is effectively high in order to effectually resolve the frequency components of the measured signal. The recovery of the THz waveform occurs in two steps. (1) First, the probe spectrum is recorded in the absence of the pre-chirped pump pulse. (2) Then, the probe spectrum is measured with the THz (i.e., in the presence of the chirped pump pulse). (3) Finally, the ratio of the difference between these signals to the chirped pulse spectrum is calculated. This ratio is proportional to the electric field of the THz pulse since it has been established that the EO retrieved THz in Equation (7) is identical to the measured electric waveform of the THz spectrum in Equation (4). Prior to performing the THz field retrieval, the chirped probe is characterized once at the beginning of the experiment by a FROG device. This is important to determine the spectral phase $\phi(\omega)$ of the probe, from which the frequency-time calibration is obtained. Since each temporal slice of the THz field is projected onto different frequency components in the chirped probe, the THz field can be reconstructed from the direct mapping of frequency to time. Our set-up is cost-effective and less bulky. Though it provides the avenue to independently analyze the signals of the different polarization, only the data of the *s*-polarization is presented in the following section.

4. Results and Discussion

There are two possibilities to calibrate the time-frequency distribution to retrieve the duration of the THz signal, either by the FROG measurement of the chirped probe or its delay scan technique. The latter is a simple technique and involves translating the delay stage in order to observe a shift in the position of the corrugated pattern seen on top of the chirped probe due to the presence of the THz signal. However, the high order terms of the spectral term cannot be effectively estimated, leading to a loss of accuracy. Instead, we adopted the former to calibrate the THz signal.

This involved characterizing the chirped probe using a FROG technique to determine its spectral phase. The information about its spectral phase is then used to associate each frequency component to a time scale. During the THz-chirped probe interaction, we know that the THz signal overlaps on the chirped probe, so by mapping out the frequency region on which the THz signal lies, we construct the corresponding time scale for the THz signal. We have shown in Figure 3 the retrieved spectrogram of the chirped probe pulse measured by the FROG device. We performed a 3rd order polynomial curve fit (red line) for the spectral phase of the chirped probe (blue circles), as shown in Figure 3b. The group delay expression T_g, is then constructed from the coefficients of the fitted spectral phase. As such, a quadratic fit was obtained in which there is an observed linearity behavior within the spectral bandwidth of the chirped probe. We observed that it was possible to retrieve the THz signal by analyzing only one of the two polarization beams from the polarizer. Hence, an unbalanced detection was utilized to reconstruct the spectrally encoded THz signal. The optical spectrometer records the chirped probe signal in two sequences. The first measurement is taken in the absence of the pre-chirped pump to give rise to the unmodulated probe signal. This unmodulated probe which serves as the reference signal, is subtracted from the measurement taken afterward in the presence of the pre-chirped pump. The result of this subtraction is proportional to the product of the THz signal and the reference beam. To extract only the THz signal shown in Figure 4b we normalized accordingly. In a way to verify the reproducibility of the spectrometer signals, several shots were recorded, and a resemblance was observed among the shots from which the average signals of these shots are, as shown in Figure 4a. In the presence of the pre-chirped pump, the intensity of the chirped probe spectrum increased due to the overlapping THz signal.

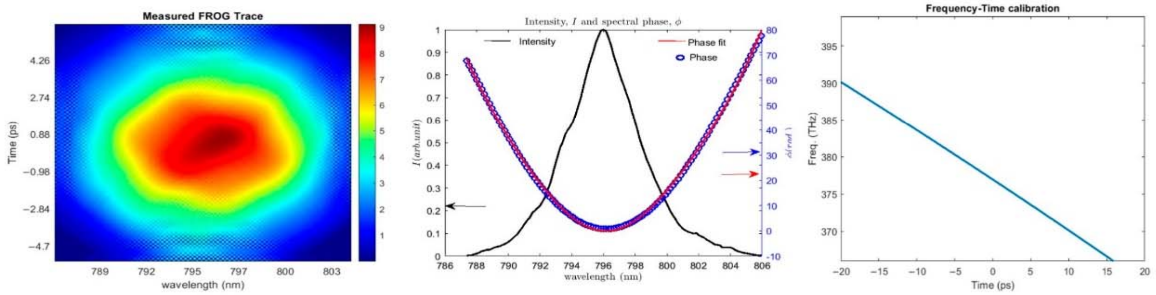

Figure 3. FROG trace of the 800 nm chirped probe pulse, spectral phase fit $\phi(\omega)$, spectrum and group delay derivation T_g. (**a**) the spectrogram of the retrieved FROG trace has well-defined regions. (**b**) The data from the retrieved FROG trace phase (blue circles) is used to create the third-order polynomial phase fit (red line). The bandwidth of the chirped probe spectrum (black line) is wide enough to accommodate THz signal. (**c**) The frequency-to-time calibration is extracted from the first-order derivative of the phase fit in which the cubic term in T_g, is ignored.

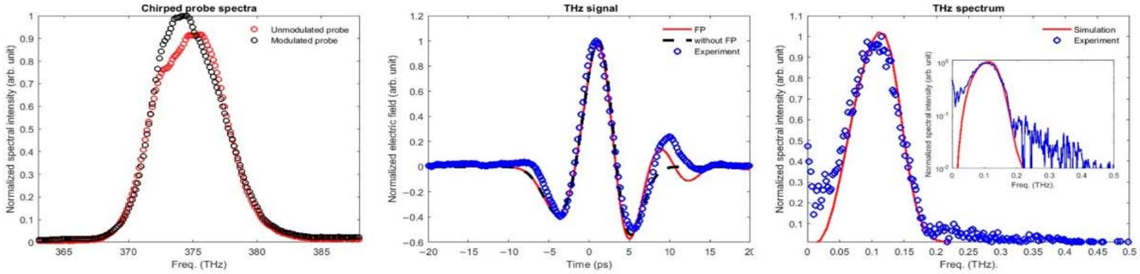

Figure 4. (**a**) Signal of the modulated and unmodulated chirped probe spectra recorded by the spectrometer in the presence and absence of the pump beam, respectively. The consistency in the spectra profile was confirmed by recording one hundred shots of each spectrum. The presence of the THz on top of the chirped probe tends to skew up the tip of the chirped probe. (**b**) The duration of the retrieved THz pulse is about 6.5 ps FWHM. The form of its shape is impacted by certain contributions. At the tail end of the field, there exists an amplitude difference between the experimental data (red circles) and simulation (blue line) due to Fabry–Pérot that gave rise to faster oscillations (**c**) The corresponding low-frequency narrow bandwidth spectrum is centered at 0.1 THz. The inset corresponds to the spectrum plotted in the log scale.

In the data analysis, only the polarization (s) of both the modulated and unmodulated probes were analyzed and presented. The measured THz pulse has an FWHM duration of 6.5 ps and exhibits few cycles of oscillations. The corresponding spectrum is centered at 100 GHz with a width of 100 GHz. The narrow bandwidth is due to the long pulse duration of the pump. This THz pulse is generated with a significant contribution of the backward THz component. There is a conspicuous impact of the Fabry–Pérot effect due to the reflection of the THz pulse at the boundary of the crystal. Though the duration of the chirped pulse is not long enough to reveal the entire oscillation length of the Fabry–Pérot effect, the calculated magnitude of the maximum reflected pulse is around 25 percent which is in agreement with our experimental plot. We also evaluated the signal-to-noise ratio from the measurement of 100 shots. It is evaluated between 5 and 20%. This value is mostly due to laser fluctuation.

It is most likely that an increase in the intensity of the pump pulse will increase the THz signal strength and heighten the effect of TPA on the chirped probe, which in turn will decrease the amplitude of the measured THz pulse. However, this was contrary to our observation in that the THz signal increased in magnitude (see Figure 5). As such, there is a reported negligible TPA effect that co-exists with the retrieved signal. Since the effect of TPA is negligible on the chirped probe, the huge number of photons in the pre-chirped pump freely participates in the DFG process, thus facilitating the optical THz conversion efficiency. In this work, the Kerr signal could not be isolated, contrary to the case of other works, where a temporally short pump pulse was used for pumping and in which the Kerr signal was situated around the overlap position between the probe and pump pulse, and lags the generated THz signal, making it possible to identify and isolate the Kerr signal to a certain extent [15,17]. We remark that since the presence of THz Kerr-like effect induced by the generated THz signal is less dominant in (110) ZnTe crystal as observed by He et al. [16], coupled with the fact that our experiment and theory are in good agreement with no significant deviation that warrants the skepticism about the presence of other effects, we believe that such cascaded nonlinear effects and Kerr effect are minimally present. Compared to the experimental data, the simulated THz signal indicates some deviations at the edges, most prominently at the right side edge because the faster oscillations in the THz waveform occur at that region. The corresponding narrow bandwidth THz spectral in Figure 4c has a peak frequency of around 0.1 THz and a cut-off at 0.2 THz. The high-frequency features in the spectrum correspond to the oscillatory part of the THz time-domain signal. The simulation and experimental data are in close agreement with only minor differences because the chirped probe is not long enough to properly retrieve the edges of the THz signal.

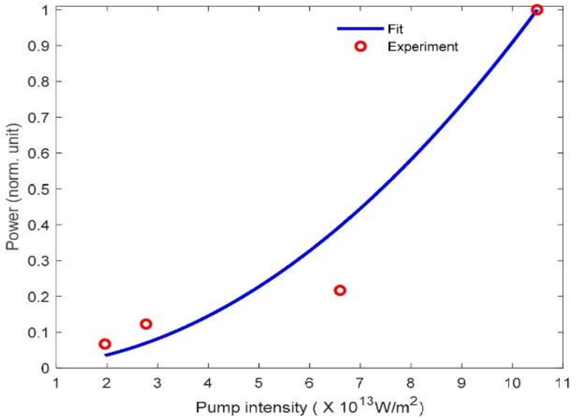

Figure 5. Influence of the pump pulse intensity on the THz signal power. The power law of the THz signal is a quadratic polynomial in terms of the pump intensity. Though the experimental data points (red circles) are few due to certain constraints, they seemingly follow the theoretical prediction (blue line).

The relationship between the pre-chirped pump intensity and THz power is shown in Figure 5. The fit (blue line) is a quadratic plot that follows the experimental data (red circles). We note that due to certain technical difficulties that arose in the laser source, only a few data points could be accurately illustrated. As earlier indicated, and in addition to the claim of the presence of the THz signal, this plot provides a conclusive note about excluding nonlinear effects in our set-up.

5. Conclusions

We have investigated the response of ZnTe crystal in the presence of a pre-chirped pump pulse. Our results indicate the feasibility of generating and detecting a few picosecond THz pulses in the same crystal. The THz pulse was characterized via the single-shot EO scheme with an accompanied high resolution. The experimental data conformed well to the predictions of optical rectification theory and the Fabry–Pérot effect with a negligible contribution of nonlinear effects such as TPA, Kerr, and Kerr-like effects. Furthermore, the polarization components of the THz-probe modulated beam were independently recovered, thanks to the simplicity and flexibility of the set-up. Usually, the set-up for THz sources and detection, which is huge and complex, does not facilitate their affordability and mobility for outdoor applications. So, there is often a need for an integrated system combining generation and detection in a miniature device. The quest for such compact THz spectroscopy systems has previously been realized using THz-integrated systems. The results of our findings further support the possibility of realizing photonic THz-integrated systems [42] with the use of ZnTe crystals.

The measured THz spectrum, which possessed a characteristic narrow bandwidth, finds useful application in condensed matter physics where the lattice vibration modes of certain solids are located within narrow frequencies; as such, broadband THz spectrums are not often suitable for their studies. With the use of narrow THz spectra, the dynamics of the phonon lattice vibration can be effectively investigated and consequently tailored to manipulate the electronic, structural and magnetic properties of the materials. With a tunable narrow-band THz spectrum, the excitation of selective phonon modes has previously been achieved [29]. Although we have generated a narrow-band THz spectrum at low frequency without focusing on the tunability of their spectrum, their frequencies can be tuned by adjusting the pump chirp rate via the separation distance between the gratings in the laser source. The choice between the selection of the bandwidth and chirp rate of the chirped probe used in this detection scheme was a compromise between the temporal window and the resolution of our measurement.

With the feature of a single-shot detection scheme, short-lived or instantaneous atomic and molecular processes have been captured in the past. In addition, molecular dynamics occurring on a fast time scale, such as laser-induced material damage, chemical reactions, and shock wave-induced structural phase transformations [31], have been monitored previously. Therefore, we propose that certain modifications in the pump's path of our set-up can be introduced in order to convert it to a time-resolved spectroscopy set-up.

Author Contributions: Conceptualization, D.B. and M.E.O.; methodology, D.B. and M.E.O.; software, F.F. and M.E.O.; validation, P.M. and D.B.; formal analysis, D.B. and M.E.O.; investigation, M.E.O.; resources, P.M.; data curation, F.F. and M.E.O.; writing—original draft preparation, M.E.O.; writing—review and editing, P.M. and D.B.; visualization, M.E.O.; supervision, P.M. and D.B.; project administration, D.B. and M.E.O.; funding acquisition, P.M. and M.E.O. All authors have read and agreed to the published version of the manuscript.

Funding: This research was funded by Petroleum Technology Development Trust Fund (PTDF, Nigeria), PhD overseas scholarship scheme.

Institutional Review Board Statement: Not applicable.

Informed Consent Statement: Not applicable.

Data Availability Statement: Not applicable.

Conflicts of Interest: The authors declare no conflict of interest.

References

1. Cassar, Q.; Caravera, S.; MacGrogan, G.; Bücher, T.; Pfeiffer, U.; Zimmer, T.; Guillet, J.-P.; Mounaix, P. Terahertz refractive index-based morphological dilation for breast carcinoma delineation. *Sci. Rep.* **2021**, *11*, 6457. [CrossRef]
2. Guillet, J.-P.; Recur, B.; Frederique, L.; Bousquet, B.; Canioni, L.; Manek-Hönninger, I.; Desbarats, P.; Mounaix, P. Review of terahertz tomography techiques. *J. Infrared Millim. Terahertz Waves* **2014**, *35*, 382–411. [CrossRef]
3. Tonouchi, M. Cutting-edge terahertz technology. *Nat. Photonics* **2007**, *1*, 97–105. [CrossRef]
4. Lee, Y.S. Terahertz Spectroscopy of Condensed Matter. In *Principles of Terahertz Science and Technology*; Springer: Boston, MA, USA, 2009; pp. 295–326. [CrossRef]
5. Jewariya, M.; Nagai, M.; Tanaka, K. Ladder Climbing on the Anharmonic Intermolecular Potential in an Amino Acid Microcrystal via an Intense Monocycle Terahertz Pulse. *Am. Phys. Soc.* **2010**, *105*, 203003. [CrossRef] [PubMed]
6. Peter, S.; Martina, B.; Stefano, B.; János, H.; Mikhail, K.; Alexey, Y.N.; Georgii, S.; Zoltán, T.; Vitali, Z.; Vitaliy, G. Matter manipulation with extreme terahertz light: Progress in the enabling THz technology. *Phys. Rep.* **2019**, *836–837*, 1–74. [CrossRef]
7. Mounaix, P.; Sarger, L.; Caumes, J.P.; Freysz, E. Characterization of non-linear Potassium crystals in the Terahertz frequency domain. *Opt. Commun.* **2004**, *242*, 631–639. [CrossRef]
8. Niessen, K.A.; Xu, M.; Markelz, A.G. Terahertz optical measurements of correlated motions with possible allosteric function. *Biophys. Rev.* **2015**, *7*, 201–216. [CrossRef] [PubMed]
9. Ajay, N.; Aniruddha, S.W.; Tony, F.H. A wideband coherent terahertz spectroscopy system using optical rectification and electro-optic sampling. *Appl. Phys. Lett.* **1996**, *69*, 2321–2323. [CrossRef]
10. Fülöp, J.A.; Tzortzakis, S.; Kampfrath, T. Laser-Driven Strong-Field Terahertz Sources. *Adv. Opt. Mater.* **2020**, *8*, 1900681. [CrossRef]
11. Chen, Q.; Tani, M.; Jiang, Z.P.; Zhang, X.C. Electro-optic transceivers for terahertz-wave applications. *J. Opt. Soc. Am. B* **2001**, *18*, 823–831. [CrossRef]
12. Rice, A.; Jin, Y.; Ma, X.F.; Zhang, X.C.; Bliss, D.; Larkin, J.; Alexander, M. Terahertz optical rectification from <110> zinc-blende crystals. *Appl. Phys. Lett.* **1994**, *64*, 1324–1326. [CrossRef]
13. Ku, S.A.; Tu, C.M.; Chu, W.C.; Luo, C.W.; Wu, K.H.; Yabushita, A.; Chi, C.C.; Kobayashi, T. Saturation of the free carrier absorption in ZnTe crystals. *Opt. Express* **2013**, *21*, 13930–13937. [CrossRef] [PubMed]
14. Vidal, S.; Degert, J.; Tondusson, M.; Oberlé, J.; Freysz, E. Impact of dispersion, free carriers, and two-photon absorption on the generation of intense terahertz pulses in ZnTe crystals. *Appl. Phys. Lett.* **2011**, *98*, 191103. [CrossRef]
15. Caumes, J.P.; Videau, L.; Rouyer, C.; Freysz, E. Kerr-like nonlinearity induced via terahertz generation and the electro-optical effect in zinc blende crystals. *Phys. Rev. Lett.* **2002**, *89*, 047401. [CrossRef]

16. He, W.Q.; Gu, C.M.; Shen, W.Z. Direct evidence of Kerr-like nonlinearity by femtosecond Z-scan technique. *Opt. Express* **2006**, *14*, 5476–5483. [CrossRef]
17. Dong, L.; Guohong, M. Pump-wavelength dependence of terahertz radiation via optical rectification in (110)-oriented ZnTe crystal. *J. Appl. Phys.* **2008**, *103*, 123101. [CrossRef]
18. Zhen, T.; Changlei, W.; Qirong, X.; Jianqiang, G.; Yanfeng, L.; Mingxia, H.; Lu, C.; Qingyue, W. Quantitative analysis of Kerr nonlinearity and Kerr-like nonlinearity induced via terahertz generation in ZnTe. *Appl. Phys. Lett.* **2008**, *92*, 041106. [CrossRef]
19. Xiaoshu, C.; Shan, H.; Zhen, S.; Fu, L.Z.; Xu, K.Y.; Gang, W.; Reng, W.; Ning, D. Influence of nonlinear effects in ZnTe on generation and detection of terahertz waves. *J. Appl. Phys.* **2009**, *105*, 023106. [CrossRef]
20. Chen, Q.; Zhiping, J.; Tani, M.; Zhang, X.-C. Electrooptic terahertz transceiver. *Electron. Lett.* **2000**, *36*, 1298–1299. [CrossRef]
21. Tie-Jun, W.; Yanping, C.; Claude, M.; Francis, T.; Marc, C.; Jacques, D.; See, L.C. High energy terahertz emission from two-color laser-induced filamentation in air with pump pulse duration control. *Appl. Phys. Lett.* **2009**, *95*, 131108. [CrossRef]
22. Erschens, D.N.; Turchinovich, D.; Jepsen, P.U. Optimized Optical Rectification and Electro-optic Sampling in ZnTe Crystals with Chirped Femtosecond Laser Pulses. *J. Infrared Millim. Terahz Waves* **2011**, *32*, 1371–1381. [CrossRef]
23. Vidal, S.; Degert, J.; Tondusson, M.; Freysz, E.; Oberlé, J. Optimized terahertz generation via optical rectification in ZnTe crystals. *J. Opt. Soc. Am. B* **2014**, *31*, 149–153. [CrossRef]
24. József, A.F.; László, P.; Matthias, C.H.; János, H. Towards generation of mJ-level ultrashort THz pulses by optical rectification. *Opt. Express* **2011**, *19*, 15090–15097.
25. Weling, A.S.; Auston, D.H. Novel sources and detectors for coherent tunable narrow-band terahertz radiation in free space. *J. Opt. Soc. Am. B* **1996**, *13*, 2783–2791. [CrossRef]
26. Krause, J.; Wagner, M.; Winner, S.; Helm, M.; Stehr, D. Tunable narrowband THz pulse generation in scalable large area photoconductive antennas. *Opt. Express* **2011**, *19*, 19114–19121. [CrossRef] [PubMed]
27. Silaev, A.A.; Romanov, A.A.; Vvedenskii, N.V. Generation of tunable mid- and far-infrared pulses during gas ionization by a chirped two-color laser field. *Opt. Lett.* **2020**, *45*, 4527–4530. [CrossRef]
28. Chefonov, O.V.; Ovchinnikov, A.V.; Hauri, C.P.; Agranat, M.B. Broadband and narrowband laser-based terahertz source and its application for resonant and non-resonant excitation of antiferromagnetic modes in NiO. *Opt. Express* **2019**, *27*, 27273–27281. [CrossRef]
29. Vicario, C.; Trisorio, A.; Allenspach, S.; Rüegg, C.; Giorgianni, F. Narrow-band and tunable intense terahertz pulses for mode-selective coherent phonon excitation. *Appl. Phys. Lett.* **2020**, *117*, 101101. [CrossRef]
30. Murakami, H. Terahertz Waveform Measurements Using a Chirped Optical Pulse and Terahertz Spectroscopy of Reverse Micellar Solution: Towards Time-resolved Terahertz Spectroscopy of Protein in Water. In *Terahertz Spectroscopy—A Cutting Edge Technology*; Intech Open: London, UK, 2017. [CrossRef]
31. Zhai, Z.H.; Zhong, S.C.; Li, J.; Zhu, L.G.; Meng, K.; Li, J.; Liu, Q.; Peng, Q.X.; Li, Z.R.; Zhao, J.H. Time-resolved single-shot terahertz time-domain spectroscopy for ultrafast irreversible processes. *Rev. Sci. Instrum.* **2016**, *87*, 095101. [CrossRef]
32. Stephanie, M.T.; Benjamin, K.O.; Christopher, A.W.; Keith, A.N. Invited Article: Single-shot THz detection techniques optimized for multidimensional THz spectroscopy. *Rev. Sci. Instrum.* **2015**, *86*, 051301. [CrossRef]
33. Koustuban, R.; Wenqian, R.H.; Sergio, C.; Emilio, A.N.; Damian, N.S.; Erich, P.I.; Franz, X.K. Theory of terahertz generation by optical rectification using tilted-pulse-fronts. *Opt. Express* **2015**, *23*, 5253–5276.
34. Klaus, R. Table-top sources of ultrashort THz pulses. *Rep. Prog. Phys.* **2007**, *70*, 1597.
35. Faure, J.; Van, T.J.; Kaind, R.A.; Leemans, W.P. Modelling Laser-Based Table-Top THz Sources: Optical Rectification, Propagation and Electro-Optic Sampling. *Opt. Quantum Electron.* **2004**, *36*, 681–697. [CrossRef]
36. Matlis, N.H.; Plateau, G.R.; Tilborg, J.V.; Leemans, W.P. Single-shot spatiotemporal measurements of ultrashort THz waveforms using temporal electric-field cross correlation. *J. Opt. Soc. Am. B* **2011**, *28*, 23–27. [CrossRef]
37. Jiang, Z.; Zhang, X.C. Measurement of spatio-temporal terahertz field distribution by using chirped pulse technology. *IEEE J. Quantum Electron.* **2000**, *36*, 1214–1222. [CrossRef]
38. Jiang, Z.; Zhang, X.C. Electro-optic measurement of THz field pulses with a chirped optical beam. *Appl. Phys. Lett.* **1998**, *72*, 1945–1947. [CrossRef]
39. Yellampalle, B.; Kim, K.Y.; Rodriguez, G.; Glownia, J.H.; Taylor, A.J. Algorithm for high-resolution single-shot THz measurement using in-line spectral interferometry with chirped pulses. *Appl. Phys. Lett.* **2005**, *87*, 211109. [CrossRef]
40. Kim, K.Y.; Yellampalle, B.; Rodriguez, G.; Averitt, R.D.; Taylor, A.J.; Glownia, J.H. Single-shot, interferometric, high-resolution, terahertz field diagnostic. *Appl. Phys. Lett.* **2006**, *88*, 041123. [CrossRef]
41. Trebino, R.; DeLong, K.W.; Fittinghoff, D.N.; Sweetser, J.N.; Krumbugel, M.A.; Richman, B.A.; Kane, D.J. Measuring ultrashort laser pulses in the time-frequency domain using frequency-resolved optical gating. *Rev. Sci. Instrum.* **1997**, *68*, 3277. [CrossRef]
42. Dekorsy, T.; Auer, H.; Waschke, C.; Bakker, H.J.; Roskos, H.G.; Kurz, H.; Wagner, V.; Grosse, P. Emission of Submillimeter Electromagnetic Waves by Coherent Phonons. *Phys. Rev. Lett.* **1995**, *74*, 738–741. [CrossRef] [PubMed]

Investigation of Oil Shale Response Using Terahertz-Time Domain Spectroscopy

By

Moses Eshovo Ojo*α, Patrick Mounaix* and Damien Bigourd*#

Abstract

Oil shale is an unconventional source of fuel distributed across the world with only few active explorations due to the competitive advantage price of crude oil and natural gas. However, oil shale holds important application in the context of a decline in the crude oil reserves and a spike in the oil prices. In order to prepare for the futuristic tail off in the conventional oil sources, efforts are since geared towards evaluating the oil yield potential of oil shale of different countries. In this work, a concise summary of related research in the study of oil shale analysis with particular emphasis on the Nigerian oil shale was investigated. We identified the shortcomings in the adopted techniques and suggested the complementation of a Terahertz-Time Domain Spectroscopy THz-TDS. Other than the indigenous Fischer Assay method of oil shale analysis, a combination of at least one other technique is usually incorporated in the analysis. The potential of the supplementary THz-TDS technique to yield perceptive results was addressed with promising recommendations to enhance the performance of the technique.

Keywords: Oil shale, THz-TDS, kerogen, oil yield, shale oil and oil shale-gas.

Introduction

Oil shale is a combustible source rock, composed of minerals and organic matter i.e. kerogen. The kerogen content of the oil shale are insoluble substances dispersed within the matrix of the inorganic minerals[1 2 3]. Oil shale is capable of generating oil and other petroleum products when subjected to pyrolytic reaction. Heating oil shale to a sufficiently high temperature causes the chemical process of pyrolysis to yield volatile vapours. The moisture content of the oil shale is firstly removed, then bitumen is formed. Bitumen is usually produced as an intermediate product during the decomposition of oil shale, with only rare exceptions. Subsequent heating of the bitumen will yield the volatile vapours which upon cooling, the shale oil will be separated from the oil shale-gas. The residue following the decomposition of the oil shale is an ash referred to as

---

[*] Université de Bordeaux, IMS UMR CNRS 5218, Bordeaux, France

[α] Corresponding email:moses-eshovo.ojo@u-bordeaux.fr

[#] Corresponding email: damien.bigourd@u-bordeaux.fr

[1] R. Bouamoud, E. Moine, R. Mulongo-Masamba, A. Hamidi, M. Halim , S. Arsalane (2020) .Type I kerogen-rich oil shale from the Democratic Republic of the Congo: mineralogical description and pyrolysis kinetics. *Petroleum science*, 17, 255–267.

[2] X. Miao, M. Chen, Y. Li, H. Zhan, K. Zhao, W. Yue (2020). Simultaneous determination of organic distribution and content in oil shale by terahertz imaging. *Energy and Fuels* 34(2), 1664-1668.

[3] K. Alstadt, D. Katti, K. Katti (2012). An *in situ* FTIR step-scan photoacoustic investigation of kerogen and minerals in oil shale. *Spectrochimica Acta Part A* 89, 105– 113.

semi-coke[4 5 6 7]. Shale oil and oil shale-gas are chemically identical to the products of fossil fuel, and thus serve as a substitute for conventional crude oil and natural gas, respectively. By adopting an efficient mining technique, they could be particularly useful when the price of crude oil rises or when the hydrocarbon reserves of the fossil fuel is no longer economical for exploration[8 9 10 11].

$$\textbf{Kerogen} \xrightarrow{\textbf{pyrolysis}} \textbf{moisture + bitumen}$$

$$\textbf{Bitumen} \xrightarrow{\textbf{pyrolysis + cooling}} \textbf{oil + gas + semi-coke} \tag{1}$$

Oil shale in widespread deposits has been reported in countries such as United States of America (USA), Estonia, China, and Brazil. USA has the largest oil shale reserve in the world, with the total of 3340 billion tons. Other countries with considerable amount of oil shale reserves includes among others; China, Israel, Romania, Egypt, Nigeria, Germany, Jordan, Morocco, Turkey, and Canada[12 13 14]. The first oil shale in Nigeria, was found in Lopkanta area of Imo state, and therefore called Lopkanta oil shale. Lokpanta is geologically situated in the Lower Benue Trough of Nigeria. The Oil shale reserve of the region has been estimated as 5.76 billion tones, of which 1.70 billion barrels are recoverable[15 18]. Moreover, economic feasibility studies on the exploration of the Lokpanta oil shale has endorsed its potential to supply petroleum products even after the supposed end of crude oil supply in the year 2057[16 17]. Since the discovery of the Lokpanta oil shale, there have been only a few numbers of experimental works to quantitatively identify their oil yield

---

[4] Y. Ma, S. Zhou, J. Li, Y. Li, K. Chen, Y. Zhang, D. Fu (2018). Pyrolysis characteristics analysis of Chang-7 oil shale using thermal analysis and pyrolysis-gas. *Energy Exploration & Exploitation*, 36(5), 1006–1021.

[5] M. Al-Harahsheh, O. Al-Ayed, J. Robinson, S. Kingman, A. Al-Harahsheh, K. Tarawneh, A. Saeid, R. Barranco (2011). Effect of demineralization and heating rate on the pyrolysis kinetics of Jordanian oil shales. *Fuel Processing Technology*, 92, 1805–1811.

[6] W. Qing, S. Baizhong, H. Aijun, B. Jingru, L. Shaohua (2007). Pyrolysis characteristics of Huadian oil shales. *Oil Shale*, 24 (2), 147–157.

[7] P. Williams, H. Chishti (2000). Two stage pyrolysis of oil shale using a zeolite catalyst. *Journal of Analytical and Applied Pyrolysis*, 55, 217–234.

[8] . A. Akash, J. O. Jaber (2003). Characterization of shale oil as compared to crude oil and some refined petroleum products. *Energy Sources*, 25, 1171–1182.

[9] D. Fenton, H. Henning, R. Richardson (2009). The chemistry of shale oil and its refined products. *Oil Shale, Tar Sands, and Related Materials*, Chapter 21 pp 315-325.

[10] L. Zhang, X. Zhang, S. Li, Q. Wang (2012). Comprehensive utilization of oil shale and prospect analysis. *Energy Procedia*, 17, 39 – 43.

[11] Q. Yanga, Q. Yang, Y. Man, D. Zhang, H. Zhou (2020). Technoeconomic and environmental evaluation of oil shale to liquid fuels process in comparison with conventional oil refining process. *Journal of cleaner production*, 255, 120198.

[12] N. E. Altun, C. Hicyilmaz, J.Y. Hwang, A. S. Bagci, M. V. Kok (2016). Oil shales in the world and Turkey; reserves, current situation, and future prospects: A review. *Oil shale*, 23(3), 211-227.

[13] J. Bartis, T. Tourrette, L. Dixon, D. Peterson, G. Cecchine (2005). Oil shale developments in the United States; prospects and policy issues. Published by RAND cooperation, ISBN 0-8330-3848-6.

[14] J. Dyn (2006). Geology and resources of some world oil-shale deposits. *Scientific Investigations Report*, series number 2005-5294.

[15] O. Ehinola, O. Sonibare, O. Akanbi (2005). Economic evaluation, recovery techniques and environmental implications of the oil shale deposits in the Abakiliki Anticlinorium, Southeastern Nigeria. *Oil Shale*, 22(1), 5-19.

[16] L. Osuji (2015). The future of petroleum in Nigeria and prospects of shale oil as an alternative energy supplier. *J. chem. soc. Nigeria*, 40 (1), 1-4.

[17] A. Okon, D. Olagunju (2017). Economic estimation of oil shale development methods in Nigeria. *J. of Scientific and Eng. Research*, 4(9), 397-408.

potential. In this present work, we aim to present a summary of these works up till date, and thereafter propose the inclusion of Terahertz-Time Domain Spectroscopy (THz-TDS) to investigate the oil shale. This paper is mainly divided into two parts. The first part which describes the current analysis methods carried out to study the Nigeria oil shale, begins with important geochemical and biological indicators employed in the study of the oil shale – it follows by the individual techniques employed till date, and ends with a suggestive note on incorporating a supplementary technique to the already employed techniques. Part two makes a brief review of the THz-TDS as the supplementary technique in the characterization of the oil shale and concludes with a possible proposal to effectively improve the performance of the oil shale THz-TDS.

Investigation of The Nigerian Oil Shale Laboratory Techniques.

The first part of this paper begins with a preliminary study of key terminologies as applied to oil shale analysis. It highlights the commonest characterization methods employed to analyse oil shale with particular emphasis to the Nigerian oil shale.

a) Indicators of oil shale yield

Geochemical analysis is a quite common technique used to determine among others; the Total Organic Carbon (*TOC*) and Extractable Organic Matter (*EOM*) of the oil shale. The information obtainable from such analysis, are often supplemented with results from Rock Eval pyrolysis technique to determine other important oil yield parameters such as oil yield due to superficial heating S_1, maximum oil high yield due to sufficient heating S_2, pyrolytic temperature at maximum oil yield T_{max}.The kerogen content i.e. maturity type, kerogen type and kerogen quantity of the oil shale is primarily responsible for their oil yields[18]. There are indicators that have been used to evaluate the kind of the kerogen content. Below are some of them.

(i) *TOC*: This measures the percentage of organic carbon present in the oil shale. It has been established that there is a positive correlation between TOC and oil yields [18] [19] [20]. Mathematical relationships have been established, linking oil yield to TOC for some selected Green River oil shales in the US. Subsequent analysis of other similar Green River oil shales, and statistical treatment of the results, have produced considerably refined relationships of the form [21],

$$Oil\ wt\% = 0.8317\ X\ TOC - 0.251 \qquad (2)$$

Where, $Oil\ wt\%$ is the oil yield by percentage weight. The minimum amount of oil yield computed from the geochemical analysis of the oil shale in order to characterize them as a potential source rock, is estimated at $2.0\ wt\%$ [22].

---

[18] O. Sonibare, O. Ehinola, R. Egashira (2005). Thermal and geochemical characterization of Lokpanta oil shales, Nigeria. *Energy Conversion and Management*, 46, 2335–2344.

[19] C. Ekweozor, G. Un omah (1990). First discovery of oil shale in the Benue Trough, Nigeria. *Fuel*, 69(4), 502-508.

[20] L. Osuji, B. Antia (2002). An Infrared spectroscopic evaluation of the petroleum potentials of some oil shale from Lokpanta in the Lower Benue trough of Nigeria. *Journal of Applied Sciences & Environmental Management*, 6(1), 34-38.

[21] P. Williams (1983). Oil shales and their analysis. *Fuel*, 62(7), 756- 771.

[22] K. Peters, X. Xia, A.E. Pomerantz, O.C. Mullins (2016). Geochemistry applied evaluation of unconventional resources. *Evaluation and development*, Chapter 3, 71-125.

(ii) $S_1$and S_2: S_1 and S_2 evaluate the oil yield at minimal and high pyrolytic temperature respectively, in *mg/g*. While S_1 comprises of volatile hydrocarbon, S_2 consists of pyrolysable hydrocarbon[23]. A plot of either S_2 or *HI* against T_{max} have been used to determine maturity state of some other kerogen sources[24].

(iii) *HI*: *HI* represents the relative amount of hydrogen to organic carbon present in the oil shale. *HI* is inversely related to *TOC* as per

$$HI = \frac{S_2(mg/g)}{\% \, TOC} \, X \, 100 \tag{3}$$

A minimum *HI* value of $196 \, mgHC/g \, TOC$ is used as an indicator of high oil yielding oil shale[24].

(iv) Kerogen type: Oil shale kerogens can be classified based on their predominant hydrocarbon constituents. The types of kerogen present in an oil shale largely controls the type of hydrocarbons generated in the oil shale. Different types of kerogen contain different amounts of hydrogen relative to their carbon and oxygen composition. Accordingly, there are four types of kerogen namely, type I, type II, type III, and type IV kerogen[25]. Type I kerogen are most likely to yield large quantities of oil and are referred to as oil prone, the type II kerogen have tendencies to yield both oil and gas and are sometimes referred to as oil & gas prone kerogen, the type III kerogen are gas prone; yielding high amount of gas, while the type IV are relatively inert under pyrolysis. A Van Krevelen diagram as shown in Fig.1 is a standard plot of Hydrogen Index (*HI*) against Oxygen Index (*OI*), commonly used to identify the kerogen type of an oil shale. The diagram has four curves which are indicatives of different kerogen type. In order to determine the kerogen type, it is customary to plot the *HI* and *OI* data of the oil shale on the Van Krevelen diagram. Fig. 1 illustrates the classification criteria of the kerogen.

(v) T_{max}: T_{max} is the maximum temperature of the oil shale pyrolytic process that corresponds to the optimum oil yield. $T_{max} > 460℃$ is the minimum temperature for efficient oil yield from an oil shale[18]

---

[23] O. Faboya, O. Sonibare, J. Xu, B. Cheng, Q. Deng, Z. Wei, A. Olowookere, Z. Liao (2019). Geochemical characterisation of Lower Maastrichtian Mamu Formation kerogens, Anambra Basin, Nigeria. *Earth Environ. Sci.* 360, 012015.

[24] B. SarkiYandoka, W. Abdullah, M. Abubakar, M. Hakimi, A. Jauro, A. Adegoke (2016). Organic geochemical characterization of shallow marine Cretaceous formations from Yola Sub-basin, Northern Benue Trough, NE Nigeria. *Journal of African Earth Sciences*, 117, 235-251.

[25] H. Dembicki (2009). Three common source rock evaluation errors made by geologists during prospect or play appraisals. *AAPG Bulletin*, 93(3), 341–356.

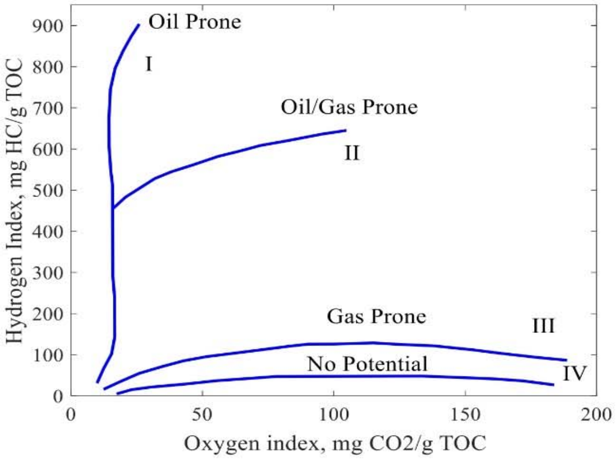

Fig.1. An example of Van-Krevelan diagram for the type I, II, III and IV kerogen.

(vi) Origin and depositional environment: Oil shale kerogen is formed millions of years ago following the decomposition of organic matter under high pressure either in the presence or absence of oxygen. The source of these organic matter (terrestrial or aquatic) and their depositional environment (anoxic, suboxic or oxic) plays important roles in determining the quality and type of kerogen in the oil shale. For example, the distribution of n-alkanes i.e. the relative fraction of short and long chain n-alkanes of an oil shale in a typical Gas chromatography plot, can be used to classify kerogen types and hence provide an idea about their origin. Moreover, the Pristane(Pr)/Phystine(Ph) ratio from the chromatography data can be used to determine the depositional environment of the organic matter. A Pr/Ph ratio in the range 1.0 - 3.0, indicates sub-oxic depositional conditions, while the Pr/Ph ratios above 3.0 and below 0.6 indicate oxidizing and anoxic conditions, respectively[26] [27] [28].

(vii) Production index (PI): PI indicates the maturity level of the oil shale. In comparison to HI, it is computed from Rock Eval pyrolysis. PI data must be interpreted with caution because they could be misleading especially when the S_1yields includes contribution from drilling additives and migrated hydrocarbons other than indigenous oils. PI ratio greater than 0.1 are indications of mature oil shale source rock. PI is related to S_1 and S_2 as per[18]

---

[26] W. He, Y. Sun, W. Guo, X. Shan, S. Su, S. Zheng, S. Deng ,S. Kan, X. Zhang (2019). Organic geochemical characteristics of the upper Cretaceous Qingshankou Formation oil shales in the Fuyu oilfield, Songliao Basin, China: Implications for oil-generation potential and depositional environment. *Energies* 12, 4778.

[27] M. Kok, I. Senguler, H. Hufnagel, N. Sonel (2001). Thermal and geochemical investigation of Seyitomer oil shale. *Thermochimica Acta*, 371, 111-119.

[28] G. Wang, M. Sun, S. Gao, L. Tang (2018). The origin, type and hydrocarbon generation potential of organic matter in a marine-continental transitional facies shale succession (Qaidam Basin, China). *Sci Rep*, 8, 6568.

$$PI = \frac{S_1}{S_1+S_2} \quad (4)$$

(viii) *EOM*: The directly measured quantity of bitumen, i.e. the soluble organic matter of oil shale, is referred to as *EOM*. The amount of bitumen increases with the maturity state of the oil shale. *EOM* in the oil shale can be computed from the geochemical analysis results. The minimum required *EOM* for a source rock to be classified as a potential oil source is about $500\ ppm$ [18].

(ix) Rock Eval oil yield: The Rock Eval oil yield is dependent on the S_1 and S_2 results following from the Rock Eval Pyrolysis. The Rock Eval oil yield is related to the Fischer Assay oil yield (*FAY*) as per

$$\text{Fischer Assay oil yield } (1\text{tonne}^{-1}) = 1.03(S_1 + S_2) + 7.23 \quad (5)$$

The relationship in (5) allows a direct comparison between these two quantities. A *FAY* of $42\ 1\text{tonnes}^{-1}$ is the minimum yield for economic exploration[19].

b) Adopted techniques of the Nigerian oil shale characterization

The initial field identification of potential oil shale deposits can be achieved by visual aid through simple examination of physical properties, e.g., colour, streak, specific gravity, smell etc[21]. The Nigerian oil shale which is typically dark-grey, laminated, and fissile in appearance has been found as outcrops and subcrops deposits in Lokpanta village of Imo state[19]. Several techniques have been employed to characterize the Nigerian oil shale namely: the Fischer Assay method supported by geochemical analysis, Infra-Red Spectroscopy Analysis, Gas Chromatography-Mass Spectrometer (GC-MS) and Thermal Analysis (ThermoGravimetric, TGA & Differential Thermal Analysis, DTA). As no single method is ideal[29] [30], a combination of two or more of these techniques were employed by the researchers. The Fischer Assay method involves the collection and evaluation of evolved shale oil during pyrolysis. Geochemical analysis in addition to Rock Eval-pyrolysis are often carried out to determine the indicators of the oil shale i.e. *TOC*, S_1, S_2, oil yield etc. A positive correlation between *TOC* and Fischer Assay oil yields, for example, is predominantly observed[21] [31] [32] [33] .Through the use of optics, the infra-red spectroscopy has provided a rapid means of estimating kerogen's aliphatic, aromatic, and alicyclic carbon contents, that are related to oil

---

[29] A. Mohammed, C. Peter, C. Alan (2012). Evaluation of several methods of extraction of oil from a Jordanian oil shale. *Fuel*, 92(1), 281-287.

[30] Z. El-Rub, J. Kujawa, E. Albarahmieh, N. Al-Rifai, F. Qaimari, S. Al-Gharabli (2019). High throughput screening and characterization methods of Jordanian oil shale as a case study. *Energies* 12, 3148.

[31] C. Gülamber, K. Ibrahim, S. Aljurf, H. Rahman (2019). Introduction of analytical methods for oil shale resource evaluation. IMCET, Antalya, Turkey, April 16 – 19.

[32] M. Barakat, E. El-Gawad, M. Gaber, M. Lotfy, A. Ghany (2019). Mineralogical and Geochemical Studies of Oil Shale Deposits in the Cretaceous/Paleogene succession at Quseir Area, Egypt. *Egyptian Journal of Petroleum*, 28, 11–19.

[33] I. Johannnes, K. Kruusement, R. Veski, J. Bojesen-Koefoed (2006). Characterisation of pyrolysis kinetics by rock-eva basic data. *Oil Shale*, 23(3), 249–257.

yields[34] [35] [36] [37]. The use of Gas chromatography-Mass Spectrometer provided fingerprint information for separating particular fractions in the kerogen; for example, the n-chain alkanes, and their subsequent identification[38] [39] [40] [41]. Another technique of importance is the thermal analysis, which involves subjecting the oil shale to increasing thermal condition. It differs from Fischer Assay Method, in that oil yield is not directly measured and no oil is collected. It studies the weight loss, kinetics of kerogen decomposition and the associated activation energy[42] [43] [44] [45]. The DTA curve of other country's kerogen has shown, that kerogen decomposition is highly exothermic in nature with high quantity of heat released which can be useful for domestic and industrial application[46] [47].

In the foremost scientific work on the Lopkanta oil shale, Chukwuemeka *et al.* collected outcrop and subsurface samples from three different locations and within 1.5 x 1.0 km belt respectively which were analysed via geochemical analysis and GC-MS analysis. The subsurface samples were retrieved from a 25.5m well at regular intervals. The average value of the estimated *FAY* of the outcrop and subcrop samples which exceeded the minimum required value was $51\ (1\text{tonne}^{-1})$ and $40.8\ (1\text{tonne}^{-1})$ respectively. The *TOC* of the outcrop and subcrop sample which were $4.6 - 7.4\ wt\%$ and $4.1 - 6.8\ wt\%$ respectively exceeded the minimum required *TOC*. The *PI* and T_{max} of both samples indicate that the oil shales are of intermediate maturity. The maturity of the subsurface samples was found to increase with depth. The *FAY* was well correlated with the geochemical results i.e. *TOC*, except for *EOM*. Regions with the lower *EOM*

---

[34] S. Palayangoda, Q. Nguyen (2012). An ATR-FTIR procedure for quantitative analysis of mineral constituents and kerogen in oil shale. *Oil Shale*, 29(4), 344–356.

[35] B. Chen, X. Han, X. Jiang (2016). In-situ FTIR analysis of the evolution of functional groups of oil shale during the pyrolysis. *Energy and fuels*, 30(7), 5611–5616.

[36] H. Ganz, W. Kalkreuth (1987). Application of infrared spectroscopy to the classification of kerogen types and the evaluation of source rock and oil shale potentials. *Fuel*, 66(5), 708-711

[37] M. Mroczkowska-Szerszeń, K. Ziemianin, P. Brzuszek, I. Matyasik, L. Jankowski (2015). The organic matter type in the shale rock samples assessed by FTIR-ATR analyses. *Nafta-Gaz*, 71(6), 361-369.

[38] W. Wang, S. Li, Y. Liu, D. Qiu, Y. Ma, J. Wu (2005). Analysis of the chemical constitutions of Yaojie shale oil in China by gas chromatography–mass spectrometry (GC–MS). *WIT Transactions on Ecology and The Environment*, 206, 91-100

[39] W. Blum, P. Ramstein, G. Eglinton (1990). Coupling of high temperature glass capillary columns to a Mass Spectrometer, GC/MS analysis of metalloporphyrins from Julia Creek oil shale samples. *Journal of high resolution chromatography*,13, 85-93.

[40] A. Al-Zuheri, H. Rashad, Ali Maliki, H. Hussain, N. Al-Ansari (2018). Determination of the chemical structure of the Iraqi oil shale and its hydrocarbon forms. *Engineering*, 10, 7-20.

[41] N. Ristic, M. Djokic, A. Konist , K. Geem, G. Marin (2017). Quantitative compositional analysis of Estonian shale oil using comprehensive two dimensional gas chromatography. *Fuel processing technology*, 167, 241–249

[42] A. Aboulkas, K. El-harfi, M. Nadifiyine, M. Benchanaa (2011). Pyrolysis behaviour and kinetics of Moroccan oil shale with polystyrene. *Journal of Petroleum and Gas Engineering*, 2(6), 108-117.

[43] N. Al-Ananzeh, M. L. Al-Smadi, A. Dawagreh (2018). Thermogravimetric and composition analysis of Jordanian oil shale. *Energy resources*, 40(11), 1374-1379.

[44] Z. Hua, Q. Wang, C. Jia, Q. Liu (2019). Pyrolysis kinetics of a Wangqing oil shale using thermogravimetric analysis. *Energy Science & Engineering*, 7(3), 912- 920.

[45]. M. Kok and E. Ozgur (2016). Combustion performance and kinetics of oil shales *Energy Sources*, 38(8), 1039–1047.

[46] T. Pihu, H. Arro, A. Prikk, T. Parve, J. Loosaar (2006). Combustion experience of Estonian oil shale in large power plants. International Conference on Oil Shale: "Recent Trends in Oil Shale", 7-9 November 2006, Amman, Jordan.

[47] A. Hepbasli (2004). Oil shale as an alternative energy source. *Energy, sources*, 26(2), 107-118.

corresponded to higher FAY, and vice versa. Their findings suggest that immature oil shale have more oil yields than mature ones. The GC-MS shows that the hydrocarbon has been composed of a mixture of type I and II kerogen, having marine algae origin. These marine algae were deposited in an anoxic condition[19].

Three years following the foremost work on the Lopkanta oil shale, a new technique was utilized to study the Lopkanta oil shale. In their work, Osuji *et. al,* subjected thirty outcrop samples to infra-red spectroscopy. The spectrum: a plot of Intensity against wavelength number (cm^{-1}), indicated absorption peaks at around $1600 - 1450\ cm^{-1}$ for a few of the samples. Absorption at this range is indicative of the presence of oil producing organic matter i.e. aromatic hydrocarbon. In addition to the spectroscopic technique, another analysis was carried out to determine the TOC; the outcrop samples were pulverized, and dissolved in series of chemicals, in order to extract the kerogen. The extracted kerogen was dried and weighed. By a simplified assumption, that the proportion of EOM is negligible, the weight of the dried kerogen was ultimately equivalent to TOC which measured between$0.98 - 8.75\ wt\ \%$. Based on the TOC values, they suggested, that the Lopkanta oil shales are mature[20].

Some years later, the research on the Lopkanta oil shale was revisited by researchers at the University of Ibadan, Nigeria. They assembled three outcrop samples labelled as LOA $21,\ 39$ & 75 (see [18] for the labelling codes), on which thermal analysis were performed. The kinetics of the oil shale decomposition revealed a two-consecutive reaction with bitumen as an intermediate product. During the first stage of the reaction i.e. at low temperature $25 - 100\ ℃$, a peak in the weight loss was recorded, corresponding to the loss of moisture. A second peak occurring at higher temperature, $300 - 570℃$ was observed in the second stage of the reaction which corresponds to the bitumen decomposition. The results from the weight loss amounted to decomposable kerogen values of $6.50 \pm 0.49,\ 4.55 \pm 0.18,\ 9.64 \pm 0.32\ wt\%$ respectively.These values generally surpassed the standard minimum decomposable kerogen of $0.5\ wt\ \%$. The results of the DTA curve and activation energy were well correlated with each other. The activation energy was maximum for the LOA 75 samples and minimum for the LOA 21 samples. Furthermore, geochemical analysis in addition to Rock Eval pyrolysis revealed the HI & T_{max} as $0.01,\ 0.01,\ 0.05$ & $427,\ 434,\ 431\ ℃$ respectively, showing the immaturity state of the oil shale. The reported TOC were $2.13,\ 3.91,$ & $3.12\ \ wt\%$, and the plot of the modified Van Krevelen diagram indicated a type II kerogen content[18].

c) Compendious note on the Nigerian oil shale analysis schemes

The foregoing techniques portrayed destructive testing and seemingly unrecoverable practice of the oil shale samples. An oil shale sample subjected to a particular analysis was destroyed due to the peculiarity of the chemical and thermal nature of the techniques. In this way, a particular oil shale cannot be subject to a subsequent analysis after the previous one. Thus, different samples, though selected from the same vicinity, are required for different analysis, instead of the usage of a unique sample for all characterization. We envisage that, comparison of the different analysis results might introduce error to the interpreted data. In addition to a source of misleading results, it is noted, that the delicacy of the oil shale may have been altered via crushing, heating, chemical treatment, and exposure to infra-red radiation[48 49]. Due to the above two reasons we recommend the usage of an analysis that preserves the state of the sample, to be incorporated in the analysis of the Nigerian Oil shale. The Terahertz-Time domain spectroscopy (THz-TDS) is a non-destructive technique that preserves the molecular configuration of the sample after analysis; such that, the exact sample is passed on for some other sort of analysis after previously subjected to an analysis[49 50]. As such, results from the data can be reliably deduced. In the following part, we discuss on the usage of THz-TDS to investigate the oil shale.

An Application Study of Thz-Tds in The Analysis Of Oil Shale

The last decades have experienced a tremendous generation of THz pulse both at large scale and table-top sources. The remarkable property of these pulses is attracting the attention of a wide community including industrialist and medical experts. THz pulses have enabled the study of a wide range of materials starting from cellular to non- living objects. In the framework of this paper, we limit our discussion to application of the THz pulse in the oil and gas industry. The part two of this work is sectioned to include the basic principle of THz pulse application in oil shale analysis, typical experimental setup involving oil shale characterization with THz pulse, correlation of THz experimental result with oil shale yields, and ends with viewpoints for future improvement on this technique.

a) Relevance of THz-TDS to oil shale.

THz pulses (0.1-10 THz) are electromagnetic waves, consisting of an electric and magnetic field component which vibrate sat right-angle to each other. Through interaction with a material, the electric component of the THz pulse is modified, of which the characteristics of the material are representatives of the alteration in the wave properties, thus information about the material may be deduced. This technique of material characterization is referred to as THz-TDS[51 52 53]. Materials such as wood, paper, fabrics, leather, plastic and rock samples are transparent in the THz frequency range, while metals and water are reflectors/absorbers of THz pulses[54]. In the case of materials that are THz-transparent, the comparison between the THz pulses transmitted through the material with respect to the incoming THz pulse can provide valuable information about the optical properties of the material.

Among its huge uses, the THz-TDS has strong applicability in the development of the oil industry, due to its non-destructive testing and strong interaction with organic matter. Conventional oil

---

[48] H. Zhan, Y. Wang, M. Chen, Ru Chen, K. Zhao, W. Yue (2020). An optical mechanism for detecting the whole pyrolysis process of oil shale. *Energy*, 190, 116343.

[49] Y. Li, X. Miao, H.Zhan, W. Wang, R. Bao, W. Leng, K. Zhao (2018). Evaluating oil potential in shale formations using Terahertz time domain spectroscopy. *Journal of Energy Resources Technology*, 140(3), 034501.

[50] W. Leng, H. Zhan, L. Ge, W. Wang, Y. Ma, Kun Zhao, S. Li, L. Xiao (2015). Rapidly determining the principal components of natural gas distilled from shale with terahertz spectroscopy. *Fuel,* 2015 159, 84-88.

[51] J. Haddad, B. Bousuet, L. Canioni, P. Mounaix (2013). Review in Terahertz spectral analysis, *Trends in Analytical Chemistry*, 44, 98-105.

[52] J. Guillet, B. Recur, L. Frederique, B. Bousquet, L. Canioni, I. Manek-Hönninger, P. Desbarats, P. Mounaix (2014). Review of terahertz tomography techniques. *J Infrared Milli Terahz Waves*, 35, 382–411.

[53] J. Lampin, G. Mouret, S. Dhillon, J. Mangeney (2020). THz spectroscopy for fundamental science and applications. *Photoniques*, 101, 33-38.

[54] R. Lewis (2107). Springer handbook of electronic and photonic material, Chapter 55 (Materials for THz engineering). 1339-1349.

source rocks and petroleum products have well been investigated via the THz-TDS[55] [56] [57] [58]. Attention, though minimal, has since been attracted to oil shale mining, since its first discovery in France around the mid-eighteenth century[59]. The kerogen constituent of the oil shale is a delicate and complex heterogeneous organic substance making up a small percentage by mass of the total weight of the oil shale. The organic component of the oil shale is of most importance in the oil industry since it determines the quality, and quantity of the oil yield. The vast majority of experiments involve probing this organic content. In the generalized study of oil shales of different country, several techniques have been employed for their investigations, including the Scanning Electron Microscope (SEM)/Transmission Electron Microscope (TEM) analysis, optical spectroscopy (e.g. Nuclear magnetic Resonance NMR, Raman, Ultra-Violet UV, Fourier Transform Infra-Red FTIR, and THz spectroscopy)[26] [60] [61] [62] [63] [64], as well as including those mentioned in II (b). In this part, we focus on the review of a particular type of optical spectroscopy application in the analysis of the oil shale-kerogen. Henceforth, the word 'kerogen' will be used to refer to oil shale-kerogen, except otherwise stated. The associated chemical bonds present in the kerogen Hydrocarbon (HC) absorbs selected frequency components in the optical pulse, and by analysing the optical spectrum, the relative percentage of the HC can be determined. As such, the nature of the kerogen can be deduced. In particular, the aromatic and functional groups which largely contributes to the oil yield of the oil shale, have rotational and vibrational modes within the THz frequency range. Therefore, observed THz spectra contain rich chemical information which is useful for petroleum-source analysis[49] [65] [66] . Moreover, the low photon energy of the THz pulse, allows a safe propagation through flammable liquids e.g. shale oil produced during the pyrolysis-THz-TDS experiment, without causing any danger of combustion[67]. Other than been able to provide abundant information on the intermolecular and intramolecular vibration modes,

---

[55] X. Miao, H. Zhan, K. Zhao (2017). Application of THz technology in oil and gas optics. *Science China Physics, Mechanics and Astronomy*, 60(2) 024231.

[56] R. Bao, F. Qin, R. Chen, S. Chen, H. Zhan, K. Zhao, W. Yue (2019). Optical detection of oil bearing in reservoir rock: Terahertz spectroscopy investigation. *IEE Acess*, 7, 121755- 121759.

[57] T. Lu, Z. Li, J. Bin, Z. Kun, Z. Qing, S. Lei, Z. Lin (2009). Optical property and spectroscopy studies on the selected lubricating oil in the terahertz range. *Science in China Series G: Physics, Mechanics & Astronomy*, 52(12) 1938-1943.

[58] H. Zhan, S. Wu, R. Bao, L. Ge, K. Zhao (2015). Qualitative identification of crude oils from different oil fields using terahertz time-domain spectroscopy. *Fuel*, 143, 189–193.

[59] C. Zou (2017). Unconventional Petroleum Geology, chapter 13 (oil shale), 371-387.

[60] J. Birdwell, K. Washburn (2015). Multivariate analysis relating oil shale geochemical properties to NMR relaxometry. *Energy Fuel*, 29, 2234−2243.

[61] S. Khatibi, M. Ostadhassan, D. Tuschel, T. Gentzis, H. Carvajal-Ortiz (2018). Evaluating molecular evolution of kerogen by raman spectroscopy: correlation with optical microscopy and Rock-Eval Pyrolysis. *Energies*, 11, 1406.

[62] K. Bake, A. Pomerantz (2017). Optical analysis of pyrolysis products of Green River Oil Shale. *Energy and Fuels*, 31(12), 13345–13352.

[63] Z. Zhang, H. Zhang, X. Yang, H. Jia (2016). Mineralogical characterization and washability of Longkou oil shale. *Energy Sources*, 38 (21), 3255-3261.

[64] X. Miao, M. Chen, Y. Li, H. Zhan, K. Zhao, W. Yue (2020). Simultaneous determination of organic distribution and content in oil Shale by Terahertz imaging. *Energy Fuels*, 34, 1664−1668.

[65] M. Yin, S. Tang, M. Tong (2015). The application of terahertz spectroscopy to liquid petrochemicals detection: A review. *Applied Spectroscopy Reviews*, 51(5), 379-396.

[66] H. Zhan, M. Chen, K. Zhao, Y. Li, X. Miao, H. Ye, Y. Ma, S. Hao, H. Li, W. Yue (2018). The mechanism of the terahertz spectroscopy for oil shale detection. *Energy*, 161, 46-51.

[67] F. Al-Douseri, Y. Chen, X. Zhang (2006). THz wave sensing for petroleum industrial applications. *International Journal of Infrared and Millimeter Waves*, 27(4), 481- 503.

the THz-TDS is also advantageous over other similar techniques such as the FTIR, in that, the amplitude and phase of the signal can be measured simultaneously[68].

b) Experimental setup

A typical THz-TDS setup in transmission mode, is shown in Fig. 2[69].The system consists of a laser source, optical chopper, delay stage, THz emitter [70], THz detector, two sets of parabolic mirrors (OAPMs), focusing lens (L1, L2), mirrors (M1, M2 M3 and M4) beam splitter (BS), oil shale sample and computer system. In this example, the detection scheme is made up of an Electro-Optic (EO) ZnTe crystal, wollaston prism, balanced photodiode, and lock-in-amplifier[71]. The optical and the THz beam pathways are shown in red and burgundy colours, respectively. The laser beam is split into two beams of high and low optical power by the BS; the high-power beam is used as the pump beam to generate the THz pulses, while the low-power beam is used as the probe beam to characterize the pulse. Single-cycle THz pulses generated by the THz emitter are focused by the first set of OAPMs onto the sample surfaces at normal incidence. The transmitted THz signal through the sample is collimated by the second set of the OAPMs and overlapped with the probe beam on the ZnTe. The information carried by the THz signal can be recovered by measuring its effect on the amplitude and phase of the probe beam. The QWP and Wollaston prism splits the signal into two beams and the balanced photodiode supplies the differential beam intensity to the lock-in-amplifier, where the lock-in amplifier and chopper amplifies the signal for noise free detection. By adjusting the time delay stage at a regular increasing interval, the probe beam will scan the entire length of the signal to produce a trace of the THz waveform. The measured amplitude of the THz signal is recorded on the computer at each time delay, until the full waveform of the signal is formed on the computer screen.

---

[68] J. Roux, F. Garet, J. Coutaz (2014). Physics and applications of terahertz radiation. Chapter 8 (Principles and applications of THz Time domain spectroscopy) , pp 203-231.

[69] H. Zhan, M. Chen, Y. Zhang, R. Chen, K. Zhao, W. Yue (2020). Utilization of oil shale as an electromagnetic wave absorbing material in the terahertz range. *IEEE Access*, 8, 46795-46801.

[70] J. Fülöp, S. Tzortzakis, T. Kampfrath (2020). Laser-driven strong-field terahertz sources. *Optical Mater*, 8, 1900681.

[71] M. Zhukova, E. Makarov, S. Putilin, A. Tsypkin, V. Chegnov, O. Chegnova, V. Bespalov (2017). Experimental study of THz electro-optical sampling crystals ZnSe, ZnTe and GaP. *Journal of Physics*, 917, 062021.

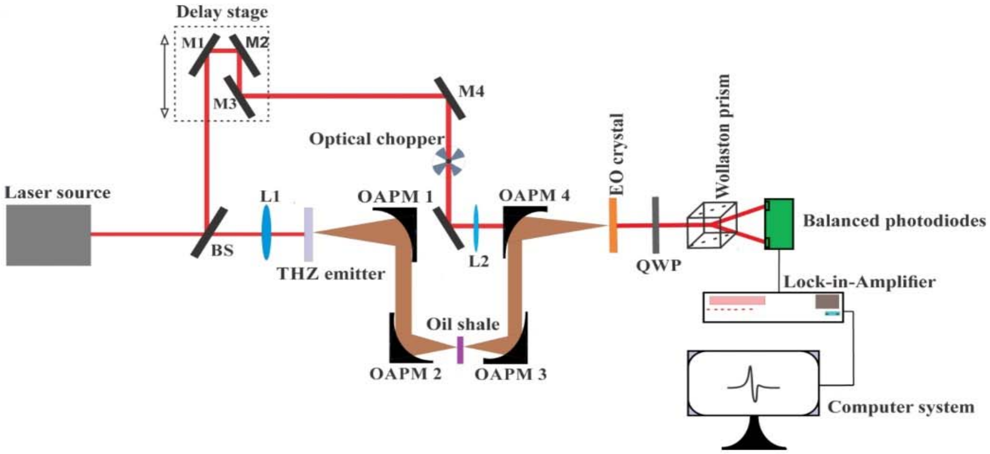

Fig. 2. A typical THz-TDS setup in the transmission mode. BS; Beam Splitter, L1-L2; Lens, M1-M4; Mirrors, OAPM1-OAPM4; Off Axis Parabolic Mirrors, QWP; Quarter Wave Plate.

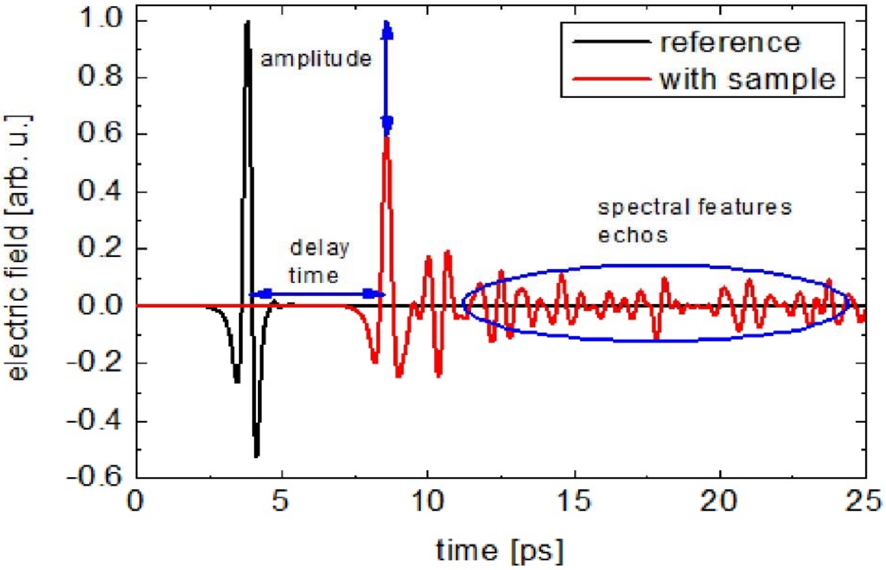

Fig. 3. The typically measured THz electric field signals. The reference (black) and sample (red) signal corresponds respectively to the detected THz pulse without and with the oil shale sample.

In order to visualize the effect of the sample on the THz pulse, the above experiment is usually performed without and with the sample. The signal obtained in the former and latter cases are respectively termed reference and sample signals. The waveform of these two signals often indicates obvious differences as shown in Fig.3. The sample signal is both delayed i.e. propagating at a lower speed and reduced in amplitude due to absorption and reflection at interfaces within the sample, as compared to the reference signal.

In practice, the signals are represented in the frequency domain in relation to each other as per [72];

$$T(\omega) = \frac{S_{sam}(\omega)}{S_{ref}(\omega)} = |T(\omega)|\, e^{-i\Delta\varphi(\omega)} \tag{6}$$

Where, ω is the THz frequencies, $\Delta\varphi(\omega)$ is the phase difference between the sample and reference signal. $|T(\omega)|$, is the transmission coefficient, and $T(\omega)$ is the complex transmittance signal. Afterwards, the $T(\omega)$ is analyzed, from which important optical properties of the oil shale can be deduced. In certain situations, the experimental setup in Fig. 2 can be adjusted in the reflection mode in order to obtain the complex reflectance signal, $R(\omega)$. In this configuration, the incoming THz pulse impinges on the sample at an inclined angle that ensures reflection. Xinyang *et al.* has utilized the reflectance configuration to generate subsurface images of the Hudian oil shale, by representing the peak amplitudes of the spectra obtained at different positions from the oil shale on a contrast image plot[64].

c) Optical properties of oil shale.

The inorganic constituent of oil shale comprises of minerals and water. Quartz, calcite, dolomite, and pyrite has been identified as been among the principal mineral constituent of oil shales[46 73 74]. During a THz-TDS at room temperature, THz pulse are mainly absorbed by the kerogen content, due to the fact, that the large macromolecules with aromatic compounds typically have vibration modes in the THz region around *0.5 – 4 THz.* When the THz-TDS is performed with a pyrolyzed oil shale sample, there are generally two major phases in the optical response of the kerogen to the THz waves. The first phase occurring at lower temperature, involves the evaporation of moisture from the oil shale thereby resulting to an increase in the strength of the transmitted THz signal. The second phase is typically characterized by a decrease in the strength of the THz pulse, due to absorption of the pulses at high temperature[49 75]. At such high temperature, the minerals are dissolved in water, then become generally conductive, and subsequently absorbing the THz pulse. Such responses are measured as the complex dielectric function of the oil shale.

$$\varepsilon(\omega) = \varepsilon_{real}(\omega) - i\varepsilon_{img}(\omega) \tag{7}$$

---

[72] M. Hangyo, M. Tani, T. Nagashima (2005). Terahertz Time-Domain Spectroscopy of solids:A review. *International Journal of Infrared and Millimeter Waves*, 26(12), 1661–1690.

[73] O. Sonibare, D. Jacob, C.Ward, S. Foley (2011). Mineral and trace element composition of the Lokpanta oil shales in the Lower Benue Trough, Nigeria. *Fuel*, 90(9), 2843–2849.

[74] R. Motlep, K. Kirsimae, P. Talviste, E. Puura, J. Jurgenson (2007). Mineral composition of Estonian oil shale semi-cokes sediment. *Oil Shale*, 24(3), 405–422.

[75] Y. Li, S. Wu, X. Yu, R. Bao, Z. Wu, W. Wang, H. Zhan, K. Zhao, Y. Ma, J. Wu, S. Liu, S. Li (2017). Optimization of pyrolysis efficiency based on optical property of semicoke in terahertz region. *Energy,* 126 202-207.

Where $\varepsilon(\omega)$, is the dielectric function, $\varepsilon_{real}(\omega)$ is the magnitude of THz electric field absorbed by the oil shale, $\varepsilon_{img}(\omega)$ is the scattered THz electric field [76]. The comparison between the first and second phases signifies that the absorption of THz pulse is interplay between the kerogen and the mineral constituent. At high temperature, the kerogen macromolecules decompose into lighter molecules mostly with short chains alkanes, while the minerals are decomposed into metals and metallic oxide. At this stage, the absorption of THz pulse is reversed, and mainly dominated by the metallic components[49] [77].Also, at such high temperatures, oil shale with significant pyrite composition decomposes to elemental Iron (Fe) and Sulphur (S), whose ferromagnetic response to an external magnetic field can also be studied to reveal the nature of the constituent minerals. Unfortunately, this has not been investigated in the oil shale. All information regarding the absorbed and scattered THz pulses are deduced by analysing the $T(\omega)$ signal, and subsequently retrieving the refractive index, absorption coefficient and dielectric function of the oil shale.

(i) Refractive index: The refractive index $n(\omega)$, is obtained by comparing the experimental result $T(\omega)$, with its theoretical form $T_{theo}(\omega)$ given by [68];

$$T_{theo}(\omega) = \frac{2n}{(n+1)} \cdot e^{-i(n-1)\frac{\omega d}{c}} . FP \tag{8}$$

Where the first term in equation (8) is the transmission coefficient which considers the effect of amplitude decreases due to absorption as seen in Fig.2. The second term is responsible for the time delay, and represents the phase acquired by the pulse on its passage through the oil shale whose thickness and refractive index is d and n respectively. The FabryPérot (FP) term, accounts for the reflections of the pulse within the oil shale. In cases where thick oil shale is employed, FP reduces to 1, while for thin oil shale, the FP can be evaluated. Similarly, in the reflection mode, the theoretical complex reflectance signal $R_{theo}(\omega)$, is given by

$$R_{theo}(\omega) = \frac{n-1}{n+1} \tag{9}$$

Solving for $n(\omega)$, involves performing the following operations: $T(\omega) = T_{theo}(\omega)$ or $R(\omega) = R_{theo}(\omega)$. The foregoing equation is an inverse value problem that can be solved analytically by assuming an initial guess solution. The fixed-point iteration, Newton Raphson and Nicolson-Ross-Weir method have been so far used to obtain $n(\omega)$ which has been shown to exhibit good correlation with oil yield of oil shales[78]. A plot of $n(\omega)$ normally indicates a narrow decrease with ω. In general, oil shales with lower $n(\omega)$, exhibits a negative correlation with oil yields, i.e. high-oil yielding oil shales have lower $n(\omega)$ and vice versa[72] [79] [80]. It is worth mentioning that the experimental techniques employed in preparing the samples, have impact on the

---

[76] R. Jesch, R. Mclaughlin (1984). Dielectric measurements of oil shale as functions of temperature and frequency. *IEEE Transactions on Geoscience and Remote Sensing, 22(2), 99-105.*

[77] Y. Mai and S. Li (2018). The mechanism and kinetics of oil shale pyrolysis at the presence of water. *Carbon Resources Conversion* , 1(2), 160-164.

[78] T. Ozturk, M.Güneşer (2018). Electrical and electronics properties of materials, chapter 5 (Measurement, methods, and extraction techniques to obtain the dielectric properties of materials).

[79] Y. Li, X. Miao, H. Zhan, W. Wang, R. Bao, W. Leng, Kun Zhao (2018). Evaluating oil potential in shale formations using terahertz time domain spectroscopy. *Journal of Energy Resources Technology*, 140(3).

[80] X. Miao, H. Zhan, K. Zhao, Y. Li, Q. Sun, R. Bao (2016). Oil yield characterization by anisotropy in optical parameters of the oil shale. *Energy and Fuels*, 30(12), 10365–10370.

outcome of the measured $n(\omega)$. Yizhang *et al.* observed that using pulverized over bulk oil shale samples possessed no true correlation with the oil yield. Due to the complex heterogeneity of the oil shale, their properties were altered upon mechanical processing[79] .Thus; it is usually preferable to work with the bulk samples, in which case the original form is preserved. Oil shale has shown to possess anisotropy, in which their optical properties differ in different plane. The presence of lamination, i.e. alternating layers with varying organic matter content in oil shale is a possible reason for anisotropy. As such, during field extraction, it is recommended to cut through the earth crust at specific plane, preferably at the bedding plane of deposition. Xinyang *et al.* [80] investigated the anisotropy of some oil shale in relation to oil yield. In their procedure, they used oil shales cut at a direction parallel to the bedding plane. The refractive index was measured when the incoming THz pulse was incident parallel to the bedding plane of the oil shale, to obtain n_0, then the oil shale is rotated up to 90° to obtain the minimum refractive index, n_{90}. They observed a symmetric behaviour in $n(\omega)$ at every 180°. The anisotropy in $n(\omega)$ is given by

$$\Delta n(\omega) = n_0(\omega) - n_{90}(\omega) \tag{10}$$

A strong positive correlation between $\Delta n(\omega)$ and oil yields from different oil shale has been observed[80] .

(ii) Absorption coefficient: The absorption coefficient $\alpha(cm^{-1})$, measures the magnitude of absorbed THz pulse. $\alpha(\omega)$ is proportional to the imaginary component of the complex refractive index [68],

$$\alpha(cm^{-1}) = \frac{2\omega}{c}\mathrm{Im}[n(\omega)] \tag{11}$$

Typically, $\alpha(cm^{-1})$ increases with THz frequency and falls between *400-1800 cm⁻¹*. A comparison between the absorption plots from different oil shales analysis has indicated that, higher $\alpha\ (cm^{-1})$ corresponds to higher oil yield, and vice versa. However, when the complex refractive index in equation (11) is replaced by $\Delta n(\omega)$, the value of the new absorption coefficient $\Delta\alpha\ (cm^{-1})$, will be lower for higher oil yields, and vice versa[69 80 81]. In order to reveal detailed information about the bulk samples of the Hudian oil shale, Yi *et al.* [75] made several absorption plots at different pyrolysis temperature, to determine the T_{max} for useful oil yields. The T_{max} value corresponded to the maximum recorded temperature just before inconsistency in the absorption plot begins to appear; possibly due to THz absorption by metallic oxides in the pyrolyzed oil shale.

(iii) Dielectric function: The relationship between n, ε and magnetic permeability μ, (wher e μ is a measure of the magnetic response of the oil shale to the THz pulse) is given by, $n = \sqrt{\varepsilon.\mu}$. As in most oil shale THz-TDS, the magnetic permeability is ignored, so that[79],

$$n^2 = \varepsilon \tag{12}$$

---

[81] B. Rima, L. Zhang, Z. Lei, Z. Kun, W. Wei, M. Yue, W. Xun, L. Hua, L. Yuan, X. Zhi (2015). Probing the oil content in oil shale with terahertz spectroscopy. *Science China Physics Mechanics and Astronomy*, 58(11), 114211.

A closely related parameter to the dielectric function is the conductivity σ. The solution of Maxwell equation shows a linear proportionality between ε and σ. Following the work of Y *et al.* [82] which have demonstrated a strong relationship between the ε (and σ) with respect to pyrite and water concentration of simulated anisotropic rock samples, there might exist a likelihood of such relationship in the oil shale.

d) Oil shale-THz waveform (spectrum) characteristics

THz-TDS is rather a comparative than a quantitative study. It serves as an important supplementary technique, to validate the findings from other techniques. The shape and the corresponding spectrum, as well as the maximum amplitude of the THz pulse upon transmission through the oil shale are among the most relevantly studied parameters, used for a qualitative evaluation of the oil shale properties.

(i) Waveform profile: The THz profile of different oil shales obtained at ambient condition i.e. room temperature can be clearly distinguished by the distinct time delay and maximum electric peak E_p, of their waveforms. The minimum peak amidst other peaks has been identified as high-oil yield oil shale, and vice versa. [69 72] Moreover, investigation has been carried out, on the waveform of a single oil shale under increasing temperature up to 1000 °C, and a different trend was observed. The plot of E_p of the waveform obtained at each pyrolysis temperature made by Honglei *et al.* [49], has revealed four stages of oil shale decomposition; from $25-200$ °C, E_p increased, then stabilized around $200-300$ °C, followed by a gradually increase from $300-500$ °C until a maximum is reached, then a sharp decrease between $500-600$ °C was observed. During the first stage, the initial increase in $E_p$was due to moisture loss and become stabilized during the second stage after the moisture content was at minimum. During the third stage, the macromolecules of the kerogen were broken down, resulting to an unexpected increase in $\mathrm{E_p}$ possibly due to the loss of more moisture. During the fourth stage, THz pulses were absorbed due to the decomposition of the minerals to their respective metallic oxides resulting to decrease in E_p nearly up to the same magnitude at 25°C. In a recent work, Honglei *et.al* [69]investigated the absorptive behaviour of oil shales at temperature beyond 600 °C, and observed that, the E_p at 1000°C, was much lesser than at 25°C, due to metallic (semi-coke) formation.

(ii) Spectrum plot: The Fourier transform of the sample THz pulse shown in Fig 3, generates the corresponding spectrum given in Fig. 4. A typical plot of an oil shale-THz spectrum and its reference spectrum are differentiable based on amplitude differences. Obvious absorption dips which could have been a good indicator of the presence of organic compounds have not been well observed in the THz spectrum of oil shale for the range of frequencies less than 2THz[79] .

---

[82] Y. Wang, J. Chen, S. Althaus, M. Yu, J. Chen (2019). Electrical properties of unconventional source rocks from micro-CT using numerical mixing law. *Fuel*, 254, 115576.

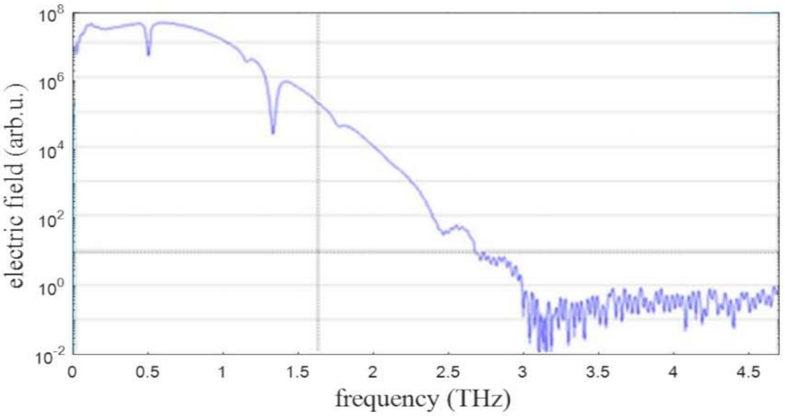

Fig. 4. A Typical spectrum plot from a THz-TDS

(iii) Amplitude measurement: THz subsurface imaging of oil shales has been achieved via the reflection mode of the THz-TDS[72]. The reflected THz amplitude from different regions of the oil shale was employed to reconstruct the non-uniform distribution of organics on the oil shale surface. Three regions corresponding to high kerogen, low kerogen and mineral regions were observed based on the intensity distribution. Results from optical micrographs and micro-Raman spectra showed good agreement with the THz contrast image .

Conclusion and Outlook

Source rocks in the Lopkanta area of Nigeria have been identified as oil shales, following the satisfaction of the requirements for such classification. Majority of the analysed samples were outcrops, whose results (from different analysis techniques) were validated against the geochemical characteristics of the oil shale. Some of the characteristics yielded the expected correlation. Generally, the oil shales were classified as been type I & II with immature to intermediate maturity level. Due to destructive nature of the techniques employed, we suggested the usage of an optical spectroscopic technique based on THz pulse irradiation. Following this suggestion, we presented a general and concise review work involving the application of THz-TDS to oil shale analysis. Single-cycle THz pulses were employed to probe the oil shale in order to determine the relative amount of oil yields, determine the maximum temperature for efficient oil yield, and generate contrast images of the oil shale constituent. Since in the past few years, there has been a growing trend in the use of THz-TDS to investigate the oil shale, we are quite hopeful that adoption of some techniques would guarantee additional information about the oil shale. As such, we make the following suggestion; firstly, we propose the adoption of a THz-Time Resolved Spectroscopy (THz-TRS) technique[83] to solve the unresolved absence of absorption peaks in the THz spectrum of the oil shale. THz-TRS are transient absorption techniques in which

---

[83] Q. Zhou, X. Zhang (2011). Applications of time-resolved terahertz spectroscopy in ultrafast carrier dynamics (Invited Paper). *Chinese Optics Letter*, 9(11) 11000.